Structural Analysis of the L-Ornithine N^5-Monooxygenase SidA from *Aspergillus* spp.

Von der Fakultät für Lebenswissenschaften

der Technischen Universität Carolo-Wilhelmina

zu Braunschweig

zur Erlangung des Grades einer

Doktorin der Naturwissenschaften

(Dr. rer. nat.)

genehmigte

D i s s e r t a t i o n

von Maike Rochon
aus Wipperfürth

1. Referent: Honorarprofessor Dr. Dirk Heinz
2. Referent: Professor Dr. Michael Steinert
eingereicht am: 29.07.2009
mündliche Prüfung (Disputation) am: 27.11.2009
Druckjahr 2009

Vorveröffentlichungen der Dissertation

Teilergebnisse aus dieser Arbeit wurden mit Genehmigung der Fakultät für Lebenswissenschaften, vertreten durch den Mentor der Arbeit, in folgenden Beiträgen vorab veröffentlicht:

Tagungsbeiträge

Rochon, M., Haas, H., Heinz, D.W.: Structural Analysis of the L-Ornithine-N^5-Monooxygenase SidA of *Aspergillus fumigatus*. (Poster) Jahrestagung der Deutschen Gesellschaft für Kristallographie, Freiburg (2006).

Rochon, M., Haas, H., Heinz, D.W.: Structural Analysis of the L-Ornithine-N^5-Monooxygenase SidA of *Aspergillus fumigatus*. (Poster) 11th International Conference on the Crystallization of Biological Macromolecules, Quebec, Canada (2006).

Rochon, M., Haas, H., Heinz, D.W.: My journey towards solving the structure of the *Aspergillus* Monooxygenase SidA. (Vortrag) 9th Heart of Europe Meeting on Bio-Crystallography, Teistungenburg (2006).

Rochon, M., Haas, H., Heinz, D.W.: Solving the Crystal Structure of the *Aspergillus* Monooxygenase SidA: A journey through a low-resolution electron-density map. (Vortrag) 10th Heart of Europe Bio-Crystallography Meeting, Bedlewo, Poland (2007).

Rochon, M., Haas, H., Heinz, D.W.: A Key to *Aspergillus* Virulence: The Monooxygenase SidA. (Poster) Murnau Conference on Structural Biology of Disease Mechanism, Murnau (2007).

Contents

Summary **1**

1 Introduction **2**

1.1 Aspergillus fumigatus: A Dr. Jekyll and Mr. Hyde Theme 2

1.2 Virulence Determinants of A. fumigatus 7

1.3 Iron Acquisition 8

1.3.1 Iron Uptake and Cellular Toxicity: A Balancing Act 8
1.3.2 Metalloreductases and Ferroxidation: Cellular Iron Import Routes 11
1.3.3 Mammalian Iron-binding Proteins 12
1.3.4 The Siderophore System 13

1.4 The Aspergillus spp. Siderophores 15

1.4.1 Siderophore Biosynthesis in *Aspergillus* spp. 16
1.4.2 Siderophores: a Key Feature in *A. fumigatus* Virulence 18

1.5 The L-Ornithine N^5-Monooxygenase SidA 19

1.6 Aim of this work 23

2 Methods **24**

2.1 Cloning, Protein Expression and Purification 24

2.1.1 Generation of Plasmid Constructs 24
2.1.2 Site-directed Mutagenesis 25
2.1.3 Bacterial Growth and Induction of Protein Expression 26
2.1.4 Harvest and Lysis of E. coli Cells 26
2.1.5 Affinity Chromatography 26
2.1.6 Ion Exchange Chromatography (IEC) 27
2.1.7 Gel Permeation Chromatography (GPC) 27
2.1.8 Anaerobic Protein Purification 27
2.2 Analytical Methods 28
2.2.1 Protein Concentration Determination 28
2.2.2 Determination of the FAD-SidA Stoichiometry 28
2.2.3 Reconstitution of PvdA Apoprotein with FAD 29
2.2.4 Concentration of Protein Solutions 29
2.2.5 Oligomerization Studies 29
2.2.6 N-terminal Sequencing 30
2.3 Enzyme Assays 30
2.3.1 NADPH Oxidation Assay 30
2.3.2 Hydroxylation (Iodine Oxidation) Assay 30
2.3.3 Determination of the Catalytic pH Optimum 31
2.3.4 H_2O_2 Detection 31

2.4 Crystallization 32

2.5 Data Collection and Structure Determination 35

2.5.1 Screening for X-ray Diffraction 35
2.5.2 Native Data 36
2.5.3 Molecular Replacement 36
2.5.4 3-Wavelength MAD Experiment 36
2.5.5 Twinning Analysis 36
2.5.6 Model Building and Refinement 36

2.6 Figure Preparation 37

3 Results 38

3.1 Biochemical Properties of SidA 39

3.1.1 Protein Expression and Purification 39
3.1.2 Enzyme Activity of SidA 44
3.1.3 Substrate Specificity of SidA 45
3.1.4 Enzyme Activity in the Absence of Substrate 47

3.2 SidA Crystallization 51

3.2.1 Crystallization of SidA from *A. fumigatus* 51
3.2.2 Crystallization of SidA from *A. nidulans* 51

3.3 Optimization Strategies for SidA Crystals 53
3.3.1 Protein Surface Modification 53
3.3.2 Replacement of Cysteines 55
3.3.3 Crystallization under Anaerobic Conditions 56
3.3.4 Crystallization of Truncated SidA Variants 57
3.3.5 Crystallization with Oil 60
3.3.6 Crystal Growth within a Gel Matrix 60
3.3.7 Crystallization with Substrates and Additives 61
3.3.8 Cryoprotection of SidA Crystals 61
3.3.9 Seeding Techniques 62

3.4 Data Collection and Phasing 64

3.4.1 Space Group Determination 64
3.4.2 Molecular Replacement 66
3.4.3 3-Wavelength MAD Experiment 68
3.4.4 Solution of the Se-substructure 71
3.4.5 Density Modification 73

3.5 Model Building and Refinement 77

3.5.1 The SidA Protomer Displays a Typical Monooxygenase Fold 86
3.5.2 The SidA Protomer Resembles the FMO from *Methylophaga* sp. 88
3.5.3 The FAD-binding Domain 92
3.5.4 The NADPH-binding Domain 94
3.5.5 The Putative Substrate Binding Site 95

3.5.6 The SidA Structure is Arranged as a Dimer of Dimers 97
3.5.7 Cysteines Contribute to SidA-Oligomerization 99

3.6 The Monooxygenase PvdA of *P. aeruginosa* 101

3.6.1 Expression and Purification of PvdA 102
3.6.2 Oligomerization of PvdA 104
3.6.3 PvdA Crystallization 106

4 Discussion 107

4.1 SidA Catalytic Activity Resembles that of IucD and PvdA 107

4.2 Substrate Binding is Required for Efficient FAD Reduction 110

4.3 Lysine Functions as NADPH Oxidase Effector 111

4.4 SidA is a Class B Flavoprotein Monooxygenase 111

4.5 SidA Tightly Embraces its Prosthetic Group 113

4.6 The Two-Domain Architecture and its Role in Catalysis 113

4.7 The Role of the ATGY Motif 117

4.8 Cys62 and Cys66 Promote SidA Crystallization 119

4.9 SidA Crystals Reveal a Loose Packing 120

4.10 Protein Flexibility versus Model Errors: Major Obstacles for Structure Determination and Refinement 121

4.11 PvdA is a Tetramer with Similar Features as SidA 122

5 Outlook 125

5.1 Structure and Function of SidA 125

5.2 The SidA Homologue PvdA 127

References 129

Danksagung 154

Appendix 157
A.1 SidA Activity Resembles that of IucD and PvdA 157
A.2 The Flavin Cofactor 158
A.3 Data Collection 160
A.4 Model Building 161
A.5 The FMO from *Methylophaga sp*. 164

Table of Figures 165

Lebenslauf 168

Abbreviations

A	Absorption
Å	Ångstroem (0.1 nm)
A. fumigatus	*Aspergillus fumigatus*
ABTS	2,2'-azino-bis-3-ethylbenzthiazoline-6-sulfonic acid
ADA	N-(2-Acetamido)iminodiacetic acid
AU	a) Absorption unit; b)Asymmetric unit
BLAST	Basic local alignment search tool
BVMO	Baeyer-Villiger monooxygenase
bZIP	basic-leucine zipper
cAMP	3'-5'-cyclic adenosine monophosphate
CC	Correlation coefficient
CCP4	Collaborative Computational Project Number 4
CV	Column volume
DALI	Distance alignment server
DLS	Dynamic light scattering
DFM-	α-difluoromethyl-
DTT	Dithiotreitol
EM	Electron microscopy
eq.	Equation
ER	Endoplasmatic Reticulum
FAD	Flavin adenine dinucleotide (oxidized)
FADH	reduced FAD
FC	Ferricrocine
FOM	Figure of merit
FMO	Flavin-containing monooxygenase
FusC	Fusarinine C
GPC	Gel Permeation Chromatography
HFC	Hydroxyferricrocine
hFMO	human FMO
His_6	His-His-His-His-His-His
HMM	Hidden Markov model
HPAH	*p*-hydroxyphenylacetate hydroxylase
HR	High energy remote
HRP	Horseradish peroxidase
IA	Invasive aspergillosis
IEC	Ion exchange chromatography
IPTG	Isopropyl-β-D-thiogalactoside
kcat	Turnover number
K_M	Michaelis-Menten constant
LM-agarose	Low-melting agarose
mFMO	FMO of *Methylophaga* sp.
MAD	Multiple-wavelength anomalous dispersion
MMZ	Methimazole (1-Methyl-1,3-dihydro-2H-imidazole-2-thione)
MO	Monooxygenase

MR	Molecular Replacement
M_r	Molecular mass
n.d.	No significant signal detected
$NADP^+$	Nicotinamide-adenine-dinucleotide phosphate (oxidized)
NADPH	Nicotinamide-adenine-dinucleotide phosphate (reduced)
NR	Non-redundant protein sequence database
Ni-NTA	Nickel(II)-nitrilotriaceticacid
OMO	Ornithine monooxygenase
p.a.	*pro analysis*
PAMO	Phenylacetone monooxygenase
P. aeruginosa	*Pseudomonas aeruginosa*
PCR	Polymerase chain reaction
PDB	Protein Data Bank
PEG	Polyethyleneglycol
PHBH	p-hydroxybenzoate-3-hydroxylase
pI	Isoelectric point
PSI-BLAST	Position specific iterative BLAST
PvdA	L-ornithine N^5-monooxygenase of *P. aeruginosa*
r.m.s.d.	Root mean square deviation
R_h	Hydrodynamic radius
RIA	Reductive iron assimilation
S. cerevisiae	*Saccharomyces cerevisiae* (baker`s yeast)
SDS	Sodium dodecylsulfate
SDS-PAGE	SDS-polyacrylamide gel electrophoresis
SidA	L-ornithine N^5-monooxygenase of *A. fumigatus*
$SidA^{SeMet}$	Selenomethionine derivatized SidA
SeMet	Selenomethionine
spFMO	FMO of *Schizosaccharomyces pombe*
TAFusC	Triacetylfusarinine C
T. fusca	*Thermobifida fusca*
TrxR	Thioredoxin reductase
V_e	Elution volume
V_M	Matthews coefficient

Summary

Aspergillus fumigatus is a ubiquitous filamentous fungus that causes more infections worldwide than any other mould. It enters the body via the lung and is the major cause for invasive mould infections. Especially immunocompromised populations are susceptible to invasive aspergillosis. Due to the high mortality rate of invasive aspergillosis and the lack of an efficient antifungal therapy there is an urgent need for new antifungal drug targets and drug development. For survival and virulence in the host *A. fumigatus* is dependent on special iron chelating compounds, so-called siderophores. The key enzyme in the hydroxamate-type siderophore biosynthesis of *A. fumigatus* is the L-ornithine N^5-monooxygenase SidA. It has been shown that SidA-knock-out mutants are no longer virulent in a mouse model of invasive aspergillosis. Since this biosynthesis system is absent in mammals, SidA represents a possible target for an antifungal drug therapy. Structural analysis of SidA may therefore contribute to a rational drug design approach.

In the present study SidA enzymes from two *Aspergillus* strains, *A. fumigatus* and *A. nidulans*, have been recombinantly expressed in *Escherichia coli*, purified and crystallized for subsequent X-ray analysis and structure solution. In the course of the present project the SidA from *A. nidulans* proved to be more suitable for crystallization than the orthologous enzyme from the more pathogenic *A. fumigatus*. Therefore attempts to solve the SidA crystal structure were continued on the *A. nidulans* protein. However, despite various efforts to improve the quality of the obtained SidA crystals, their X-ray diffraction potential could only be improved to a maximum resolution of 3.2 Å. The SidA crystal structure was finally accomplished by the multiple-wavelength anomalous dispersion (MAD) technique. The structural model obtained so far displays a typical flavin-oxidoreductase fold with a topology that is highly homologous to the flavin monooxygenases (FMOs) from *Methylophaga* sp.

In addition to studies with L-ornithine monooxygenating enzymes from *Aspergillus* spp., the homologous enzyme (PvdA) from the gram-negative bacterium *Pseudomonas aeruginosa* was also cloned and crystallization conditions have been set up − primarily for comparative analysis.

1 Introduction

This century's medical challenges, in particular HIV, cancer and immunosuppressive therapy, have given rise to an increasing number of immunocompromised patients. Their weakened immune system opens the door to many microbial invaders entering the body without being defended, leading to systemic infections and as a consequence to increased mortality rates. Despite antibiotic therapies the occurrence of resistant pathogens creates the need for a continuous antimicrobial defense. In addition to bacterial and viral infections, an ever increasing number of invasive fungal infections has been observed. This third class of infections is difficult to diagnose and causes high rates of morbidity and mortality that still exceeds 50 % in most human studies (Singh *et al.*, 2003; Lin *et al*., 2001; Singh *et al.*, 1997; Kusne *et al*., 1992). Fungal pathogens possess sophisticated strategies to survive within the host. Being eukaryotes fungi share numerous biological features with humans. Many antifungal drugs therefore prove to be toxic when used therapeutically. Currently standardized vaccines are not available to protect against any of the human infections by fungi. Therefore the research of fungi as well as the investigation of new antifungal drug targets is a pressing demand to human health and to the survival of many debilitated and severely diseased individuals.

1.1 *Aspergillus fumigatus*: A Dr. Jekyll and Mr. Hyde Theme

The genus *Aspergillus* belongs to the phylum of Ascomycota (sac fungi) and comprises over 185 species. The majority of aspergilli are saprophytes that live in soil or on organic decaying matter thereby contributing to the recycling of environmental carbon and nitrogen sources (Tekaia and Latgé, 2005). A number of *Aspergillus* species are frequently used for industrial applications. *A. niger* for example is one of the most widely used "cellular factories" in the production of food ingredients, enzymes and organic acids such as citric acid and gluconic acid (Hertz-Fowler and Pain, 2007) (Table 1-1). Aspergilli furthermore provide a precious resource of secondary metabolites used not only in industry but also in pharmacology and medicine. One example is the cholesterol suppressant drug Mevinolin (Lovastatin) (Alberts *et al.*, 1980), a secondary metabolite of *A. terreus*. Many aspergilli moreover produce potent toxins (Table 1-1). Such mycotoxins

serve to poison the substrate and hence fend off other organisms or have immunosuppressive effects like the gliotoxin from *A. fumigatus* (Sugui *et al.*, 2007; Kamei and Watanabe, 2005; Pahl *et al.*, 1996).

Table 1-1: Examples of *Aspergillus* species, their secondary metabolites, toxins and pathogenicity.

***Aspergillus* spp.**	**Secondary metabolites/Enzymes**	**Pathogenicity**	**References**
A. fumigatus	Fumagillin, gliotoxin	Opportunistic human pathogen	Sugui *et al.*, 2007; Larsen *et al.*, 2007; Kamei and Watanabe, 2005; Pahl *et al.*, 1996; Amitani *et al.*, 1995.
A. nidulans	Caspase-like proteases	Opportunistic, rare human pathogen	Thrane *et al.*, 2004; Segal *et al.*, 1998.
A. niger	Actibind (RNase), glucose oxidase, alpha-galactosidase	Occasional pathogen of man	Kona *et al.*, 2001; Johnson *et al.*, 1998; Gromada and Fiedurek, 1997; Brizova *et al.*, 1992; Voget *et al.*, 1988.
A. oryzae	Amylases, tyrosinases, carboxypeptidases	Domesticated clone of *A. flavus*, non-pathogenic	Ichishima *et al.*, 1984; Azarenkova *et al.*, 1976; Feniskova and Segal, 1953.
A. flavus	Aflatoxin	Opportunistic human and plant pathogen	Hedayati *et al.*, 2007; Nenoff *et al.*, 1997.
A. clavatus	Cytochalasin E	Opportunistic human pathogen	Demain *et al.*, 1976; Buchi *et al.*, 1973.
A. versicolor	Sterigmatocystin	Opportunistic, rare human pathogen	Rippon, 1988; Reiss, 1976; Steyn and Rabie, 1975.
A. terreus	Mevinolin (Lovastatin)	Intrinsically amphotericin B resistant, opportunistic human pathogen	Lass-Florl *et al.*, 2005; Walsh *et al.*, 2003; Baddley *et al.*, 2003; Alberts *et al.*, 1980.

Apart from their metabolic diversity, saprophytic lifestyle and usage in biotechnology, about 10 % of the species live as opportunistic pathogens in humans and animals (Hohl and Feldmesser, 2007) (Table 1-1). Among these *A. fumigatus* is the most common representative causing more invasive infections worldwide than any other mold (Hissen *et al.*, 2005; Wasylnka and Moore, 2002; Latgé, 1999; Sessa *et al.*, 1996). Moreover *A. fumigatus* is unique in its ability to be both, a primary and opportunistic pathogen and a major allergen (Nierman *et al.*, 2005).

Within the phylogenetic kingdom *A. fumigatus* (Figure 1-1 A) is not the most prevalent fungus. However, among fungi with airborne conidia it is the most ubiquitous (Nolard, 1994; Mullins *et al.*, 1984; Mullins *et al.*, 1976). During sporulation every conidial head produces thousands of conidia (Figure 1-1 B and C) that are disseminated through turbulences within the environment and by airflow. Due to their ubiquity and their small size humans inevitably inhale *Aspergillus* spores and with a diameter of 2−3 µm conidia are small enough to bypass the mucociliary clearance of airway epithelia (Ibrahim-Granet *et al.*, 2003; Abarca, 2000; Schaffner *et al.*, 1982; Austwick, 1966). According to environmental surveys all humans inhale several hundred *A. fumigatus* conidia per day (Hospenthal *et al.*, 1998; Goodley *et al.*, 1994).

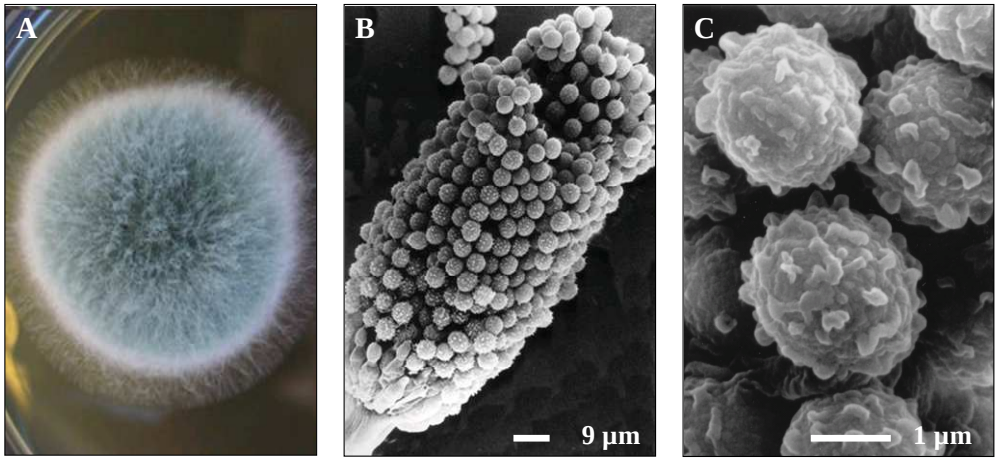

Figure 1-1: *Aspergillus fumigatus* morphology. (A) A four day *A. fumigatus* culture on malt extract agar. (B) Electron micrograph of *A. fumigatus* conidial head. (C) Scanning electron micrograph of *A. fumigatus* conidia. Images A and B: The Fungal Research Trust; Image C: Jahn *et al.*, 2000.

In contrast to other pathogens *A. fumigatus* causes disease in both, immunocompetent as well as in immunocompromised individuals (Figure 1-2). The resulting pathogenic spectrum hence involves allergic diseases such as allergic pulmonary aspergillosis and aspergilloma formation as well as the fatal case of invasive aspergillosis (IA) (Purkayastha *et al.*, 2000; Tenholder, 1985; Forman *et al.*, 1978; Bardana *et al.*, 1975). Its ability to cause damage at the extremes of both weak and strong immune response defines *A. fumigatus* as a prototypical “class four” microorganism (Casadevall and Pirofski, 1999). In the case of allergy, damage is mediated by the host’s disproportionate immune response to *Aspergillus* antigens while in the case of IA damage of the host is primarily caused by the pathogen itself due to hyphal tissue invasion and the release of hydrolytic

enzymes (Alp and Arikan, 2008; Kamai *et al.*, 2006; Lopes Bezerra and Filler, 2004; Tomee *et al.*, 1997; Amitani *et al.*, 1995).

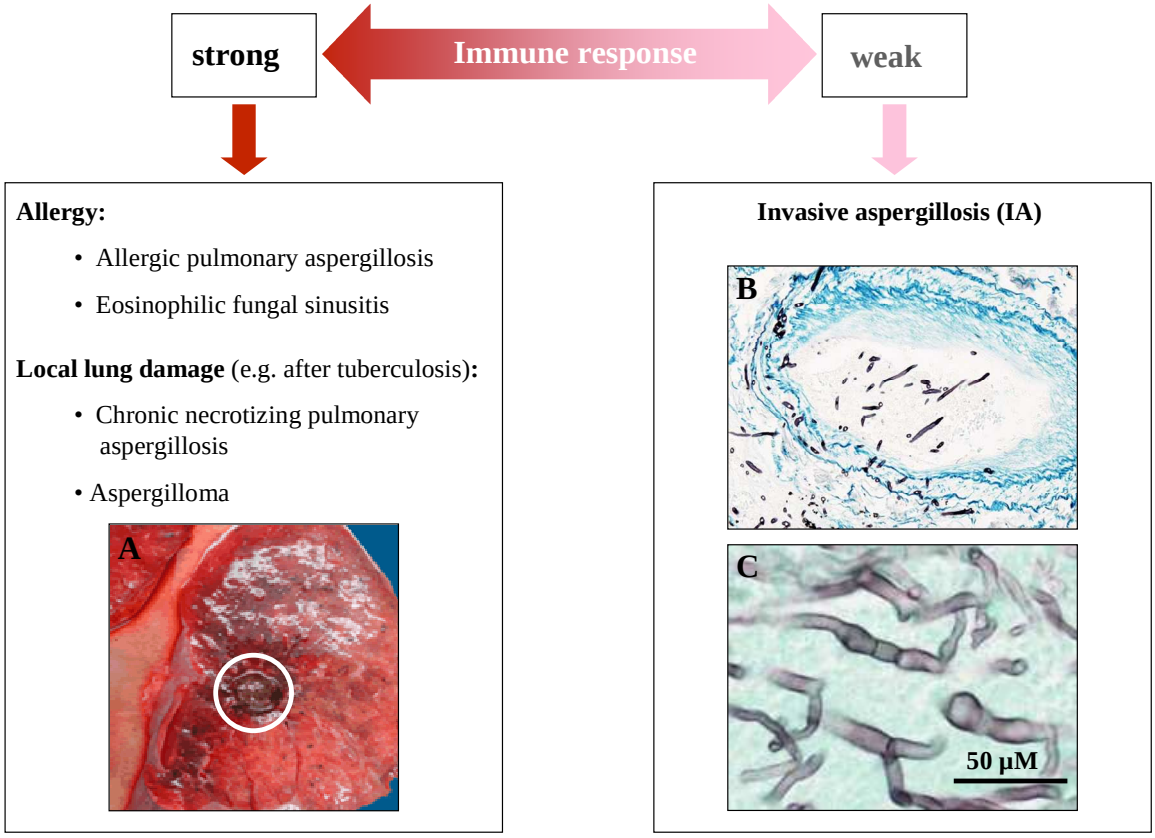

Figure 1-2: *Aspergillus* spp. pathogenicity spectrum. *A. fumigatus* can cause disease in both extremes of host immunity. (A) Gross section of lung at autopsy showing a discrete, well-demarcated dark/black mass surrounded by a fibrotic capsule, an aspergilloma (highlighted by a white circle). (B) Histopathologic image representing angioinvasive aspergillosis (invasion of a lung artery) in an immunocompromised host (autopsy material; Grocott's methenamine silver with Victoria-blue elastica stain). The lung artery appears in light blue, *Aspergillus* hyphae are visible as dark rod-like objects. (C) Histopathologic image of *Aspergillus* hyphae growing in the lung tissue of a patient with pulmonary invasive aspergillosis (autopsy material; Grocott's methenamine silver stain). Image A: Fungal Research Trust; Images B and C: (wikibooks.org, 2006).

Figure 1-3 schematically depicts the infection cycle of *A. fumigatus* in the case of IA. While inhaled conidia are eliminated by alveolar macrophages and polymorphonuclear leukocytes in immunocompetent individuals (Walsh *et al.*, 2005; Clemons *et al.*, 2000), the lung tissue of an immunosuppressed individual provides a nutrient rich substrate for conidial germination. Without an appropriate immune response the fungus continues to grow within the lung producing a network of hyphae that penetrates membranes (Kamai *et al.*, 2006; Wasylnka and Moore, 2003) and finally spreads throughout the lung tissue.

As soon as the fungus enters the blood stream it reaches to other organs like liver and brain where hyphal growth proceeds initiating a systemic infection (Denning, 1998).

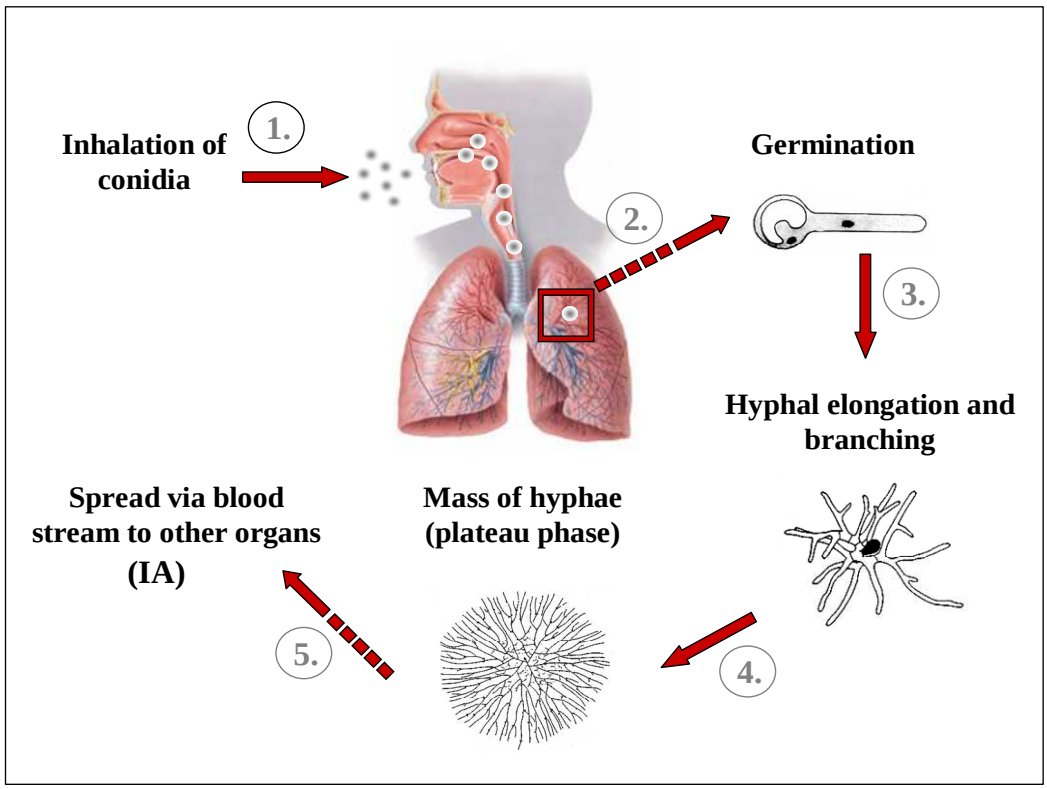

Figure 1-3: Infection cycle of *Aspergillus* spp. leading to invasive aspergillosis (IA). (1) Inhalation of spores that reach the lungs via the respiratory tract. (2) Conidia start to germinate within the lung tissue. (3) Hyphal growth occurs inside the lung tissue. (4) Hyphal growth enters a plateau phase where a mass of hyphae has been produced. (5) Spread of the fungus via the blood to other organs and initiation of a systemic fungal infection (IA). The image was adopted from Jenny Bartholomew and modified (www.aspergillus.org.uk/indexhome.htm?education/slides.htm~main: "An introduction to fungi and *Aspergillus* in health and disease" (The Fungal Research Trust)).

Currently IA accounts for 4 % of the lethal cases in modern, tertiary-care hospitals. It is also the leading infectious cause of death in leukemia and bone marrow transplant patients (Denning *et al.*, 2002; Denning, 1998). A hospital survey revealed that airborne spores of *A. fumigatus* constitute less than 1 % of all spores compared to 50 % of *A. niger*. Nevertheless, close to 50 % of patient isolates were identified as *A. fumigatus* whereas only 17 % were assigned *A. niger* (Schmitt *et al.*, 1990).

The question of how a saprophytic fungus like *A. fumigatus* can turn into an opportunistic pathogen has been raised since the very first description of an aspergillosis in human lung tissue in 1842 by John Hughes Bennett (Bennett, 1842):

"*Are we to consider, that these fungi draw their nourishment from the living animal tissue, and originate disease, or that they are deposited and grow in the inorganic products occasionally found in the textures, and are the results rather than the cause of morbid actions?*"

The ability of *A. fumigatus* to switch from a harmless Dr. Jekyll into a destructive Mr. Hyde is symptomatic for a polygenetic mechanism that favors the survival of the fungus within a hostile environment. Deciphering this mechanism and assigning *Aspergillus* specific virulence factors is one of today's major objectives in the framework of the *Aspergillus* genome project (Nierman *et al.*, 2005).

1.2 Virulence Determinants of *A. fumigatus*

Several putative virulence factors associated with *A. fumigatus* pathogenicity have been identified over the last ten years (Table 1-2). A milestone in identifying genes associated with virulence came with the completion of the *A. fumigatus* genome (Nierman *et al.*, 2005). A range of genes involved in the production of specific secondary metabolites as well as a set of essential genes that might serve as potential drug targets have been revealed by this approach. Table 1-2 summarizes the main *Aspergillus* virulence traits observed to impact on *Aspergillus* pathogenicity. The majority of these potential virulence factors are however involved in multifactorial processes during infection and do not individually promote pathogenicity of *A. fumigatus*. Exceptions include the *A. fumigatus* pigment dihydroxynaphthalene (DHN)-melanin (Brakhage and Liebmann, 2005; Youngchim *et al.*, 2004; Tsai *et al.*, 1998) as well as the siderophore biosynthesis system (Hissen *et al.*, 2005; Wasylnka *et al.*, 2005; Schrettl *et al.*, 2004). The latter system will be the main topic of the following chapters.

Table 1-2: Virulence traits of *Aspergillus* spp.

Feature	Examples of virulence traits	References
Conidial size	–	Rementeria *et al.*, 2005.
Thermotolerance	Nucleolar protein CgrA	Bhabra and Askew, 2005; Araujo and Rodrigues, 2004; Chang *et al.*, 2004.
Pigment biosynthesis	Conidial (DHN)-melanin (*pksP/alb1*)	Brakhage and Liebmann, 2005; Youngchim *et al.*, 2004; Tsai *et al.*, 1998.
Cell wall composition	ß(1-3)-glucan, galactomannan, galactomannanproteins (Afmp1 and Afmp2), chitin synthetases (Chs; *chsE* and *chsG*)	Latgé, 2007; Hohl *et al.*, 2005; Woo *et al.*, 2002; Mellado *et al.*, 1996.
Resistance to oxidative stress	Catalases (Cat1 and Cat2), superoxide dismutases (Mn-SOD and Cu/Zn-SOD)	Sugui *et al.*, 2008; Tekaia and Latgé, 2005; Paris *et al.*, 2003; Levitz and Diamond, 1985.
Adhesins	Hydrophobin RodA (*rodA/hyp1*)	Paris *et al.*, 2003; Wasylnka and Moore, 2000; Girardin *et al.*, 1999; Thau *et al.*, 1994; Parta *et al.*, 1994.
Toxin production	Gliotoxin	Orciuolo *et al.*, 2007; Lewis *et al.*, 2005; Stanzani *et al.*, 2005; Pahl *et al.*, 1996; Sutton *et al.*, 1996; Amitani *et al.*, 1995; Waring *et al.*, 1988.
Growth rate	*cgrA*, *chsC*, *chsG*, *rhbA* (implicated in nitrogen sensing), cAMP-signalling	Rhodes *et al.*, 2006; Paisley *et al.*, 2005; Panepinto *et al.*, 2003; Liebmann *et al.*, 2003; Mellado *et al.*, 1996.
Nutrient uptake	ZafA (transcriptional activator in zinc homoeostasis), Histidine kinase FOS1, *rhbA* (enhances growth on nitrogen-poor sources), cAMP/Pka pathway	Moreno *et al.*, 2007; Rhodes, 2006; Panepinto *et al.*, 2003; Clemons *et al.*, 2002; Oliver *et al.*, 2002; Rhodes *et al.*, 2001.
Siderophore mediated iron acquisition	hydroxamate-type siderophores (L-ornithine N^5-monooxygenase SidA)	Hissen *et al.*, 2005; Wasylnka *et al.*, 2005; Schrettl *et al.*, 2004.

1.3 Iron Acquisition

1.3.1 Iron Uptake and Cellular Toxicity: A Balancing Act

The overwhelming majority of living organisms, including microbial pathogens, are dependent on the availability of iron. Many proteins, and more particularly many

enzymes, depend on iron and iron-containing cofactors such as iron-sulfur clusters or heme. Essential functions of iron-containing proteins include O_2 transport and activation, electron transfer, iron transport and iron storage (Crichton, 2001). Due to its two readily accessible ionization states (reduction potential at neutral pH E_0 = -0.77 V (Loach, 1968)) the Fe^{2+}/Fe^{3+} couple is often used in oxidation/reduction reactions catalyzed by enzymes. However, despite being the second most abundant metal on earth, the supply of soluble iron in aerobic environments is severely limited (Guerinot, 1994; Spiro *et al.*, 1966) due to the formation of insoluble hydroxides by ferric iron at neutral pH under aerobic conditions. The concentration of iron in water is about 10^{-18} M and even lower in human serum (10^{-24} M) (Raymond *et al.*, 2003). Except for a few microorganisms as for example the Lyme disease pathogen *Borrelia burgdorferi* (Nguyen *et al.*, 2007; Posey and Gherardini, 2000) and the probiotic bacterium *Lactobacillus plantarum* (Imbert and, Blondeau, 1998; Archibald, 1986), all pro- and eukaryotes are strictly dependent on iron. Particularly for pathogenic microorganisms the availability of iron within a host organism is highly limited due to host-specific iron binding mechanisms (Smith, 2007; Ratledge, 2007; Ward *et al.*, 2002). Pathogens are therefore only able to survive when possessing specific iron acquisition strategies that can out-compete those of the host organism. As essential as iron is for reproductive growth, it is equally cytotoxic: Fe^{2+} is a strong pro-oxidant and its auto-oxidation produces superoxide radicals (Byers and Arceneaux, 1998; Fleischmann and Lehrer, 1985). Moreover, as depicted in Figure 1-4, ferrous iron reacts with H_2O_2 to produce hydroxyl radicals in the even more favorable Fenton reaction (Halliwell and Gutteridge, 1989).

$$\text{Iron reduction: } \cdot O_2^- + Fe^{3+} \rightarrow Fe^{2+} + O_2 \quad (1)$$

$$\text{Fenton reaction: } Fe^{2+} + H_2O_2 \rightarrow Fe^{3+} + OH^- + HO\cdot \quad (2)$$

$$\text{Haber} - \text{Weiss reaction: } (1) + (2):$$

$$\cdot O_2^- + H_2O_2 \xrightarrow{\text{Fe catalysis}} HO\cdot + OH^- + O_2 \quad (3)$$

Figure 1-4: Key reactions of iron with reactive oxygen species. The one- and two-electron-reduction products of oxygen, superoxide ($\cdot O_2^-$) and H_2O_2, are only mildly reactive physiologically. Iron interacts with these species generating the highly reactive and extremely biotoxic hydroxyl radical ($\cdot$OH) in the Fenton reaction (2). The net reaction of (1) and (2) is known as Haber-Weiss reaction (3).

Thus the cell has to manage the balancing act of providing iron for metabolism without risking the drawback of metal-based oxidation and radical formation resulting in DNA-,

lipid- and protein- damage. In fungi there are four known iron uptake systems: (1) direct Fe^{2+} uptake, (2) reductive iron assimilation, (3) heme uptake and (4) siderophore-mediated Fe^{3+} uptake (Figure 1-5) (Haas *et al.*, 2008; Philpott, 2006).

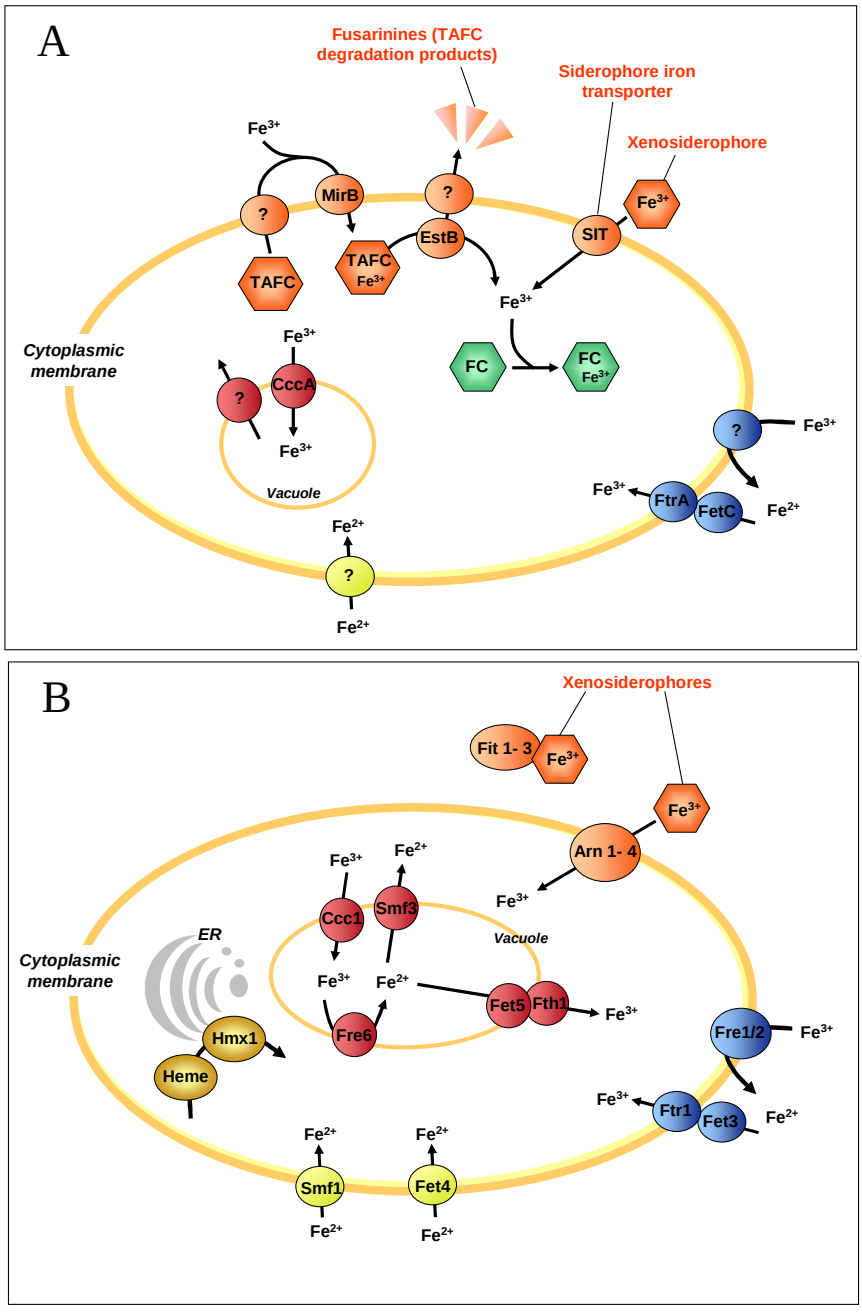

Figure 1-5: Schematic presentation of iron uptake systems in (A) *A. fumigatus* and (B) *S. cerevisiae*. Orange: siderophore-mediated iron uptake; blue: reductive iron assimilation (RIA); green: siderophore-mediated iron storage; red: vacuolar iron storage; dark-yellow: recycling of heme iron; yellow: low-affinity Fe^{2+} iron uptake. Components that have not yet been characterized at the molecular level are denoted by a question mark. The image was adopted from Haas *et al.* (2008) and modified.

With an apparent K_M of ~0.2 µM both, siderophore-mediated iron uptake and reductive iron assimilation belong to the high-affinity iron uptake systems (Kosman, 2003), which are activated under iron-limiting conditions ([Fe] < 100 nM). Heme iron uptake on the other hand is applied by some pathogenic fungi within the host organism environment. If iron is accessible in concentrations equal to or above 1 mM the fungal cell relies on a low-affinity iron uptake system with a K_M for iron in the range of 2−30 µM (Kosman, 2003).

1.3.2 Metalloreductases and Ferroxidation: Cellular Iron Import Routes

For the uptake of ferrous iron two mechanisms are known: either ferrous iron is transported directly into the cell or Fe^{2+} is reoxidized to Fe^{3+}, generally known as ferroxidation (Figure 1-5). Examples include the *S. cerevisiae* Fe^{2+}-transporter proteins Smf and Fet4 where ferrous iron is directly transported into the cell (Cohen *et al.*, 2000; Dix *et al.*, 1997). These low-affinity iron uptake systems do not exclusively transport Fe^{2+} but also other divalent metal ions such as Cu^{2+} and Zn^{2+} (Cohen *et al.*, 2000; Hassett *et al.*, 2000). A homologous ferrous iron uptake system however has not yet been identified for *A. fumigatus*.

In *A. fumigatus* and *S. cerevisiae* the high affinity Fe^{2+} uptake is performed via the FetC/FtrA and Fet3/Ftr1 iron permease/ferroxidase complexes. Unlike the low-affinity iron transport systems, these enzyme complexes are specific for iron. Prior to uptake into the cell the ferrous iron is oxidized to Fe^{3+} by the plasma membrane ferroxidase Fet3. The crystal structure of Fet3 (Taylor *et al.*, 2005) reveals a single transmembrane domain and an extracellular multicopper oxidase domain that catalyzes the oxidation of Fe^{2+} in a Cu^{2+}-dependent mechanism with subsequent reduction of dioxygen to water. The ferric iron produced by Fet3 is the ligand for the iron permease, Ftr1. Most fungi including *Candida albicans*, *Schizosaccharomyces pombe*, *Fusarium graminearum* and *Ustilago maydis* possess homologs of Ftr1, while *A. nidulans* and *Coprinus cinereus* lack this system (Hoegger *et al.*, 2006) being dependent on alternative high-affinity uptake systems such as siderophore-mediated iron acquisition systems.

1.3.3 Mammalian Iron-binding Proteins

In mammals a substantial amount of iron is tightly bound to specific iron-binding proteins such as hemoproteins, ferritin, transferrin and lactoferrin (Bullen and Griffith, 1999). Apart from storing iron in a non-toxic but available form within the body this kind of iron sequestration serves also as defense mechanism against invading pathogens (reviewed by Ong *et al.*, 2006). The majority of the human body iron is constituted by Hemoglobin (Figure 1-6 A) which makes up ~66 % of the total iron pool (Bauer, 2001). Intracellularly iron is stored in the form of ferritin (Figure 1-6 B), a multi-subunit shell composed of 24 subunits of two types, H (heavy) and L (light) (Hempstead *et al.*, 1997), which accumulates up to 45000 Fe^{3+} as ferrihydrite minerals (Harrison and Arosio, 1996).

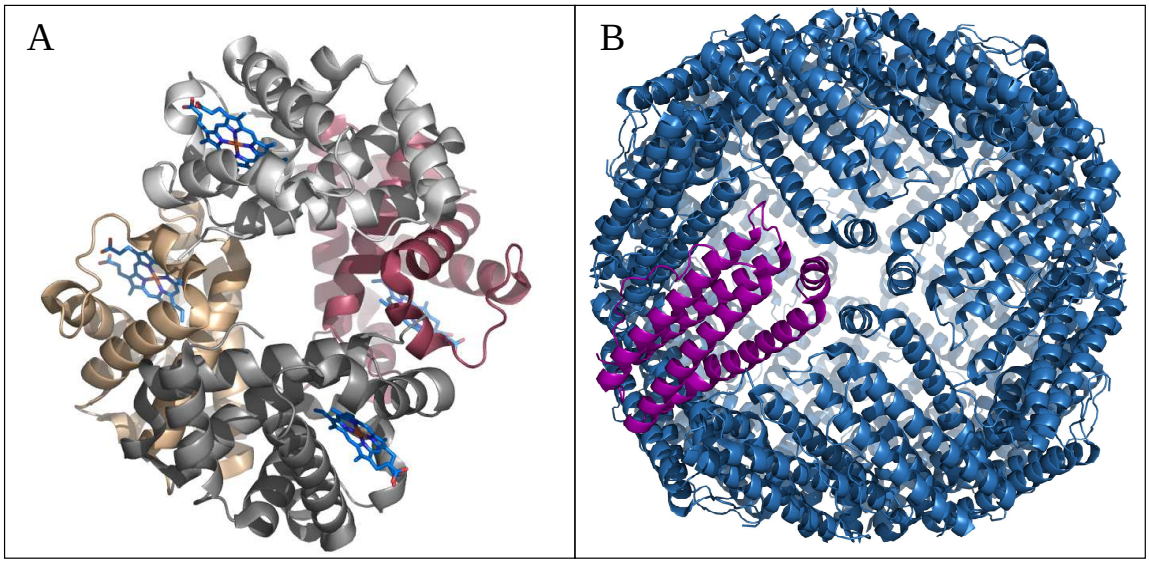

Figure 1-6: Crystal structures of haemoglobin and ferritin. (A) Tetrameric Hemoglobin with four molecules of heme bound (PDB entry: 1gzx; Paoli *et al.*, 1996). (B) L-chain ferritin (monomeric ferritin is highlighted in violet). Image: Vossman (2006) (http://commons.wikimedia.org/wiki/File:Ferritin.png) (PDB entry: 1lb3; Granier *et al.*, 2003).

Extracellularly all circulating plasma iron is essentially bound to transferrin and lactoferrin (Dunn *et al.*, 2007). Transferrin is the most important physiological source of iron for erythropoietic cells (Ponka, 1997) and the major iron transport protein in the human body which makes up ~0.1 % of the human body iron pool (Fleming and Bacon, 2005). Rather than providing iron to cells, the function of lactoferrin is to withhold iron from infectious agents. Being part of the innate immune defense lactoferrin exhibits antimicrobial functions and has fungistatic effects on *A. fumigatus* spores (Jenssen and

Hancock, 2009; Gallin and Zarember, 2007). Due to the limited availability of iron in the host organism many bacterial pathogens have the ability of capturing host iron proteins like ferritin and lactoferrin via extracellular receptors, where the iron is released and imported into the bacterial cell (Ekins *et al.*, 2004; Braun and Killmann, 1999; Schryvers *et al.*, 1998). In fungi binding and uptake of only heme has been found. Heme uptake and utilization depend on an extracellular heme-binding protein (e.g. the GPI-anchored mannoprotein Rbt5p of *C. albicans* (Protchenko *et al.*, 2008)) in conjunction with an intracellular heme oxygenase (e.g. HMX1 from *S. cerevisiae*) (Santos *et al.*, 2003) that degrades the imported heme within the endoplasmatic reticulum (ER) to extract its iron.

1.3.4 The Siderophore System

A fourth high-affinity mechanism of acquiring environmental iron involves the use of siderophore-bound iron. Iron acquisition with the help of low molecular weight (< 1000 Da) high-affinity iron chelating compounds, known as siderophores (Greek for "iron carrier"), is a common strategy for many microorganisms. Enterobactin from *Enterobacteriaceae* and pyoverdin from *Pseudomonas* species represent prominent examples of bacterial siderophores (Figure 1-7).

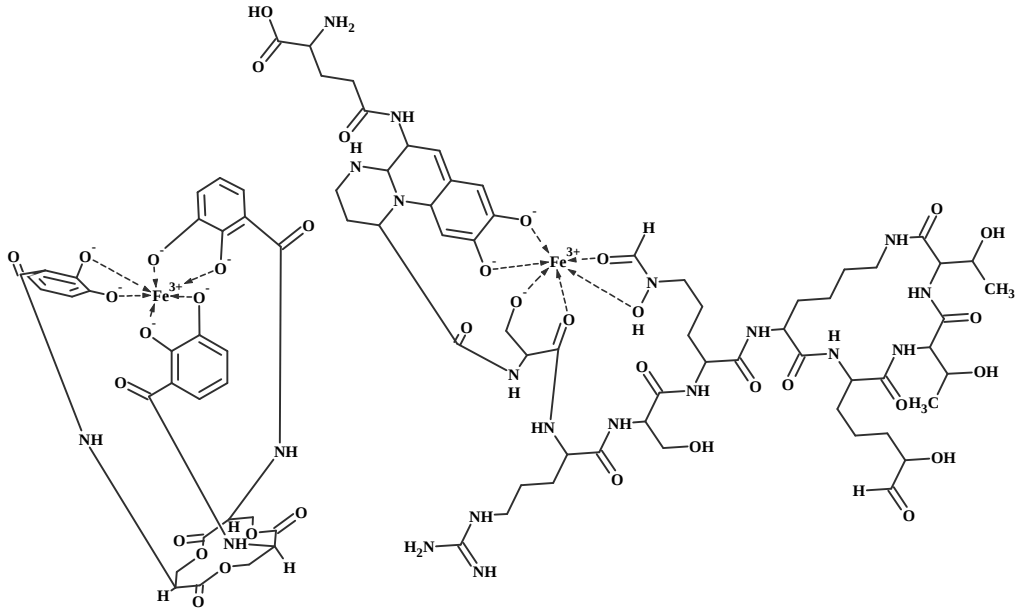

Figure 1-7: Bacterial siderophores. Left: catecholate-type siderophore enterobactin of *Enterobacteriaceae*; right: catecholate-hydroxamate siderophore pyoverdin of *P. aeruginosa*.

Depending on the chemical nature of the moieties donating the oxygen ligands for Fe^{3+}, siderophores can mainly be classified into three groups (Dunn *et al.*, 2007; Drechsel and Jung, 1998): i) aryl caps (catecholates and phenolates), ii) carboxylates and iii) hydroxamates. Moreover mixed variants of all three siderophore types (i - iii) are to be found in nature. Except for the carboxylate siderophore rhizoferrin (Thieken and Winkelmann, 1992), all fungal siderophores identified so far are hydroxamates (Howard, 1999; van der Helm and Winkelmann, 1994).

Because siderophores are used throughout the microbial kingdom, strategies to utilize siderophores of other species (xenosiderophores) have evolved in siderophore-producers and non-producers. For instance *S. cerevisiae*, lacking a siderophore biosynthesis pathway, still uses siderophore-bound iron for its own metabolism. In general fungi apply two mechanisms for siderophore-bound iron utilization (Figure 1-5):

1. Reductive iron assimilation by membrane-bound metalloreductases and subsequent release of ferrous iron from its chelating siderophore.
2. Uptake of ferro-siderophores via siderophore-specific transporters.

Fe^{3+} is usually tightly bound to its specific binding proteins or chelators – in part due to its strong positive charge. One strategy to liberate siderophore-bound iron hence involves reduction of Fe^{3+} to Fe^{2+} thus weakening the interaction to its chelator. In *S. cerevisiae* this reduction is accomplished by ferric reductases of the Fre-family of plasma-membrane proteins (Figure 1-5 B). In fact Fre1p and Fre2p are able to reduce enterobactin-bound iron despite enterobactin being the siderophore with the most negative reduction potential (-750 mV at pH 7; Cooper *et al.*, 1978). Following reduction by Fre1p/Fre2p, Fe^{3+} is released from its chelating siderophore and taken up into the cytosol via the high-affinity iron uptake system (Fet3p/Ftr1p). As part of this process Fe^{2+} is oxidized by the multicopper oxidase Fet3p and transferred to the permease Ftr1p for import into the cytosol. Membrane reductases comparable to yeast Fre1p/Fre2p have not been characterized in *Aspergillus* spp. as yet. However, Fe^{2+}-uptake is presumably accomplished by the putative ferroxidase FetC and the iron-permease FtrA (Figure 1-5 A).

In addition to reductive iron assimilation, Ascomycota like *S. cerevisiae* and *Aspergillus* spp. possess siderophore transporters, which are part of the major facilitator superfamily transporters (MFS) (reviewed by Saier *et al.*, 1999 and Nelissen *et al.*, 1997). Presumably these facilitators function as secondary transporters that depend on an (electro-) chemical gradient to transport the respective iron-loaded molecule. In *A. fumigatus* a putative *A. nidulans* MirB-homolog (Afu3g03640) was identified apparently specific for iron-loaded *Aspergillus* siderophore tiacetylfusarinine C (see next section). Release of tiacetylfusarinine C (TAFusC) bound iron involved hydrolysis of TAFusC-Fe^{3+} by the esterase EstB and an additional unknown mechanism (Figure 1-5 A) (Kragl *et al.*, 2007; Oberegger *et al.*, 2001). TAFusC degradation products are excreted, whereas Fe^{3+} is transferred to the metabolic machinery or stored being bound to FC (Oberegger *et al.*, 2001; Emery, 1976).

At present, only siderophore transport proteins of bacteria have been structurally characterized, the most prominent example being the TonB/FhuA ferrichrome β-barrel transporter of *Escherichia coli* (Carter *et al.*, 2006; Ferguson and Deisenhofer, 2002). FhuA functions as an outer membrane receptor and facilitates transport of hydroxamate-type siderophores and siderophore-antibiotic conjugates to the periplasm while the cytoplasmic membrane complex TonB-ExbB-ExbD provides energy for transport via the proton motive force. Fungal siderophore transporters are presumed to be structurally distinct from the bacterial siderophore transporters (Ratledge, 2007).

1.4 The *Aspergillus* spp. Siderophores

Among the siderophore producing fungi *Aspergillus* spp. are the most thoroughly studied ones. *A. fumigatus* produces mainly two types of siderophores: fusarinine (Fus) and ferricrocin (FC) (Konetschny-Rapp *et al.*, 1988) (Figure 1-8). Both belong to the class of hydroxamate-type siderophores and are synthesized via the same initial biosynthetic pathway (Plattner and Diekmann, 1994). Fusarinine C (FusC) and triacetyl-fusarinine C (TAFusC) are employed for extracellular scavenging of iron while ferricrocin and hydroxyferricrocin (HFC) serve for intracellular iron storage. Thus FC is the main hyphal iron storage compound while HFC is developmentally regulated and used for conidial iron storage in *A. fumigatus* (Schrettl *et al.*, 2007).

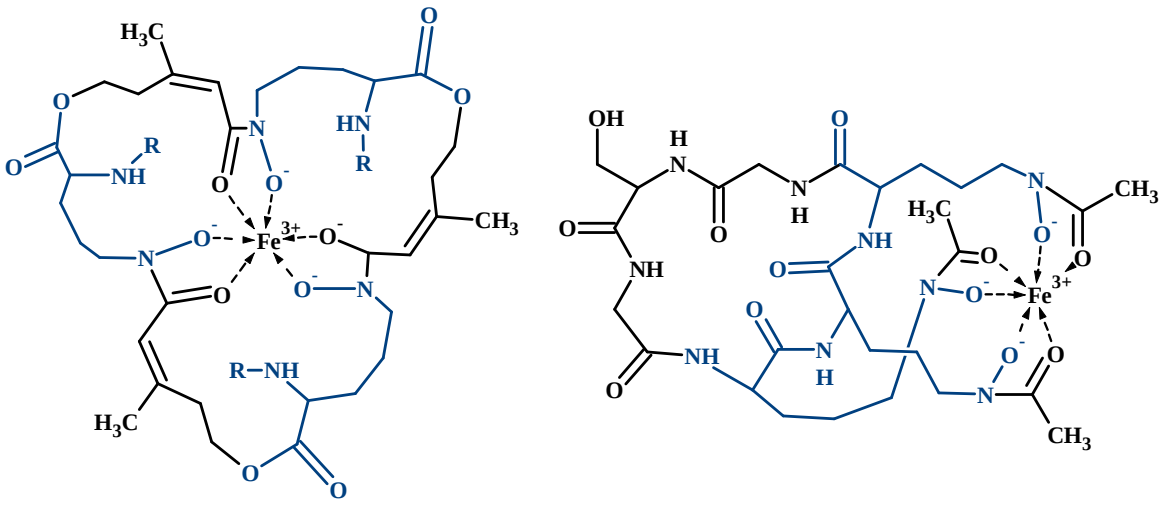

Triacetylfusarinine C Ferricrocin

Figure 1-8: Chemical structures of the *A. fumigatus* siderophores N', N'', N'''-triacetylfusarinine C and ferricrocin. Triacetylfusarinine is used for extracellular, ferricrocin for intracellular iron scavenging. Siderophore building blocks derived from L-ornithine are highlighted in blue. R = acetyl. Image adopted from Winkelmann (1993) and modified.

Extracellular and intracellular iron chelators both have a range of distinct cellular and disease-related roles during mammalian *Aspergillus* infection. Apart from iron deposition intracellular siderophores also serve to ensure non-toxic storage of intracellular Fe^{3+}. In addition siderophores also participate in germ tube formation, asexual sporulation, oxidative stress resistance, catalase A activity and virulence (Schrettl *et al.*, 2007).

1.4.1 Siderophore Biosynthesis in *Aspergillus* spp.

The postulated pathway for *Aspergillus* siderophore biosynthesis (Plattner and Diekmann, 1994) is depicted in Figure 1-9. The basic compound of all four siderophores produced by *Aspergillus* is the non-proteinaceous amino acid L-ornithine. In the initial catalytic step L-ornithine is hydroxylated at its N^5 by the L-ornithine monooxygenase SidA under the expense of NADPH and molecular oxygen yielding N^5-hydroxy-ornithine. In the following steps the hydroxy-N^5-ornithine is activated via coenzyme A and the catalytic cascade is split up into two branches. In one branch the activated hydroxylamine intermediate is linked to cis-anhydromevalonyl-CoA whereas in the other it is linked to acetyl-CoA. In the adjacent biosynthesis steps different non-ribosomal synthetases are involved that accomplish the formation of the siderophore structures consisting of either

three N^2-acetyl-N^5-cis-anhydromevalonyl-N^5-hydroxyornithine residues linked by ester bonds in the case of TAFusC or a cyclic hexapeptide with the structure Gly-Ser-Gly-(N^5-acetyl-N^5-hydroxyornithine)$_3$ in FC. While one branch of this pathway delivers the siderophore equipment for intracellular iron storage (FC, HFC) the other results in siderophores that are used for secretion and extracellular iron scavenging (TAFusC).

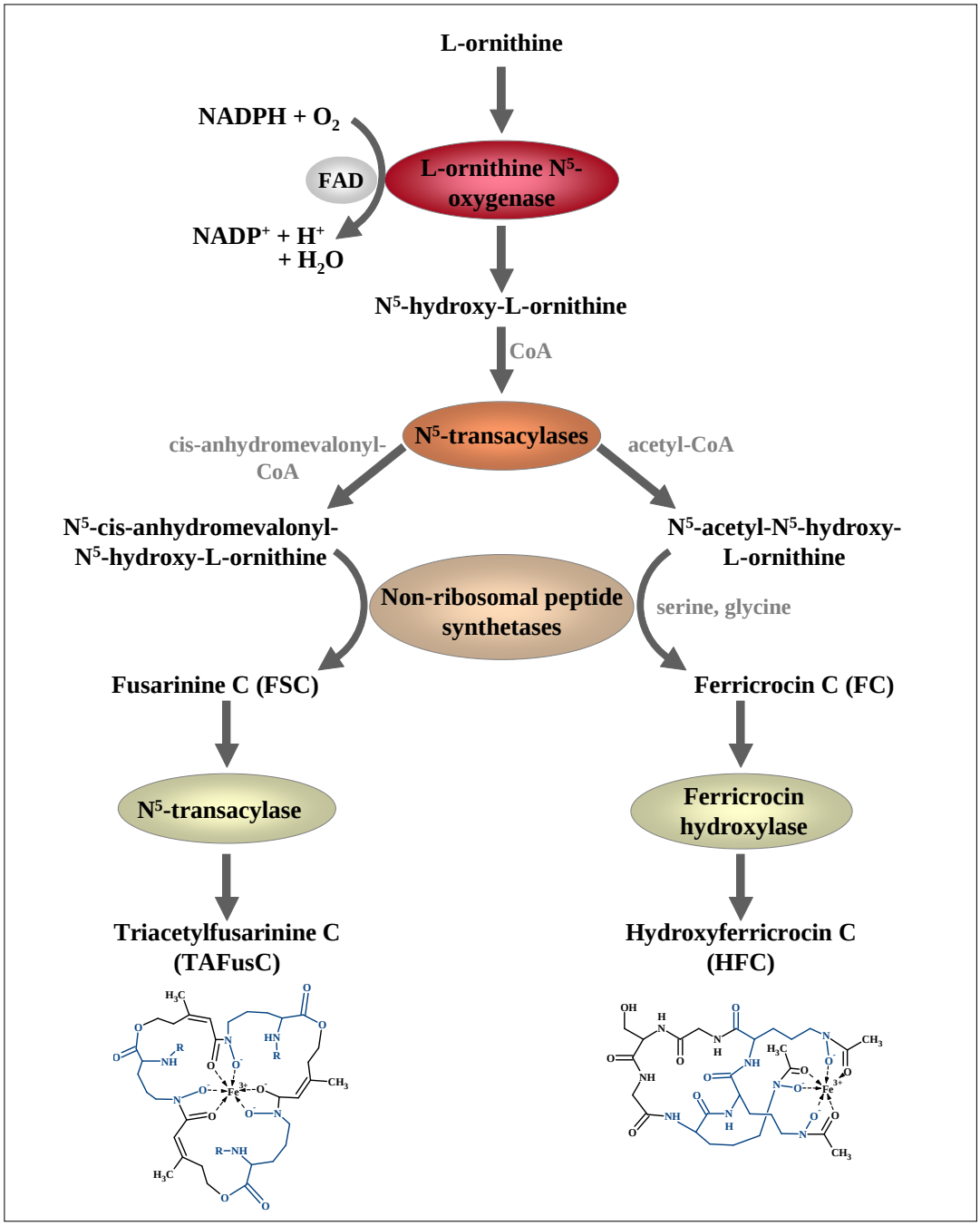

Figure 1-9: Schematic representation of the postulated *A. fumigatus* siderophore biosynthetic pathway. Adopted from Schrettl *et al.* (2007) and modified.

1.4.2 Siderophores: a Key Feature in *A. fumigatus* Virulence

The *A. fumigatus* siderophore system has recently been identified as a major virulence determinant during host invasion (Schrettl *et al.*, 2007; Wasylnka *et al.*, 2005; Hissen *et al.*, 2005; Schrettl *et al.*, 2004). *A. fumigatus* strains impaired in siderophore production are unable to grow on blood agar plates and moreover are avirulent in a mouse model of IA (Schrettl *et al.*, 2004) while conidia defective in siderophore biosynthesis are more susceptible to oxidative stress and killing by alveolar macrophages (Eisendle *et al.*, 2006; Philippe *et al.*, 2003). Deletion of the gene encoding the key enzyme in siderophore biosynthesis, *sidA*, abrogates both intra- and extracellular siderophore production (Schrettl *et al.*, 2004). *In vitro* experiments with *A. fumigatus* mutants grown on blood agar plates indicate that *sid*A is essential for growth in serum whereas activity of the reductive iron permease FtrA did not affect growth under these conditions (Figure 1-10). Supplementation of iron free media with the intracellular siderophore ferricrocin (FC) restores growth of Δ*sid*A mutants (Schrettl *et al.*, 2004).

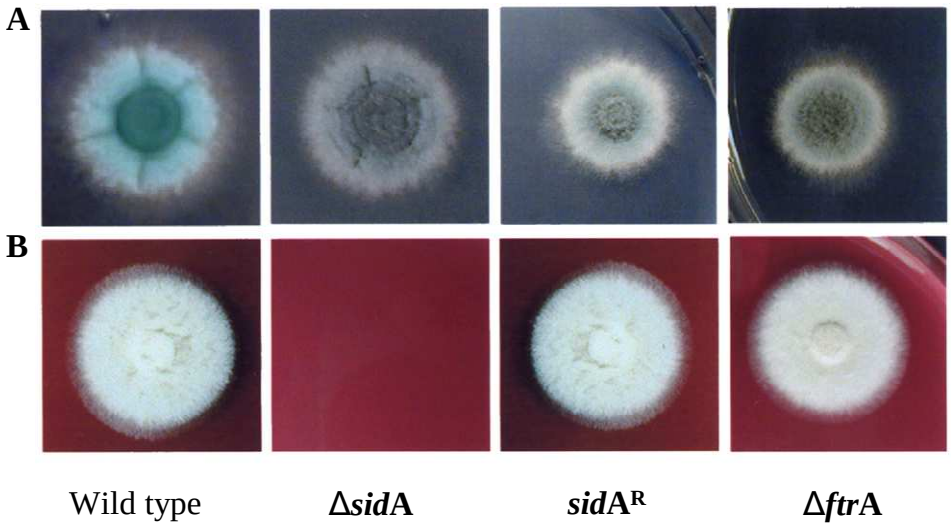

Figure 1-10: Growth phenotypes of *A. fumigatus* wild type and mutant strains. (A) Growth on agar plates supplemented with ferricrocin (FC) as sole iron source. (B) Growth on blood agar plates. *A. fumigatus* wild type strain: ATCC 46645. Image adopted from Schrettl *et al.* (2004) and modified.

In vivo studies using a mouse model for IA moreover demonstrate that deletion of *sid*A leads to the absolute avirulence of *A. fumigatus* (Hissen *et al.*, 2005; Schrettl *et al.*, 2004). Loss of intra- or extracellular siderophore production by deletion of the respective genes *sid*C, *sidF* or *sidD* similarly leads to attenuation of virulence (Schrettl *et al.*, 2007).

In *A. fumigatus* the intracellular siderophore equipment differs between conidia and hyphae and is hence developmentally regulated (Schrettl *et al.*, 2007). In particular the conidial iron storage compound HFC is important in initial stages of infection demonstrated by the fact that supplementation of avirulent Δ*sidA* conidia with the conidial siderophore HFC partly recovers virulence. Derogation of the extracellular siderophore production on the other hand leads to a significant decrease in virulence as well as to an increased sensitivity towards oxidative stress.

Siderophore systems of other fungi have also been designated as true virulence factors. In *Candida albicans* for example the siderophore transporter Arn1p/Sit1p is essential to epithelial invasion and penetration (Heymann *et al.*, 2002) whereas systemic infection is dependent upon ferric reductase activity (Ramanan and Wang, 2000). In the dimorphic fungal pathogen *Histoplasma capsulatum* that colonizes alveolar macrophages and replicates within the phagolysosome, SID1, an orthologue of the *Aspergillus* L-ornithine N^5-monooxygenase SidA, is essential for host colonization (Hwang *et al.*, 2008). Under iron depletion conditions *Histoplasma capsulatum* Δ*sid1* mutants are unable to produce siderophores and are impaired in growth. Similarly Δ*sid1* variants are attenuated in a mouse model of infection and are defective in growth within murine macrophages. In the phytopathogens *Cochliobolus miyabeanus*, *Cochliobolus heterostrophus*, *Alternaria brassicicola* and *Fusarium graminearum* loss of extracellular siderophore production similarly leads to avirulence (Oide *et al.*, 2006; Birch and Ruddat, 2005; Mei *et al.*, 1993).

1.5 The L-Ornithine N^5-Monooxygenase SidA

As outlined above, the L-ornithine N^5-monooxygenase SidA from *A. fumigatus* represents a promising drug target for antifungal therapy both because the siderophore system and its underlying biosynthetic pathway are essential for *A. fumigatus* virulence and because the corresponding biosynthetic enzymes are not present in humans. Inactivating SidA could therefore be a reasonable approach for an antifungal therapy. Moreover many pathogenic fungi share a similar siderophore biosynthesis pathway in which SidA-homologs perform the first committed step in siderophore biosynthesis. Drugs inhibiting SidA could thus combat other fungal pathogens as well.

SidA is an enzyme of 501 amino acid residues with an estimated molecular mass of 56.9 kDa. The catalytic reaction involves the hydroxylation of L-ornithine N^5 at the expense of NADPH and molecular oxygen yielding N^5-hydroxy-ornithine. By sequence comparison SidA can be assigned to the class of oxidoreductases acting on paired donors, with NADH or NADPH as one (hydride) donor and incorporation of one atom of oxygen (EC 1.14.13).

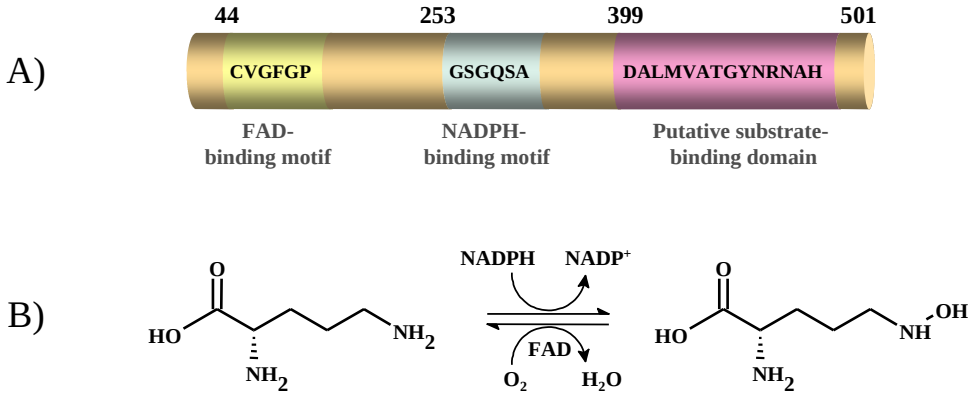

Figure 1-11: Schematic presentation of the SidA domain structure (A) and the hydroxylation reaction catalyzed by SidA (B). (A) The location of the two nucleotide binding motifs as well as the putative substrate binding domain at the C-terminus of the protein are indicated. (B) Conversion of L-ornithine to L-N^5-hydroxy-ornithine by SidA is dependent on FAD and proceeds at the expense of NADPH and molecular oxygen.

Analysis of the SidA sequence reveals three signature motifs typical for ω-amino acid hydroxylases (Stehr *et al.*, 1998) (Figure 1-11): i) A flavin adenine dinucleotide (FAD)-binding motif (GXGXXG) at residues 44-49, ii) a putative nicotinamide adenine dinucleotide phosphate (NADPH)-binding motif (GXGXX($^{G}/_{A}$)) beginning with residue 253 and iii) the ATGY motif (D(X)$_3$($^{L}/_{F}$)ATGY(X)$_4$($^{H}/_{P}$)) beginning with residue 399. The latter (known as the FATGY motif) is a conserved component of mammalian FMOs (reviewed by Krueger and Williams, 2005; Lawton and Philpott, 1993) and was proposed to be involved in substrate binding (Stehr *et al.*, 1998). In SidA the fifth residue of this conserved motif, which is usually occupied by a leucine or phenylalanine is replaced by valine. The FAD-binding motif in SidA displays some special features compared to other flavin binding proteins. Thus the first glycine residue of the GXGXXG binding motif is replaced by a cysteine, while the last glycine is replaced by proline, a feature characteristic of hydroxylases involved in siderophore biosynthesis (Eisendle *et al.*, 2003;

Stehr *et al.*, 1998). The typical fingerprint motif ($FXG(X)_3H(X)_3(^{Y}/_{F})$) of flavin-containing monooxygenases (FMOs) (Fraaije *et al.*, 2002; Ziegler and Poulsen, 1998) is also present though slightly modified through replacement of phenylalanine, by glutamine and of glycine by proline yielding $QXP(X)_3H(X)_3Y$.

Within the class of flavin-dependent oxidoreductases FAD (Figure A-2, Appendix) is used as an electron relay during catalysis. The catalyzed reaction consists of two half-reactions: a reductive half-reaction in which a hydride is transferred from NADPH to the flavin and an oxidative half-reaction in which the reduced flavin is reoxidized. The proposed catalytic cycle is depicted in Figure 1-12.

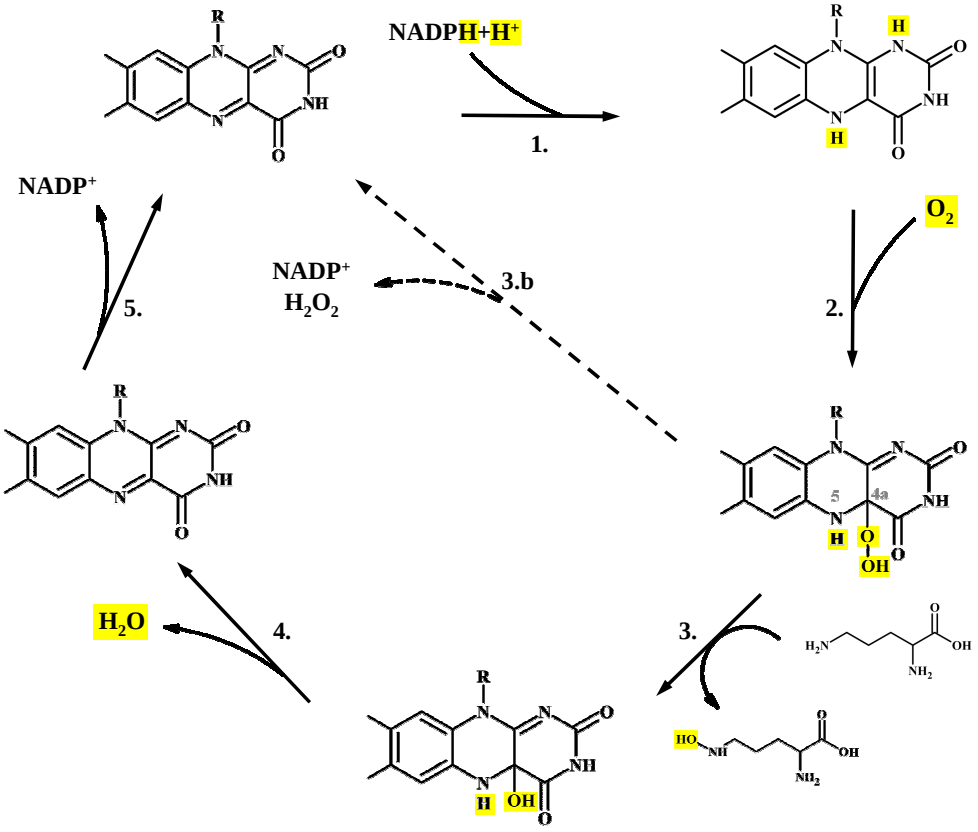

Figure 1-12: Theoretical scheme of the presumed SidA catalytic cycle. The scheme only shows the flavin's isoalloxazine ring and highlightes (in yellow) hydrogen and oxygen atoms involved in hydride transfer and oxygenation reactions. R = adenine, ribose and phosphate moiety of FAD. The reaction cycle can be split up into five steps: (1) Reduction of FAD by NADPH. (2) Formation of the C4a-hydroperoxyflavin upon reaction with O_2. (3) Substrate oxygenation. (4) Regeneration of the flavin cofactor and formation of H_2O. (5) Release of $NADP^+$, which presumably remains bound throughout to stabilize the C4a-hydroperoxy-FAD. In the absence of substrate the reaction cycle can be uncoupled. The enzyme thus functions as a NADPH oxidase (3.b) producing H_2O_2 (dashed line). Image adopted from Alfieri *et al.* (2008) and modified.

Following flavin reduction, the latter binds and activates molecular oxygen to yield the labile C4a-hydroperoxyflavin intermediate. One of the oxygen atoms is inserted into a substrate molecule leaving a second intermediate C4a-hydroxy-FAD. The flavin cofactor is regenerated by protonation and loss of the second oxygen atom as a water molecule. $NADP^+$ is presumed to remain bound to the enzyme throughout the catalytic cycle to stabilize the C4a-hydroperoxy-FAD (Alfieri *et al.*, 2008). Due to the reactivity of the reduced flavin generated during the reductive half-reaction of the proposed catalytic cycle the enzymatic reaction can have different outcomes (compare Figure A-4, Appendix). In the absence of an appropriate substrate the reaction can be uncoupled and NADPH oxidation leads to either oxygen radical formation or to the formation of hydrogen peroxide (Figure 1-12, reaction route 3.b).

SidA shares a high degree of sequence identity (up to 75 %) with L-ornithine N^5-oxygenases from different human- and plant-pathogenic fungi (compare Figure A-1, Appendix). Correspondingly SidA is 33 % identical to L-ornithine N^5-oxygenases from the plant pathogen *Ustilago maydis* (Sid1) and more than 46 % to that of the human pathogens *Histoplasma capsulatum* and *Coccidioides immitis*, respectively. Moreover, SidA is functionally related to many bacterial oxygenases involved in siderophore biosynthesis including PvdA from *Pseudomonas aeruginosa* and IucD from *Escherichia coli* and *Yersinia* species. Like SidA, PvdA and IucD catalyze the first step in hydroxamate-type siderophore biosynthesis (Visca *et al.*, 1994; Herrero *et al.*, 1988; de Lorenzo *et al.*, 1986). PvdA hydroxylates ornithine as the initial precursor substance for the biosynthesis of pyoverdin (Ge and Seah, 2006) whereas IucD catalyzes the hydroxylation of L-lysine at N^6 for the biosynthesis of aerobactin (Stehr *et al.*, 1999). Sequence identity between SidA and PvdA is 38 % and between SidA and IucD variants is ~26 %. Both, IucD as well as PvdA have been biochemically thoroughly characterized (Awaya and Dubois, 2008; Meneely and Lamb, 2007; Stehr *et al.*, 1999; Visca *et al.*, 1994; Thariath *et al.*, 1993; Plattner *et al.*, 1989), though structural data for any of the SidA orthologs or homologs is currently still lacking.

1.6 Aim of this work

As outlined above the L-ornithine N^5-monooxygenase SidA is a major virulence factor of *A. fumigatus* and is discussed as a potential drug target for an antifungal therapy. The aim of this work was therefore to biochemically and structurally characterize SidA variants from *Aspergillus* spp. (*A. fumigatus* and *A. nidulans*) in order to establish a basis for a rational drug design approach. This included (i) establishing of a protocol for expression, purification and crystallization of SidA and (ii) determination of the three-dimensional structure of SidA by X-ray analysis of SidA crystals. Furthermore soaking and co-crystallization experiments with L-ornithine and NADPH were planned to gain structural information on SidA when complexed with substrate. A sufficiently high resolution crystal structure of SidA will provide for detailed insights into the enzyme's catalytic mechanism and allows for the design of future experiments including the use of inactive mutant variants of SidA as well as soaking experiments with potential SidA inhibitors.

2 Methods

All chemicals were purchased from the following companies, if not stated otherwise: Difco, Fluka, GE Healthcare, Hampton Research, Invitrogen, Merck, Millipore, Qiagen, Riedel de Haen, Roche, Roth, Sigma-Aldrich and Stratagene. The quality standard was "*pro analysis*" (p.a.). Molecular-biological methods used in this work are adapted from standard collections of methods and protocols (Ausubel *et al.*, 2007; Coligan *et al.*, 2002; Sambrook and Russell, 2000). These methods will not be explained in detail. Only variations of standard protocols have therefore been described below.

2.1 Cloning, Protein Expression and Purification

2.1.1 Generation of Plasmid Constructs

The DNA for cloning of the *sidA* from *A. fumigatus* (pQE9*sidA*) and *A. nidulans* (cDNA) was provided by Prof. Dr. Hubertus Haas (Medical University of Innsbruck). The genomic DNA for cloning of the *pvdA* gene from *Pseudomonas aeruginosa* PAO1 was kindly offered by Prof. Dr. Susanne Häußler (Helmholtz Centre for Infection Research, HZI, Braunschweig). Within the present work confirmation of positive clones and successful mutagenesis was accomplished using the DNA sequencing service of GATC or Eurofins MWG Operon. Sequencing primers were provided by these companies.

The plasmid construct pQE9*sidA*, cDNA of *A. nidulans* and genomic DNA of *Pseudomonas aeruginosa* (PAO1) were used as templates for amplification of *sidA* and *pvdA* within the polymerase chain reaction (PCR). The respective PCR-primers used and the restriction sites for subsequent cloning into corresponding expression vectors are summarized in Table 2-1.

Table 2-1: Primers used for PCR. Restriction sites are underlined.

Variant	Primer 5´- 3´	Restriction sites
$sidA^{AF}$ **fw**	AGGAGGAATTCATGGAATCTGTTGAACGGAAGTCAGAA	EcoRI
$sidA^{AF}$ **rv**	AGGAGCTCGAGTTACAGCATGGCTCGTAGCTGGTGG	XhoI
$sidA^{AN}$ **fw**	AGGAGCATATGGAGCCCCTCCAGCGGAAGTCA	NdeI
$sidA^{AN}$ **rv**	AGGAGGAATTCTTACAGCATAGCGCGGAACCTGGTGT	EcoRI
pvdA **fw**	AGGAGCATATGACTCAGGCAACTGCAACCGCC	NdeI
pvdA **rv**	AGGAGCTCGAGTCAGCTGGCCAGGGCGTGCTCG	XhoI
$sidA^{AF}$ΔN32	AGGAGCATATGTCAACACCCCAGGATGAGCTTC	NdeI
$sidA^{AN}$ΔN17	AGGAGCATATGCCTCTCGCGCAACAACGGACTC	NdeI
$sidA^{AN}$ΔN26	AGGAGCATATGTTAAAACCAACGTCTCCTGAGGAGCTG	NdeI

fw: forward primer; **rv**: reverse primer; reverse primer used for generation of the N-terminal deletion constructs corresponds to $sidA^{AF}$ and $sidA^{AN}$ **rv**, respectively.

The PCR was performed according to established standard protocols based on the manufactures instructions using Pfu DNA polymerase and respective amplification buffer

as well as a mixture of dNTPs. PCR amplified DNA was subjected to an agarose-gel electrophoresis and extracted from the agarose using the Qiagen gel extraction kit. Digestion of expression vectors and PCR amplificates was performed using restriction enzymes from New England Biolabs (NEB) according to the manufacturer's protocol. After purification of digested DNA amplificates and vectors, following the generally established methods, inserts and vectors were ligated (Ligase from Roche) and transformed into chemically competent or electro-competent *E. coli* XL1-Blue cells (*recA1 endA1 gyrA96 thi-1 hsdR17 supE44 relA1 lac* [*F´proAB lacIqZΔM15 Tn10 (Tet$_r$)*], Stratagene).

Table 2-2: Plasmids and host strains used for protein expression.

Protein	Plasmid/expression strain	Origin
SidA^{AF}	pQE9/M15(pREp4)	H. Haas
SidA^{AF}	pET-28c(+)/Tuner	This work
SidA^{AN}	pET-28c(+)/Tuner	This work
SidA^{AN}C151S	pET-28c(+)/Tuner	Lisson, 2007
SidA^{AN}ΔN17	pET-28c(+)/Tuner	This work
SidA^{AN}ΔN26	pET-28c(+)/Tuner	This work
SidA^{AF}ΔN32	pET-28c(+)/Tuner	This work
SidA^{AN}R314S	pET-28c(+)/Tuner	This work
SidA^{AN}R16S	pET-28c(+)/Tuner	This work
PvdA	pET-28c(+)/Tuner	This work

2.1.2 Site-directed Mutagenesis

For site-directed mutagenesis reactions the QuikChange^{TM} Kit (Stratagene) was used to mutate the pET-28c(+)*sidA^{AN}* expression plasmid. The desired mutations were introduced during a PCR using an excess of mutagenesis primers. After specific digestion of the methylated, original template DNA, the amplified mutated plasmids were transformed into supercompetent *E. coli* XL1-Blue cells. The following oligonucleotides were used as forward PCR primers for the mutagenesis reactions (reverse primers are complementary), mutated sites are highlighted in red:

SidA^{AN}R16S:	GACTTCCCAGAGTTATAGCAAGATGCCTCTCGCGC
SidA^{AN}R314S:	GCTGAGCGCGAGAGTTCGCTCAAGGCG
SidA^{AN}Y404S:	GTCGCTACGGGTTCCAACCGCAACGCGCAT
SidA^{AN}E311S/E313A/K317A/K320S:	CTCGGCCGCTTCGCGCGCGTTCGCTCGCGGCGGATTCG GCTACCAACTAG
SidA^{AN}Q253A:	CTGGGAAGCGGCGCGAGTGCTGCTGAG
PvdAG15C:	GGGCCGAAGCCGACACAGATGAGATCGTGAACC

Expression and purification of SidA mutants was performed as described for the wild-type protein.

2.1.3 Bacterial Growth and Induction of Protein Expression

The majority of the constructs produced within the scope of this work was cloned in a way that the resulting protein construct featured an N-terminal His_6-fusion-tag. In general proteins were produced in *E. coli* Tuner cells (F^- *ompT hsdS*$_B$(r_B^- m_B^-)*gal dcm lacY* (DE3) pLacI (Cm^R), Novagen) in LB-medium supplemented with 30µg/ml kanamycin. At an OD_{600} of 1.0 (37°C), protein expression was induced by 0.3 mM IPTG (isopropyl-β-D-thiogalactoside) and continued for either ~5 h at 25°C or for 15-27 h at 20°C (Table 2-3). For the production of Se-derivatized SidA the expression protocol established by Guerrero and coworkers (Guerrero *et al.*, 2001) was used. To optimize incorporation of the FAD cofactor during SidA expression, the SeMet containing medium was supplemented with riboflavin (1.25 mg/l), nicotinamide (1 mg/l) and pyridoxine (1 mg/l).

Table 2-3: Protein expression conditions.

Protein construct*	Expression temperature	Expression period
$SidA^{AF}$	20ºC	15 to 17 h
$SidA^{AN}$	25ºC	5 h
$SidA^{SeMet}$	20ºC	15 to 17 h
PvdA	20ºC	15 to 17 h

*All protein variants produced contained an N-terminal His_6-tag.

2.1.4 Harvest and Lysis of E. coli Cells

Bacterial cells were harvested by centrifugation (15 min at 6000×g), resuspended in PBS (containing 2.5 mM β-mercaptoethanol and 1 µl benzonase (4.2 U/µl, Merck) per liter of bacterial culture), either disrupted by means of a French press (Thermo Scientific) or by a high pressure cell disrupter (Constant Systems). The lysis-buffer was composed of 100 mM K_2HPO_4/KH_2PO_4 pH 8.0, 100 mM NaCl and one tablet "Complete" (EDTA-free) protease inhibitor cocktail (Roche). Cell debris was removed by centrifugation (45 min at 39800×g). All steps were performed at a maximum temperature of 4ºC.

2.1.5 Affinity Chromatography

Initial purification was achieved by Ni-NTA affinity chromatography (Qiagen). Immobilized proteins were washed with ~500 ml wash-buffer (100 mM K_2HPO_4/KH_2PO_4 pH 8.0, 100 mM NaCl, 5 mM β-mercaptoethanol). The proteins were eluted by stepwise addition of elution buffer (wash-buffer supplemented with 0.5 M imidazole; steps: 20, 40, 60, 100, 200, 500 mM imidazole). Subsequent to elution purified protein fractions were dialyzed against respective buffer solutions: 50 mM sodium phosphate buffer pH 7.0 supplemented with 0.1 M NaCl, 5 mM DTT in the case of $SidA^{AF}$, 10 mM CHES pH 10.0 supplemented with 0.1 M NaCl, 5 mM DTT for dialysis of $SidA^{AN}$ and 10 mM Hepes pH 8.5 supplemented with 0.1 M NaCl, 5 mM DTT in the case of PvdA. The presence of NaCl was crucial to the stability of all purified proteins which otherwise precipitated within 12-24 h.

2.1.6 Ion Exchange Chromatography (IEC)

The dialyzed protein solution obtained by affinity chromatography was loaded onto an ion exchange column (MonoS or MonoQ HR10/10, GE Healthcare) equilibrated with low salt buffer (Table 2-4). The protein was loaded onto the column in the presence of 2 mM NaCl. Elution of the protein was achieved with a linear gradient from 2-800 mM NaCl within 10 column volumes (CV) finishing with a final step to 1.0 M NaCl in one CV. The IEC run was performed with a flow rate of 2-3 ml/min. Fractions (1.5 ml) were collected and OD_{280} measured. Fractions absorbing stronger than buffer were analyzed by gel electrophoresis, pooled if appropriate and stored at 4ºC.

Table 2-4: Conditions used for protein purification by IEC.

Protein construct	Estimated pI[b]	IEC-buffers[a]	Elution gradient/No. CV
$SidA^{AF}$-His_6	8.62	50 mM sodium phosphate pH 7.5, 2 mM NaCl, 5 mM DTT	0-800 mM/12
$SidA^{AN}$-His_6	8.1	10 mM CHES pH 10.0, 2 mM NaCl, 5 mM DTT	2.0-800 mM/10
PvdA-His_6	6.81	10 mM Hepes pH 8.5, 2 mM NaCl, 5 mM DTT	2.0-800 mM/10

a) Low and high salt buffer compositions are identical except for the amount of NaCl which is 1 M NaCl for the high salt buffer and 0 to 2 mM for the low salt buffer.
b) For estimation of the theoretical pI the PROTPARAM on the ExPASY server (Gasteiger *et al.*, 2003) was used.

2.1.7 Gel Permeation Chromatography (GPC)

The proteins were further purified by GPC. Prior to GPC protein solutions were concentrated to 1-4 ml and filtered (0.45 µM pore diameter). Each protein solution was applied to a GPC column (Superdex 75 16/60 or Superdex 200 16/60, GE Healthcare) equilibrated with the appropriate buffer (Table 2-5). Proteins were separated with 1.0 to 1.5 CV of buffer (120 ml or 180 ml) with a flow rate of 0.5−1 ml/min and sampled in fractions of 2 ml. With a few exceptions 5 mM DTT or β-mercaptoethanol were added to prevent cysteine oxidation. Proteins were stored at 4°C at concentrations of 5 mg/ml to 30 mg/ml. For long-term storage (> 2 weeks) the protein solution was supplemented with 10 % glycerol and shock frozen with liquid nitrogen for storage at -70ºC.

Table 2-5: Buffers used for GPC experiments.

Protein construct	Gel filtration buffer
$SidA^{AF}$	50 mM Tris/HCl pH 7.5, 0.1 M NaCl, 5 mM DTT
$SidA^{AN}$	10 mM CHES pH 10.0, 0.1 M NaCl, 5 mM DTT
PvdA	10 mM Hepes pH 8.5, 0.1 M NaCl, 5 mM DTT

2.1.8 Anaerobic Protein Purification

For anaerobic protein purification bacterial cell pellets were obtained as described in section 2.1.3. Cell pellets were then transferred into glass bottles and sealed with a special rubber septum useful for application within anaerobization systems. Generally oxygen was replaced with forming gas. This equally applies for all buffers and solutions used.

After anaerobization of chemicals and solutions all experiments were performed using either the anaerobic glove box (Coy Laboratory Products) or the anaerobic miniMACS box (DG250 workstation, Don Whitley Scientific). Cell lysis was performed as described. Mechano-physical disruption of bacterial cells was accomplished by ultrasonication of the resuspended cell pellet. Anaerobic protein purification was limited to the affinity chromatography step. Concentration of purified protein fractions was accomplished with an Amicon stirred cell protein concentrator (Millipore). In between the purification procedure protein samples were removed and the protein concentration was determined as described in section 2.2.1.

2.2 Analytical Methods

2.2.1 Protein Concentration Determination

The concentration of a given protein was determined photometrically by using a conventional UV/Vis spectrophotometer (Ultrospec 3000, Pharmacia Biotech) and applying either the Beer-Lambert law (eq. 1) or the protein assay according to Bradford (Bradford, 1976).

c: concentration [mg/ml]

M_r: molecular mass [mg/mmol]

ε: molar extinction coefficient[$M^{-1}cm^{-1}$]

d: layer thickness of cuvette

A_{280}: absorption at λ = 280 nm

$$c = \frac{M_r}{\varepsilon d} A_{280} \qquad \text{(eq. 1)}$$

Alternatively, the Nanodrop spectrophotometer system (PEQLAB Biotechnologie) was used where only 2 µl of a given protein solution needs to be applied for photometrical determination of a protein concentration. The estimated extinction coefficients (Gill and von Hippel, 1989) for $SidA^{AN}$, $SidA^{AF}$ and PvdA are listed in Table 2-6.

Table 2-6: Protein constructs and estimated extinction coefficient.

Protein construct	Extinction coefficient ε
A. fumigatus SidA-His_6	45090 $M^{-1}cm^{-1}$
A. nidulans SidA-His_6	54620 $M^{-1}cm^{-1}$
P. aeruginosa PAO1 PvdA-His_6	35700 $M^{-1}cm^{-1}$

2.2.2 Determination of the FAD-SidA Stoichiometry

SidA protein samples of known molarity were denatured by heating to 100°C for 10 min to release FAD. Denatured protein was removed by centrifugation and the supernatant was transferred to a cuvette, to measure the absorbance at 450 nm using a UV/Vis spectrophotometer (Ultrospec 3000, Pharmacia Biotech). The extinction coefficient of FAD at 450 nm (11300 $M^{-1}cm^{-1}$) (Macheroux, 1999) was used to determine the concentration of cofactor in solution.

2.2.3 Reconstitution of PvdA Apoprotein with FAD

For FAD reconstitution 15 ml of purified PvdA apoprotein (~97 µM) was mixed with a 30-fold excess of FAD and dialysed under gentle stirring for ~15 h at 4ºC against 3 l buffer containing 10 mM Hepes pH 8.5, 0.1 M NaCl and 5 mM DTT. Subsequent to dialysis the protein was concentrated and applied on a GPC to get rid of unbound FAD. For crystallization experiments the purified and concentrated apoprotein was equally mixed with an excess of FAD (5 mM FAD per 2.7 mg of protein) and directly used for crystallization (see section 2.4).

2.2.4 Concentration of Protein Solutions

Protein solutions were concentrated by ultracentrifugation using Viva-Spin-concentrators (Vivascience) according to the manufacturer's instructions.

2.2.5 Oligomerization Studies

To estimate the molecular weight and to determine the oligomerization state of the SidA and PvdA proteins in solution, analytical GPC experiments as well as dynamic light scattering (DLS) analysis have been performed.

Dynamic Light Scattering

DLS allows the translation diffusion coefficient of a protein to be determined. Assuming the molecule to be globular allows estimation of the hydrodynamic radius (eq. 2) and hence the molecular mass of the protein.

R_h: Hydrodynamic radius

k: Boltzman constant

T: Temperature

D: Diffusion coefficient

η: Dynamic viscosity

$$R_h = \frac{kT}{D6\pi\eta} \qquad \text{(eq. 2)}$$

Protein solutions (concentration 6-10 mg/ml) were centrifuged at 20800×g for 20 min at 4ºC prior to the DLS experiment. Measurements were performed at ambient temperature using a DynaPro-801 (Protein Solutions) analyzer and interpreted by the evaluation software DYNAMICS (version 5.26.38, Protein Solutions).

Analytical GPC

Analytical GPC was performed with a collection of standard proteins using the LMW and HMW Gel Filtration Calibration Kit (Amersham Biosciences). The following standard proteins were used: chymotrypsinogen A (25 kDa), ovalbumin (43 kDa), aldolase (158 kDa) and ferritin (450 kDa). The amount of protein that has been loaded on the column was performed according to the manufacturer's protocol. The column used was a new Superdex 200 high-load 16/60 global (GE Healthcare). The GPC-buffer used was 50 mM Tris/HCl pH 7.5, 0.1 M NaCl, 5 mM DTT.

2.2.6 N-terminal Sequencing

Proteins were separated by SDS polyacrylamide gel electrophoresis (SDS-PAGE) and thereafter blotted onto a PVDF-membrane. The PVDF-membrane was shortly incubated in Ponceau red staining solution to visualize the protein bands which were finally dissected and sent to N-terminal sequencing. N-terminal sequencing was performed by Rita Getzlaff (HZI, Braunschweig) according to the method of Edman and Begg (Edman and Begg, 1967).

2.3 Enzyme Assays

2.3.1 NADPH Oxidation Assay

The standard assay buffer contained 100 mM Tris/HCl, pH 8.0, 0.1 M NaCl and 0.15 mM NADPH dissolved in 20 mM NaOH. 5 µM SidA (0.25 mg, 5 µM) were incubated in 1 ml of assay buffer for 20 s at 25°C before the reaction was initiated by the addition of 10 mM L-ornithine. NADPH oxidation was monitored at 340 nm (ε = 2850 $M^{-1}cm^{-1}$) using an Ultrospec 3000 spectrophotometer (Pharmacia Biotech) at 25°C for 120 s with 1 s time points according to the protocol described by Plattner and coworkers (Plattner *et al.*, 1989). Substrates and potential substrate analogs were usually prepared as 0.1 M stock solutions dissolved in purified deionized water. A maximum degree of water purity was achieved using the MilliQ Ultrapure Water Purification System (Millipore).

2.3.2 Hydroxylation (Iodine Oxidation) Assay

The enzymatic generation of hydroxylated product formed by SidA was assayed by a variation (Stehr *et al.*, 1999; Plattner *et al.*, 1989; Tomlinson *et al.*, 1971) of the Csaky test (Csaky, 1948) and is depicted in Figure 2-1.

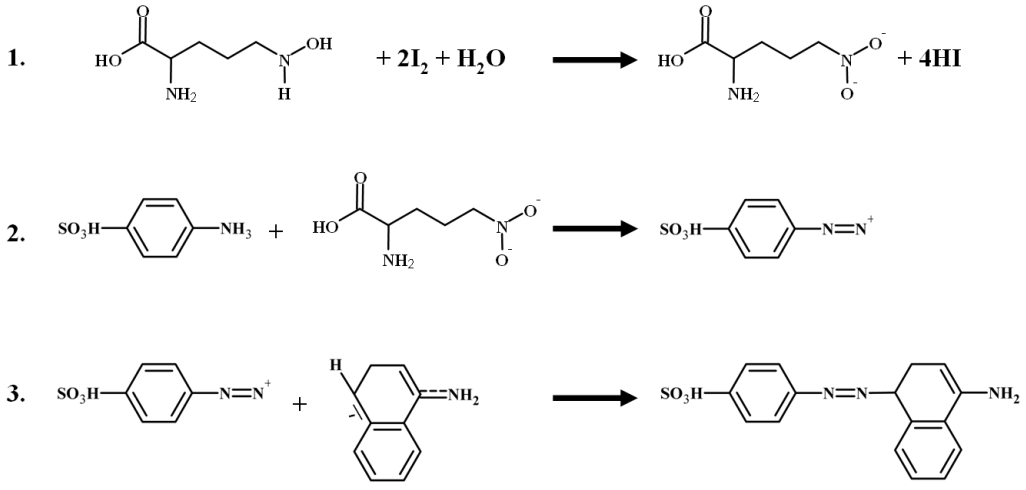

Figure 2-1: Iodine oxidation assay for quantification of hydroxylated amines. (1) The N^5-hydroxylamine group of N^5-hydroxy-ornithine is oxidized by iodine. (2) The nitrous acid derivative from (1) reacts with sulfanilic acid to yield a diazonium ion, which in (3) reacts with α-napthylamine to form an azo dye of pink color. The amount of azo dye formation can finally be quantified photometrically at λ = 562 nm.

The standard assay buffer is the same as described for the NADPH oxidation assay (section 2.3.1). The reaction was initiated by the addition of 10 mM L-ornithine to 0.25 mg of enzyme (5 µM) in 1 ml of assay buffer at 25ºC. 830 µl of the assay mixture were withdrawn and added to 420 µl of 0.2 N trichlor acetic acid (TCA) to terminate the reaction. A centrifugation step was added to get rid of precipitated protein that may have affected the measurement within the photometric step of the assay. Following centrifugation the supernatant was transferred into a 96-well plate and the reaction mixture was neutralized by adding 50 µl of a 5 % (w/v) sodium acetate solution. Subsequently 50 µl of 1 % (w/v) sulfanilic acid in 25 % (v/v) glacial acetic acid and 20 µl of 1.3 % (w/v) potassium iodide in glacial acetic acid were added to each well and the reaction was allowed to incubate at room temperature for 5−7 min. Excess iodine was then removed with 20 µl of 0.1 N sodium thiosulfate and the color was developed by adding 20 µl of 0.6 % (w/v) α-naphthylamine in 30 % (v/v) glacial acetic acid. The absorbance at 562 nm was measured after 15 min using a microplate reader (Infinite 200 series, Tecan).

2.3.3 Determination of the Catalytic pH Optimum

Determination of the optimal pH for SidA enzymatic activity was performed according to the reaction set-up in section 2.3.1. The different buffer solutions were used in concentrations of 0.1 mM supplemented with 0.1 mM NADPH, 0.1 mM L-ornithine and 0.15 M NaCl. To start the reaction 1 µM of purified enzyme was added to the reaction set-up. The decrease of NADPH absorption was monitored as described in section 2.3.1. Buffers used with adjusted pH were the following:

Citrate	5.5
MES	6.5
Hepes	7.0, 7.5, 8.0
Bicine	9.0
CAPS	10.0, 11.0

2.3.4 H_2O_2 Detection

The detection of hydrogen peroxide was performed by an enzyme coupled assay using horseradish peroxidase (HRP) together with 2,2'-azino-bis-3-ethylbenzthiazoline-6-sulfonic acid (ABTS) (Figure 2-2).

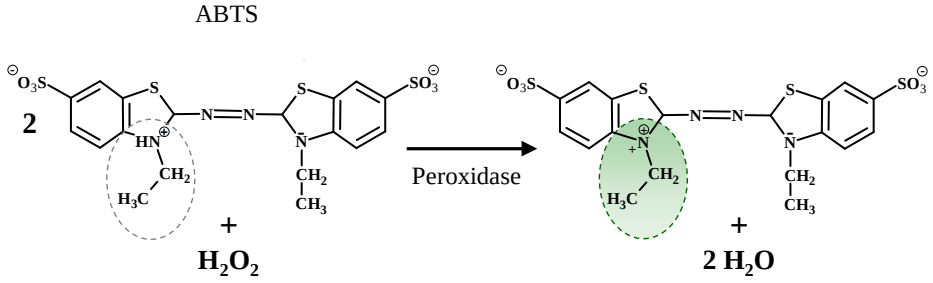

Figure 2-2: Enzyme coupled assay for detecting H_2O_2 formation.

HRP catalyzes the oxidation of ABTS in the presence of hydrogen peroxide resulting in the formation of an ABTS radical cation which develops a characteristic blue-green color which can be quantified photometrically at λ = 405 nm. Both reagents were purchased from Sigma Aldrich and the assay was performed according to the manufacturer's protocol (see also Sun and Yagasaki, 2003; Szutowicz *et al.*, 1984). Briefly, the enzymatic reaction mixture obtained as described in section 2.3.1 was incubated for 10 min at ambient temperature and then stopped by adding 2 N HCl such that the pH reaches 2.0. 100 µl of the reaction solution were mixed with 75 µl 100 mM Tris/HCl pH 8.0 and 150 µl of ABTS reagent (0.2 mg/ml) in a 96-well plate. The colorimetric assay was started by adding 2.5 µl HRP (1 mg/ml). Monitoring of the absorbance at 405 nm was performed by means of a microplate reader (Infinite 200 series, Tecan).

2.4 Crystallization

Screening

Proteins were crystallized by hanging drop and sitting drop vapor diffusion methods. For screening of lead crystallization conditions different commercial screens (Qiagen) were used. Pure protein solutions were pipetted as sitting drops on 96-well plates suited for usage with a pipetting roboter Mosquito robot (TTP LabTech). Reservoir solutions were pipetted in volumes of 70 to 100 µl. Drops were mixed with equal volumes of protein and reservoir solutions (100 to 200 nl). The plates were sealed with Manco™ Crystal Clear Sealing Tape (Jena Bioscience) and incubated at different temperatures (20ºC, 4ºC and 25ºC). The screens that have been used are listed below:

The AmSO4 (Qiagen)
The Anions (Qiagen)
The Cations (Qiagen)
The Classics I + II (Qiagen)
The Classics Lite (Qiagen)
The Cryos (Qiagen)
The MbClass I + II (Qiagen)
The Sparse Matrix 1-5 (Qiagen)
The MPDs (Qiagen)
The Pegs (Qiagen)
The pHClear I + II (Qiagen)
The SM 2, 3, 4 and 5 (Qiagen)

Optimized Crystal Growth

Initial hit conditions were optimized manually in 24-well hanging drop and sitting drop formats, using drop volumes of 2-3 µl by varying the physico-chemical parameters such as precipitant concentration, protein concentration, pH, ionic strength and temperature to

produce crystals suitable for X-ray diffraction experiments. Methods used for improving crystal quality are summarized in Table 2-7 and are described in detail below.

Table 2-7: Methods used within this study to improve crystal quality.

Method	Reference
Screening with additives	(Vuillard *et al.*, 1995; Sousa, 1995; Cudney *et al.*, 1994)
Varying crystallization temperature	(Karlsson and Sauer-Eriksson, 2007; Wiencek, 1999)
Soaking of substrates	(Hassell *et al.*, 2007)
Crystallization under oil	(Chayen, 1997)
Cryoprotection	(Garman and Owen, 2007; Pflugrath, 2004)
Crystal annealing	(Heras and Martin, 2005; Hanson *et al.*, 2003)
Anaerobic crystallization	(Hsieh *et al.*, 2005)
Seeding	(Bergfors, 2003; Bergfors, 1999)
Crystal growth in agarose matrix	(Bernard *et al.*, 1994)
Truncation of flexible regions	(Dale *et al.*, 2003)
(Mutational) surface modification	(Derewenda, 2004)
Methylation of surface residues	(Boeshans *et al.*, 2006; Walter *et al.*, 2006)
Cysteine replacements	(Fritz *et al.*, 2002; Moser *et al.*, 2001)

SidA crystals with improved diffraction quality were achieved with the hanging drop vapor diffusion technique using equal volumes (2 µl) of protein (10-20 mg/ml) and reservoir solutions (0.1 M NaCl, 0.1 M Na-citrate pH 5.5, 30 % (v/v) PEG 400 for $SidA^{AF}$ and 350 mM NaCl, 180 mM sodium formate for $SidA^{AN}$). The optimal growth temperature was 20°C. In the case of $SidA^{AN}$ crystals suitable for X-ray data collection were obtained by the streak seeding technique. For cryoprotection, 20 to 30 % glycerol was added to the reservoir solution. Small crystals (space group P3121, a = b = 49 Å, c = 208 Å) appeared already after ~8 h but growth was continued for a minimum of two weeks to obtain maximum sized crystals. A plausible V_M of 2.9 $Å^3$/Da and a solvent content of 57.6 % were obtained by assuming four monomers/asymmetric unit. Native and isomorphous SeMet-substituted crystals, obtained by streak-seeding, were used for X-ray data collection.

Crystallization under Oil

To slow down crystal growth, a layer of oil was placed over the reservoir solution. The oil acts as a barrier between reservoir and crystallization drop and reduces the rate of water diffusion between reservoir and crystallization drop. Depending on the type of oil used the rate of vapor diffusion and hence the speed of crystal growth can be influenced. Accordingly oils of distinct viscosities were used. Briefly, crystallization experiments were set up as either sitting drops or hanging drops with a reservoir volume of 500 µl. Reservoir or crystallization drops were then covered with oil in volumes of 2 µl and 400 µl, respectively. Oils used within this study were the following: Paratone N, Silicone No. 100, Silicone No. 5000 and Paraffine.

Crystal Growth within a Low-melting Agarose Matrix

For crystal growth within a matrix of low melting (LM-) agarose (Hampton Research) was used. Crystallization was performed according to the manufacturer's protocol. A 2 % working stock of LM-agarose was thus prepared heated to 28ºC and gently mixed with crystallization reagents and protein sample. SidA crystals were grown as hanging drops within a 0.2 % LM-agarose matrix and different concentrations of sodium formate and NaCl as crystallization reagent. Protein crystallization was then continued as described.

Methylation of Surface Residues

Methylation of surface exposed lysine residues was performed according to the JBS Methylation Kit protocol (Jena Bioscience). This technique reductively methylates free amino groups by employing formaldehyde as alkylating reagent and a dimethylamine borane complex as reducing agent. A total of 5 mg of purified protein was added to the reaction. Dialysis and a final GPC experiment (GPC column: Superdex 200 16/60, GE Healthcare) was performed, using 50 mM Hepes, pH 7.5, 0.1 M NaCl as buffer, to separate the protein from the methylation reaction mixture.

Anaerobic Crystal Growth

All crystallization set-ups were pipetted by hand and crystallization solutions used for screening of new crystallization leads were previously treated with forming gas to substitute for oxygen. For cryo-cooling prior to X-ray experiments crystals were fished and directly transferred from the anaerobic box (see section 2.1.8) into a container with liquid nitrogen.

Seeding Techniques

In this study macroseeding, microseeding and streak seeding were employed, the latter proving the most successful. The crystal seed can grow into larger crystals early in the equilibration phase rather than nuclei formation occurs when the solution is supersaturated. During streak seeding existing crystals were touched with a thin, flexible needle such that small crystal seeds cling to the seeding tool. The seeds were then transferred to a new crystallization drop. Crystal growth and quality was thus improved by mixing a droplet of 2 µl of a 10 mg/ml pure protein solution in 10 mM Ches buffer pH 10.0 and 100 mM NaCl containing 10 % of glycerol with an equal volume of reservoir solution consisting of 350 mM NaCl and 180 mM sodium formate. The droplets were placed on siliconized glass coverslips and incubated in 24-well hanging drop plates at 20°C. Crystal growth was initiated using previously obtained SidA crystals for streak seeding. Growth was allowed to continue for at least one week to obtain crystals of up to 500 × 200 × 50 µm.

Soaking and Co-crystallization Experiments

In the case of enzymes the addition of substrates, cosubstrates and potential inhibitors are known to enhance crystal growth and improve crystal quality and morphology. These small molecules are suspected to perturb and manipulate protein-protein and protein-solvent interactions, as well as perturb water structure. It is suspected that additives can stabilize or engender conformity by specific interaction with the macromolecule. In the case of SidA ($SidA^{AF}$ and $SidA^{AN}$) crystal soaking and co-crystallization of additives

(Hampton Research additive screen) as well as different combinations of substrate and cosubstrates (L-ornithine, NADPH, $NADP^+$) have been applied. Soaking and co-crystallization with additives was performed according to the manufacturer's protocol. Soaking experiments with substrate and cosubstrates were preformed either with solutions of the respective soaking compound or with the compound used as a solid. Soaking solutions contained substrate in a 3−6 fold molar excess compared to the protein concentration within the crystallization droplet and 50 % of reservoir solution. To a 4 µl sitting drop experiment 1−2 µl of soaking solution was successively pipetted. Solid substrate salts were added in small crumbles to the crystals in the crystallization droplet. Soaking times varied between 5 min to several h. Most soaking experiments however were performed within a time period of 10 min previous to cryoprotection and cryo-freezing of crystals. For co-crystallization the general experimental set-up was as described. Substrate containing solutions were either added in a 1:2 ratio compared to the crystallization drop volume or were mixed with the protein solution subsequently used for setting up the sitting drop experiment. Again the respective substrate or compound used for co-crystallization was added in 3−6 fold molar excess compared to the final protein concentration within the crystallization drop. Compounds used for soaking and co-crystallization were the following: L-ornithine, DFM-ornithine, ADP, NADPH, $NADP^+$, L-homoserine and sodium-dithionite (anaerobic conditions).

Preparation of crystals for X-ray experiments at Cryogenic and Ambient Temperature

Most macromolecular X-ray data is collected at cryogenic temperatures (~100 K). For cryoprotection of SidA crystals an aliquot of the reservoir solution of the original crystallization condition was mixed with glycerol to yield a final glycerol concentration of 20-30 %, depending on the size of the crystal and the actual crystallization condition. Crystals were fished with a nylon loop, shortly transferred into the cryoprotecting solution and then flash frozen in liquid nitrogen. For X-ray experiments at ambient temperature (~25ºC) crystals were mounted in sealed quartz glass capillaries or in polyester tubes (MiTeGen MicroRT^{TM} Tubing Kit system, Jena Bioscience). X-ray data were subsequently collected at ambient temperature.

2.5 Data Collection and Structure Determination

2.5.1 Screening for X-ray Diffraction

Hundreds of crystals had to be screened for their potential to diffract X-rays. Diffraction images were collected using different experimental set-ups and X-ray sources. X-ray screening of crystals was in part performed at the HZI homesource being composed of a rotating copper anode generator and an R-AXIS IV++ image plate detector (Rigaku). The majority of screening experiments was however performed at different synchrotron beamlines (X12 and BW7A at DESY, European Molecular Biology Laboratory, Hamburg outstation, Germany; BL 14.1 and BL 14.2 at BESSY, Berlin, Germany; ID 14-2, ID 23-1, ID 23-2 and ID 29 at the European Synchrotron Radiation Facility (ESRF), Grenoble, France).

2.5.2 Native Data

Native X-ray diffraction data of crystals from wild-type SidA and SidA variant C151S were collected at the ESRF in Grenoble. The dataset for the wild-type SidA crystal was collected at beamline ID23-1 (0.90000 Å wavelength) on a Quantum Q315R (ADSC) detector. Correspondingly a dataset was collected for the crystal of SidA variant C151S at beamline ID14-2 (0.93300 Å wavelength) on a Quantum 210 (ADSC) X-ray detector. Diffraction data were processed and evaluated by XDS (Kabsch, 1993), MOSFLM (Leslie, 1992) and SCALA (CCP4, 1994).

2.5.3 Molecular Replacement

Potential models intended to use in molecular replacement (MR) calculations were obtained by means of the Homology detection & structure prediction server HHPred (Soding *et al.*, 2005). The program PHASER (McCoy *et al.*, 2005) was used for MR calculations. In addition to the original structural models modified variants of the respective MR search models were applied. Polyalanine and polyserine models were generated with the program MOLEMAN (Kleywegt, 1999). The program CHAINSAW (CCP4, 1994) was used to thread the amino acid sequence of SidA onto the respective MR search model by pruning non-conserved residues while conserved residues were left unchanged thus approximating the amino acid sequence of the search model to that of SidA. A minimal number of clashes (2-4) and a clash distance of 3.0 Å was allowed to avoid a priori rejection of potentially correct translation solutions within the packing step that might arise due to differences in small surface loops.

2.5.4 3-Wavelength MAD Experiment

X-ray diffraction datasets of a SeMet derivatized SidA crystal were collected at three wavelengths (inflection: 0.97853 Å, peak: 0.97776 Å, high-energy remote: 0.97537 Å) at beamline X12 (DESY, EMBL Hamburg outstation) on a MARCCD detector (Marresearch, Norderstedt, Germany). Data were processed using the HKL2000 (Otwinowski and Minor, 1997) and CCP4 suites (CCP4, 1994). Statistics are listed in Table 3-3. Phasing was achieved by multiple anomalous dispersion (MAD) techniques. SHELXD was used to locate Se sites (Pape and Schneider, 2004; Schneider and Sheldrick, 2002). Phase calculation, phase extension and improvement as well as density modification were performed by means of SHELXE (Pape and Schneider, 2004; Sheldrick, 2002). A final density modification step was performed with the program DM (CCP4, 1994) by applying the NCS operators identified by PROFESSS (CCP4, 1994) on basis of the calculated Se sites.

2.5.5 Twinning Analysis

Analysis of data quality and twinning analysis in particular was performed using the programs PHENIX Xtriage (Adams *et al.*, 2002) and SFCHECK (Vaguine *et al.*, 1999).

2.5.6 Model Building and Refinement

The program COOT (Emsley and Cowtan, 2004) was used for manual model building. Optimization of the SidA structure was performed by iterative rounds of refinement calculations. Iterative rounds of refinement improve the positions of individual atoms, the

overall model and hence the model-derived phases. Correspondingly the calculated model-based structure-factor amplitudes (F_{calc}) approach the observed values (F_{obs}) thus minimizing the R-factor. Generally the R-factor (eq.3) is a measure for the convergence of F_{obs} and F_{calc}.

$$R = \frac{\sum ||F_{obs}| \sum |F_{calc}||}{\sum |F_{obs}|} \qquad \text{(eq. 3)}$$

In addition to the traditional crystallographic R-factor (R_{work}) a more unbiased free R-factor (R_{free}) (Brunger, 1992) was calculated with the same formula (eq. 3) using a subset (5 %) of the diffraction data that has explicitely been omitted during the refinement.

Programs used within refinement calculations included the maximum likelihood-based programs REFMAC (Murshudov *et al.*, 1997), CNS (Brunger, 2007; Brunger *et al.*, 1998) and PHENIX Refine (Terwilliger *et al.*, 2008; Adams *et al.*, 2002). Refinement strategies used for simulated annealing were performed with PHENIX and CNS. Twin refinement and NCS refinement strategies were mainly performed with refinement protocols of PHENIX and REFMAC. The structure of SidA was refined to a resolution of 3.2 Å. Structures were validated using PROCHECK (Laskowski *et al.*, 1993) and WHATIF (Vriend, 1990). Refinement statistics are listed in Table 3-5.

2.6 Figure Preparation

All structural figures were graphically presented using the program PyMOL (DeLano, 2002) and ChemSketch (ACD/Labs). Sequences were aligned with CLUSTALW (http://www.ebi.ac.uk/clustalw*)* and displayed using ESPript (Gouet *et al.*, 1999).

3 Results

Within the scope of this thesis, orthologous SidA variants from two closely related *Aspergillus* species, *A. fumigatus* and *A. nidulans*, have been successfully expressed, purified and crystallized. As work progressed the enzyme from *A. nidulans* ($SidA^{AN}$) proved superior in terms of crystallizability and X-ray diffraction than that of *A. fumigatus* ($SidA^{AF}$). The work was therefore focused on $SidA^{AN}$ and most results presented in the following sections reflect data based on this enzyme variant. However, as illustrated by the alignment in Figure 3-1 the sequence identity between both proteins (78 %) is such that either enzyme is equally suited for biochemical and structural analysis. A crystal structure of $SidA^{AN}$ will thus provide an optimal basis for a three-dimensional model of $SidA^{AF}$. If not otherwise stated, the denotation "SidA" will generally refer to the enzyme from *A. nidulans* within the forthcoming sections.

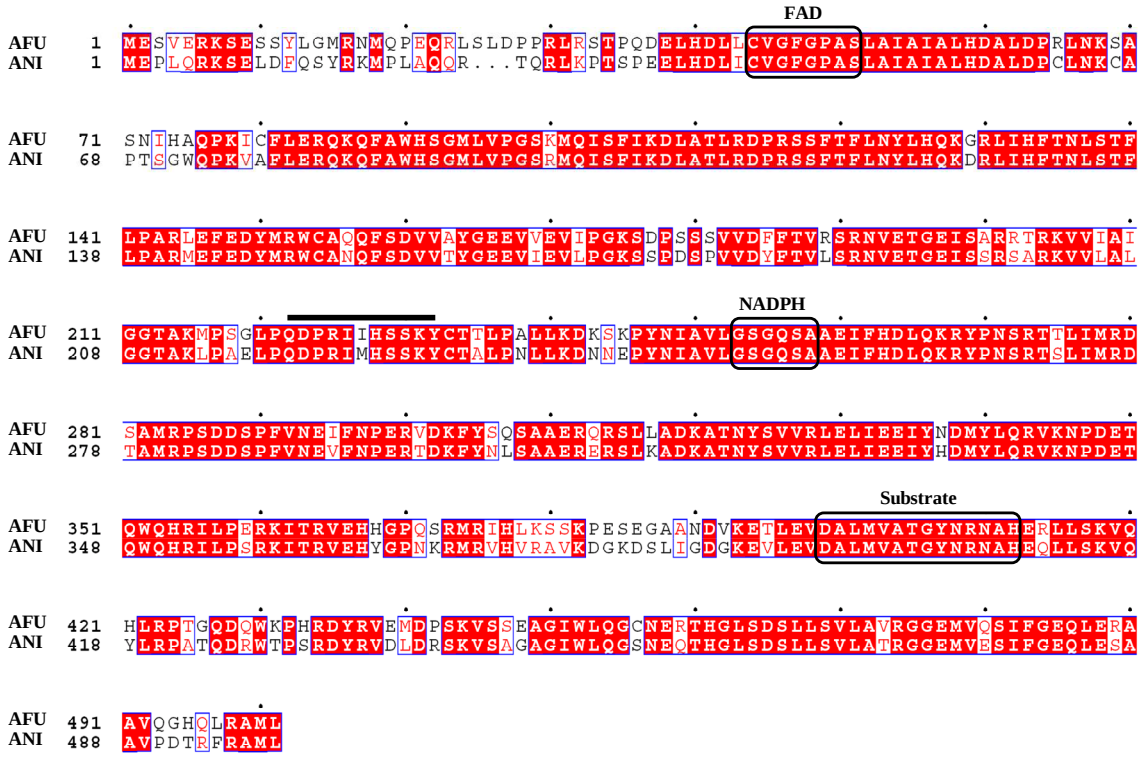

Figure 3-1: Alignment of SidA from *A. fumigatus* (AFU) and SidA from *A. nidulans* (ANI). FAD-binding motif, NADPH-binding motif and the putative substrate-binding site are indicated by black boxes. The FMO identifying sequence is marked by a black bar. In contrast to $SidA^{AN}$, $SidA^{AF}$ harbors three additional amino acid residues (Ser25−Asp27).

3.1 Biochemical Properties of SidA

3.1.1 Protein Expression and Purification

For recombinant expression of SidA in *E. coli* the respective *sidA* gene had to be cloned into a suitable expression vector. The DNA used to generate an expression plasmid containing the *sidA* gene either from *A. nidulans* or from *A. fumigatus* was provided by Prof. Dr. Hubertus Haas (Medical University Innsbruck). Following PCR-based amplification the *sidA* gene was cleaved by specific restriction enzymes (NdeI and EcoRI in the case of $sidA^{AN}$, EcoRI and XhoI in the case of $sidA^{AF}$) and ligated into the expression vector pET-28c(+). This resulted in two constructs in which the gene is provided by a sequence encoding for an N-terminal His_6-tag. To obtain SidA in amounts sufficient for biochemical characterization and crystallization experiments, most SidA variants were produced in *E. coli* Tuner™ cells. After testing different expression conditions, optimal production was achieved with bacterial cells grown in LB medium until reaching an optical density (OD at 600 nm) of 1.0. Being under control of the *lac*-operon, expression of *sidA* was induced with 0.3 mM IPTG and growth of bacterial cells was allowed to continue for ~5 h at 25ºC. Purification of overexpressed SidA was achieved by a combination of different chromatography techniques such as affinity chromatography, ion exchange chromatography (IEC) and gel permeation chromatography (GPC). Typically, about 10 mg per liter of bacterial culture were obtained for His_6-tagged SidA. A selenomethionine (SeMet) derivative of SidA ($SidA^{SeMet}$) was later on prepared to solve the SidA crystal structure by anomalous dispersion techniques. For this purpose, a SeMet-containing minimal medium was used to overexpress the protein (Guerrero *et al.*, 2001). Thereafter, purification of $SidA^{SeMet}$ was performed analogous to that of the native protein. During SeMet-incorporation the final yield of $SidA^{SeMet}$ accounted for only ~30 % of the native protein.

Initial purification of the ~59 kDa SidA-His_6 was performed by means of an affinity chromatography step. Coupling of the heterologously expressed SidA to a nickel(II)-nitrilotriaceticacid (Ni-NTA) resin was accomplished via the N-terminal His_6-tag. Prior to elution from the Ni-NTA resin the protein was subjected to several washing steps with increasing imidazole concentrations. The final elution fractions already displayed a high

degree of purity as demonstrated by SDS-PAGE (Figure 3-2, right panel). Moreover these fractions revealed an approximate molecular mass (M_r) between 46 and 66 kDa roughly corresponding to monomeric SidA (~59 kDa). The intense yellow color of the purified protein (Figure 3-2, left panel; Figure 3-4 A) indicated the presence of a flavin cofactor. Notably the cofactor remained bound to the apoprotein throughout the purification procedure. Due to the absorption maximum of FAD at 450 nm the amount of bound cofactor could be monitored photometrically. The spectrum of the fully oxidized enzyme exhibited typical absorption maxima at λ = 280 nm, 380 nm and 457 nm, with a ratio A_{280}/A_{457} of 10 indicating ~1.0 mol of FAD per mol of SidA. Except for the SidA variant Y404S which proved devoid of FAD, similar results have been obtained with all other SidA variants that were generated within the scope of this work.

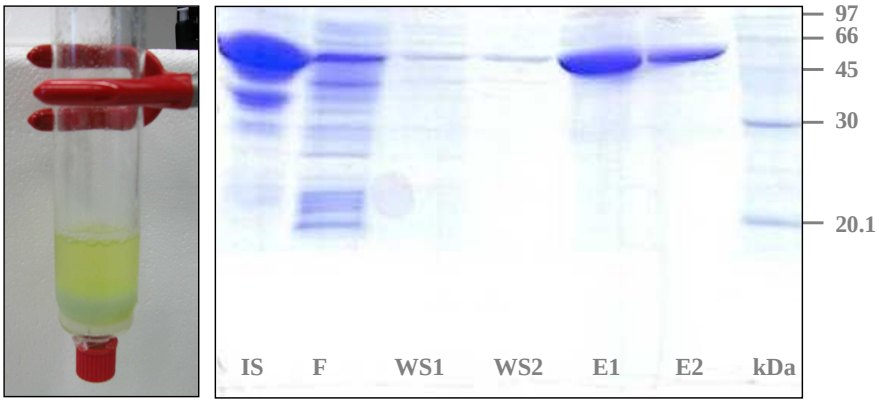

Figure 3-2: Purification of SidA via Ni-NTA affinity chromatography. Right panel: Coomassie brilliant blue-stained SDS-PAGE with insoluble (IS), unbound (F), wash- (WS1, WS2) and elution fractions (E1, E2) from the affinity chromatography steps performed with *E. coli* cell extract containing SidA-His_6. The last lane contains the protein standard with respective molecular masses indicated in kDa. Left panel: SidA elution fraction and Ni-NTA resin in a glass column.

The flavin content of SeMet derivatized SidA ($SidA^{SeMet}$) was only ~0.5 mol of FAD per mol of protein. Attempts to saturate the flavin content of $SidA^{SeMet}$ by adding FAD during dialysis or crystallization did not increase the FAD-content within the purified protein samples. By contrast supplementing for FAD during protein expression through addition of riboflavin, nicotinamide and pyridoxin successfully increased the amount of functional $SidA^{SeMet}$. The use of supplemented minimal-medium led to an improved FAD to protein ratio resulting in ~0.8 mol of FAD per mol of purified $SidA^{SeMet}$.

After affinity chromatography an IEC step was performed. With a theoretical pI of 8.1 the protein was initially buffered at pH 6.8 to obtain the required positive net charge for subsequent purification via a MonoS column. This protocol was however changed since SidA proved more stable at basic pH and was less prone to degradation (see section 3.3.6). Therefore purification by IEC was performed at pH 10 using a MonoQ column. Upon binding of SidA to the IEC resin, the column material was subjected to a salt gradient ranging from 2−800 mM NaCl over an elution volume of ~100 ml. As depicted in Figure 3-3 most of the protein eluted at a salt concentration of 160 mM, which corresponds to a conductance of 16 mS/cm.

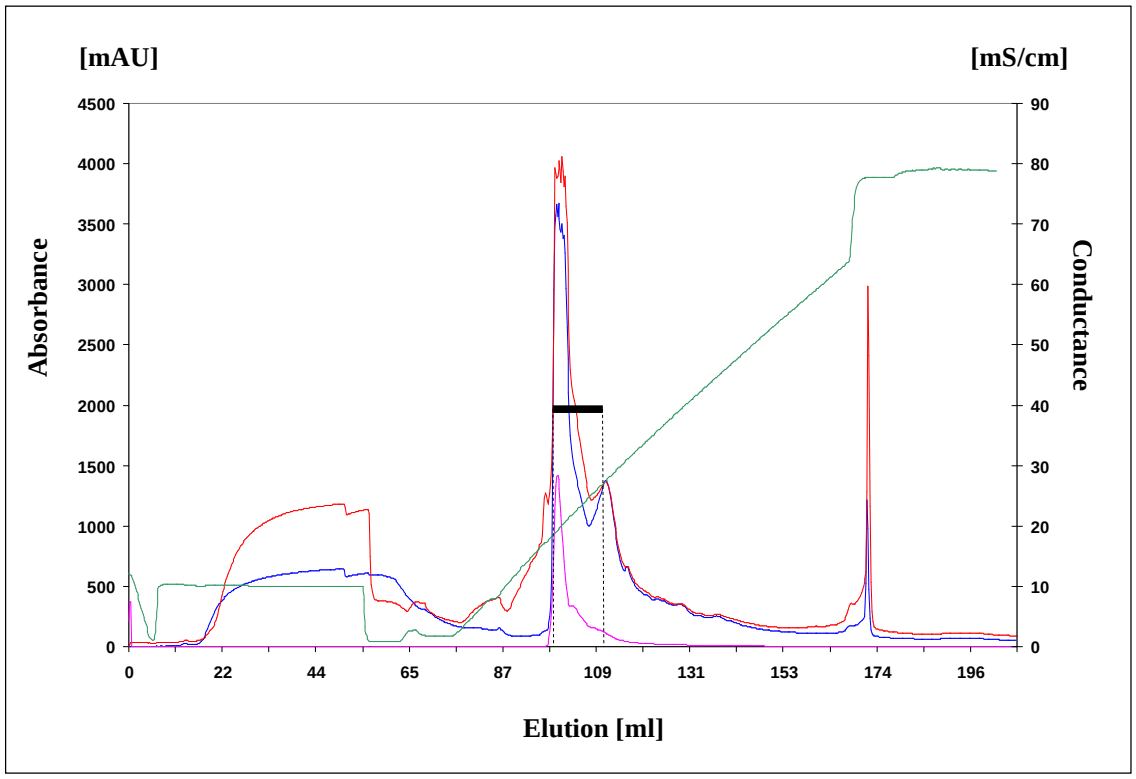

Figure 3-3: Ion exchange chromatography. The elution fractions of the preceding Ni-NTA affinity chromatography step were buffered at pH 10 and further purified via an anion exchange column (MonoQ HR 10/10). The chromatogram shows the absorption at three different wavelengths at λ = 280 nm (blue line), 260 nm (red line) and 450 nm (pink line), corresponding to the absorption maxima of protein, nucleic acid and the FAD cofactor. The concentration that corresponds to the applied NaCl gradient monitored by conductance in [mS/cm] is shown as a dark green line. The black bar marks the pooled elution fractions.

As documented by SDS-PAGE (Figure 3-4 B) the corresponding peak fractions contained relatively pure protein and displayed an intense yellow color due to bound FAD (Figure 3-4 A).

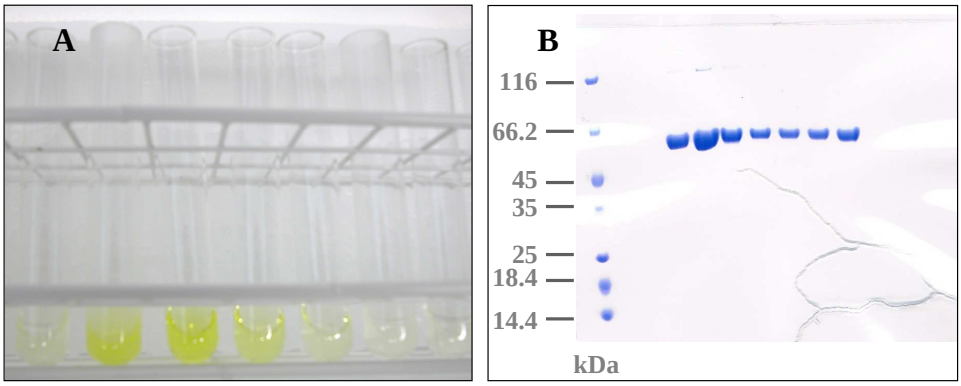

Figure 3-4: SDS-PAGE of IEC-peak fractions. (A) Peak fractions of the IEC run are yellow due to bound FAD. (B) First lane: protein standard, second lane: flowthrough fraction.

Pure fractions of the IEC run were pooled and subjected to a GPC. This final purification step served to remove remaining traces of impurities and to estimate the extent of SidA oligomerization in solution. Although SidA has an estimated molecular mass (M_r) of ~59 kDa, previous experiments preformed with the orthologous enzyme variant from *A. fumigatus* indicated that $SidA^{AN}$ could form a tetramer in solution as well. The protein was therefore loaded onto a GPC column suited for separation of proteins between 67 and 440 kDa, which thus includes the M_r of tetrameric $SidA^{AN}$ (Figure 3-5).

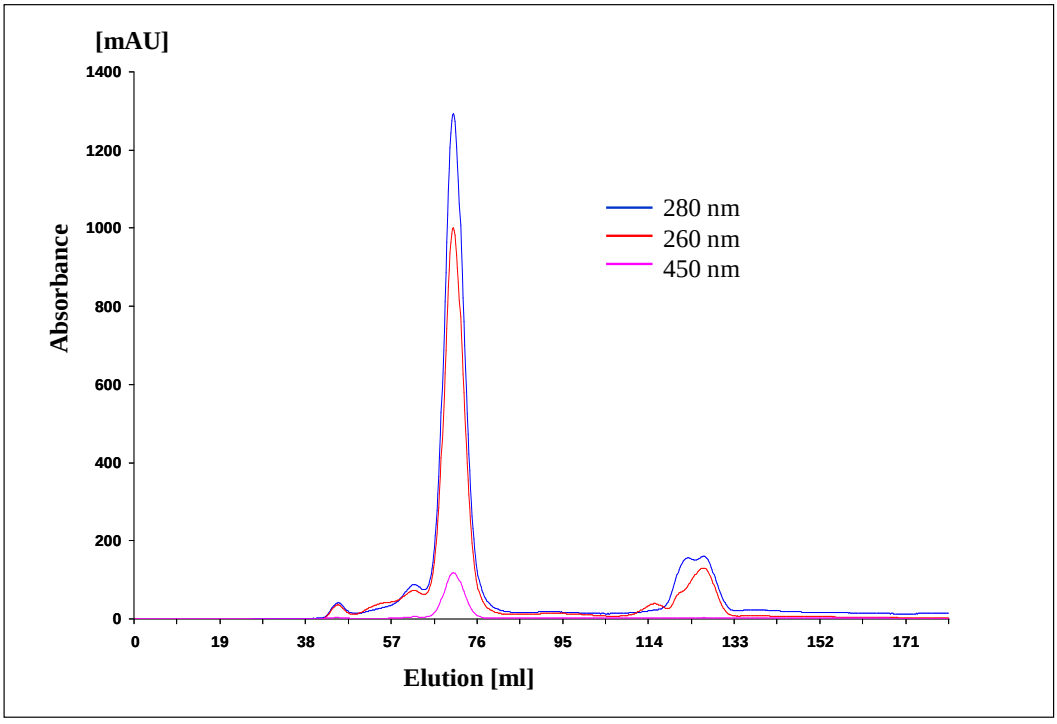

Figure 3-5: Gel permeation chromatography with IEC-purified SidA. The elution volume of the peak fraction is V_e = 67 ml.

Apart from a shoulder at ~59 ml elution volume (V_e) there is a sharp peak at V_e = 67 ml which, according to the physicochemical properties of the column used, thus pointed at a tetrameric oligomerization of SidA. This interpretation was further confirmed by analytical gel filtration and DLS analysis. As demonstrated in Figure 3-6 the V_e of SidA is located within the linear range of the calibration curve between the standard proteins aldolase (M_r = 158 kDa) and ferritin (M_r = 450 kDa). The average hydrodynamic radius (R_h) determined by DLS analysis accounted for ~6.2 nm corresponding to a calculated M_r of ~235 kDa with a proportionate polydispersity of 13.2 %.

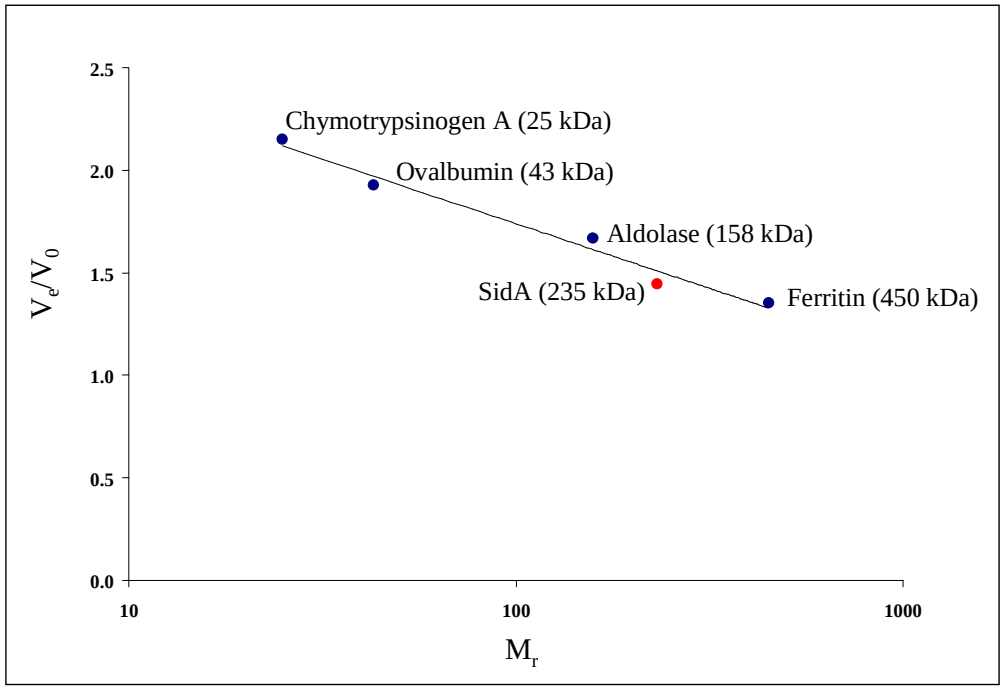

Figure 3-6: Calibration curve of an analytical GPC. The SidA sample had previously been purified by IEC. The column used was a Superdex 200 (16/60). V_e: elution volume; V_0: void volume; M_r: molecular mass.

3.1.2 Enzyme Activity of SidA

The reaction catalyzed by SidA proceeds at the expense of L-ornithine, NADPH and molecular oxygen and yields L-N^5-hydroxy-ornithine. The consumption of NADPH during catalysis as well as the generation of the hydroxylamine product served to verify the catalytic activity of the purified enzyme by means of two photometrical protocols:

1. Monitoring the decrease in absorption at 340 nm to account for the consumption of NADPH during catalysis.
2. Quantification of the hydroxylated product N^5-hydroxy-ornithine via a coupled iodine oxidation assay resulting in an azo dye formation that can be quantified at λ = 562 nm (Plattner *et al.*, 1989; Csaky, 1948).

The first approach was used for kinetic analysis of SidA and to determine the pH optimum for the SidA enzymatic activity while the second approach was applied for product quantification as well as for the analysis of substrate specificity.

Determination of the catalytic pH optimum for the reaction was performed under steady state conditions with 150 µM NADPH, 10 mM L-ornithine and different buffer solutions with varying pH values ranging from pH 5.5 to pH 11.0 (Figure 3-7).

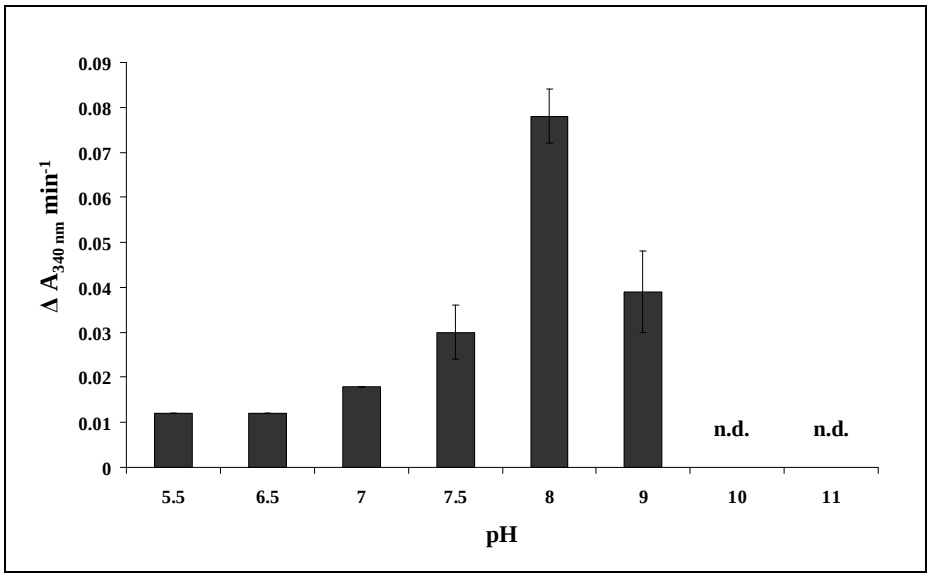

Figure 3-7: Catalytic pH optimum of SidA. The pH at which SidA displays optimal activity was determined by the NADPH oxidation assay with saturated concentrations of L-ornithine and NADPH, respectively. The results shown are the mean of three independently performed experiments. n.d.: no significant detection of enzyme activity as determined by the decrease in NADPH absorption at λ = 340 nm.

The decrease in NADPH absorption increased with increasing pH values and reached a maximum at pH 8.0. At pH 9.0 a significant consumption of NADPH was still detected. Above pH 9.0 enzymatic activity was completely abolished as indicated by the absence of a measurable decrease in NADPH absorption at λ = 340 nm. The pH optimum of SidA catalysis thus lies in the basic pH range between pH 7.5 and pH 9.0.

To determine kinetic parameters of SidA, L-ornithine concentrations between 0.05 and 20 mM were used for the analysis of the enzymatic reaction. Both, $SidA^{AF}$ and $SidA^{AN}$, were thereby tested and displayed typical Michaelis-Menten kinetics with similar kinetic parameters. The corresponding K_M and k_{cat} values were determined to be 292 (± 0.02) µM and 3.2 s^{-1} for $SidA^{AF}$ and 311 (± 0.02) µM and 3.3 s^{-1} for $SidA^{AN}$, respectively. Moreover, as can be inferred from the non-sigmoidal curves in Figure 3-8, no obvious cooperativity could be observed between the individual subunits of the SidA tetramer.

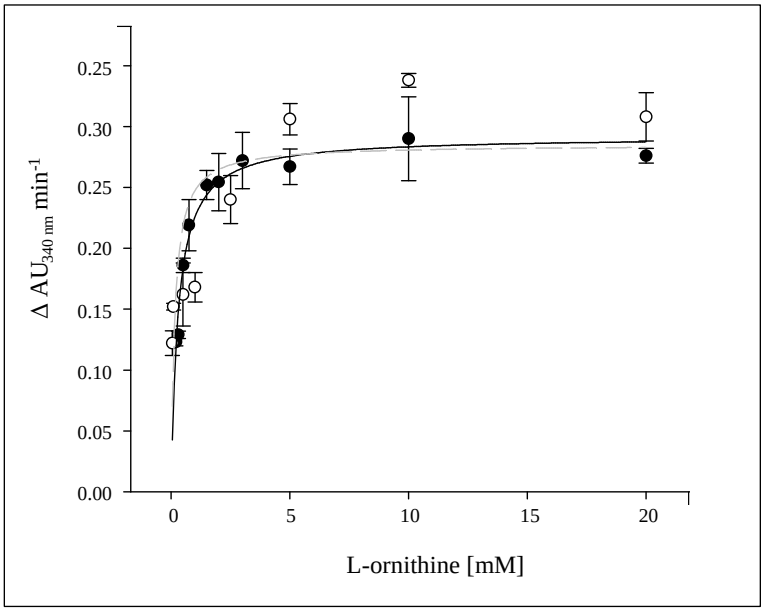

Figure 3-8: Michaelis-Menten kinetics of $SidA^{AF}$ and $SidA^{AN}$ at different L-ornithine concentrations. The kinetic parameters were determined by measuring the decrease in NADPH absorption at λ = 340 nm over time at intervals of one second and varying L-ornithine concentrations. Filled circles and black regression curve: data correspond to $SidA^{AF}$; white circles and gray, dashed regression curve: data correspond to $SidA^{AN}$. For K_M and k_{cat} values see text above.

3.1.3 Substrate Specificity of SidA

Using the iodine oxidation assay it turned out that the SidA substrate specificity is narrowly confined to its natural substrate L-ornithine and a few closely related ornithine-

derivatives (Figure 3-9). Despite the modification at their N^5-atom both L-ornithine analogs tested, N^5-iminoethyl-ornithine (IME-ornithine) and α-difluoromethyl-ornithine (DFM-ornithine), were subjected to hydroxylation by SidA.

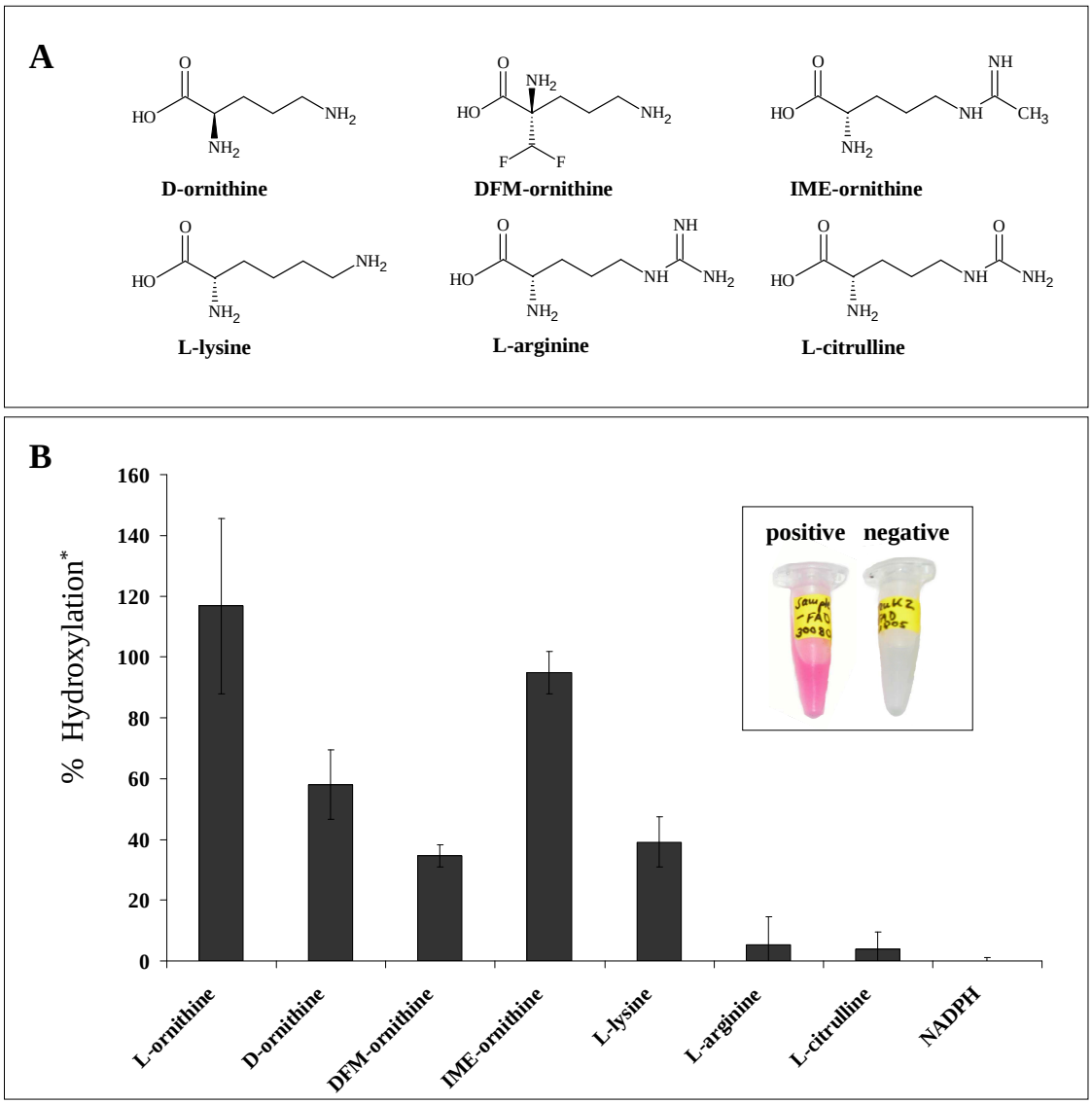

Figure 3-9: Detection of hydroxylated product formation by means of the iodine oxidation assay. (A) Structures of substrates used within the iodine oxidation assay. (B) The data shown are the result of three independently performed experiments. Addition of only NADPH to the reaction set-up did not result in product formation and thus served as a negative control. The inset shows the result of azo dye formation in case of a positive and a negative test outcome. * % Hydroxylation refers to the hydroxylated product formation by SidA in the presence of L-ornithine under steady state conditions.

IME-ornithine hydroxylation was detected in a range comparable to that obtained with the natural SidA-substrate L-ornithine. DFM-ornithine on the other hand, an ornithine analog known to function as an irreversible inhibitor of ornithine decarboxylase

(Takigawa *et al.*, 1990), was only slightly converted to the respective hydroxylamine derivative (35 % compared to L-ornithine). Of those substrates with extended side chains only L-lysine resulted in a significant conversion to its hydroxylated product compared to L-ornithine. Accordingly azo dye formation as a result of substrate hydroxylation was neither observed for L-arginine nor for L-citrulline. L-lysine, which is the natural substrate of the bacterial SidA homologue IucD, accounted for ~39 % hydroxylation relative to equimolar amounts of L-ornithine. SidA is furthermore not strictly confined with regard to stereospecificity as both L- and D-ornithine were hydroxylated. Under steady state conditions, D-ornithine is however hydroxylated ~40 % less efficiently than the natural substrate L-ornithine.

Regarding the specificity for the electron donor of the monooxygenation reaction catalyzed by SidA, the enzyme is strictly dependent on NADPH. Using the iodine oxidation assay substitution of NADPH by NADH did not result in the formation of a hydroxylation product (Lisson, 2007).

3.1.4 Enzyme Activity in the Absence of Substrate

The presence of a slight, intrinsic NADPH oxidase activity in the absence of substrate as reported for other flavin-monooxygenases (Palfey *et al.*, 1997) could also be observed for SidA (Figure 3-10). Immediately after NADPH addition, the color of the protein solution changes from bright yellow to pale yellow indicating the reduction of the flavin cofactor. Over a time period of ~30 min, the characteristic 457 nm peak of the oxidized enzyme reappears. Conversely, addition of excess substrate reestablishes the spectrum of the fully oxidized flavin within a few seconds (Figure 3-10). The accompanying formation of the C4a-hydroperoxyflavin intermediate, characterized by an absorbance peak at ~360 nm (Suh *et al.*, 1996; Poulsen and Ziegler, 1995; Beaty and Ballou, 1981), was not observed for SidA under the reaction conditions chosen. Probably the transient C4a-hydroperoxyflavin intermediate decays too rapidly to be detected at ambient temperature. For spectral visualization of the C4a-hydroperoxyflavin the reaction has to be set up and repeated at 4ºC (Alfieri *et al.*, 2008; Entsch *et al.*, 2005).

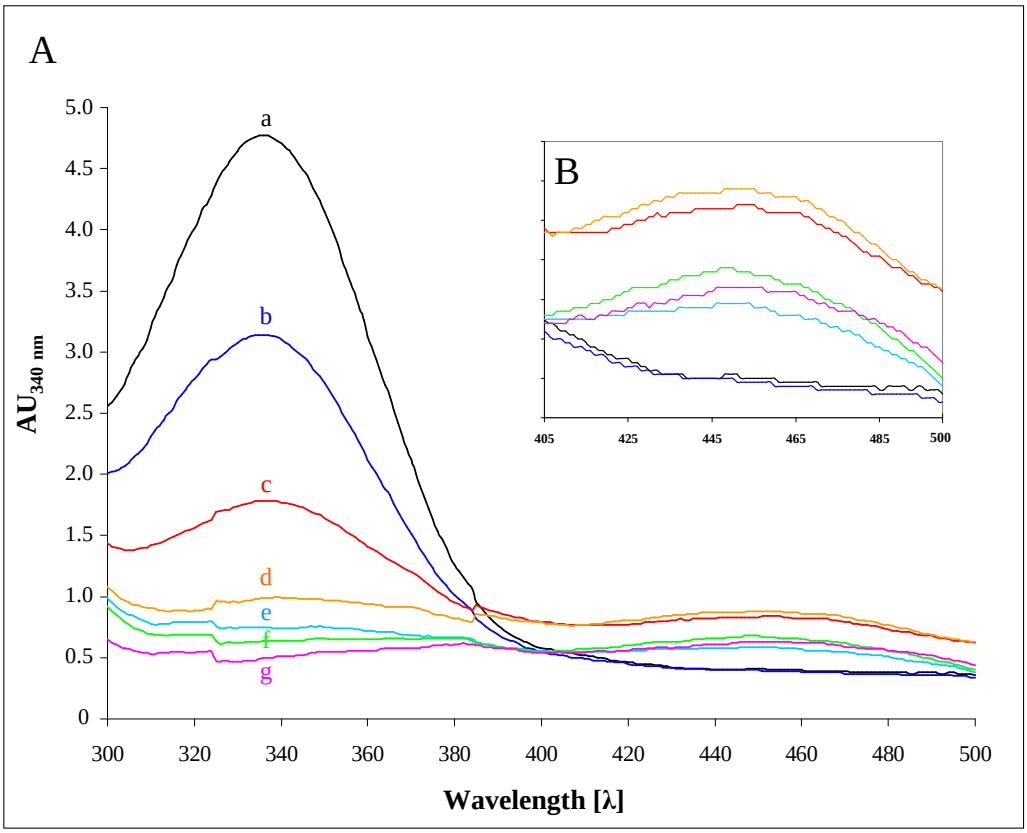

Figure 3-10: Absorbance spectra of SidA. (A) Trace (**a**) represents the reduced form of SidA after addition of excess amounts of NADPH represented by a maximum absorption at 340 nm. SidA reoxidation can be observed over time by the recovery of FAD-absorption at 457 nm. Traces (**b**) and (**e**) represent 5 and 20 min after NADPH addition. After ~30 min the enzyme is almost fully reoxidized (trace (**f**)). The reoxidation reaction of the FAD cofactor can be accelerated by addition of L-ornithine as shown in trace (**c**), which was directly monitored after addition of L-ornithine and trace (**d**) 60 seconds later. Trace (**g**) represents the fully oxidized SidA in the absence of NADPH and substrate. (B) Enlargement of (A) within λ = 405-500 nm.

Due to the reactivity of the reduced flavin generated during the reductive half-reaction of the presumed catalytic cycle in the absence of an appropriate substrate the enzymatic reaction is uncoupled and NADPH oxidation can result in hydrogen peroxide formation (Figure 1-12). The actual production of H_2O_2 in the absence and presence of L-ornithine was verified using an enzyme coupled assay employing horseradish peroxidase (HRP) together with ABTS (Sun and Yagasaki, 2003; Szutowicz *et al.*, 1984). Comparing SidA incubated with both substrates L-ornithine and NADPH to conditions where SidA is incubated with NADPH alone, a 50 % increase in ABTS oxidation is observed in the absence of L-ornithine. By contrast ABTS oxidation is unaffected when the reaction occurs at L-ornithine concentrations between 1 and 10 mM (Figure 3-11).

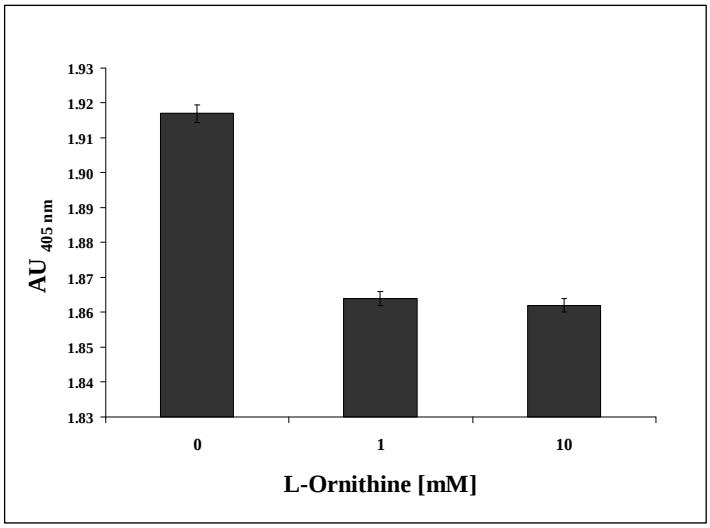

Figure 3-11: H_2O_2 production of SidA. H_2O_2 production was measured by means of a colorimetric enzyme coupled assay using HRP and ABTS. In the presence of H_2O_2 the otherwise colorless ABTS reagent is converted by HRP to develop a characteristic green color that can be photometrically detected at $\lambda = 405$ nm. Without L-ornithine HRP product formation is increased, while addition of L-ornithine (1 or 10 mM) decreases product formation. The absorption measured in the absence of H_2O_2 accounted for 0.06 AU.

For determination of the kinetic parameters of the intrinsic NADPH oxidase activity first experiments have been performed using NADPH concentrations between 0.001 and 150 µM in the absence of L-ornithine. Though this kinetic analysis has to be repeated in more detail first results indicate that the NADPH oxidase activity of SidA follows a typical Michaelis-Menten kinetic profile with an approximate K_M value of 5.5 (± 1.4) µM and a ~1000 fold slower turnover ($k_{cat} = 0.003\ s^{-1}$) compared to the reaction performed in the presence of L-ornithine.

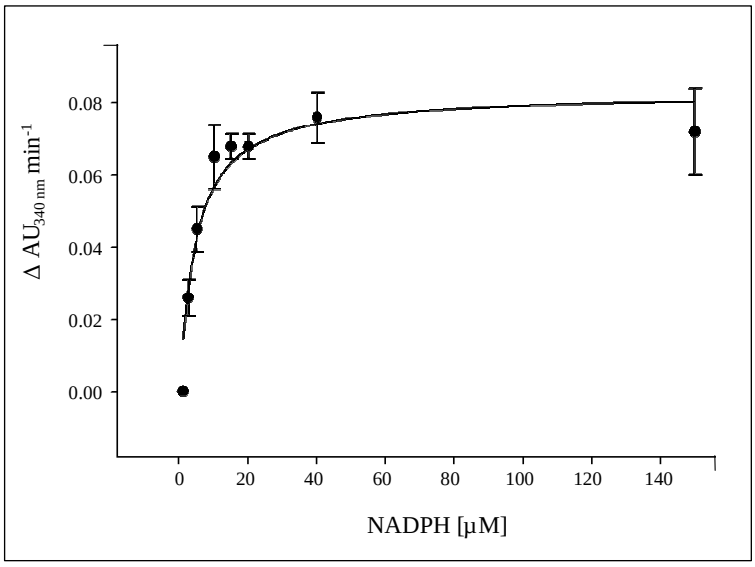

Figure 3-12: Kinetic analysis of the intrinsic SidA NADPH oxidase activity. The intrinsic NADPH oxidase activity was monitored in the absence of the natural SidA substrate L-ornithine via the NADPH oxidation assay.

Potential SidA substrates/inhibitors that have been investigated using the iodine oxidation assay were again used to analyze their potential as NADPH oxidase effectors. In contrast

to the other substrates tested, L-lysine, which is only inefficiently (~39 %) converted to its hydroxylamine derivative (Figure 3-9), proved to be a potent effector of the SidA NADPH oxidase activity. Using L-lysine as substrate thus resulted in an efficient progression of the first half of the catalytic cycle. The monitored decrease in NADPH absorption was thus comparable to that observed with the natural SidA substrate L-ornithine. Except for those ornithine derivatives previously shown to be hydroxylated by SidA none of the other substrates (L-arginine, L-citrulline) tested did promote consumption or oxidation of NADPH beyond the intrinsic SidA (NADPH)-oxidase activity (Table 3-1).

Table 3-1: Substrates and their capacity to be hydroxylated and to promote NADPH oxidation.

Substrate	Hydroxylation*	NADPH oxidation†
D-ornithine	58 % (± 11)	-
DFM-ornithine	35 % (± 4)	-
IME-ornithine	95 % (± 10)	94 % (± 23)
L-lysine	39 % (± 8)	103 % (± 21)
L-arginine	n.d.	n.d.
L-citrulline	n.d.	n.d.

***** % Hydroxylation is a comparison that refers to the quantity of hydroxylated L-ornithine under steady state conditions, measured by the iodine oxidation assay. The results are mean values of three independent experiments each performed at least in triplicates.

† % NADPH consumption as measured by the decrease in NADPH absorbance at λ = 340 nm. Consumption of NADPH with L-ornithine as substrate was set to 100 %.

n.d.**:** The photometrically determined values measured are considered as not significant or as not detected, e.g. the signal was not sufficient (compare iodine oxidation assay) or the signal was equal to that measured without addition of an appropriate substrate (compare photometric assay for detection of NADPH).

3.2 SidA Crystallization

Following purification both, SidA^{AF} and SidA^{AN}, were screened for lead crystallization conditions within small scaled experimental set-ups using numerous commercially available crystallization screens. Resulting protein crystals were reproduced and improved using an increased sample volume and the hanging drop vapor diffusion technique.

3.2.1 Crystallization of SidA from *A. fumigatus*

In the case of SidA^{AF}, crystals were only observed in a single of the approximately 2000 crystallization conditions tested. The conditions were: 0.1 M NaCl, 0.1 M Na-citrate pH 5.5 and 30 % (v/v) PEG 400, resulting in crystals with a rod-like habitus and a yellow color due to bound FAD (Figure 3-13).

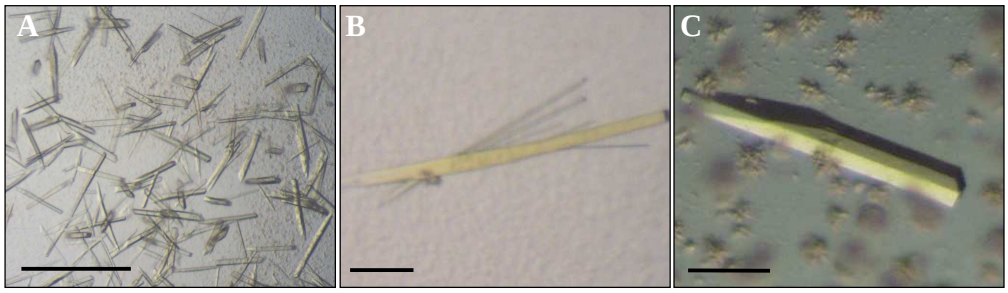

Figure 3-13: SidA^{AF} crystals. (A) SidA^{AF} crystals obtained within screening crystallization set-ups. (B) and (C) SidA^{AF} crystals obtained within optimization crystallization set-ups. Black scale bars: ~100 µm.

Crystals were reproduced and increased in size, however, as mentioned, these SidA^{AF} crystals proved to diffract X-rays only weakly (~ 8 Å). Attempts to improve both, crystal quality (see section below) and X-ray diffraction including the use of powerful synchrotron radiation improved resolution to only ~5 Å (Table A-1, Appendix). The work on this enzyme was thus discontinued.

3.2.2 Crystallization of SidA from *A. nidulans*

As previously shown (Derewenda, 2004) replacement of amino acid residues that affect solubility and/or modify the surface charge can significantly influence the crystal quality and crystal packing arrangement of a given protein. Usually patches of charged residues potentially located at the protein surface such as lysines and glutamates are replaced by

alanine or serine residues through site-directed mutagenesis. Alternatively, instead of protein surface engineering, the method of choice often is to switch to a highly homologous protein thus taking advantage of the variations in amino acid composition (especially of surface residues) that have emerged during evolution. Compared to $SidA^{AF}$, $SidA^{AN}$ has a 78 % identical amino acid composition, providing enough differences to allow for new crystal contacts potentially leading to a different crystal packing arrangement. The alignment in Figure 3-1 (p. 38) reveals marked differences in potentially surface exposed residues between $SidA^{AF}$ and $SidA^{AN}$. Examples include Lys100, Glu359, Glu384, Glu386, Lys431 and Glu448 of $SidA^{AF}$ opposed to Arg97, Ser356, Gly381, Asp383, Thr428 and Gly445 of $SidA^{AN}$. As described for $SidA^{AF}$, pure $SidA^{AN}$ was subjected to various crystallization screens. In contrast to $SidA^{AF}$, $SidA^{AN}$ crystallized under several of the screening conditions chosen (compare also Figure 3-14):

(i) 0.1 M Tris/HCl pH 8.5, 1.2 M $(NH_4)_2SO_4$

(ii) 0.1 M NaH_2PO_4, 0.1 M K_3PO_4, 0.1 M Mes pH 6.5, 2 M NaCl

(iii) 0.1 M Hepes pH 7.5, 4.3 M NaCl

(iv) 0.1 M sodium formate, 2 M NaCl

(v) 0.1 M $(NH_4)_2HPO_4$, 0.1 M ADA pH 6.5

(vi) 0.1 M Li_2SO_4, 0.1 M sodium citrate pH 5.5, M NaCl, 12 % (w/v) PEG 4000

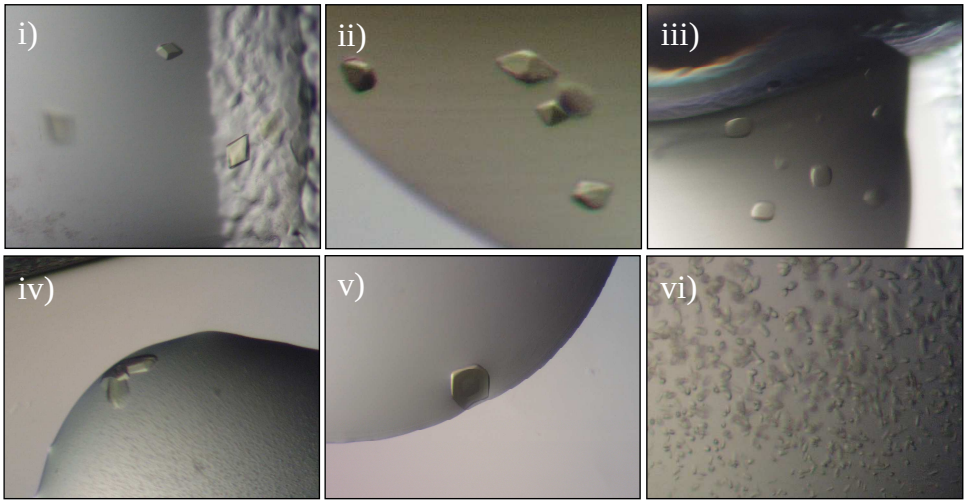

Figure 3-14: $SidA^{AN}$ crystals obtained after screening. 200-400 nl sitting drops were set-up in a 96-well plate format. (i)-(vi) correspond to lead crystallization conditions mentioned in the text above. The size of the crystals obtained was in the range of ~10−20 µm in the longest dimension.

Crystals were yellow in color due to bound FAD and mainly revealed a hexagonal crystal habitus. Reproduced and optimized SidA^{AN} crystals are shown in Figure 3-15. Among the reproduced SidA^{AN} crystals that were tested within X-ray experiments those optimized using sodium formate and NaCl (condition (iv), p.52) as crystallization agents revealed the best results (compare Table A-1, Appendix). Although these crystals diffracted X-rays to higher resolution than SidA^{AF} crystals, the maximum resolution of 4.6 Å that has been obtained was not sufficient for structure determination.

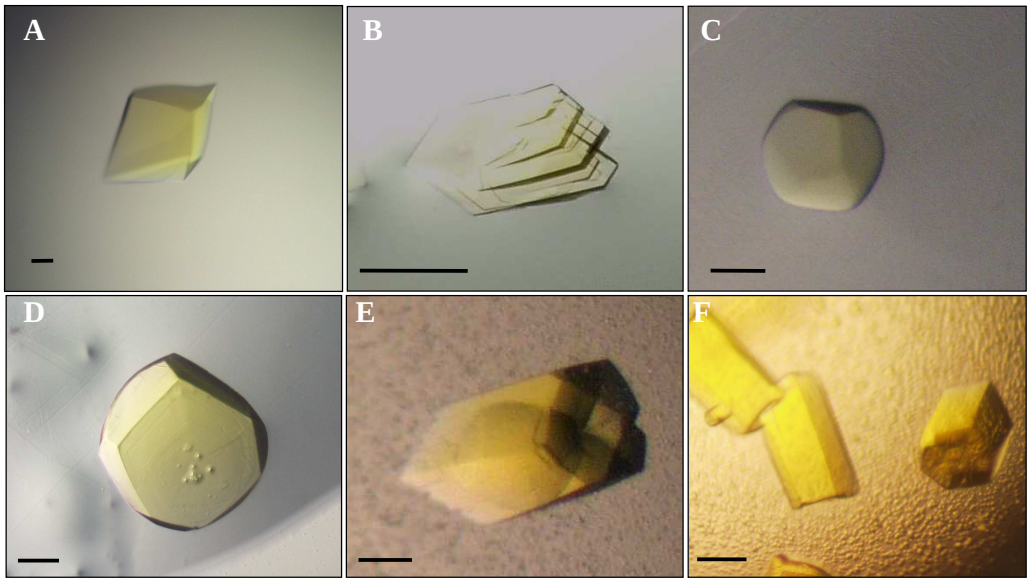

Figure 3-15: Optimized SidA^{AN} crystals. Crystals A, B and C were obtained through optimization of screeening conditions (i), (iii) and (v) (compare p. 52). Crystals D, E and F (SidA^{AN}C151S, SeMet derivative) were obtained through variations of screening condition (iv). Black scale bars: ~100 µm.

3.3 Optimization Strategies for SidA Crystals

Due to the poor diffraction quality of SidA crystals different methods were applied in order to optimize crystal quality rather than to search for new crystallization conditions.

3.3.1 Protein Surface Modification

To allow for alternative crystal contacts potentially leading to an improved crystal packing arrangement and higher X-ray diffraction quality one approach included protein surface modification via site-directed mutagenesis or methylation. As described above, one strategy includes the replacement of patches of potentially surface exposed lysine and

glutamate residues by alanine or serine to decrease the surface entropy and enhance the crystallisability (Derewenda, 2004). Following this approach residues Glu313 and Lys317 and residues Glu311 and Lys320 were substituted with alanine and serine, respectively. The resulting variant E311S/E313A/K317A/K320S was screened for new crystallization conditions (Figure 3-16). However, none of the crystals tested resulted in improved X-ray diffraction quality.

Figure 3-16: Crystals obtained with SidA E311S/E313A/K317A/K320S. Crystals were grown in 0.1 M Na-tartrate, pH 5.6 and 0.6 M K/Na-tartrate.

In a second strategy methylation of surface exposed lysine residues was tested to provide for alternative crystal contacts. The SidA^{AN} sequence contains 25 potentially surface exposed lysine residues that could be methylated. Following the methylation protocol, modified SidA^{AN} was subjected to a GPC. The resulting chromatogram (Figure 3-17) demonstrates that the modified protein has a high tendency to form larger oligomers eluting in the void volume of the GPC-column ($V_0 \approx 42$ ml).

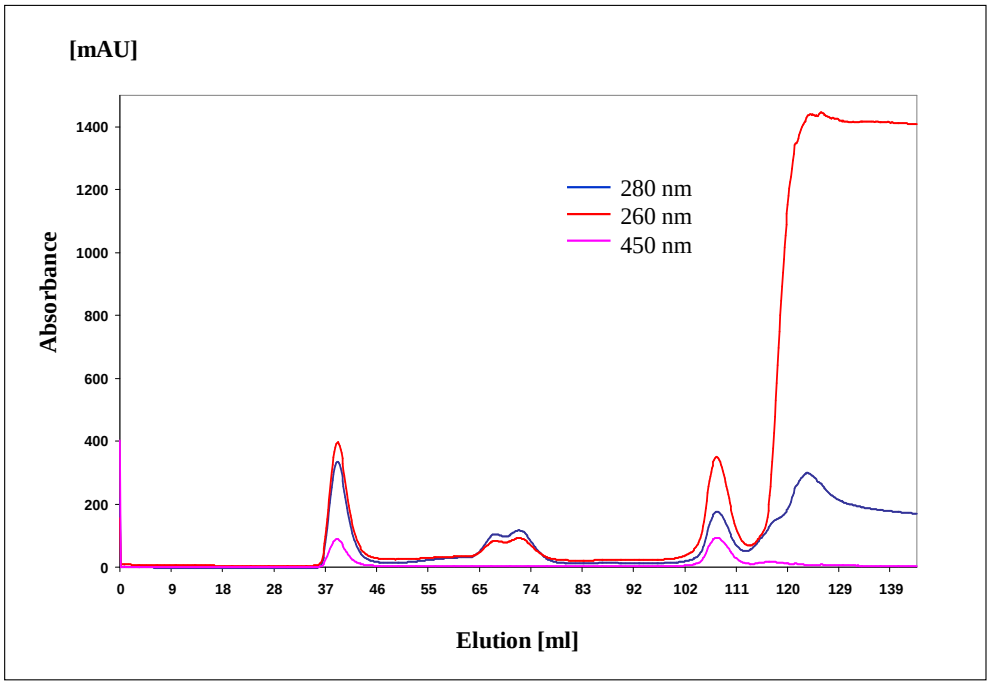

Figure 3-17: GPC of SidA modified by methylation. The GPC experiment was performed with a Superdex 200 16/60 column. The chromatogram demonstrates the absorption at three wavelengths: $\lambda = 280$ (blue line), 260 (red line) and 450 nm (pink line), corresponding to the absorption maxima of protein, nucleic acids and the FAD cofactor. The void volume (V_0) of the GPC column is ~42 ml.

3.3.2 Replacement of Cysteines

Surface exposed cysteines can impair crystallization and crystal quality due to unfavorable aggregation of the protein through non-specific intermolecular disulfide bond formation (Ray *et al.*, 2004; Moser *et al.*, 2001). The amino acid sequence of SidA^{AN} includes five cysteines of which some are presumably surface exposed (Lisson, 2007). This interpretation was among others based on the structure of phenylacetone monooxygenase (PAMO) from *Thermobifida fusca* (Malito *et al.*, 2004) which was identified as structurally homologous to SidA by using the homology dectection and structure prediction server HHPred (Soding *et al.*, 2005). To get an idea about the location of cysteines the PAMO crystal structure was thus used for computational modeling of the three-dimensional structure of SidA. With the program CHAINSAW (CCP4, 1994) the amino acid sequence of SidA was threaded onto the structural model of PAMO by pruning non-conserved residues while conserved residues were left unchanged. The resulting model and distribution of the five cysteines is shown in Figure 3-18.

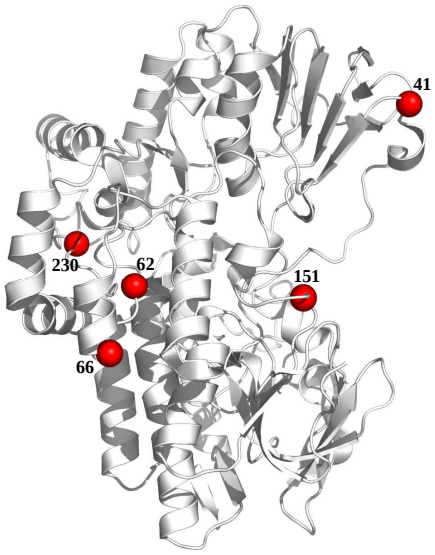

Figure 3-18: Inferred location of SidA cysteine residues based on the crystal structure of PAMO. The model is shown as cartoon representation. Cysteines present within the SidA sequence (Cys41, Cys62, Cys66, Cys151 and Cys230) are highlighted as red spheres.

In fact a non-reducing SDS-PAGE analysis indicated that purified SidA^{AN} tended to aggregate over time in the absence of reducing agents like DTT or β-mercaptoethanol (Figure 3-19 A and B). Freshly purified protein, however resulted in a single SidA tetramer peak within GPC experiments − even in the absence of reducing agents (Figure 3-19 C).

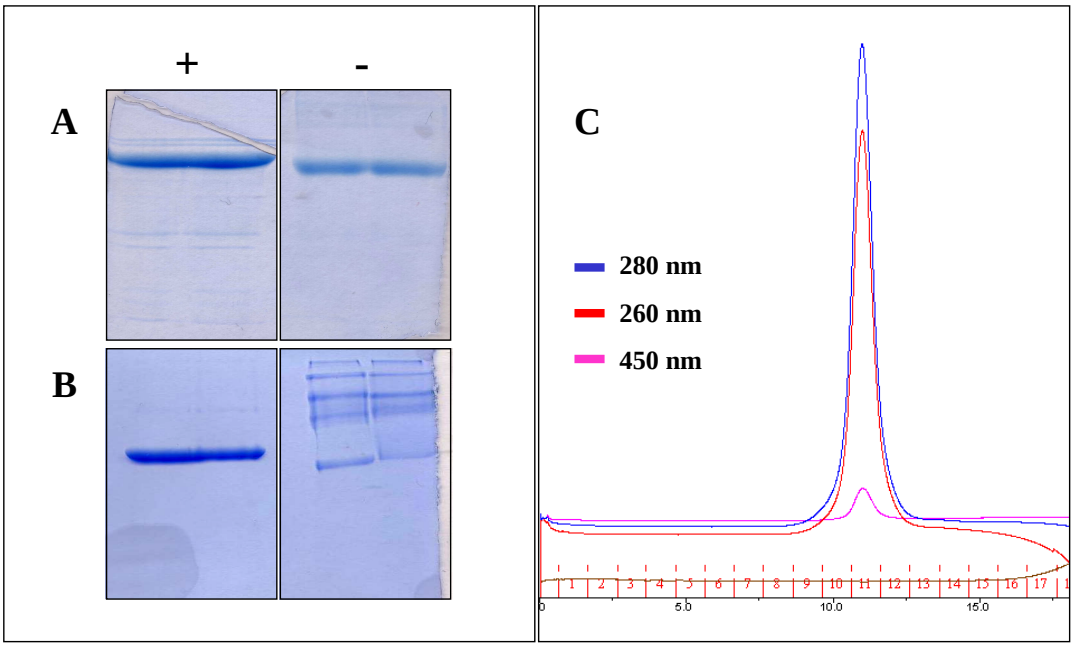

Figure 3-19: Non-reducing SDS-PAGE of purified SidA. SidA purified without reducing agents was either subjected to SDS-PAGE with (+) or without (-) addition of reducing agents. SDS-PAGE: (A) Immediately after protein purification, (B) ~10 days after purification. (C) GPC-run with SidA samples that have been prepared and purified in the absence of reducing agents.

To exclude these residues being responsible for the poor diffraction quality of SidA crystals, the five cysteines (Cys41, Cys62, Cys66, Cys151 and Cys230) were successively replaced by serines through site-directed mutagenesis and the resulting SidA^{AN} variants were used for setting up crystallization experiments (Lisson, 2007). One of these SidA variants, SidAC151S, resulted in improved crystal quality diffracting X-rays up to 4 Å (Lisson, 2007). Some of the SidA^{AN} crystals analyzed as part of this thesis are based on this cysteine variant (Table A-1, Appendix).

3.3.3 Crystallization under Anaerobic Conditions

Another strategy to circumvent multimerization of SidA due to disulfide formation included purification and crystallization under anaerobic conditions (Figure 3-20). Such a reducing atmosphere would not only maintain cysteine residues in the reduced state, but would reduce the FAD cofactor as well. Since molecular oxygen is one of the substrates of SidA, crystallization under anaerobic conditions could potentially affect the quality of SidA crystals. Crystals obtained under anaerobic conditions were furthermore soaked and/or co-crystallized with L-ornithine, NADPH and sodium-dithionite. However, X-ray

experiments with anaerobically grown crystals did neither reveal improved diffraction quality, nor did crystals soaked with L-ornithine and/or NADPH. Addition of sodium-dithionite quickly reduced the crystals bleaching the yellow color. Within a few hours the yellow color of the crystals returned indicating that the FAD cofactor was again present in its oxidized form (Figure 3-20). The reoxidation of FAD was probably caused by traces of oxygen that have accidentally been introduced during channeling of experimental equipment (in particular plastic wear) into the anaerobic working station.

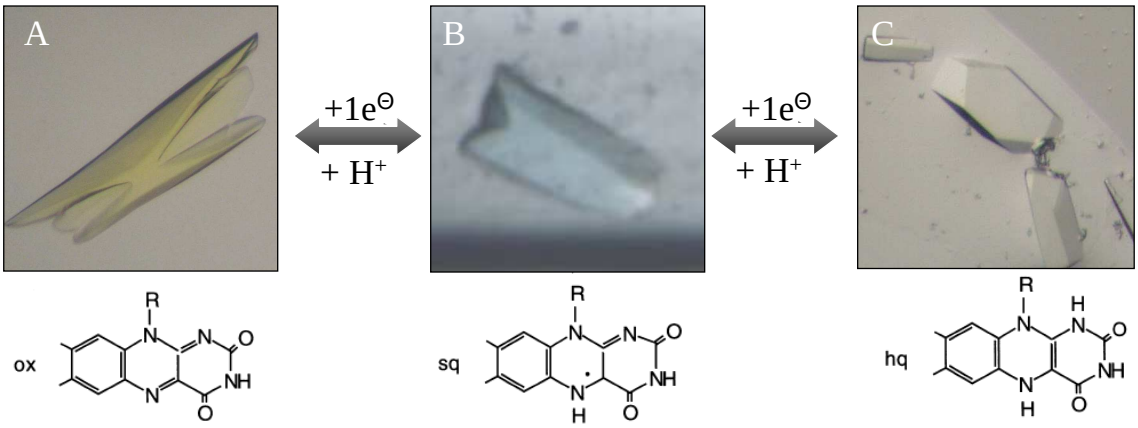

Figure 3-20: Aerobically versus anaerobically grown SidA crystals. The FAD cofactor of SidA can be reduced by one or two electron transfer. (A) SidA crystals grown aerobically with oxidized (yellow) flavin bound. (B) and (C) show crystals grown anaerobically or under limited exposure to molecular oxygen. (B) SidA crystal with the flavin cofactor in its neutral (blue) semiquinone state. (C) SidA crystal with completely reduced FAD (colorless). Reoxidation of the reduced FAD proceeds via a neutral (blue) semiquinone indicating that the reduced FAD is oxidized in two successive one-electron steps. The neutral (blue) semiquinone form, an intermediate in air oxidation, is unstable in the presence of O_2.

3.3.4 Crystallization of Truncated SidA Variants

Successful protein crystallization depends on the homogenity of the protein solution used. Despite the addition of different protease inhibitor cocktails for both $SidA^{AF}$ and $SidA^{AN}$, protein degradation was observed over time. Degradation in $SidA^{AF}$ produced a continuous smear of bands (Figure 3-21 A) whereas $SidA^{AN}$ degraded such that distinct degradation bands were visible on SDS gels (Figure 3-21 B). In the case of $SidA^{AN}$ there are at least three protease cleavage sites. N-terminal sequencing revealed cleavage sites between Arg15 and Lys16 and between Arg311 and Ser312 of $SidA^{AN}$. Analysis of the cleavage pattern pointed at putative trypsine cleavage sites (Figure 3-22, red triangles). The two fragments generated as a result of protein degradation are ~36 kDa and ~20 kDa

in size which corresponds to the size of the protein bands that are visible on the SDS gel in Figure 3-21 B.

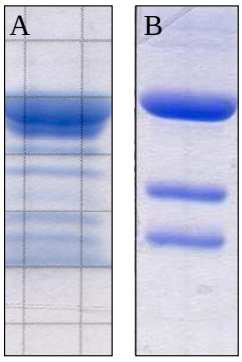

Figure 3-21: Proteolytic degradation of SidA. Protein degradation over time was observed for SidA^{AF} (A) and for SidA^{AN} (B) after 15 days storage at 25ºC. The two distinct protein fragments that resulted from SidA^{AN} degradation were later-on analyzed by N-terminal sequencing.

To destroy the identified proteolytic cleavage sites protein variants SidA^{AN}R16S and SidA^{AN}R311S were generated by site-directed mutagenesis. These protein variants resulted in crystals with a different habitus compared to wild-type SidA^{AN} crystals (Figure 3-22). Protein degradation was however still observed over time. Noteably the distinct fragments (Figure 3-21 B) unintentionally generated by proteolytic degradation of SidA^{AN} were neither observable within GPC nor in DLS experiments presumably indicating cleavage of the protein chain without dissociation of the fragments. The protein would hence be cleaved at the specific positions without affecting protein function or structure. This kind of proteolytic nicking can occur in surface exposed loop regions easily accessible for proteases (Hubbard, 1998; Busen, 1982).

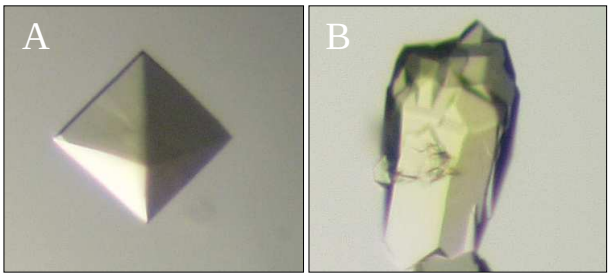

Figure 3-22: Crystals of SidA^{AN} variants R311S (A) and R16S (B).

Potentially flexible/disordered protein loops that are prone to proteolytic degradation and/or impair crystal quality were subsequently identified using the computational program DisEMBL (Linding *et al.*, 2003), which predicts disordered/unstructured regions within a given protein sequence. Potential loops with a high degree of mobility as

determined from C_α temperature factors (B-factors) are defined as “hot loops” and are considered as disordered. According to DisEMBL the first ~30 residues of SidA^{AN} (and SidA^{AF}) N-terminus and large stretches within the C-terminal domain of SidA were thus identified as disordered (Figure 3-23).

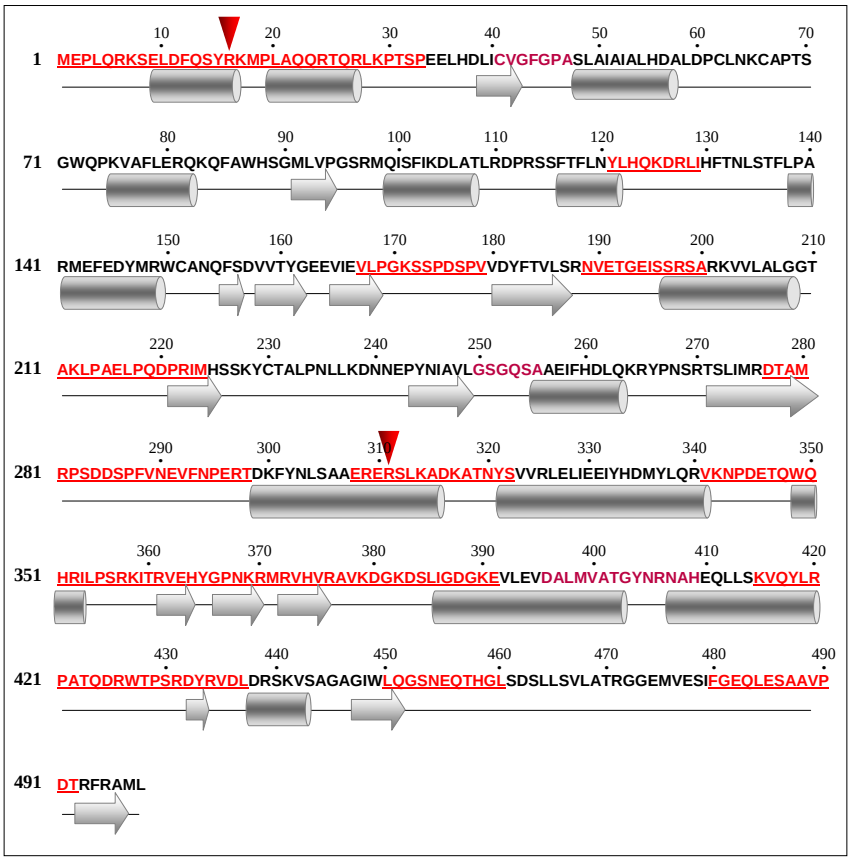

Figure 3-23: Overview of identified protease cleavage sites and predicted disordered loops within SidA^{AN}. N-terminal sequencing identified two proteolytic cleavage sites at Arg16 and Arg311 (indicated by red triangles). Red underlined sequence stretches indicate putative loop regions with a potentially high degree of flexibility as predicted by DisEMBL. Corresponding secondary structure elements like α-helices (cylinders) and β-sheets (arrows) were predicted by the program GOR V (Garnier *et al.*, 1996).

First, N-terminal protein regions presumed to be disordered were eliminated by site-directed mutagenesis resulting in SidA variants SidA^{AN}ΔN17, SidA^{AN}ΔN26 and SidA^{AF}ΔN32. As for SidA^{AF}ΔN32 the N-terminal stability was markedly improved (confirmed by SDS-PAGE and N-terminal sequencing). However, diffraction of SidA^{AF}ΔN32 crystals did not improve within X-ray experiments. SidA^{AN} variants ΔN17 and ΔN26 by contrast neither decreased N-terminal protein degradation nor improved X-ray diffraction (Lisson, 2007). Degradation of SidA^{AN} could finally be curtailed by

purifying and storing the protein at pH 10.0. For purification and storage this pH was favourable although the protein is catalytically inactive at pH values above 9.0. However enzymatic activity could be recovered through re-buffering of the protein at pH 7.5-8.0.

3.3.5 Crystallization with Oil

Crystals of $SidA^{AN}$ grew within a few hours after setting up the crystallization drop potentially indicating that supersaturation occured too rapidly. Excessively fast crystal growth can result either in a shower of small crystals rather than in single big ones or in twinned or intergrown crystals (Oswald *et al.*, 2008). To slow down crystal growth and thereby obtain single large-sized high quality crystals, a layer of oil was placed over the reservoir solution (Figure 3-23). The oil acts as a barrier between reservoir and crystallization drop, reducing the rate of diffusion of water between reservoir and crystallization drop (Chayen, 1997). The rate of vapor diffusion and hence the speed of crystal growth depend on the type of oil used. In the case of SidA crystallization oils of distinct viscosities were used. However, despite slightly retarded crystal growth none of the crystals tested resulted in improved X-ray diffraction quality.

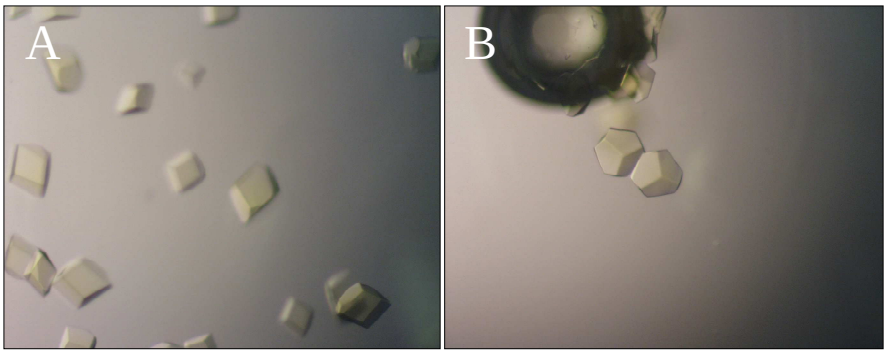

Figure 3-24: $SidA^{AN}$ crystals grown under vapor diffusion with a layer of oil placed over the reservoir solution. Crystals were grown in 1.4 M ammonium sulfate, Tris/HCl pH 8.5 (A) and 0.2 M sodium formate, 1.5 M NaCl (B) as hanging drops with 500 µl reservoir solution that was covered with a layer of 400 µl silicone oil.

3.3.6 Crystal Growth within a Gel Matrix

Another method to improve crystal quality is the crystallization in agarose gels. The agarose can reduce convection and the diffusion of biological macromolecules and crystallization reagents. This contributes to a more regulated growth of the protein

crystals. Located within the gel matrix, sedimentation effects are largely eliminated allowing crystal growth to occur in three dimensions. The SidA crystals obtained by this method have an unusually regular morphology despite some protein precipitation (Figure 3-25). However, X-ray diffraction of these crystals was not superior to that of other crystals.

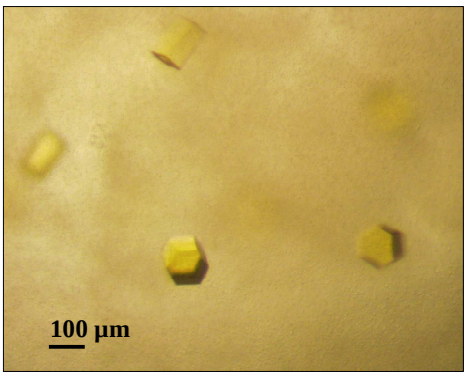

Figure 3-25: SidA crystals that have been grown within a matrix of low-melting agarose.

3.3.7 Crystallization with Substrates and Additives

In the case of enzymes the addition of substrates, cosubstrates and potential inhibitors are known to enhance crystal growth and improve crystal quality and morphology (Hassell *et al.*, 2007; Vuillard *et al.*, 1995; Sousa, 1995; Cudney *et al.*, 1994). These small molecules are suspected to perturb and manipulate protein-protein and protein-solvent interactions as well as to perturb the arrangement of surrounding water molecules. It is supposed that additives can stabilize or generate conformity through specific interactions with the protein molecule. In the case of SidA ($SidA^{AF}$ and $SidA^{AN}$) crystal-soaking and co-crystallization with additives as well as with different combinations of substrate and cosubstrates (L-ornithine, NADPH, $NADP^{+}$) have been applied. Again, of those crystals that have been tested within X-ray experiments none resulted in measurably improved diffraction potential (data not shown).

3.3.8 Cryoprotection of SidA Crystals

The majority of macromolecular X-ray data is collected at cryogenic temperatures (~100 K). As a result most crystals need to be cryoprotected before cooling and data collection. The cryoprotectant can however hugely impact on the diffraction quality of protein crystals (Garman and Owen, 2007). The choice of cryoprotectant and the handling of crystals during cryo-cooling are therefore crucial elements within the X-ray experiment. To exclude damaging of the crystals by the cryoprotectant crystals were

mounted in sealed quartz glass capillaries or in polyester tubes. X-ray data were subsequently collected at ambient temperature. This procedure demonstrated that the chosen cryoprotectant (20-30 % glycerol) does not impact on diffraction quality of the SidA crystals. A variety of SidA crystals irradiated at room temperature diffracted X-rays equally well at 100 K after remounting the crystal, adding cryoprotectant and flash-cooling in liquid nitrogen (Figure 3-26).

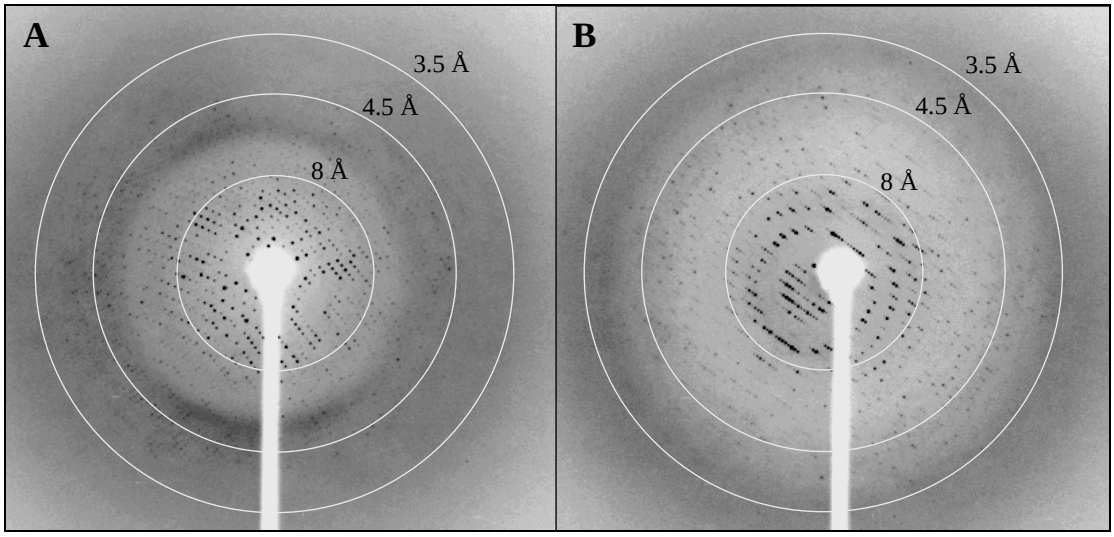

Figure 3-26: Comparison of diffraction images before (A) and after (B) cryo-cooling of a SidA^{AN} crystal. (A) The SidA^{AN} crystal was irradiated at room temperature. (B) For cryoprotection prior to flash-cooling in liquid nitrogen the crystal was transferred into a protecting solution of reservoir and glycerol. X-ray diffraction of the crystal was measured in a cryostream at 100 K. Diffraction images were collected on a rotating copper anode generator and an R-AXIS IV++ image plate detector (Rigaku).

3.3.9 Seeding Techniques

Seeding is a method to introduce pre-formed crystal nuclei into a drop to control nucleation and alter the way in which crystals grow. It uses the basic conditions under which crystals normally grow, sometimes modified slightly. In this case, macroseeding (Zhu *et al.*, 2005), microseeding and streak seeding (Bergfors, 2003) were employed, the latter proving the most successful (Figure 3-27) with regard to improvement of X-ray diffraction of SidA^{AN} crystals. Small crystals became already visible within twelve hours after set up of the crystallization experiments but growth was allowed to continue for at least one week to obtain crystals of up to 500 × 200 × 50 µm. The crystal size was crucial to the X-ray diffraction quality. Whereas SidA^{AN} crystals smaller than

~100 × 100 × 100 µm never diffracted X-rays to more than 7 Å, crystals with improved size diffracted X-rays to 3.2 Å resolution (compare Table 3-3, section 3.4).

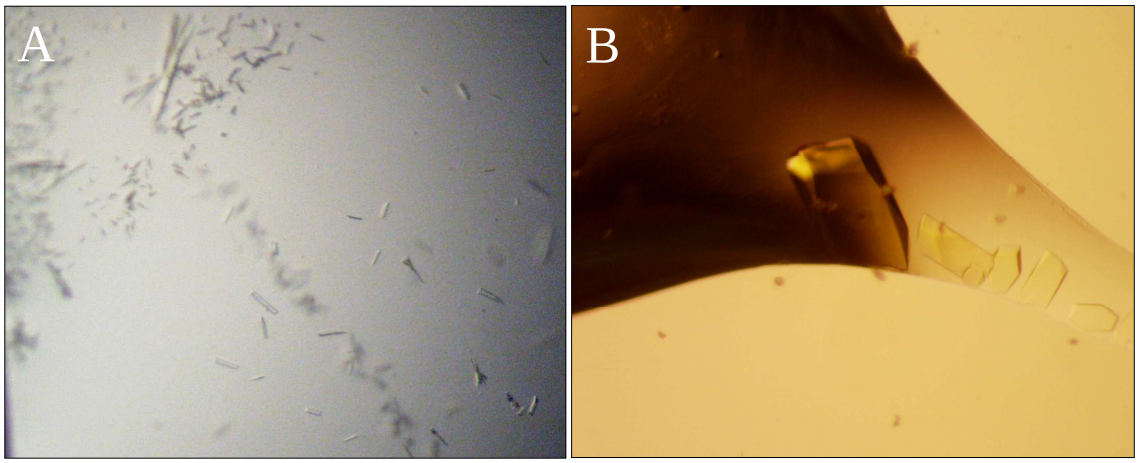

Figure 3-27: Streak seeding. Crystallization drops were set up with (A) SidA^{AF} and (B) SidA^{AN}. Crystal nuclei have been placed into the crystallization drops using a thin, flexible needle.

3.4 Data Collection and Phasing

3.4.1 Space Group Determination

Using synchrotron radiation diffraction of optimized SidA crystals (including SidAC151S crystals) was improved to 3.2 Å resolution. Corresponding data collection statistics are summarized in Table 3-3 (p. 70, at the end of this section). Indexing of SidA diffraction data was achieved using the program package HKL2000 (Otwinowski and Minor, 1997), indicating a trigonal symmetry (P3) with unit cell dimensions of a = b = 148.2 Å and a c-axis of 208.7 Å. Assuming a tetramer of SidA per asymmetric unit (AU) the calculated Matthews coefficient (V_M) (Matthews, 1968) accounts to 2.9 $Å^3$/Da with a solvent content of ~57.6 %. A self-rotation function was calculated using the General Locked Rotation Function (GLRF) (Tong and Rossmann, 1997) which revealed three crystallographic twofold axes spaced at 60° intervals in the ab-plane perpendicular to the c-axis (Figure 3-28). The choice of possible space groups was thus further narrowed down to P321.

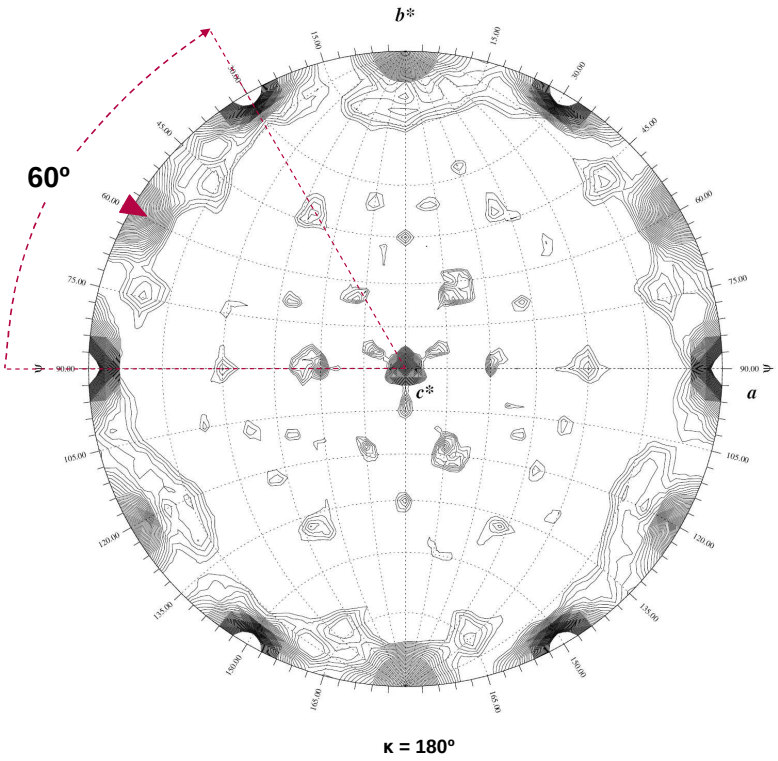

Figure 3-28: Self-rotation function of a SidA crystal at κ = 180°. Heights of peaks are indicated by contour lines. Weaker contour lines inbetween the crystallographic axes point at the presence of a non-crystallographic twofold axis and is indicated by a red triangle.

Due to the proven tetrameric organization of SidA and an estimate of four molecules per AU the self-rotation function was checked for additional symmetry elements in particular non-crystallographic symmetry (NCS) which arises from the point-group symmetry of the protein's oligomeric assembly (Tong, 2001). Additional twofold axes were observed to lie in the ab*-plane at an offset of 30º with respect to the crystallographic symmetry axes (marked by a red triangle in Figure 3-28) indicating the presence of NCS.

Analysis of a pseudo-precession image of the *h0l*-plane of the SidA data sets revealed systematic absences of reflections along the *l*-axis (Figure 3-29). The systematically absent reflections with indices $l \neq 3n$ (n = integer) on the *l*-axis indicate either a 3_1 or a 3_2 screw axis along the c-axis (Figure 3-29).

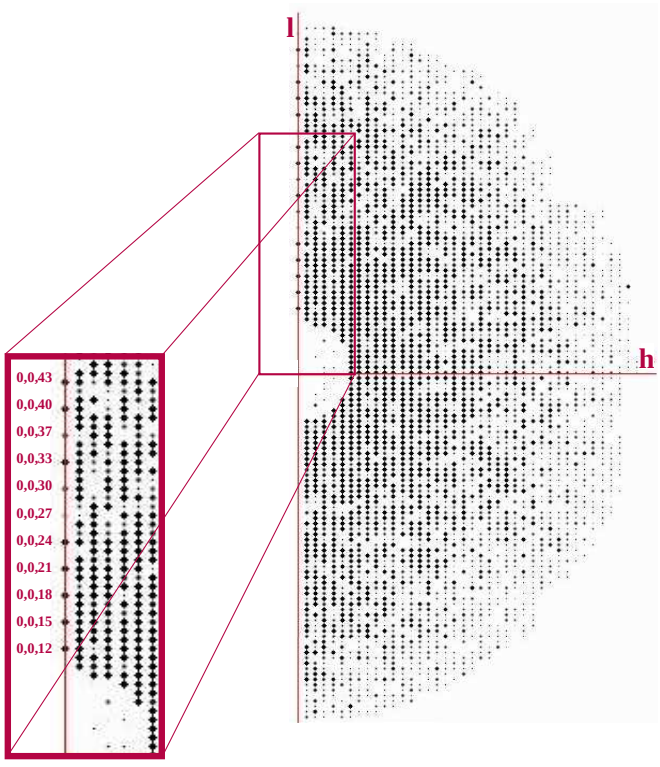

Figure 3-29: Pseudo-precession image of the *h0l*-plane of the peak data set of a SidA crystal. The magnification shows reflections lying on the *l*-axis. Reflections with indices $l \neq 3n$ are absent.

Following space group determination corresponding diffraction data were integrated and scaled by the programs DENZO and SCALEPACK (Otwinowski and Minor, 1997). The

respective diffraction data statistics are summarized in Table 3.3, together with a native data set that was crucial for structure determination (p. 70, at the end of this section).

3.4.2 Molecular Replacement

SidA belongs to the enzyme class of flavin-dependent oxidoreductases (EC 1.14.13) implying that its three-dimensional structure would be similar to other proteins of this enzyme class. In general successful use of molecular replacement primarily depends on two factors: 1) the quality of the model of the protein available and 2) the nature of the crystal symmetry, packing and diffraction quality. Although sequence identity of at least 25 % between the model structure and the target protein is desirable (Taylor, 2003) it is the structural similarity between the two proteins that is crucial for successful MR calculations. Whereas BLAST searches against the Protein Data Bank (PDB) revealed no crystal structure that could have served as a model for MR calculations, similarity searches with the HHPred server (Soding *et al.*, 2005) revealed several related monooxygenases (Table 3-2).

Table 3-2: PDB entries found by the HHpred server.

Description	Organism	Sequence Identity [%]	E-value[1]	Prob[2]	Score[3]	Reference
Phenylacetone monooxygenase	*Thermobifida fusca*	14	0	100	378.5	Malito *et al*., 2004
Flavin-containing† monooxygenase	*Methylophaga sp*.	18	1.8 E-44	100	292.0	Alfieri *et al*., 2008
Flavin-containing monooxygenase	*Schizosaccharomyces pombe*	14	3.1 E-42	100	287.3	Eswaramoorthy *et al*., 2006
NADPH oxidase†	*Staphylococcus aureus*	15	1.1 E-34	100	200	JCSG, 2008*
Lipoamide dehydrogenase	*Saccharomyces cerevisiae*	16	1.9 E-24	100	198.8	Werner *et al*., 2007 (unpublished)
Coenzyme A-disulfide reductase	*Lactobacillus sanfranciscensis*	15	2.1 E-22	100	206.6	Lountos *et al*., 2006

1 E-value: expected number of false positives per database search with a score at least as good as the score of this sequence match; HHpred *E*-values do not take into account the secondary structure similarity.
2 Prob: probability in [%] that the database match is a true positive, i.e. that it is homologous to the query sequence at least in some core part.
3 Score: total score that includes the score from the secondary structure comparison.
† These structures were not used in initial MR calculations since they were published later at a time when a preliminary structural model for SidA had already been built on basis of experimentally derived phases (see section 3.4.3).
*** JCSG:** Joint Center for Structural Genomics.

HHpred uses search methods that are based on pairwise comparison of profile hidden Markov models (HMMs) rather than sequence-sequence comparison methods (Soding *et al.*, 2005). Profile HMMs are similar to simple sequence profiles used in profile-sequence comparison methods such as PSI-BLAST (Altschul *et al*., 1997). In addition to amino acid frequencies within a multiple sequence alignment, position-specific probabilities for inserts and deletions are considered as well. Moreover HHpred searches alignment databases like Pfam (Sonnhammer *et al.*, 1997) and SMART (Schultz *et al.*, 1998) rather than sequence databases such as UniProt (Boutet *et al.*, 2007) or the NR (non-redundant protein sequence database) which reduces the list of hits to a number of sequence families instead of a series of single sequences (Soding *et al.*, 2005). Search options provided by HHPred also include local or global sequence alignments and a score for secondary structure similarities.

Related monooxygenases that have been revealed as a result of the HHPred search were tested as structural models for phase calculation and structure solution of native SidA data. In addition models generated with the program CHAINSAW (CCP4, 1994) were used for MR calculations. Based on an alignment of target and model sequences CHAINSAW prunes non-conserved residues from the model but leaves conserved residues unchanged (compare section 3.3.4). Poly-alanine and poly-serine models of related structures were similarly used in MR calculations. MR calculations were performed in both space groups $P3_121$ or its enantiomorph $P3_221$ and in a way that allowed for a minimal number of clashes (2-4) and a clash distance of 3.0 Å. However, none of the models used resulted in a reasonable solution in molecular replacement procedures using the CCP4 program PHASER as reflected by too low Z-scores (number of standard deviations above the mean value) and no or unreasonable MR-solutions. Generally for a translation function the correct solution will have a Z-score (TFZ) above 5 and be well separated from that of alternative solutions. For a rotation function the correct solution may have a Z-score (RFZ) below 4, and will not be found until a translation function is performed that selects the correct solution. A TFZ between 5-6 indicates a rather unlikely solution whereas solutions with a TFZ of 6 are classified as possible and those above 8 as definite solutions (McCoy *et al.*, 2005). Using MR with different native data sets none of the above criteria was fulfilled - the obtained scores for TFZ ususally

were ≤ 5. Furthermore these TFZ values were not well separated from the corresponding list of potential solutions. For example several attempts for MR have initially been made with phenylacetone monooxygenase from *T. fusca* (PDB entry: 1w4x). The structure was used as a monomeric and as an artificial dimeric search model. Moreover these search models have been used in MR after modification with CHAINSAW. However, none of these models resulted in a reasonable solution within MR procedures. Using PHASER the corresponding Z-scores accounted only for 2.4 and 4.1 for the translation and the rotation function, respectively. Most calculations proceeded over several days, which ususally indicates the search model to be unsuitable. Similar results (RFZ: 3.7, TFZ: 5.2) have been obtained with FMO from *Methylophaga* sp. (PDB entry: 2vq7), which later on proved to be a close structural homologue of SidA. Presumably the coordinates of the available models do not resemble the structure of SidA sufficiently close to allow its structure to be solved by MR. For comparison, a MR calculation later on performed with a recently collected native data set (Table A-2, Appendix) and SidA structures from early and final stages of model building (section 3.6) revealed Z-scores of 4.5 (RFZ) and 31 (TFZ), and 24 (RFZ) and 72 (TFZ), respectively.

3.4.3 3-Wavelength MAD Experiment

As MR was ineffective in solving the structure of SidA a next option was to attempt phasing by multiple wavelength anomalous dispersion (MAD). For this purpose a selenomethionine derivatized SidA ($SidA^{SeMet}$) was produced and crystallized. Prior to data collection, an X-ray fluorescence scan at the Se K-edge was used to verify the presence of selenium in the derivatized crystal. As shown in Figure 3-30 A the scan was performed over an excitation energy range of 12.60 keV to 12.72 keV. All of the $SidA^{SeMet}$ crystals scanned within the scope of this project resulted in a sufficient fluorescence signal confirming the incorporation of selenomethionine during protein expression. One of the SeMet-derivatized SidA crystals diffracted to a reasonable resolution (3.5 Å) adequate for subsequent data collection within a MAD experiment. Based on the X-ray fluorescence scan, wavelengths representing the peak of the absorption edge (λ = 0.97776 Å; E = 12.680 keV), the inflection point (λ = 0.97853 Å; E = 12.670 keV) and the high energy remote (HR) region (λ = 0.97537 Å; 12.713 keV) were chosen for MAD data collection.

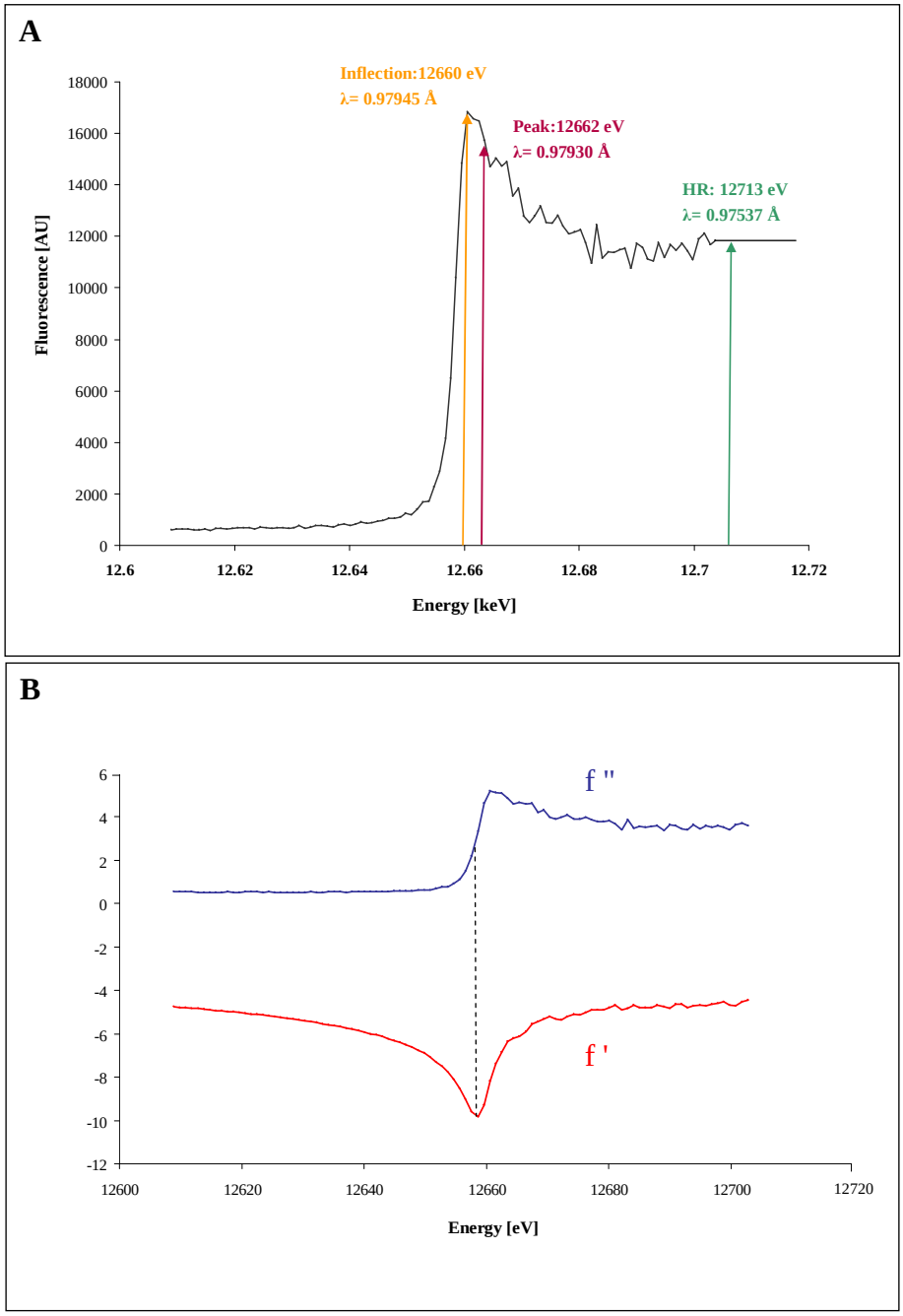

Figure 3-30: X-ray fluorescence scan at the Se K-absorption edge. (A) To confirm the presence of selenium in the SidA^{SeMet} crystals the fluorescence was monitored between 12.600 and 12.720 keV. The scan presented here was recorded at beam line ID23-1 (ESRF, Grenoble). A multi-channel analyzer (MCA) counted the number of detected photons during the fluorescent scan. (B) The differences between the imaginary (f'') and the real (f') part of the anomalous scattering factor at different energies are the basis for MAD data collection and subsequent phase calculation.

At the peak wavelength the imaginary part of the anomalous scattering factor (f'') is at a maximum, whereas the value for the real part of the scattering factor (f') reaches its minimum at the inflection point (Figure 3-30 B). Due to the characteristic behavior of f''

and f', MAD data collection is equivalent to collecting diffraction data from three distinct heavy-atom derivatives with the additional advantage of maximal isomorphism as all data are collected from a single crystal.

Subsequent to data collection and space group determination, the three anomalous data sets were integrated and scaled by the programs DENZO and SCALEPACK (Otwinowski and Minor, 1997) as has been described above for the native diffraction data. The respective diffraction data statistics are summarized in Table 3-3. All four data sets (one native data set from crystal SidAC151S and three anomalous data sets from crystal $SidA^{SeMet}$) revealed reasonable statistics to a maximum resolution of 3.2 and 3.6 Å, respectively. However, these data sets suffered from a severe loss of diffraction power with resolution which results in poor quality high resolution data as reflected by strikingly high Wilson B-factors between 75 and 81 $Å^2$.

Table 3-3: Data collection statistics for SidA datasets.

Diffraction data	**Native SidA[1]**	**Peak[2]**	**Inflection[2]**	**HR[2]**
Beamline	ID 14-2 (ESRF)	X12 (DESY)	X12 (DESY)	X12 (DESY)
Wavelength [Å]	0.93330	0.97776	0.97853	0.97537
Unit cell [Å]	a = 148.9	a = 148.5	a = 148.5	a = 148.5
	b = 148.9	b = 148.5	b = 148.5	b = 148.5
	c = 210.25	c = 209.8	c = 209.8	c = 209.8
V_M [$Å^3$/Da]	2.9	2.9	2.9	2.9
Monomers/AU	4	4	4	4
Solvent [%]	57.6 %	58 %	58 %	58 %
Space goup	$P3_121$ ($P3_221$)	$P3_121$ ($P3_221$)	$P3_121$ ($P3_221$)	$P3_121$ ($P3_221$)
Resolution range [Å]	48.0–3.2 (3.7-3.2)	48.0–3.5 (3.7-3.5)	48.0–3.5 (3.7-3.5)	48.0–3.6 (3.8-3.6)
Mosaicity [º]	0.64	0.64−0.68	0. 59−0.69	0.57−0.69
Completeness [%]	99.9 (99.8)	100.0 (100.0)	100.0 (100.0)	100.0 (100.0)
Redundancy	5.2 (4.9)	8.8 (8.9)	10.6 (10.7)	11.1 (9.9)
Unique reflections	45013 (6465)	34150 (4905)	34232 (4916)	31838 (4598)
Wilson B-factor [$Å^2$]	75.3	78.3	80.2	80.5
I/σ	6.6 (2.3)	7.9 (2.2)	6.9 (2.0)	6.4 (2.0)
R_{merge} [%]	7.5 (33.8)	7.7 (34.2)	8.6 (39.7)	8.7 (37.8)

(**1**) Data were collected with crystals of the C151S variant of SidA; (**2**) Data were collected with Se-derivatized crystals of wild-type SidA. Values in brackets correspond to data for the highest resolution shell. **ESRF**: European Synchrotron Radiation Facility; **DESY**: Deutsches Elektronen Synchrotron.

A subsequent quality assessment of all data sets by the program PHENIX Xtriage (Adams *et al.*, 2002) revealed merohedral twinning for the native data. The corresponding twinning fraction was estimated to be 10 % and the twinning operator is (-h, -k, l).

3.4.4 Solution of the Se-substructure

For determination of the Se-substructure scaled anomalous data sets were further processed using the program SHELXC (Pape and Schneider, 2004). Corresponding SHELXC data statistics are summarized in Figure 3-31 A. Despite reasonable data statistics up to 3.5 Å resolution the signal-to-noise ratio indicated usable anomalous signal to a maximum resolution of only 4.0−4.2 Å. The data up to 4.2 Å were therefore used to calculate the Se-substructure with the help of the program SHELXD (Schneider and Sheldrick, 2002). The HR data were not included in substructure and phasing calculations due to poor correlation statistics with the anomalous data of the peak and the inflection data sets (Figure 3-31 B).

A

Peak data set											
Resolution	8	6	5	4.6	4.4	4.2	4	3.8	3.6	3.4	3.22
N(data)	2988	3965	4927	3313	2135	2543	3059	3733	4624	5684	4140
<I/sig>	25.3	20.8	19.3	20.6	17.6	15.6	11.6	8.4	5	2.5	1.2
%Completeness	97.6	99.9	99.9	99.9	99.9	100	99.9	100	100	97.9	65.5
<d"/sig>	1.53	1.44	1.08	0.98	0.88	0.84	0.81	0.79	0.74	0.81	0.67
Inflection data set											
Resolution	8	6	5	4.6	4.4	4.2	4	3.8	3.6	3.4	3.22
N(data)	2988	3965	4927	3313	2135	2543	3059	3733	4624	5749	4763
<I/sig>	30.8	24.7	22.9	22.9	18.4	12.3	9.5	8.1	5.4	2.5	1.2
%Completeness	97.6	99.9	99.9	99.9	99.9	100	99.9	100	100	99.1	75.3
<d"/sig>	1.64	1.48	1.14	0.97	0.87	0.68	0.73	0.78	0.78	0.72	0.57
HR data set											
Resolution	8	6	5	4.6	4.4	4.2	4	3.8	3.6	3.4	3.22
N(data)	2982	3965	4927	3313	2135	2543	3059	3733	4624	5600	3796
<I/sig>	22.5	18.2	17	18.7	16.1	14	9.7	6.4	4.7	2	1.3
%Completeness	97.4	99.9	99.9	99.9	99.9	100	99.9	100	100	96.5	57.7
<d"/sig>	1.2	1.11	0.93	0.87	0.85	0.82	0.78	0.76	0.79	0.8	0.75

B

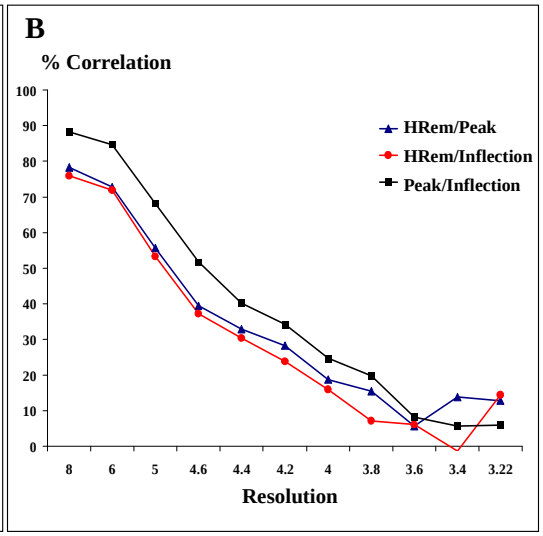

Figure 3-31: SHELXC data statistics. (A) SHELXC output. Each table lists the number of reflections (N(data)), the overall signal to noise ratio (I/sig), completeness and anomalous signal to noise ratio (d"/sig) for a given resolution range for each of the collected data sets (peak, inflection and HR). For zero signal <d"/sig> should be about 0.80. (B) Correlation between data sets versus resolution**.**

Compared to peak and inflection data the HR data have a lower signal to noise ratio (I/σ) in the higher resolution shells and a weaker anomalous signal (d”/σ) – presumably because of radiation damage of the crystal during collection of the HR data, which was the last data set collected. Moreover inclusion of the HR data in substructure calculations

did not result in any significant solution even after allowing for several thousand trial rounds. An optimal substructure solution was found when combining only the diffraction information from peak and inflection data sets, resulting in a correlation coefficient (CC) of 43 % (Figure 3-32 A). For MAD data a CC of 40−50 % indicates a good solution while optimal CC values usually lie in the range of 65 % and higher (Sheldrick, 2005).

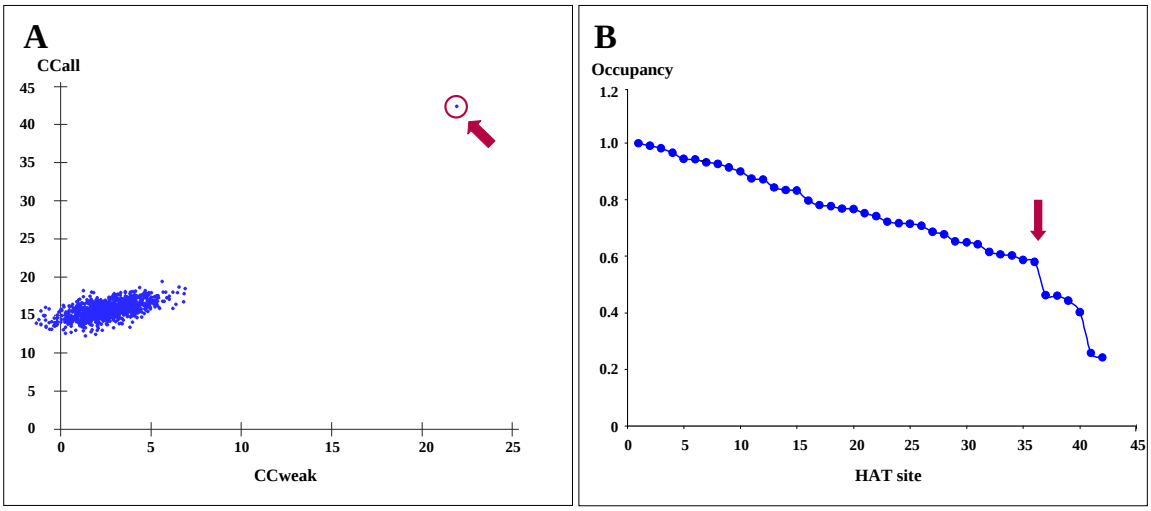

Figure 3-32: Se-substructure solution with SHELXD. (A) A clearly separate solution (marked by an arrow and a red circle) of high correlation coefficients between observed and calculated heavy-atom structure factors indicates a correctly solved Se-substructure. (B) Se sites calculated by SHELXD and their respective site-occupancies. The decrement in site occupancy (marked by a red arrow) indicates the edge between true and incorrectly located Se sites.

SidA contains 14 methionines per monomer. The maximum number of Se sites to identify per tetramer in the AU thus amounts to 56 sites. Out of 42 Se sites located by SHELXD, only 30 resulted in reasonable statistics (site-occupancy ≥ 0.6) (Figure 3-32 B). Thus despite a distinct solution this accounts only for about half of the theoretically expected Se sites. Moreover the difference in site-occupancy between true and incorrectly located Se sites is not as clear as in cases where higher resolution data with improved anomalous signal-to-noise ratio are available.

Initial phasing and density modification was performed with the program SHELXE (Pape and Schneider, 2004; Sheldrick, 2005) using the Se-substructure and an estimated solvent content of 60 %. For phase extension the anomalous data were combined with a native data set from a SidAC151S crystal that diffracted to higher resolution (3.2 Å). The proposed substructure and its inverted image cannot be distinguished by SHELXD.

Density modification with SHELXE therefore had to be performed twice, once for each hand. The solution for the incorrect hand generally has a lower correlation coefficient (mapCC) and a lower contrast and finally results in a featureless map. Thus only one solution will be the correct one leading to a density map featuring recognizable secondary structure elements such as α-helices and β-sheets. Within 20 cycles of density modification the ambiguity between the space groups $P3_121$ and $P3_221$ could be solved and resulted in a significant contrast difference (0.67 for the correct hand versus 0.3 for the incorrect hand) (Figure 3-33 A). The electron density map obviously improved with the space group $P3_121$ clearly revealing secondary structure elements like β-sheets and particularly α-helices (Figure 3-33 B).

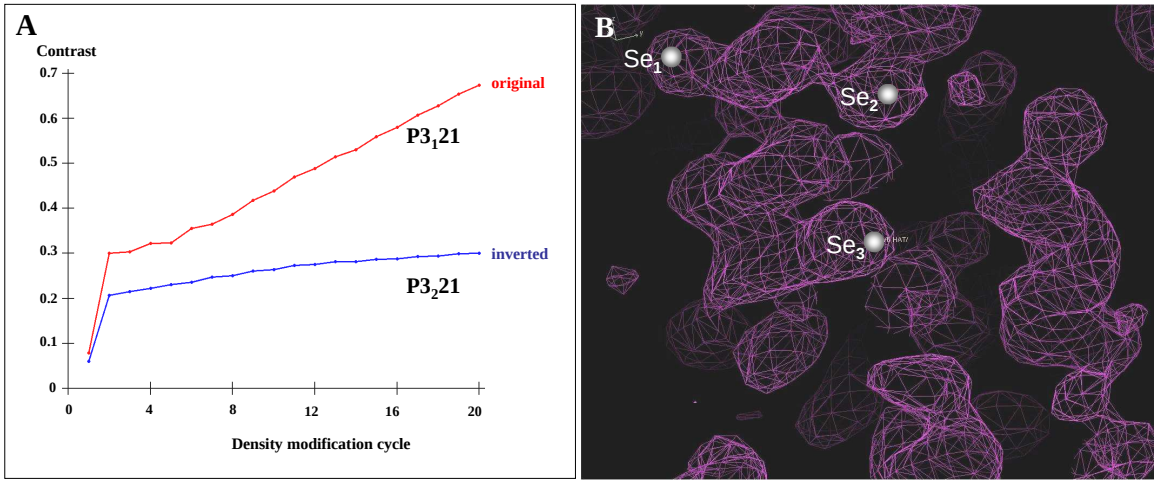

Figure 3-33: SHELXE output and first experimentally determined electron density map. (A) Density modification with SHELXE. The contrast of the electron density map for both possible heavy-atom enantiomorphs is plotted versus the cycles of density modification. Obviously the space group $P3_121$ is the correct hand. (B) Initial experimental electron density map (violet mesh, contoured at 1.5 σ) as calculated from SeMet phases in space group $P3_121$ at 3.5 Å resolution. Selenium atoms (white spheres) are located in regions interpretable as SeMet side chains and were later-on identified as Met148 (Se_1), Met98 (Se_2) and Met148 (Se_3) of SidA.

3.4.5 Density Modification

In addition to SHELXE further density modification was achieved by exploiting the NCS previously identified by the self-rotation function (Figure 3-28). NCS operators were calculated by the program PROFESSS (CCP4, 1994) based on NCS related atoms in a list of heavy atom positions. The strategy involves the identification of similar atom triangles in different regions of the AU. The program then calculates the NCS operators relating

the three atoms which generate pairs of similar triangles. Every Se site is then assigned to one NCS equivalent. In the case of SidA a set of three orthogonal twofold axes are required to generate the tetramer comprising chains A, B, C and D. Of the 42 Se sites identified by SHELXD, PROFESSS could relate 33 Se atoms via NCS operators (Figure 3-34). As required, three orthogonal twofold symmetry axes transform the Se sites of one monomer into those of the other monomers of the SidA tetramer. As discernable in Figure 3-34, the number of Se sites in the asymmetric unit is not equally distributed between the four SidA molecules. Eight Se sites can be located in each of the four sets, while another three Se sites have only been found in three of four sets, namely A, B and C. Two further sites are exclusively present in sets A and B while one site is only present in set A.

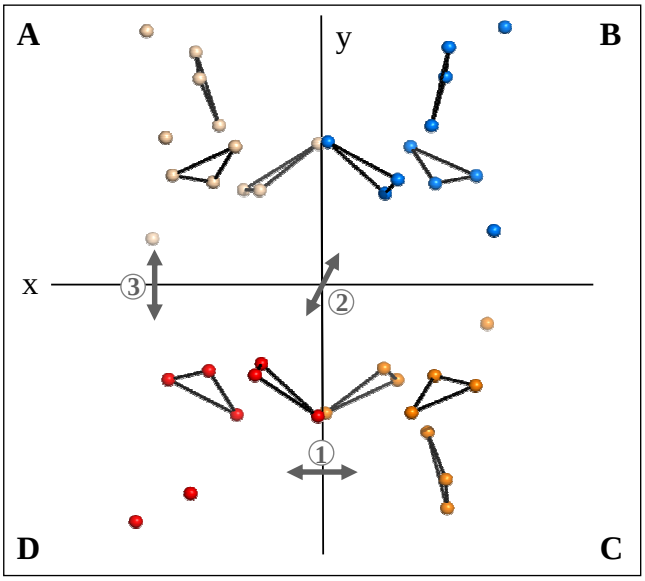

	Operator 1	Operator 2	Operator 3
Polar angle	31.6 57.1 180.0	121.4 60.8 180.0	92.1 -30.2 179.8
Translation [Å]	27.8 48.5 -34.3	46.1 70.1 136.8	73.8 118.9 102.5
Rotation order	2	2	2
Number of atoms paired	30	28	24

Figure 3-34: Non-crystallographic symmetry operators. Upper panel: Of 42 Se sites (schematically shown as spheres) the program PROFESSS computed 33 sites to be NCS related. For each potential SidA subunit the respective Se sites have a different coloring with the corresponding protein chain ID being indicated (A, B, C and D). Lower panel: The three NCS operators that inter-relate the Se triangles as determined by PROFESSS are listed.

Notably the Se sites are not equally well defined in the first experimental electron density map. Figure 3-35 depicts twelve representative Se sites (three per subunit) related by NCS. Whereas Se sites for chains A, B and C lie within and thus account for electron density, the corresponding sites of subunit D are not well defined by the density mesh. This pattern of electron densities of distinct quality proves to be representative for the entire SidA subunits: Using the same nomenclature for the subunits as for the sets of Se sites, chains A and B are well defined while the electron density of chain C is of clearly intermediate quality and that of chain D is only poorly defined (Figure 3-34, right panel).

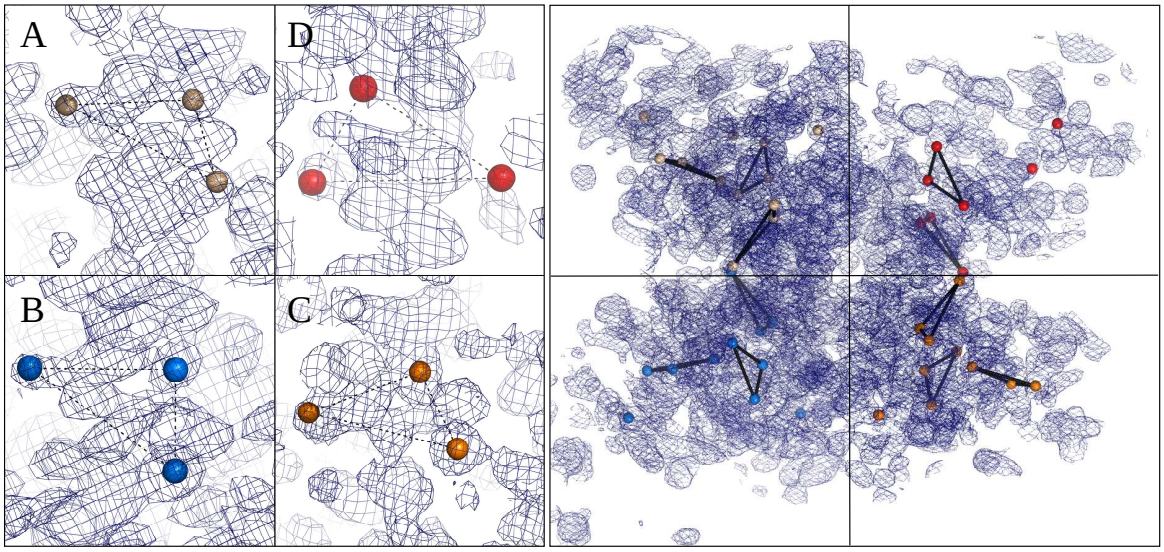

Figure 3-35: Experimental electron density map with NCS related Se sites. The map is contoured at 1.0 σ. Se sites assigned to each of the four SidA subunits are schematically shown as spheres with a different coloring for each subunit. Left panel: Whereas subunit A (light-yellow spheres) and B (light-blue spheres) are well defined by the electron density map, subunit C (orange spheres) and especially subunit D (red spheres) are less well defined. Right panel: Overview of the electron density distribution for the four regions that are assigned for each subunit. The Se sites shown correspond to the color code used for the image on the left. Subunit A and B are well defined with a dense mesh of electron density. Subunit C and D are less well defined.

The PROFESSS-derived NCS operators were also used for density modification by the program DM (Cowtan and Zhang, 1999; CCP4, 1994). DM refines the NCS operators, performs solvent flattening (averaging) and conducts phase extension calculations. After 20 cycles of density modification the electron density map clearly improved (Figure 3-36). However, due to the low resolution of the data the quality of the resulting electron density map was still not sufficient for automatic tracing by programs such as PHENIX/Resolve (Terwilliger *et al.*, 2008; Terwilliger, 2003; Adams *et al.*, 2002) or

Arp/wARP (Morris *et al.*, 2003). Model building therefore had to be performed manually using the electron density calculated by DM.

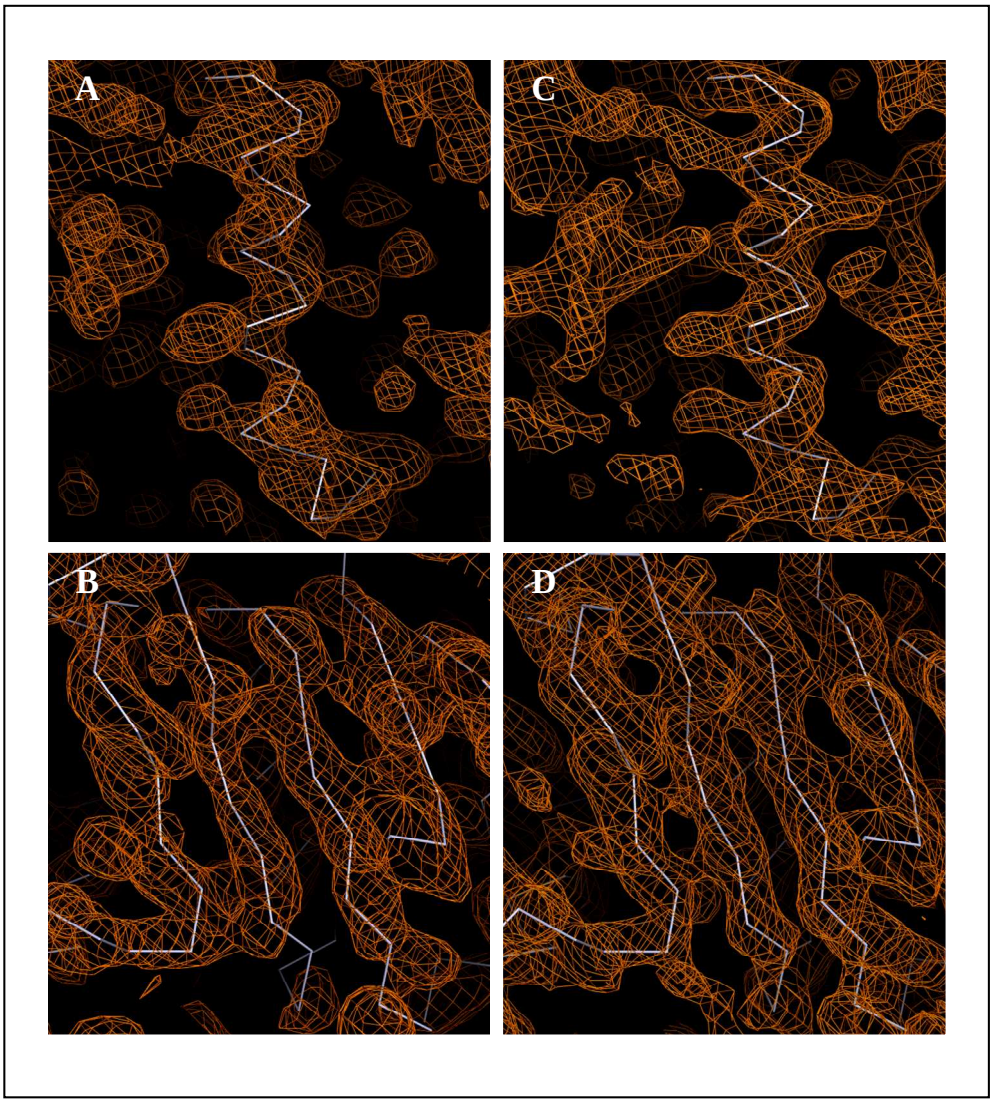

Figure 3-36: Density modification of experimental data. Experimental electron density map at 1.0 σ before (A) and after (B) solvent flattening and NCS averaging with the program DM. In the unmodified electron density map secondary structure elements such as α-helices (A) and β-sheets (B) are already visible. After density modification these structures appear more clearly defined (C and D).

3.5 Model Building and Refinement

The density-modified experimental map was of sufficient quality to build an initial structural model for a single polyalanine chain using the program COOT (Emsley and Cowtan, 2004). α-helices could be placed in the electron density with confidence as they are clearly visible at the resolution then available. Identifying the course and direction of the protein backbone, especially within β-sheets and potential loop regions, proved difficult. After completing an initial poly-alanine model of one SidA subunit (chain A) the Se site derived NCS operators were used to generate the remaining three subunits of the tetramer using the program PDBSET (CCP4, 1994). Because the NCS operators are solely based on the positions of Se sites the fit was less perfect than for the complete amino acid chain of several hundred alanines. Each NCS-generated monomer therefore had to be manually optimized with respect to the electron density map. Moreover as noted above, the electron density was generally only well defined for subunits A and B. In monomer D, the least-defined region, large parts of a β-sheet were only partly visible (Figure 3-37).

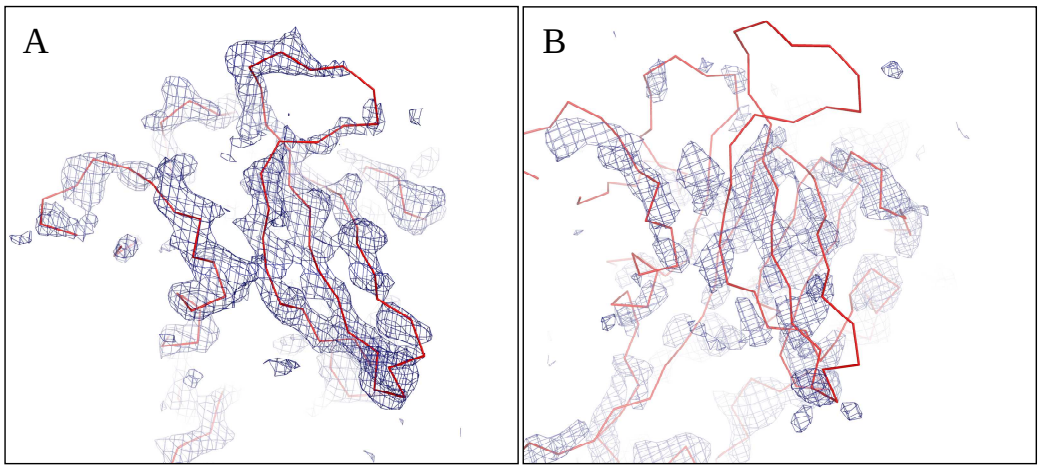

Figure 3-37: Comparison of the electron density in a β-sheet region of SidA subunits A and D. The respective protein backbone is shown in a ribbon representation (red). (A) β-sheet region of subunit A, (B) corresponding β-sheet region of subunit D. To stress the quality differences in electron density between the two subunits the corresponding (2Fo-Fc)-maps (blue mesh) are contoured at 1.5 σ.

Assigning individual amino acid residues of SidA to the electron density was mainly based on the known location of the SeMet sites. In addition to the SeMet sites secondary structure predictions (Figure 3-39) were used in assigning SidA sequence stretches to

corresponding features of the electron density map like α-helices, β-sheets and in part loops and hinges. As shown in Figure 3-37 there are three predicted α-helices that contain methionines. Since the calculated electron density map featured three corresponding α-helices which harbored SeMet sites, the correct sequence could be assigned and respective amino acid residues were inserted into the map.

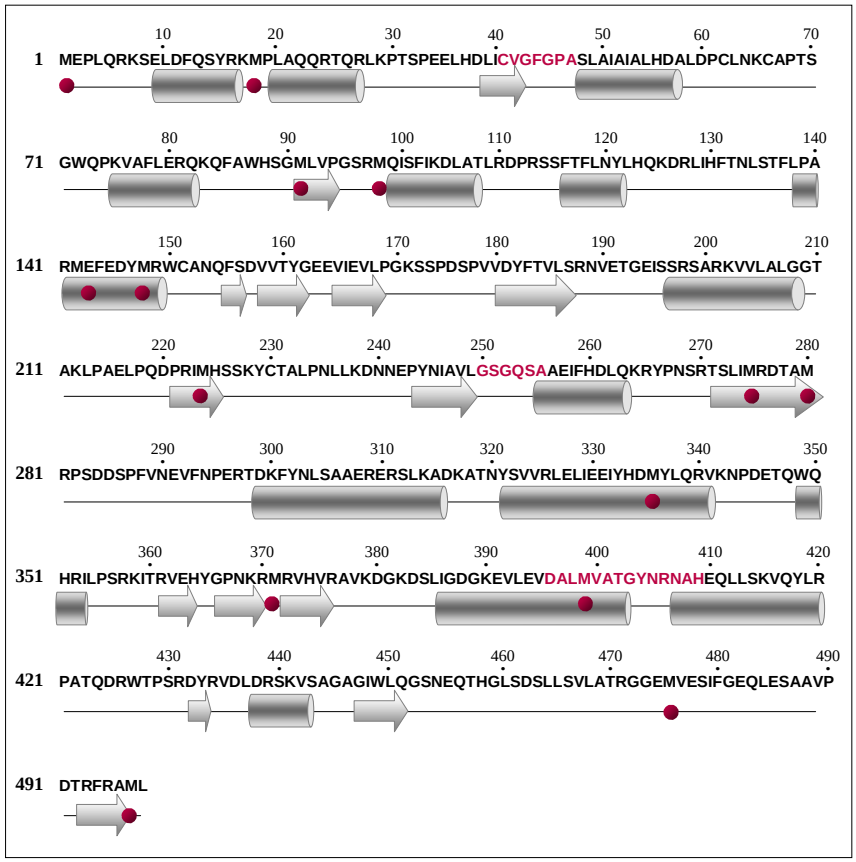

Figure 3-38: Sequence-based secondary structure prediction for SidA and location of SeMet sites. Secondary structure elements were assigned to SidA using GOR V (Garnier *et al.*, 1996). The sequence motifs for the two nucleotide binding sites and the putative substrate binding site are highlighted in red. Methionines are highlighted by red spheres.

For example only one of these α-helices bears two methionines (Met142 and Met148) separated by five intervening residues (Figure 3-38 A). The correct sequence, RMEFEDYMR, could hence unequivocally be assigned (Figure 3-39 B, following page).

Sequence assignment proved especially difficult in regions that did not contain SeMet sites. Moreover, the limited resolution of the X-ray data reduced the visible details of all side chains. In addition the partially lacking electron density did not allow for a

continuous insertion of the protein backbone into the density map resulting in chain breaks and thus in a fragmentary structural model. Besides some well defined exceptions most side chains were placed into the electron density based on their size or bulkiness as well as on their hydrophobic/hydrophilic characteristics.

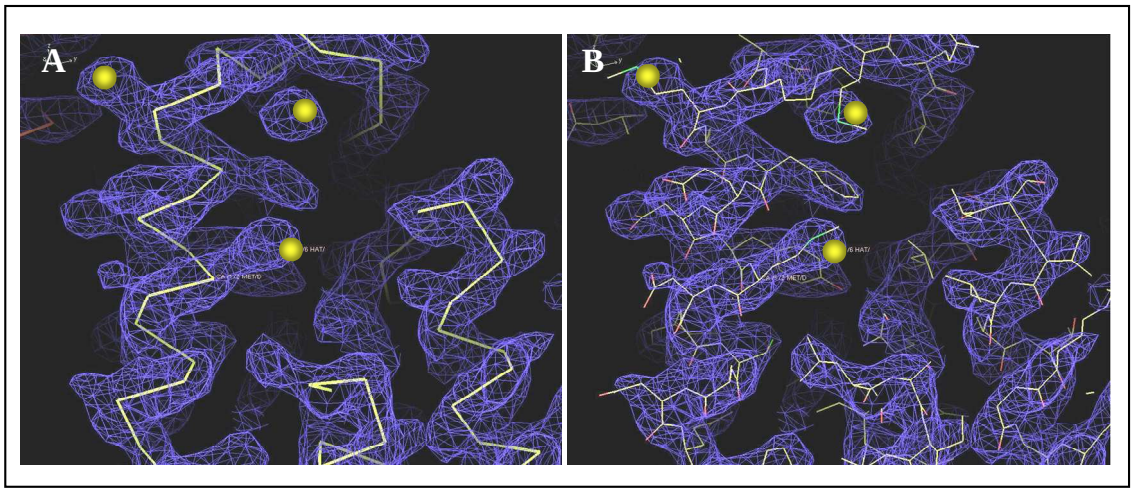

Figure 3-39: DM-modified experimental electron density map at 3.2 Å resolution. (A) Ribbon presentation of initially built poly-alanine model within experimental electron density map (contoured at 1.0 σ) and Se sites (depicted as yellow spheres). On basis of the known (Se-) methionine sites parts of the actual SidA sequence could be manually traced and were inserted into the electron density map. The α-helix shown contains two methionines separated by five amino acid residues and was later on identified as sequence stretch Arg141 - Phe145 as depicted in (B).

The structural model was finally optimized by iterative rounds of refinement using a range of refinement programs inluding the maximum likelihood based programs REFMAC (Murshudov *et al.*, 1997), CNS (Brunger *et al.*, 1998) and PHENIX (Adams *et al.*, 2002). Refinement strategies used for SidA included simulated annealing (Brunger and Adams, 2002) and restrained NCS averaging. The first method involves heating of the model structure *in silico* based on temperature-controlled molecular dynamics with a subsequent cooling routine. NCS averaging by contrast limits the physical differences allowed between NCS-related monomers. At later stages of model building and refinement the twin fraction was taken into account by applying the twin refinement protocols of PHENIX and REFMAC.

As soon as the R_{free}-value dropped below 40 %, the initial SidA model was used in MR in conjunction with different native data sets using MOLREP (CCP4, 1994) and PHASER (McCoy *et al.*, 2005). The latter identified a solution with significant Z-scores for both,

translation and rotation functions (RFZ > 10, TFZ = 40). Subsequent model building and refinement was then continued using the higher resolution native data. Despite improved model data, the electron density (2Fo-Fc) for monomers C and especially D remained poorly defined. Detailed model building was therefore largely confined to the superior defined monomer A.

All four subunits (chain A-D) revealed electron density for the flavin cofactor. Especially the location of the pyrophosphate and the adenine moiety of the cofactor were sufficiently well-defined within weighted difference electron density maps ((Fo-Fc)-maps) (Figure 3-40). As can be depicted from Figure 3-40 the FAD is best defined in chains B and C. Despite its obvious presence within SidA crystals the chromophoric element of FAD, the isoalloxazine ring, is thus not equally well defined for each of the four subunits indicating its potentially high flexibility.

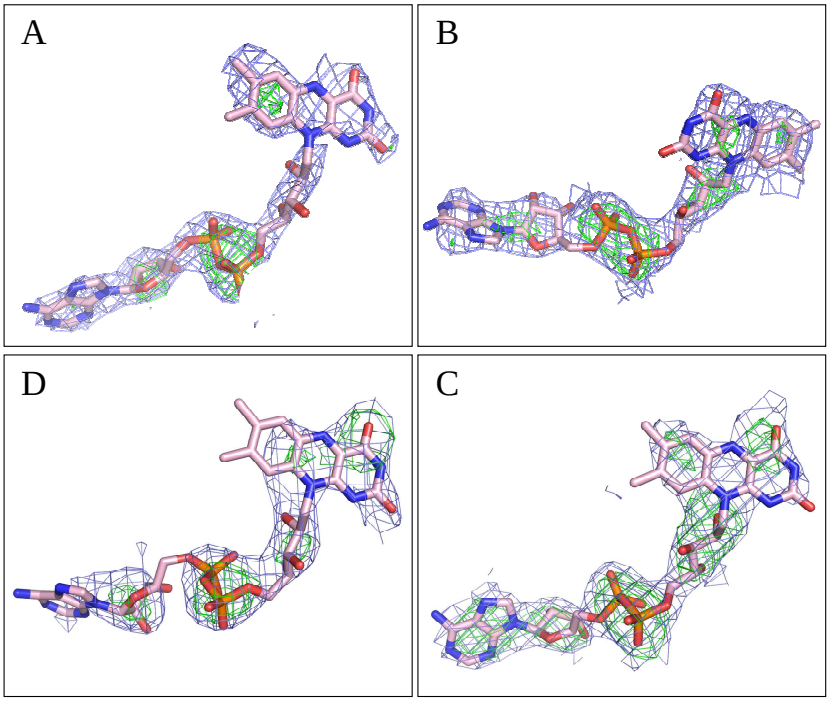

Figure 3-40: Electron density maps for the flavin-cofactor in SidA subunits A-D. The difference electron features for FAD are mainly restricted to the adenine and pyrophosphate moiety of the cofactor. Panels A, B, C and D refer to the corresponding SidA subunits. Blue mesh: (2Fo-Fc)-map, contoured at 1.0 σ; Green mesh: (Fo-Fc)-map, contoured at 3.0 σ.

As mentioned above the course of the amino acid chain for the SidA protomer was difficult to assign. Moreover the electron density map was not continuously defined and

thus exhibited some gaps in potential loop regions or missing secondary structure elements. Therefore the SidA amino acid sequence could not be completely and continuously be inserted into the density map and is thus fragmentary. Examples of those parts of the structural model that could reliably be inserted into the corresponding electron density map leading to a drop in the R-value are shown in Figure 3-41 and as stereo view representations in Figure A-6 (Appendix). In Table 3-4 the modeled fragments of each of the four SidA subunits (chains A, B, C and D) are listed.

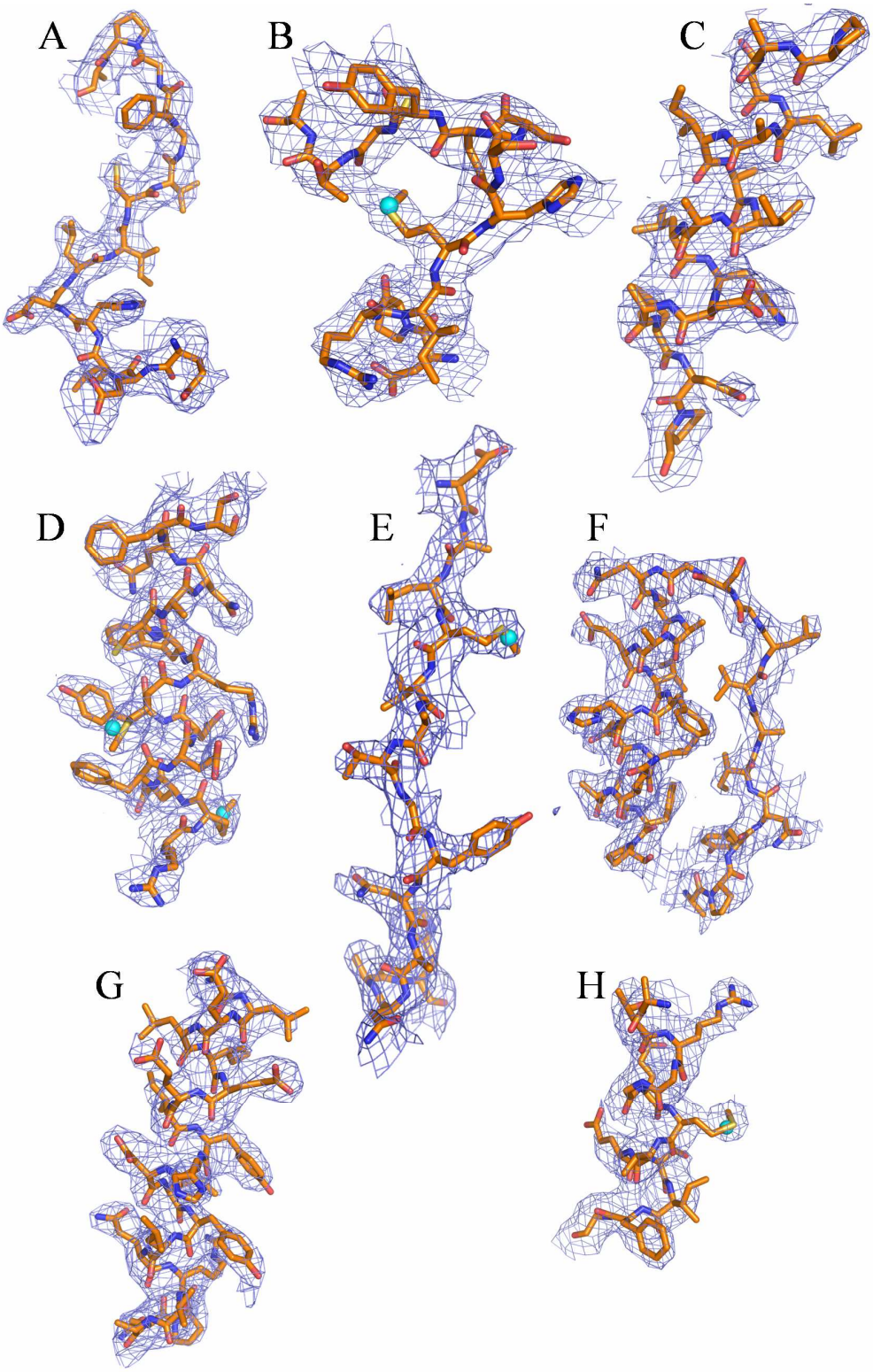

Figure 3-41: Selected regions in the SidA protomer with refined electron density. The (2Fo-Fc)-map is shown as blue mesh and is contoured at 1.0 σ. SeMet sites identified during phase calculation are shown as cyan spheres. (A) Glu34–Ala47 including the FAD binding motif; (B) Sequence stretch with FMO-identifying motif (Arg22-Ala232); (C) α-helix (I) (Ala47-Pro61); (D) α-helix (II) (Arg141-Phe155); (E) Sequence stretch Asp396-His409 including the ATGY motif; (F) Pro243-Pro267, including the NADPH-binding motif; (G) α-helix (IV) (Arg325-Pro344); (H) α-helix (V) (Ala469-Gly481).

Table 3-4: Overview of modeled and missing sequence stretches of the current SidA structure.

	Modeled	Residues that were replaced by alanines	Missing
Chain A	Q26-P287, N320-H364, A377-T428, D432-S453, H468-V489	E26, R27, K29, K65, K75, E80, R81, S96, K125, E163, Q164, I166, S174, S175, D177, S178, Y182, L186, R188, L207, L213, E216, L217, L233, L236, L237-E242, L264, R265, R280, P287, K342, R357-I359, E363, K379, K382, D383, K390, L393, R406, E410, Q411, K415,Q417, R420, T423, Q424, R426-T428, D432-R434, L437, T457-D462, R471, E485, V489	M1-T25†, F288-T319, Y365-R376, P429-R431, N454-T457, P490-L498
No. of Residues	**413 (82.9 %)**	**69 (16.7 %)**	**85 (17.1 %)**
Chain B	Q26-P170, V181-P214, Q216-D239, N241- Q291, Y321-G366, K379-Q424, D437-N454, S463-Q483	Q26, R27, K29, E34-L36, P61, N64, K65, T69, S70, Q73, K75, E80, K83, F85, L92, R97, K125, E163, E164, I166, E167, V180 -Y182, L186, R188, V190, T192, E194, R198, L207, K212-P214, E216, Q219, R222, K228, L236-D239, E242, K264, N268, R270, T278, R281, S283, D284, V289-E291, Y321, V323, R325, K342, Q348-Trp350, R352, R357-G366, K379, K382, I386, E391, L393, R406, N407, E410, Q411, L413, K415, L419, R420, T423, D432-R434, D437, L438, R440, K442, L463, R471, Q483	M1-T25†, G171-V180, A214, L233, N240, D285, V286-N320, P367-V378, D425-R436, E455-D462, L484-L498
No. of Residues	**389 (78.1 %)**	**87 (22.3 %)**	**109 (20.9 %)**
Chain C	Q26-P214, P218-N294, K317-H364, A377-Trp427, R439-G459, D462-L484	Q26-K29, E34-L36, K65, T69, S70, Q73, K75, L92, Q124, K125, E163, E164, K172, R188, E191, E194, R198, R201, K202, L207, K212, L213, L233, L236-E242, K264, R265, R270, D278, T279, S286, F288-N294, K317, T319, N320, E327, K342, E346, Q348, R357-I359, V378, K379, K382, D383, L398, R406, N407, E410, Q411, K415, Q417, L419, R420, T422, D425, Y433-V435, K441, D462, Q483, L484	M1-T25†, A215-L217, R276, P295-D316, Y365-R376, T428-R431, L460, S461, E485-L498
No. of Residues	**412 (82.7 %)**	**145 (35.2 %)**	**86 (17.3 %)**
Chain D	Q26-L169, Y182-F288, N320-E363, V378-P421, R434-E455, L460-E485	Q26-K29, E35-H38, L40, I41, F44, L63-K65, T69, Q73-K75, F78-K83, Trp87, M91-V93, S96, R97, R113, F116, L122, Q124, K125, R127, R129, R149, N153, D157, Y161, E163-V168, D181-F183, L186, R189-E191,E194, I195, R198, R201, K202, L205-L207, K212, L213, E216, L217, R222-M224, K229, Y230, L233, N235-E242, Y244-I246, L262, K264, R265, R270, M275-D277, D284, N320-R325, K342, E346, Q348, Q350 R352, R357-I359, R361-E363, V378-D380, K382, D383, L385, I386, K390, I393, E394, Y404-Q417, R434-K441, I448-Q451, S453-E455, L460-D462, E482-E485	M1-T25†, P170-D181, V289-T319, H364-A376, A422-Y433, Q456-G459, S486-L498
No. of Residues	**387 (77. 7 %)**	**141 (36.4 %)**	**111 (22.3 %)**

† The N-terminally to Met1 attached 13 residue linker and the His_6-tag could not be modeled either.

As can be depicted from Table 3-4 the most thoroughly built subunit is chain A with 413 amino acid residues out of 517 of which only 16.7 % had to be modeled as alanines due to lacking electron density for the side chain of the respective amino acid residue. Chain D on the other hand is the worst of all four SidA subunits and could only be modeled with 387 residues of which almost 40 % had to be replaced by alanines due to the poor electron density within this subunit.

Model refinement was finally accomplished to an R_{work} of 30 % and an R_{free} value of 35 %. Upon refinement, the fit of the model to the electron density was inspected using difference Fourier density maps calculated by REFMAC (Murshudov *et al.*, 1997) and PHENIX (Adams *et al.*, 2002). The results of the refinement and the stereo-chemical analysis of the model, carried out with PROCHECK (Laskowski *et al.*, 1993) and WHATIF (Vreind, 1990), are summarized in Figure 3-42 and Table 3-5.

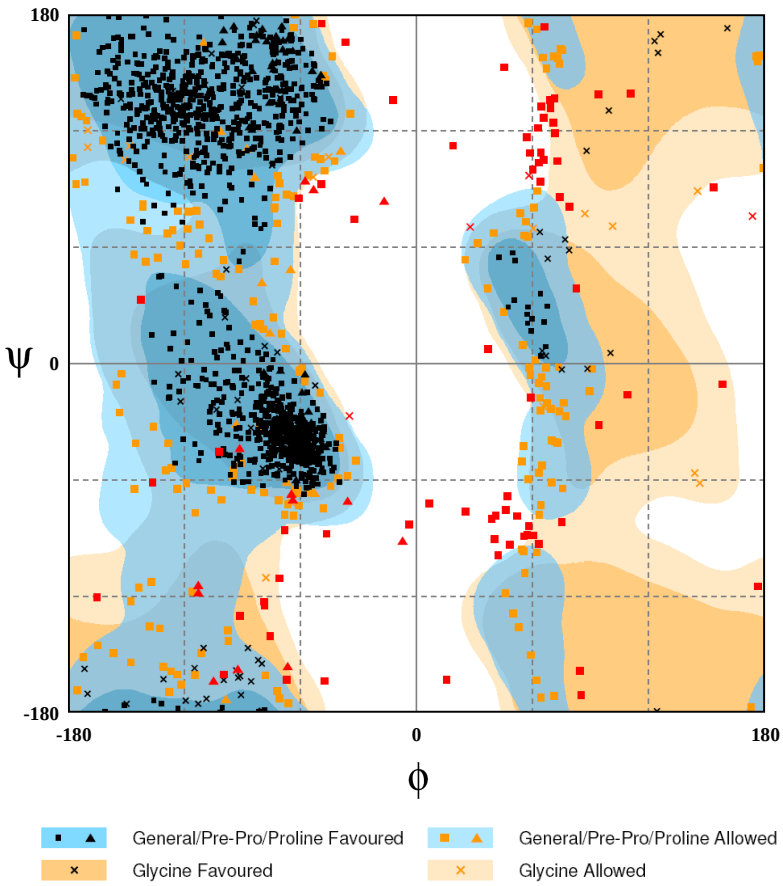

Figure 3-42: Ramachandran plot of the current SidA model. Allowed regions of the plot are colored blue (favourable) and in shades of orange (allowed/generously allowed). Forbidden regions of the plot are shown in white. Outliers are highlighted in red.

Table 3-5: Structure refinement statistics.

Refinement:			
Resolution range [Å]	48.6−3.2		
Molecules/AU	4		
No. of reflections	45164		
Working set	42781		
Test set	2258		
No. of residues	1605		
Figure of merit	0.68		
R_{work} / R_{free} [%]	29.7/34.7		
RMSD bonds [Å]	0.022		
RMSD angles [°]	1.86		
Average B-factors for the C_α-backbone [$Å^2$] of chains A, B, C and D	A: 65; B: 86; C: 86; D: 126		
Ramachandran statistics	preferred	allowed	outliers
	80.1 %	14.2 %	5.7 %

As outlined above model building within this work was rather difficult due to poorly defined and partly missing electron density. Parts of the current SidA structure may therefore be erroneous and elements of secondary structure may be connected wrongly by poorly defined loop regions. This explains the mediocre refinement statistics as it is reflected by the exceptionally high average B-factors, poor Ramchandran statistics including 5.7 % outliers and the suboptimal R-values.

Overall Structure of SidA

3.5.1 The SidA Protomer Displays a Typical Monooxygenase Fold

Due to limited resolution and the resulting fragmentary electron density only a partial model is currently available. The description and discussion of SidA will thus emphasize those parts that have been reliably modeled. Figure 3-43 provides an overview of secondary structure motifs and assigned amino acid sequences and is based on chain A which is the best defined monomer within the current SidA structure.

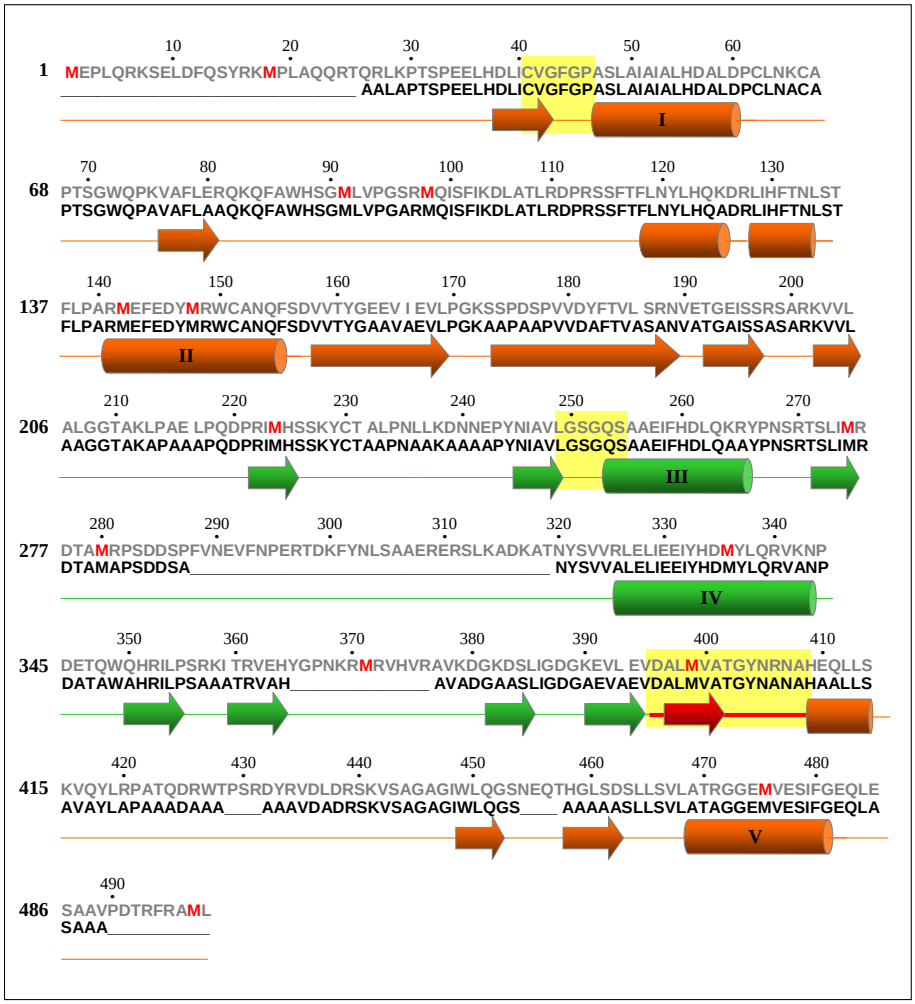

Figure 3-43: Overview of secondary structure motifs of the current SidA structural model. Secondary structure elements of the FAD and the NADPH binding domain are depicted in orange and green, those of the putative substrate binding site in red. Cylinders depict α-helices, arrows β-sheets and straight lines loops. The primary sequence of SidA is shown in gray. Methionine sites are highlighted in red. Sequences assigned to the current structural model are shown in black. Poorly defined residues were modeled as alanines. Chain breaks are shown as black lines. The nucleotide binding motifs as well as the ATGY motif $D(X)_3(^{L}/_{F})ATGY(X)_4(^{H}/_{P})$ are marked by yellow boxes. Major α-helices of SidA are indicated by roman numerals.

The structural model of SidA (chain A) thus consists of five larger α-helices, three smaller α-helical elements and thirteen β-strands. In addition several loop regions connecting these secondary structure motifs could be modeled. Parts not visible in the electron density maps and hence missing in the structural model include i) the N-terminal residues 1 to 25 as well as the His_6-tag and the associated 13 residue linker, ii) the C-terminal residues Pro490 to Leu498 and iii) putative loop regions inlcuding two short chain breaks (Pro429−Arg431 and Asn454−Thr457), one medium sized chain break (Tyr365−Arg376) and one extended region from Phe288−Thr319. Regions of poor electron density that did not improve during refinement or where the amino acid sequence could not be assigned are modeled as (poly-)alanines. In total 344 of 498 residues of the SidA protomer could thus be located and incorporated into the structural model plus 69 residues of unassigned sequence, which were inserted as alanines. Out of 14 methionine sites per monomer that have been theoretically expected, nine have been included in the model and served to support the assignement of the amino acid sequence. In addition both nucleotide binding motifs (CVGFGP and GSGQSA for FAD- and NADPH-binding, respectively) and the ATGY motif ($D(X)_3(^{L}/_{F})ATGY(X)_4(^{H}/_{P})$) could be located and incorporated into the SidA structural model.

The topology of SidA is clearly related to that of other flavin-monooxygenase structures. The monomer consists of two distinct domains (Figure 3-44), a larger FAD-binding domain (residues 26–229 and 409–489) and a smaller NADPH-binding domain (residues ~230–408). Both domains exhibit a typical dinucleotide-binding or Rossmann fold and are connected by two larger loop elements (sequence stretches 206−252 and 401−447, respectively). The nucleotide-binding motifs comprise a β-α-β structural motif in which the first β-strand and the α-helix are connected by a glycine-rich phosphate-binding loop with the motif CVGFGP for FAD-binding and GSGQSA for NADPH cosubstrate binding. The first glycine residue of each motif allows for a tight turn between β-strand and α-helix. The second conserved residue, Pro46 or Gln253, permits a close contact of the main chain to the phosphate group of the nucleotide. The overall SidA protomer structure has a curved appearance with the concave side enclosing the active site with the FAD cofactor (Figure 3-44).

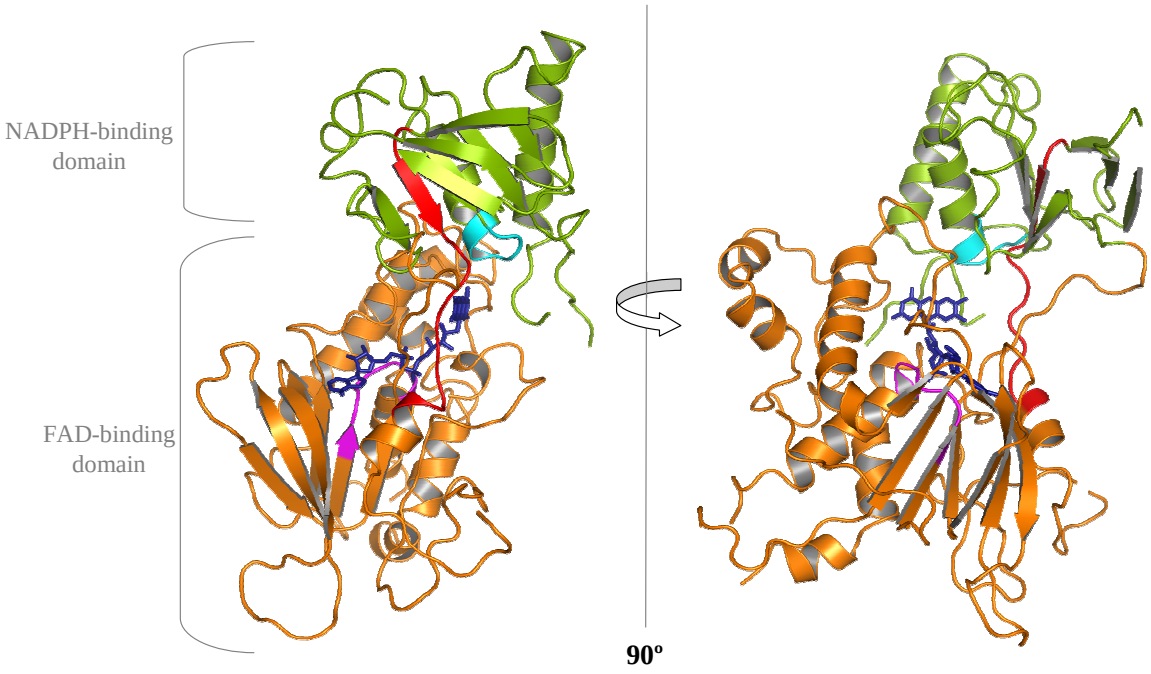

Figure 3-44: Refined, partial structural model of the SidA protomer. The larger FAD-binding domain with FAD (blue) bound is highlighted in orange and the smaller NADPH-binding domain is shown in green. The FAD- and NADPH-binding sites are depicted in magenta and cyan. The $D(X)_3(^{L}/_{F})ATGY(X)_4(^{H}/_{P})$ sequence stretch is highlighted in red. The FAD does not directly interact with the NADPH-binding domain.

3.5.2 The SidA Protomer Resembles the FMO from *Methylophaga* sp.

An initial search for homologous structures based on probable secondary structure elements (HHpred server, Table 3-2) has already indicated SidA to be structurally related to other monooxygenases. The structural model of SidA finally allowed this analysis to be repeated against the protein data bank (PDB) based on its three-dimensional structure using DALI (Holm and Sander, 1999) (Table 3-6). Similarity is thus measured by DALI *Z*-scores. Significant similarities have a *Z*-score above 2 and usually correspond to similar folds. Strong matches usually have a sequence identity above 20 % or a *Z*-score above a cutoff that depends on the size of the query protein. The *Z*-score cutoff is empirically set to $n/10 - 4$, where n is the number of residues in the query structure (Holm *et al.*, 2008). This search placed SidA firmly into the flavoprotein class of oxidoreductases (EC 1.14.13) (Table 3-6) which is in close agreement with results obtained with the HHpred server. Despite a minimal degree of sequence conservation (sequence identity between 9 % and 18 %), the structural hits found by DALI display significantly high Z-scores of >15. The closest structural homologs of SidA are the flavin-containing

monooxygenases (FMOs) from i) *Methylophaga* sp. (mFMO) (PDB entry: 2vq7) with 18 % sequence identity and a root mean square deviation (r.m.s.d.) of 3.3 Å for 278 C_α-atoms and from ii) *Staphylococcus aureus* (PDB entry: 3d1c) with 15 % sequence identity and 3.4 Å r.m.s.d. for 278 C_α-atoms. The top ten DALI hits also include a thioredoxin reductase (PDB entry: 1f6m) from *Escherichia coli* (14 % sequence identity and 2.8 Å r.m.s.d. for 262 C_α-atoms), which is a prototypical disulfide oxidoreductase with the conserved dinucleotide binding scaffold. The structural neighbors of SidA convert substrates structurally distinct from L-ornithine. *Methylophaga* FMO thus converts the aromatic amine N,N-dimethylaniline to its N-oxide form. *E. coli* NADPH oxidase and *Trypanosoma cruzi* trypanothione oxidoreductase by contrast convert thioredoxin and the glutathione derivative trypanothione to their respective disulfide variants. Thus despite different substrate specificities and the distinct biochemical reactions being catalyzed, the DALI-derived flavoproteins share a strikingly conserved fold (Figure 3-45).

Table 3-6: SidA structural homologues found by DALI.

PDB entry	Description	Oligomeric state	Source	Substrate/Product	Identity	Z-score	r.m.s.d.	Reference
2vq7	FMO	2	*Methylophaga sp.*	N,N-dimethylaniline/N,N-dimethylaniline-N-Oxide	18 %	17.9	3.3 Å	Alfieri *et al.*, 2008
3d1c	NADPH oxidase	(1)*	*Staphylococcus aureus*	unknown	15 %	17.5	3.6 Å	JCSG, 2008†
2gv8	FMO	2	*Schizosaccharomyces pombe*	N,N-dimethylaniline/N,N-dimethylaniline-N-Oxide	14 %	16.8	3.8 Å	Eswaramoorthy *et al.*, 2006
1vqw	Protein with similarities to FMOs and to mammalian dimethylaniline MOs	2	*Schizosaccharomyces pombe*	N,N-dimethylaniline/N,N-dimethylaniline-N-Oxide	9 %	16.7	3.7 Å	Eswaramoorthy *et al.*, 2006
1f6m	NADPH oxidase	2	*Escherichia coli*	thioredoxin/ thioredoxin disulfide	14 %	16.1	2.9 Å	Lennon *et al.*, 2000
2cfy	Thioredoxin reductase 1	2	*Homo sapiens*	thioredoxin/ thioredoxin disulfide	9 %	16.0	4.0 Å	Debreczeni *et al.*, 2006†
1nda	Trypanothione oxidoreductase	2	*Trypanosoma cruzi*	trypanothione/ trypanothione disulfide	10 %	15.5	3.8 Å	Lantwin *et al.*,1994

* Oligomerization state not clearly defined.
† To be published.

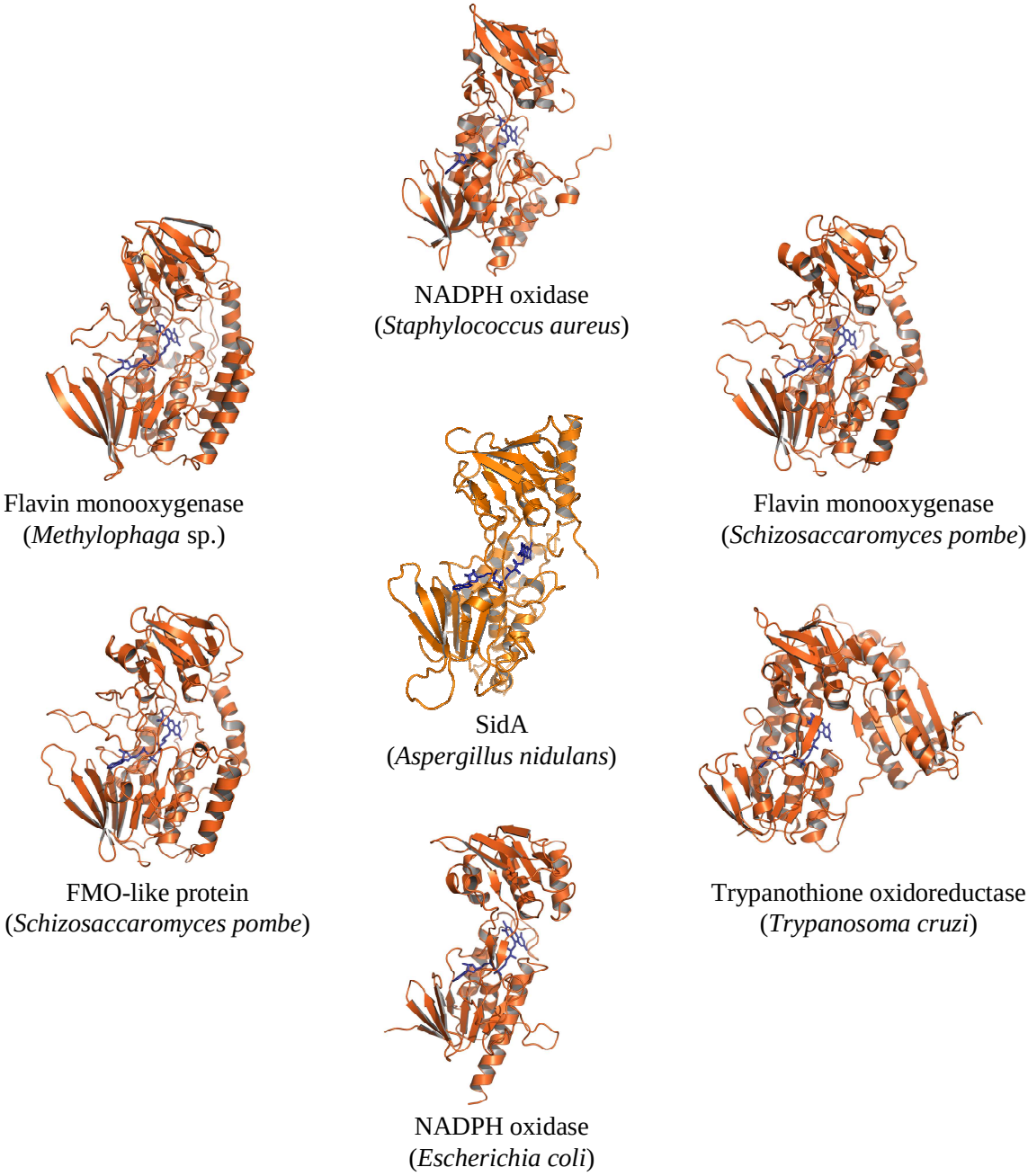

Figure 3-45: DALI search results. The structures displayed are all monooxygenases and were found by the program DALI to have the highest structural similarity to the current SidA structural model (displayed in the center of the figure).

In Figure 3-46 SidA is superposed on four structurally related enzymes. The major difference in the overall topology is the presence of two additional C-terminal α-helices in the related enzymes. Visual inspection would thus indicate that SidA is most similar to *E. coli* thioredoxin reductase. However, it should be borne in mind that additional

secondary structure elements may simply not have been located in SidA as yet due to undefined or missing regions within the currently available electron density map. Secondary structure predictions of SidA support the possibility of additional secondary structure elements being present within the SidA structure (compare Figure 3-38).

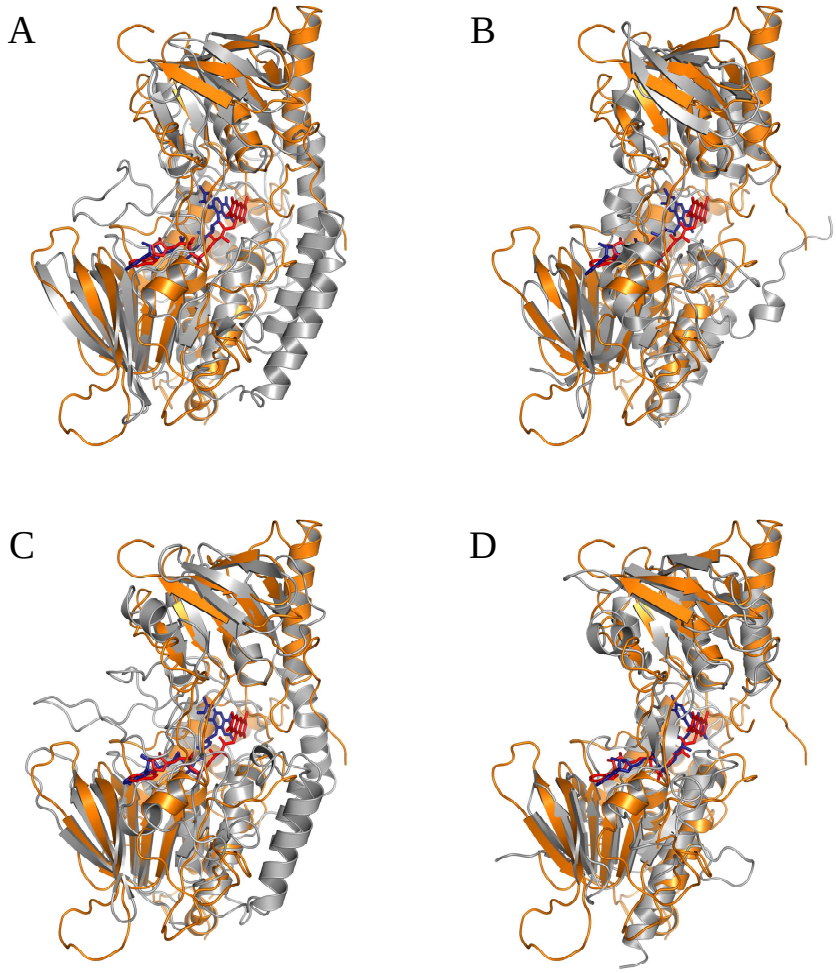

Figure 3-46: Superposition of the SidA structural model with homologous structures found by DALI. The *A. nidulans* SidA structure is depicted in orange and the homologous structures are shown in light-gray. The flavin cofactor of SidA is depicted in red, that of the structural homologue in blue. Superposition with (A) *Methylophaga* sp. FMO, (B) *S. aureus* NADPH oxidase, (C) *S. pombe* FMO and (D) *E. coli* NADPH oxidase.

3.5.3 The FAD-binding Domain

The FAD-binding domain of the current SidA model bears two larger N-terminal α-helices. One of these contributes to the nucleotide binding fold (Figure 3-47 A). An additional N-terminal α-helix covers the *re*-side of the FAD isoalloxazine ring. The FAD

is located between the two domains of the protomer with the isoalloxazine ring largely accessible to the solvent and thus displays the same binding mode as in other flavoenzyme structures. The FAD adenosine diphosphate moiety is bound to the bottom of the cleft which separates the two protein domains and involves the flavin-binding motif CVGFGP being located within the strand-turn-helix motif (Figure 3-47 A). In other structures the FAD is surrounded by a network of water molecules to bridge the protein and the flavin's phosphate and ribitol group oxygen atoms (Eswaramoorthy *et al.*, 2006; Malito *et al.*, 2004) (compare Figure A-5, Appendix). Except for one molecule, waters contributing to hydrogen bonds between FAD and residues of SidA could, however, not be located with confidence in the current SidA structure. Residues that are likely candidates for hydrogen bonding interactions with the FAD cofactor include Trp87, Arg141, Ser322 and Ser463 (Figure 3-47 B).

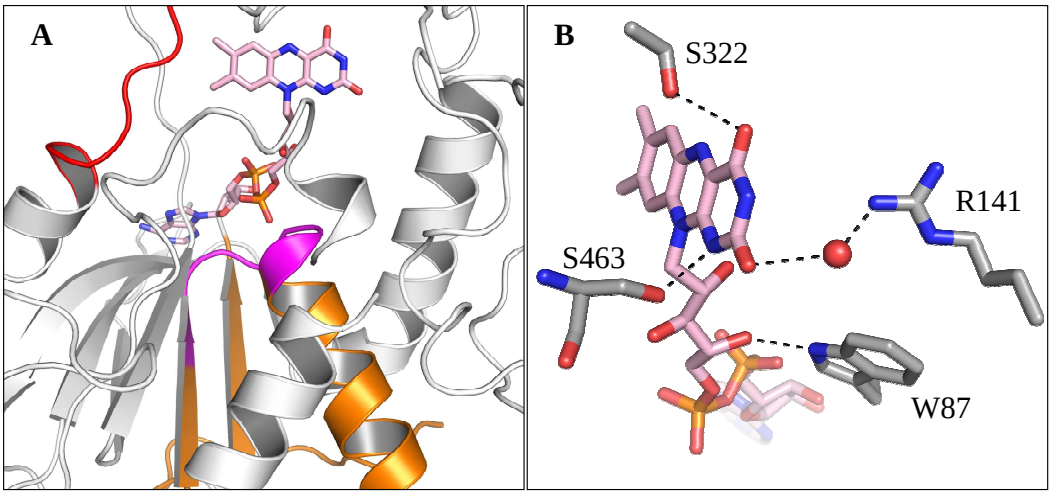

Figure 3-47: The FAD-binding domain. (A) The α-helix and β-sheets of the nucleotide binding fold are shown in orange. The FAD binding motif CVGFGP is highlighted in magenta. The putative substrate binding site within the loop connecting the FAD- and the NADPH-binding domains is colored in red. (B) Amino acid residues that may contribute to FAD binding. Dashed lines mark atomic distances between 2.8 and 3.0 Å. Red sphere: water molecule.

The Nε1 nitrogen of Trp87 could form hydrogen bonds with oxygen atome O4* of the cofactor's ribitol moiety while Ser322 and Ser463 may form a hydrogen bond with the oxygen atom at C4 and the nitrogen atom N1 of the isoalloxazine ring, respectively. Arg141 uses a water molecule for hydrogen bonding with the oxygen atom at position C2 of the isoalloxazine ring (Figure 3-47 B).

Superposition of the SidA structure with its structural homologues reveals that the FAD cofactor occupies a rather outward position thus being more exposed to the solvent. Compared to the FAD of mFMO, spFMO and NADPH oxidase from *S. aureus* the SidA cofactor (shown in red in Figure 3-48) is turned in a ~65º angle and shifted ~5.1 Å in direction of the solvent.

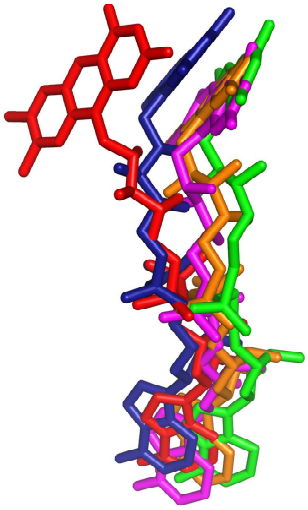

Figure 3-48: Conformation of FAD in SidA structural homologs. The FAD of SidA is shown in red. Superposed FAD structures: *Methylophaga* FMO (orange), NADPH oxidase of *S. aureus* (magenta), NADPH oxidase of *E. coli* (blue) and *S. pombe* FMO (green).

3.5.4 The NADPH-binding Domain

The NADPH-binding domain is the smaller of the two protein domains. It comprises two larger and one shorter α-helix. Of the seven β-strands, the most C-terminal strand is part of the putative substrate binding domain. Despite co-crystallization and soaking with $NADP^+$ and NADPH, none of the crystals diffracted X-rays sufficiently well, worthwhile to collect a data set. The conserved binding motif (GSGQSA) for the NADPH ribose moiety could however be inserted into the SidA structural model. The position of the oxidized prosthetic group within the protein can thus be inferred by comparisons with NADPH-containing crystal structures of related flavoenzymes such as FMO from *Methylophaga* sp. and NADPH oxidase from *E. coli*. This comparison would imply that NADPH binds in an extended conformation on the surface of the NADPH-binding domain (Figure 3-49). The adenine-ribose moiety would correspondingly be bound by the second β-turn-helix motif (shown in green in Figure 3-49) that faces the β-sheet of the putative substrate binding stretch (shown in red in Figure 3-49). In the mFMO structure the nicotinamide-ring faces the *re*-side of the flavin ring at the domain interface. By

contrast, in SidA the nicotinamide ring woul face the *si*-side of the flavin ring due to the exposed conformation of the FAD. NADPH binding in SidA would therefore require the FAD to adopt a conformation more in direction of the catalytic cleft and away from the solvent (Figure 3-49).

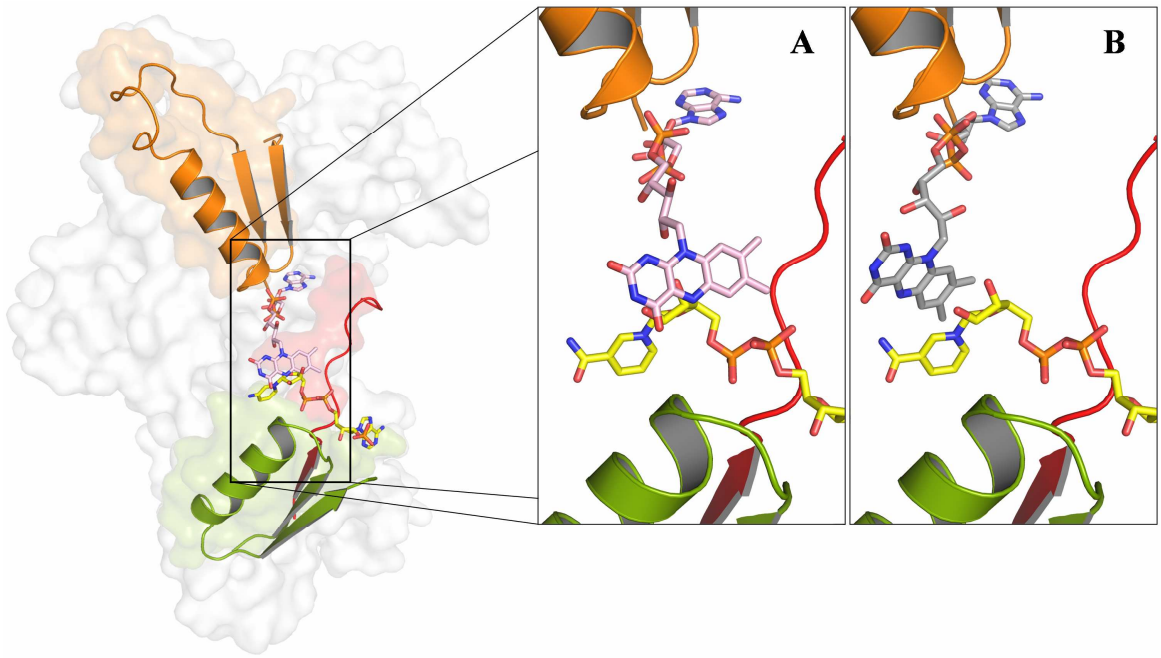

Figure 3-49: Overview of the NADPH-binding site at the domain interface. Left panel: The FAD cofactor is shown in pale pink together with the β-turn-helix motif (orange) important for cofactor binding. The β-turn-helix motif important for NADPH-binding and the sequence stretch harboring the ATGY motif are highlighted in green and in red, respectively. A NADPH molecule (yellow) is modeled in the conformation observed in topologically similar enzymes. Right panel: Magnification of NADPH binding site with modeled NADPH. (A) Conformation of FAD as observed in SidA. (B) Conformation of FAD (gray) as observed in the structure of mFMO.

3.5.5 The Putative Substrate Binding Site

The putative SidA substrate binding site is located in a central β-sheet that leads into one of the flexible stretches connecting the NADPH- with the FAD-binding domain of the SidA protomer (shown in red in Figure 3-50). The ATGY motif proceeds across the cleft between the two domains and along the *re*-side of the flavin cofactor. Interestingly, the tyrosine residue (Tyr404) of this motif is facing towards the isoalloxazine ring and is the only residue that markedly extends in direction of the reactive part of the flavin cofactor (inset in Figure 3-50). Within this work mutational replacement of Tyr404 with serine resulted in the FAD-free SidA variant Y404S. This variant was prone to aggregation and

heavily precipitated within 24-48 h (at 4ºC) after protein purification indicating Tyr404 to be essential for FAD binding and protein integrity.

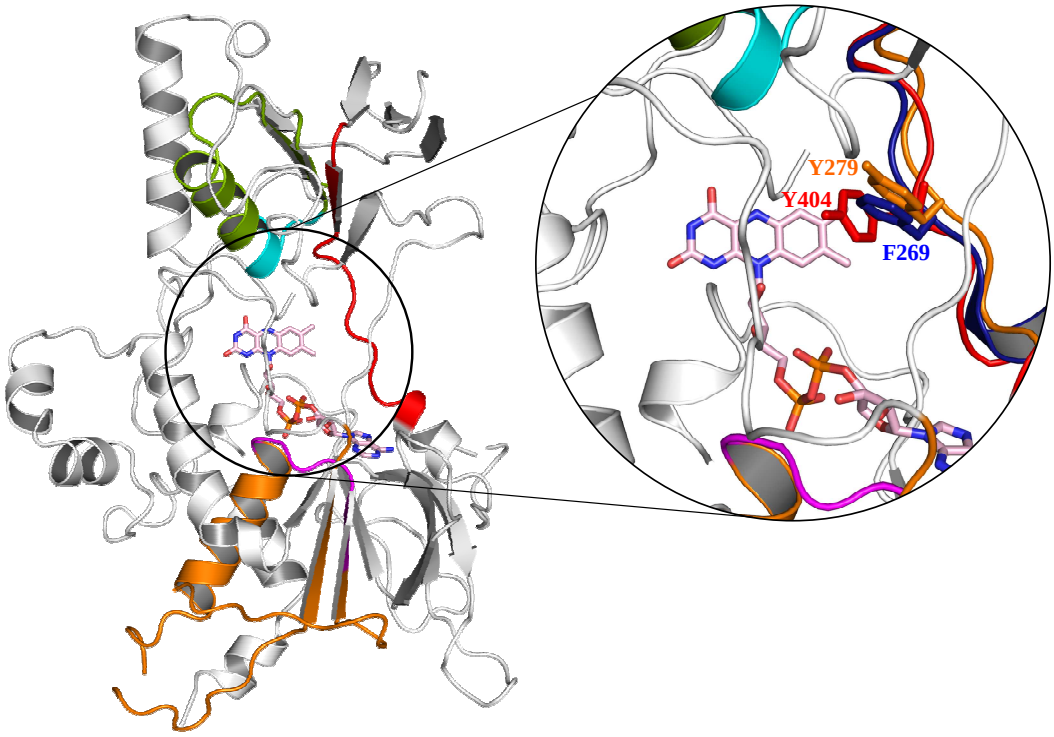

Figure 3-50: Presumed substrate binding region of SidA. The substrate binding site is presumed to be located within one of the stretches that interconnect the two domains of the protomer (red). The inset (black circle) shows a superposition of residues of the SidA stretch harboring the ATGY motif (red; residues 396-409) and residues of homologous protein structures (orange: residues 271−284 of mFMO; blue: residues 261−274 of NADPH oxidase from *S. aureus*) that are located at this position.

In accordance with the SidA structure both FMO from *Methylophaga* sp. as well as the NADPH oxidase from *E. coli* contain a conserved aromatic amino acid at the position occupied by Tyr404 as part of the ATGY motif: Tyr279 in mFMO and Phe269 in *E. coli* NADPH oxidase (Figure 3-50). How the $(D(X)_3(^{L}/_{F})ATGY(X)_4(^{H}/_{P}))$ sequence stretch is involved in substrate binding and catalysis and which additional residues define the SidA active center remains to be elucidated. Despite several soaking and co-crystallization experiments with L-ornithine the diffraction data obtained did not result in difference electron density maps with unambiguously defined substrate.

3.5.6 The SidA Structure is Arranged as a Dimer of Dimers

Unlike its structural homologues, which mainly form dimers (Table 3-6), the SidA from *Aspergillus* exists as a homotetramer in solution. This was demonstrated by DLS and analytical GPC and is also manifested in the crystal structure. The four monomers occupying the asymmetric unit make up the tetramer and can be described as a dimer of dimers A/D and B/C, related by three orthogonal twofold axes of NCS that were previously identified during data processing and structure solution (Figure 3-51).

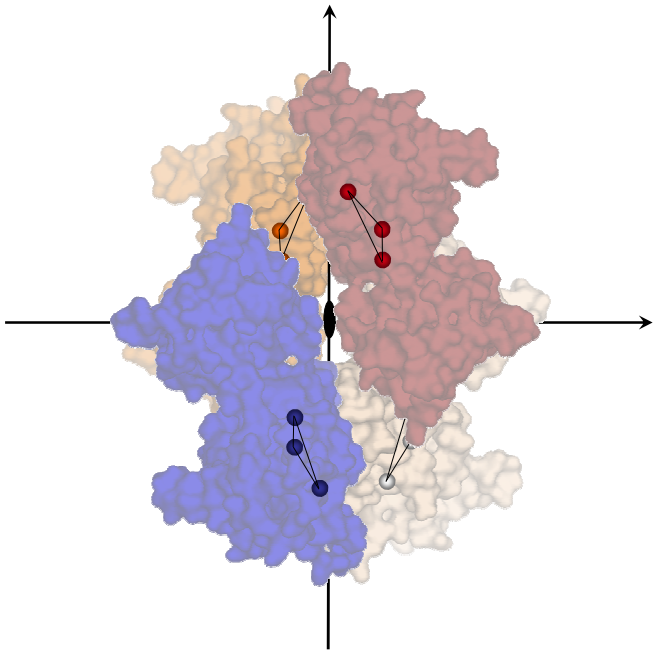

Figure 3-51: Surface representation of the SidA tetramer. The four monomers are highlighted in different colors. Three representative selen sites per monomer identified by PROFESSS are shown as spheres. The three orthogonal NCS-axes are indicated.

The SidA tetramer has approximate dimensions of 97 × 88 × 74 Å. As calculated by the PISA server (http://www.ebi.ac.uk/msd-srv/prot_int/pistart.html) (Krissinel and Henrick, 2007) the largest interaction surface in the complex involves the FAD-binding domains of chains A and B (~1166 Å^2) or the equivalent domains of C and D (~1146 Å^2). This area exceeds that between chains A and C (~954 Å^2) or D and B (~959 Å^2). Monomers A and B are tilted with respect to C and D by an angle of ~57º (Figure 3-52) (Table 3-7). The tetramer is formed by merging the roughly V-shaped dimers (A/B and C/D) with their open sides.

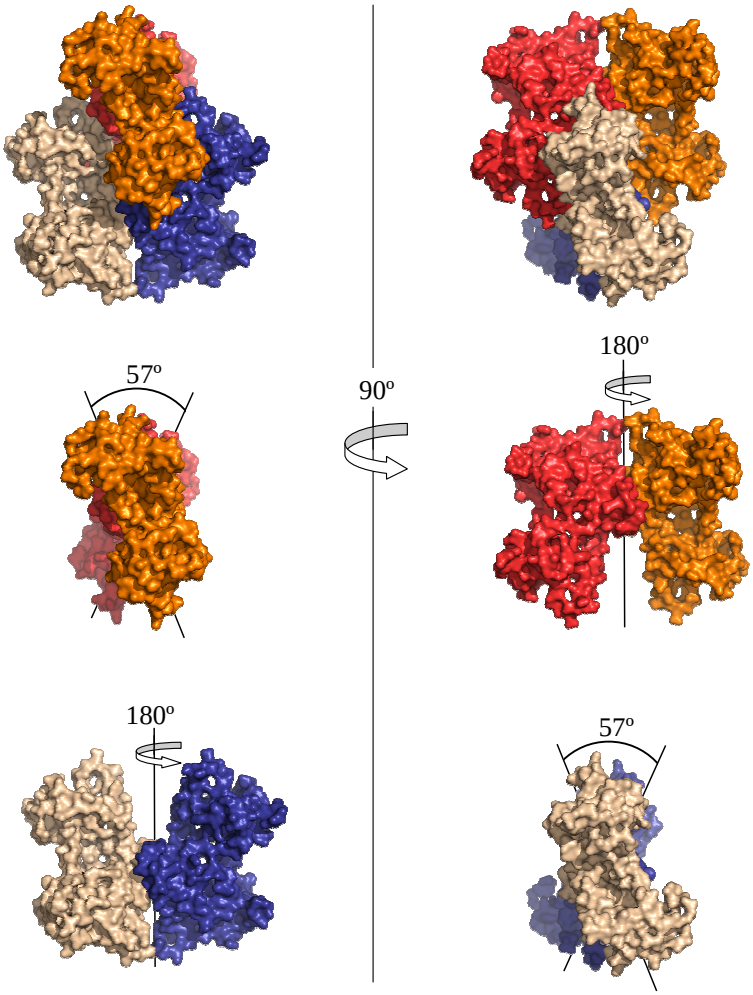

Figure 3-52: Surface representation of the geometric arrangement of the SidA tetramer. Chain A is rendered in cream, B in blue, C in orange and D in red.

Table 3-7: Interface area of the four SidA subunits as calculated by PISA.

Monomer interfaces	No. of interfacing residues	Interface area [Å^2]
A/B	36 (36)	1167 (1226)
C/D	33 (34)	1146 (1176)
A/C	27 (29)	954 (935)
B/D	32 (31)	969 (962)
A/D	15 (11)	472 (359)
B/C	17 (10)	477 (345)

Numbers in brackets refer to values obtained with an idealized SidA tetramer that has been generated by using only the best defined monomer (chain A) resulting in an AAAA model. This model is thus only theoretical and does not reflect the actual model corresponding to the currently available electron density.

The interface between the four monomers is mainly constituted of α-helices and loops (Figure 3-53). Conversely, the concave side is mainly made up of β-sheets and faces the solvent (Figure 3-53). Each active site is exclusively composed of residues of a single subunit. This subunit arrangement is distinct from that of the *Methylophaga* FMO-dimer where the subunit interaction surface mainly consists of β-sheets with the concave sides of each monomer facing each other (compare Figure A-7, Appendix).

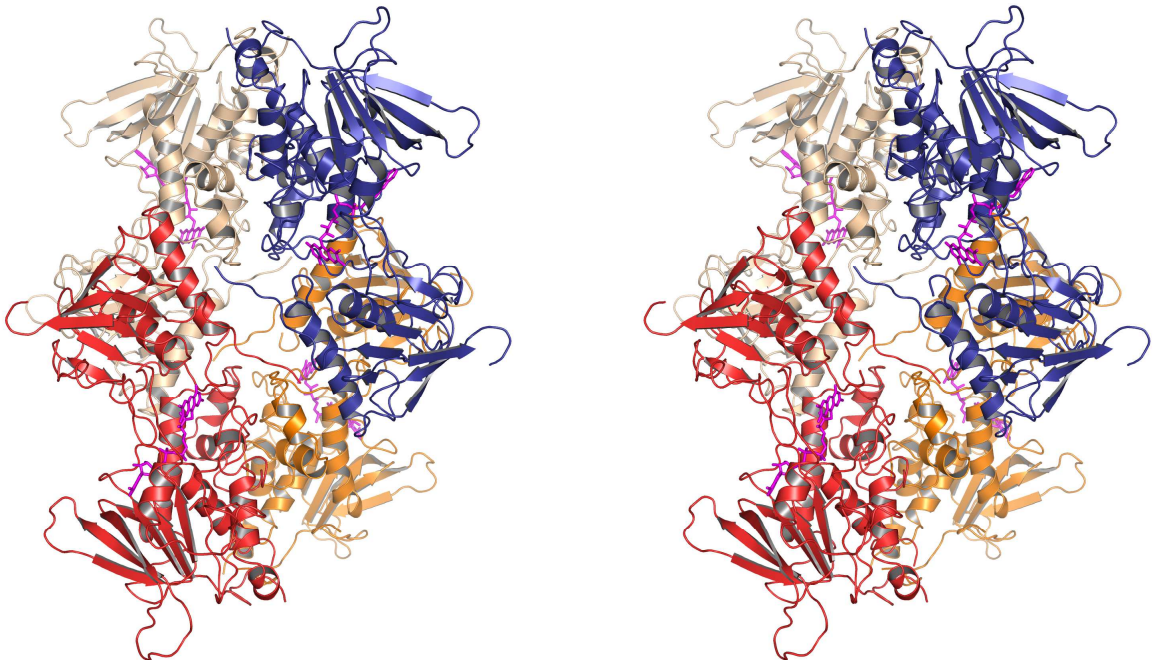

Figure 3-53: Stereo view of tetrameric SidA with bound FAD. The cartoon presentation shows the SidA tetramer generated using the best defined monomer A. The monomer's active sites are defined by the position of the FAD isoalloxazine ring (magenta sticks) and oppose each other.

3.5.7 Cysteines Contribute to SidA-Oligomerization

The SidA sequence contains five cysteines Cys41, Cys62, Cys66, Cys151 and Cys230 (Figure 3-54). Some of these cysteines have previously been suspected to contribute to SidA oligomerization as indicated by non-reducing SDS-PAGE with different SidA cysteine substitution variants (Lisson, 2007). Although the protein was purified and cyrstallized in the presence of reducing agents, structure solution and refinement finally revealed residues Cys62 and Cys66 to form disulfide bridges with respective residues Cys62 and Cys66 of their neighboring subunit thus contributing to SidA dimerization.

Respective disulfide bridge formation was thus observed between subunits A/B and C/D. Accordingly the cysteines initially suspected at early stages of this work to impair crystal quality may rather promote than disturb crystallization due to their stabilizing role through intermolecular disulfide bridge formation within the SidA tetramer.

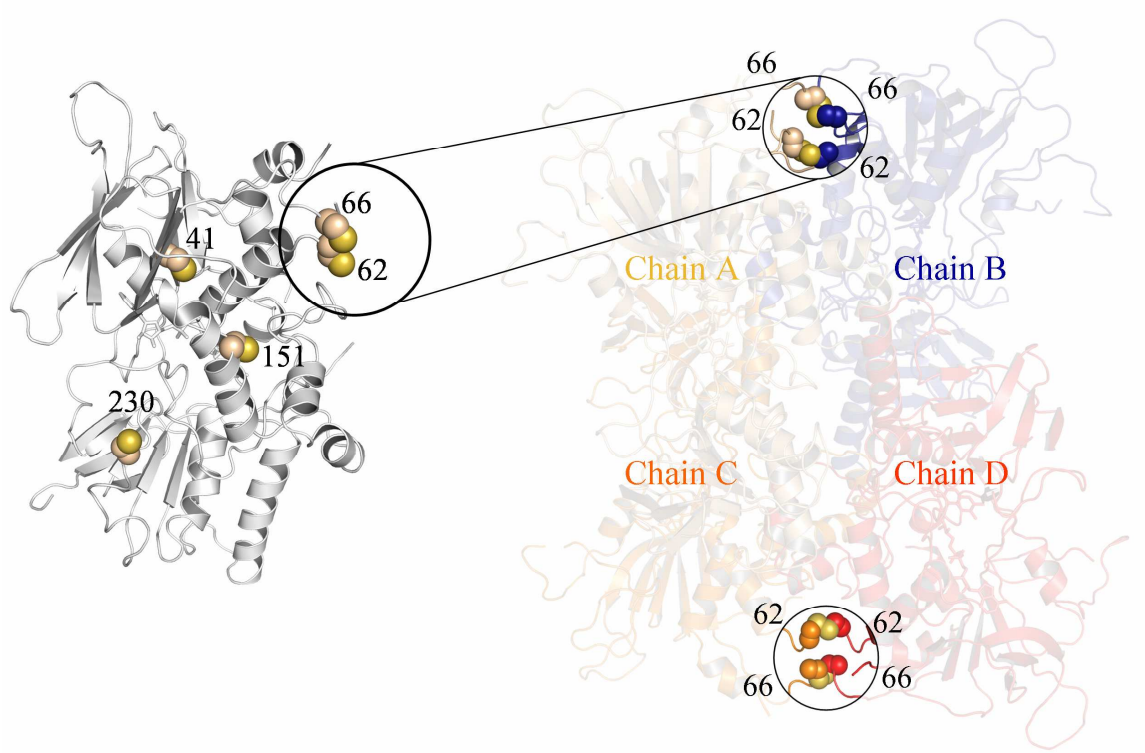

Figure 3-54: Cysteine residues and disulfide bridges within the SidA structure. Cartoon representation of the SidA protomer (left) and tetramer (right) with cysteine residues shown as spheres (sulfur atoms in yellow). Numbering of cysteines corresponds to their respective position within the SidA sequence. Cysteine residues involved in intermolecular disulfide bridge formation are highlighted by a black circle.

3.6 The Monooxygenase PvdA of *P. aeruginosa*

In parallel to fungal SidA expression, purification and crystallization of the SidA homologue PvdA from *Pseudomonas aeruginoas* was accomplished. PvdA catalyzes the hydroxylation of L-ornithine, the first step in the biosynthesis of the siderophore pyoverdin. Similar to the reaction catalyzed by SidA hydroxylation of L-ornithine occurs at N^5 at the expense of NADPH and molecular oxygen and with FAD as prosthetic group. The sequence identity of the biochemically thoroughly studied PvdA relative to SidA is 38 % (Figure 3-55). A structural model of PvdA could therefore have substituted for that of SidA as the structures are expected to be largely similar.

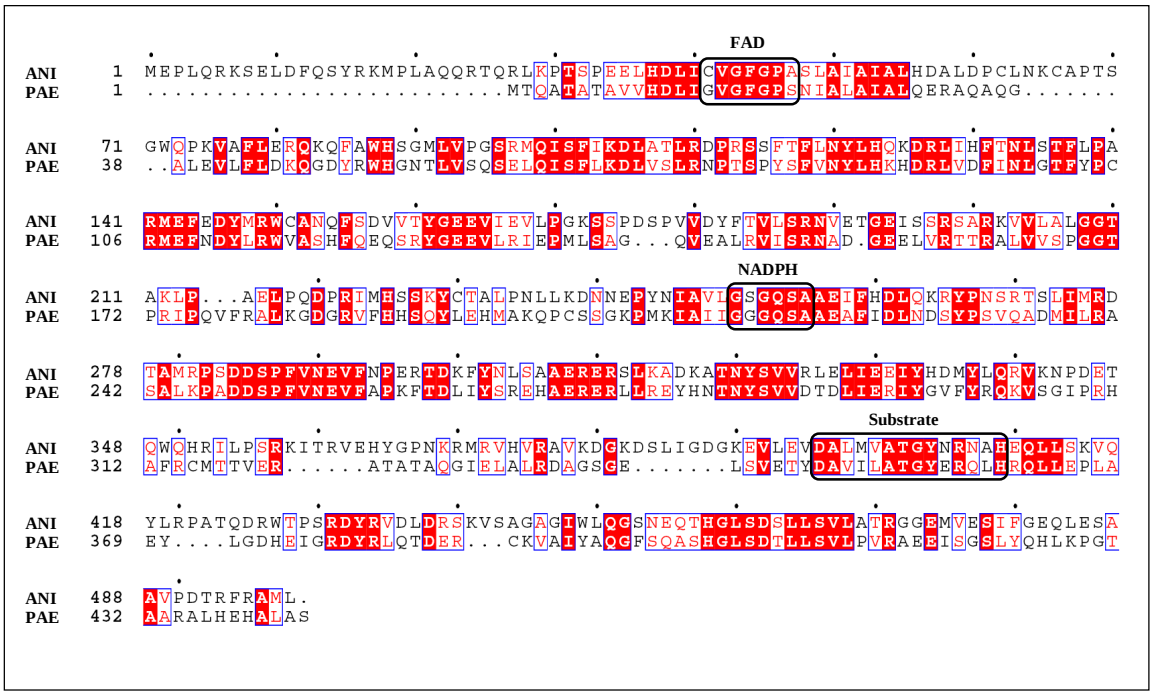

Figure 3-55: Sequence alignment of SidA and PvdA. FAD-binding motif, NADPH-binding motif and the putative substrate binding site are indicated by black boxes. ANI: *A. nidulans*, PAE: *P. aeruginosa*.

Relative to SidA, PvdA lacks 26 N-terminal residues in addition to some deletions throughout the protein. Overall the estimated mass of PvdA (49.5 kDa) is slightly lower than that of SidA (59 kDa). The nucleotide binding motifs as well as the putative substrate binding site are, however, well conserved. The FAD-binding motif of PvdA shares the characteristic replacement of the last glycine by proline (GxGxxP instead of GxGxxG), a unique feature of hydroxylases involved in siderophore biosynthesis

(Stehr *et al.*, 1998). However, unlike SidA where cysteine is the first residue of the FAD-binding motif, PvdA has a glycine residue at the corresponding position. The ATGY motif suspected to be involved in substrate binding slightly differs from that of SidA (DAVILATGYERQLH instead of DALMVATGYNRNAH) despite catalyzing identical reactions on L-ornithine. The NADPH-binding motif is identical in both enzymes.

3.6.1 Expression and Purification of PvdA

Like SidA, PvdA was cloned into the expression vector pET-28c(+) using genomic DNA from *P. aeruginosa* PAO1 and appropriate primers. The expression construct thus encodes for an N-terminal His_6-tag to allow for purification via Ni-NTA affinity chromatography. Optimal production of PvdA in *E. coli* Tuner cells was achieved in LB medium at 20ºC for a time period of ~15 h after induction with 0.3 M IPTG. In contrast to SidA, the FAD cofactor of PvdA is lost during purification. Whereas the initial cell extract retains an intense yellow color when coupled to the Ni-NTA resin, this is rapidly lost during the subsequent washing procedure. PvdA was thus mainly obtained as apo-enzyme. As depicted in Figure 3-56 A, the affinity chromatography already yields relatively pure protein.

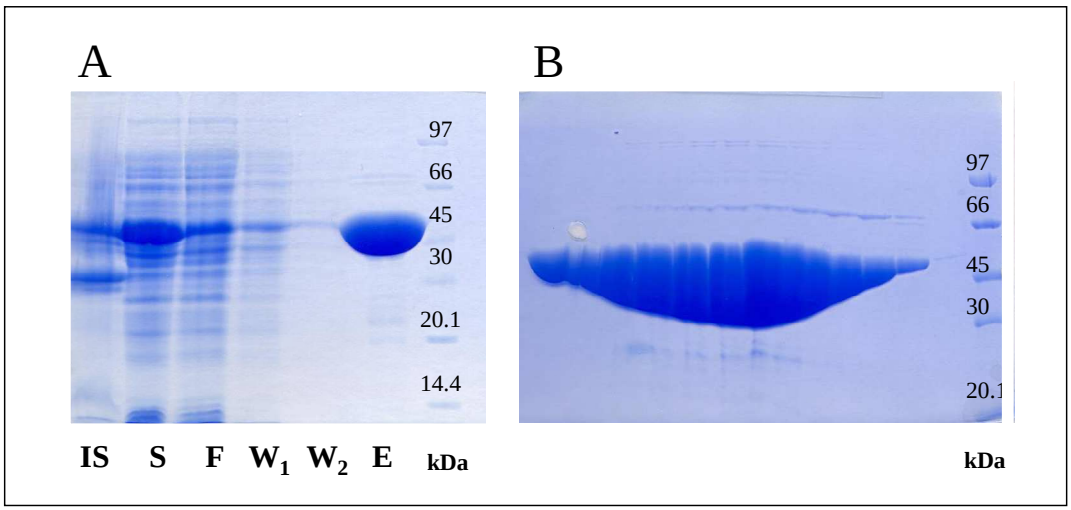

Figure 3-56: PvdA purification steps: Ni-NTA affinity chromatography (A) and IEC (B). Coomassie brilliant-blue stained 12 % SDS-PAGE with (A) protein samples obtained after bacterial cell disruption and subsequent Ni-NTA affinity chromatography and (B) peak fractions obtained within the IEC run. IS: insoluble protein fraction of cell extract, S: soluble protein fraction of cell extract, F: flow through of Ni-NTA affinity chromatography step, W1 and W2: wash fractions, E: elution fractions. Last lanes in (A) and (B): molecular weight marker (LMW, Fermentas).

Compared to SidA, the yield of 20-30 mg Ni-NTA-purified PvdA per liter of bacterial culture is remarkably high. Except for buffer compositions the remaining purification steps for PvdA are identical to those for SidA. The estimated pI of PvdA at 6.5 is more acidic than that for SidA (7.84). The buffers for the subsequent IEC purification were thus adjusted to pH 8.5 to yield a negative net charge to allow binding to a MonoQ resin. PvdA reproducibly eluted at a salt concentration of 220 mM with a corresponding conductance of 22 mS/cm (Figure 3-57). The eluting peak fractions contained already relatively pure protein as demonstrated by SDS-PAGE (Figure 3-56 B).

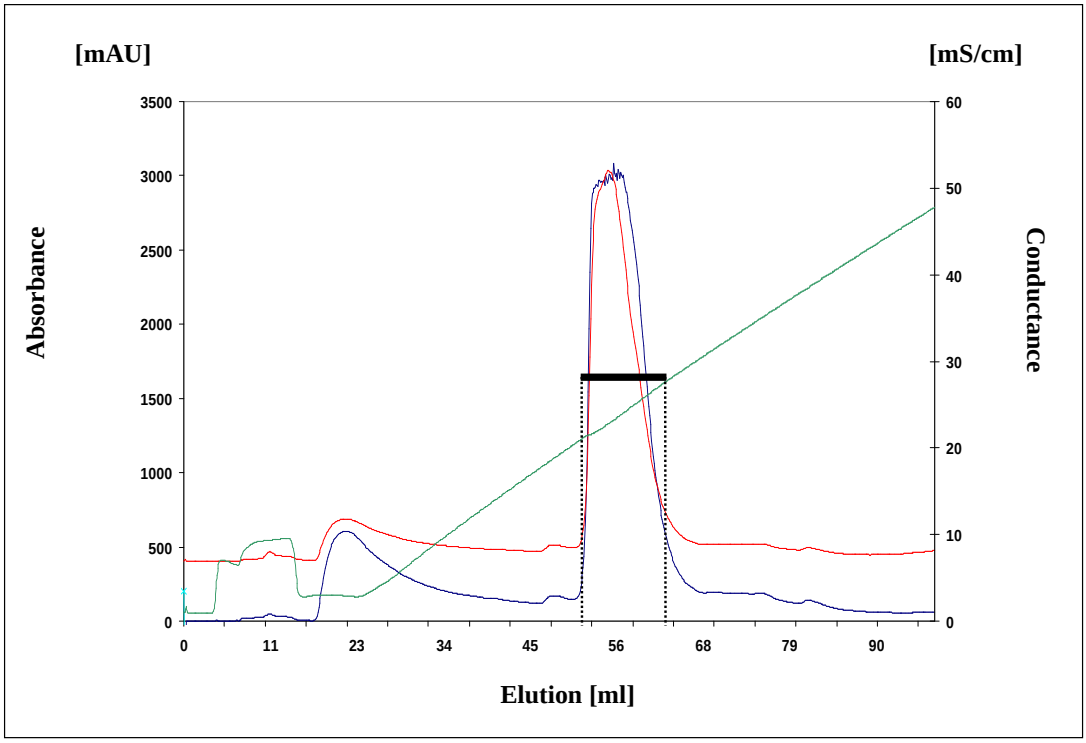

Figure 3-57: Ion exchange chromatography. The PvdA elution fractions of the preceding Ni-NTA affinity chromatography step were buffered at pH 8.5 and further purified via an anion exchange column (MonoQ HR 10/10). The chromatogram shows the absorption at two different wavelengths at λ = 280 nm (blue line) and λ = 260 nm (red line), corresponding to the absorption maxima of proteins and nucleic acids. The concentration that corresponds to the applied NaCl gradient is shown as a green line. The black bar marks the pooled elution fractions.

Following protein purification the enzymatic activity of PvdA was tested using the iodine oxidation assay. FAD-free enzyme was observed to be inactive. By contrast FAD-supplemented PvdA converted L-ornithine to hydroxylated product resulting in azo-dye-formation. (Figure 3-58). The catalytically impaired PvdA variant G15C was used as an internal negative control.

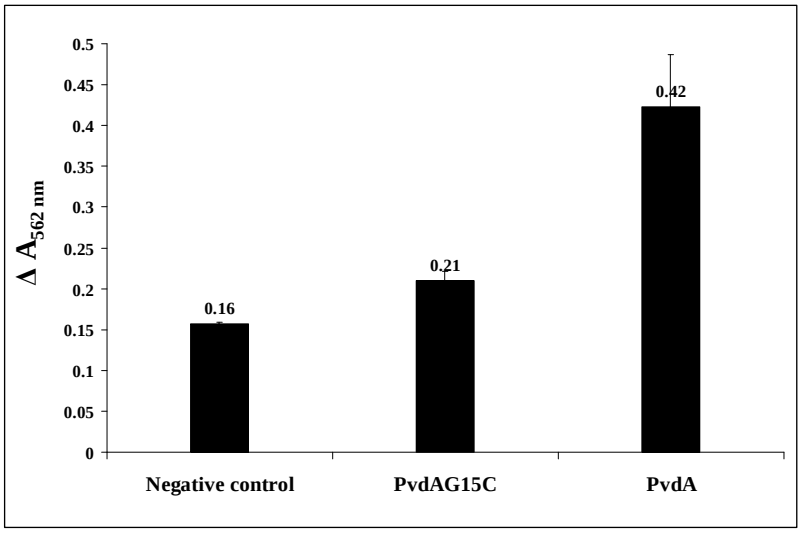

Figure 3-58: Hydroxylation activity of PvdA. Enzyme activity of PvdA was checked after supplementation with 10 mM FAD using the iodine oxidation assay. The catalytically inactive variant PvdAG15C was included in the assay as an internal control. Negative control: the reaction proceeded in the absence of additional FAD.

3.6.2 Oligomerization of PvdA

PvdA, like SidA, appeared to form a homotetramer in solution as evidenced by GPC and DLS measurements. Considering the physico-chemical properties of the GPC column used (Superdex 200 16/60), the V_e of 75 ml is comparable to that of SidA (V_e = 67 ml) (Figure 3-59, next page). DLS analysis of purified PvdA moreover indicated a hydrodynamic radius of R_h = 6.0 nm corresponding to a calculated molecular mass of 227.1 kDa (Figure 3-59). With a polydispersity of 12.8 % the level of homogeneity of the sizes of particles can still be considered as being high (DynaPro user manual) thus being tolerable for subsequent experiments.

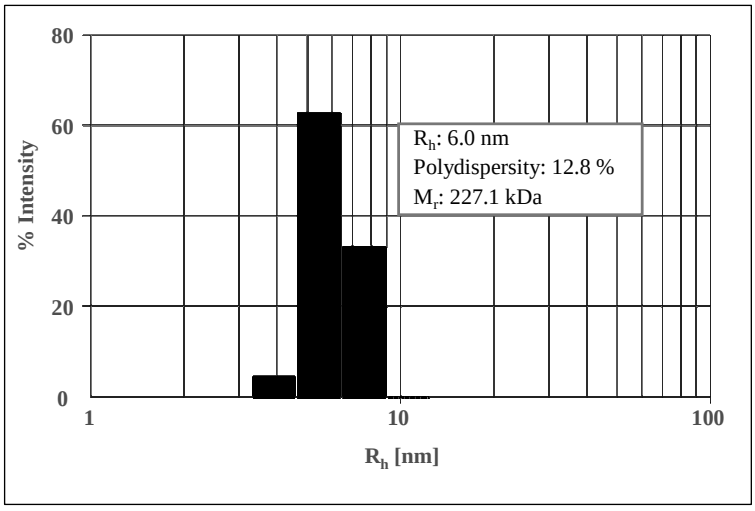

Figure 3-59: DLS measurement with purified PvdA. The DLS measurement was performed at 25ºC. The figure shows the intensity of the measured signal in % and the corresponding hydrodynamic radius (R_h) of the particle population. For PvdA an average R_h of 6.0 nm was determined, which corresponds to an estimated M_r of 227.1 kDa. The polydispersity of the solution was calculated with 12.8 %.

To finally crystallize PvdA in its active form efforts were undertaken to reconstitute the FAD cofactor after purification. Following procedures that allowed FAD reconstitution in related enzymes, PvdA was incubated with an excess of FAD with gentle stirring and subsequent GPC to remove unbound FAD. The resulting GPC chromatogram however reveals that this step completely separates the cofactor from the protein (Figure 3-60). The protein thus elutes at an V_e of 75 ml whereas the FAD elutes significantly later at an V_e of 112 ml as visible by the peaks in absorption at $\lambda = 280$ nm and $\lambda = 450$ nm, respectively. This would indicate an extremely weak association between protein and cofactor. Unlike SidA, PvdA was extremely stable with regard to protein degradation over time. However, after storage for 1-2 weeks at 4°C PvdA was prone to aggregation and denaturation resulting in the formation of a dense white protein precipitate.

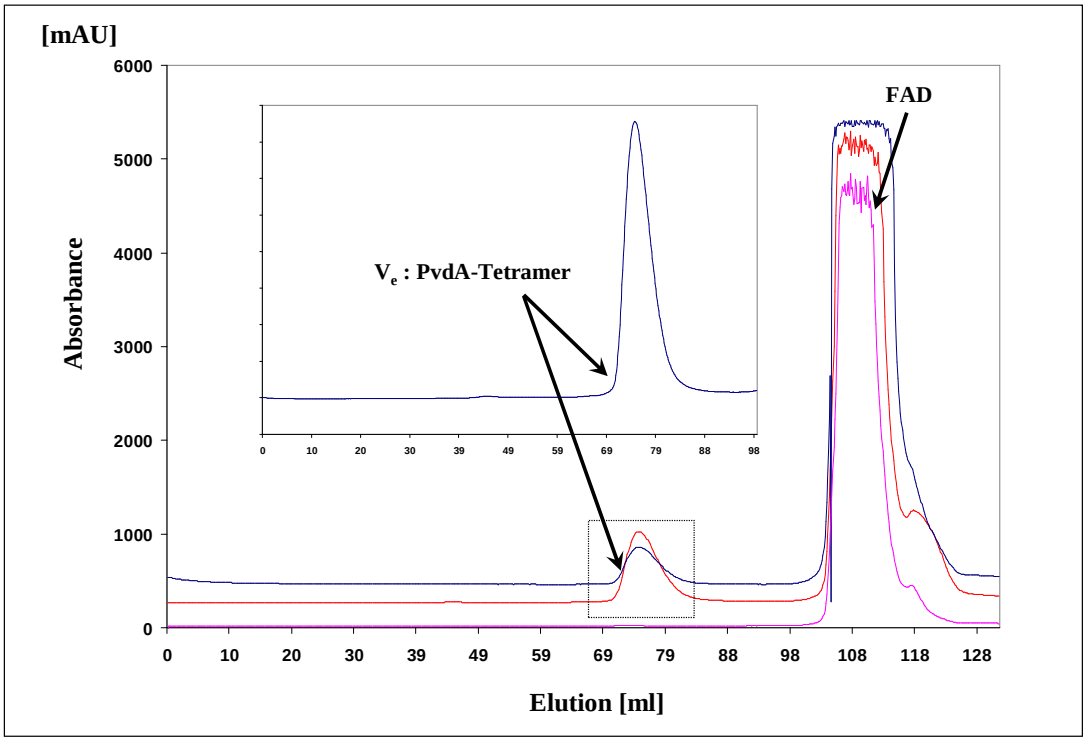

Figure 3-60: GPC with IEC-purified and FAD-supplemented PvdA. The sample applied on a Superdex 200 (16/60) column was previously purified by IEC and dialysed against buffer supplemented with FAD. The elution volume (75 ml) of the peak fraction indicates a tetrameric organization of PvdA. The chromatogram records the absorption at three different wavelengths, $\lambda = 280$ nm (blue line), 260 nm (red line) and 450 nm (pink line), corresponding to absorption maxima of protein, nucleic acid and the FAD. Clearly the FAD elutes significantly later (V_e: 108 ml) than apo-PvdA. Inset: magnification of dotted box with PvdA elution peak.

3.6.3 PvdA Crystallization

Several hundred crystallization conditions in 96-well plate sitting drop format were set up for PvdA. In each case, 100 or 200 nl of protein solution at concentrations between 5 and 10 mg/ml were mixed with 100 nl of the screening solutions. The protein solution was moreover supplemented with FAD to obtain crystals of active PvdA. As described above, PvdA proved particularly prone to aggregation. Under most of the screening conditions chosen, initially clear crystallization drops revealed precipitated protein within a few hours up to several weeks. Crystallization screens were also set up at 4ºC, 20ºC and 25ºC. Precipitation was though observed irrespective of the temperature chosen. Crystals were finally obtained in one of the screening conditions (Figure 3-61). However these crystals could not be reproduced so far. Due to their small size they could not be tested within X-ray diffraction experiment to identify them as consisting of protein. Therefore it remains possible that these crystals consist of salt, although similar crystals were not found in the respective reservoir solution.

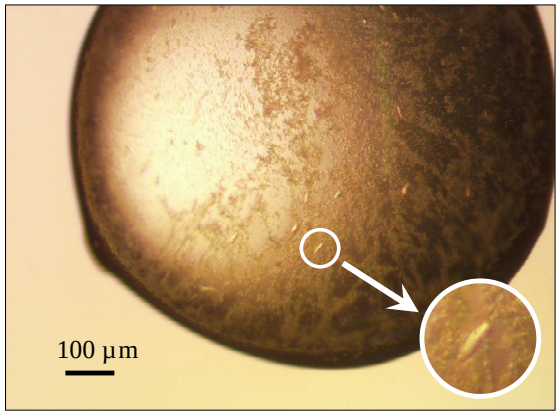

Figure 3-61: Crystallization of PvdA. Crystals appeared under a layer of precipitant about one week after the experiment was set up and had a needle-like habitus (highlighted by a white circle). The sitting drop crystal set-up was incubated at 20ºC with a reservoir solution being composed of 0.3 M $MgCl_2$, 0.1 M Bicine pH 9.0, 25 % (w/v) PEG 2000 and 15 % (w/v) glycerol. Drop volume: ~200 nl. Inset shows a crystal in a 5-fold magnification.

4 Discussion

Essentially all living organisms depend on the bioavailability of iron. Though it is the second most abundant metal on earth, access to iron is limited in most ecological niches. A variety of strategies have therefore evolved to overcome this limitation. Accordingly, iron acquisition has become highly competitive in particular for pathogenic microorganisms. Whereas the host actively retracts iron in response to invading pathogens, the latter are forced to use elaborate iron acquisition strategies that circumvent the host's immune response. One such strategy is the production of siderophores. The siderophore enterobactin from the enteric pathogen *Salmonella typhimurium* is one prominent example of these iron chelating compounds (Crouch *et al.*, 2008; Gorbacheva *et al.*, 2001; Yancey *et al.*, 1979; Pollack and Neilands, 1970). Due to their crucial role during microbial host infections, siderophores have been assigned as true virulence factors (Hwang *et al.*, 2008; Ratledge, 2007). In conclusion their biosynthesis pathways are potential targets for new antimicrobial therapies. The present study offers first insights into the biochemistry and three-dimensional structure of SidA, a key enzyme of siderophore biosynthesis in *Aspergillus* spp. providing a first basis for future studies on this enzyme as well as on functionally and structurally related monooxygenases from other organisms such as prokaryotes and mammals.

4.1 SidA Catalytic Activity Resembles that of IucD and PvdA

SidA is functionally related to IucD from *E. coli* and PvdA from *P. aeruginosa*, key enzymes in the biosynthesis of the bacterial siderophores aerobactin and pyoverdin. These enzymes share a high degree of sequence identity with SidA and both have been thoroughly studied biochemically though not structurally as yet (Meneely and Lamb, 2007; Visca *et al.*, 1994; Dick *et al.*, 1999; Macheroux *et al.*, 1993; Plattner *et al.*, 1989; Stehr *et al.*, 1999; Thariath *et al.*, 1993). The results obtained within this work demonstrate that SidA is also catalytically similar to IucD and PvdA. This includes the pH-optimum for enzymatic activity, its binding affinity and specificity for its natural substrate as well as the dependence on NADPH as electron donor (Table 4-1).

Table 4-1: Overview of kinetic parameters for SidA and functionally related enzymes.

Enzyme	Source	Siderophores	Substrate	Cofactor	pH-optimum	K_M [mM]
$SidA^{AN}$	*A. nidulans*	TAFusC, FC	L-ornithine	FAD, NADPH	~8.0	0.3
$SidA^{AF}$	*A. fumigatus*	TAFusC, FC	L-ornithine	FAD, NADPH	~8.0	0.3
IucD	*E. coli*	Aerobactin	L-lysine	FAD, NADPH	8.0	0.1[a]
PvdA	*P. aeruginosa*	Pyoverdin	L-ornithine	FAD, NADPH	8.0	0.58[b]

a) Plattner *et al.* (1989); b) Ge and Seah (2006)

Like IucD and PvdA, the pH-optimum of SidA lies within the basic pH-range between pH 8.0 and 9.0. Similar optima have been observed for other flavin-dependent monooxygenases such as human FMO3 (hFMO3) and liver microsomal FAD-containing monooxygenase where an increase in pH improves enzymatic activity (Brunelle *et al.*, 1997; Beaty and Ballou, 1981). In p-hydroxybenzoate-3-hydroxylase (PHBH) for example, the monooxygenation reaction has been rationalized to depend on a network of hydrogen bonds, which is sensitive to changes in pH and extends from the active center to the protein surface (Ortiz-Maldonado *et al.*, 2004).

SidA displays a relatively strict substrate specificity. The substrate range of SidA has been shown to include its natural substrate L-ornithine, D-ornithine and in part the ornithine analog DFM-ornithine and L-lysine. As monitored within the iodine oxidation assay (compare Figure 3-9, section 3.1.2) using L-arginine and L-citrulline as substrates did not result in any hydroxylated product formation. By contrast DFM-ornithine and L-lysine were converted to their hydroxylated products − though only inefficiently compared to L-ornithine (35 % and 39 %, respectively). The efficient hydroxylation observed for IME-ornithine, which was comparable to results obtained with L-ornithine, can only be explained with either chemical instability or with an insufficient degree of substrate purity. In both cases the reaction set-up would contain traces of L-ornithine, the substrate best converted to its hydroxylated product by SidA. Otherwise L-arginine and L-citrulline, both featured with a substituted Nδ amino group (as is IME-ornithine), would have been hydroxylated as well. Probably the naturally occurring amino acids L-arginine

and L-citrulline are chemically more inert than IME-ornithine. Therefore the results obtained with IME-ornithine presumably have to be considered as an artifact, which requires mass spectrometry techniques for a detailed analysis.

In conclusion the experimental results obtained so far indicate that the size of the substrate is crucial for the hydroxylation reaction to proceed. Thus substrates carrying an additional methylene group (L-lysine) and/or a terminal guanidine or carbamoyl group (L-arginine and L-citrulline) were not hydroxylated or only to a very limited extent presumably due to sterical conflicts. Similar results were reported for PvdA and IucD. Both have been shown to display a strict substrate specificity. Accordingly PvdA only converts L-ornithine into hydroxylated product. Unlike SidA PvdA is unable to convert L-lysine to L-N^6-hydroxy-lysine (Meneely and Lamb, 2007). IucD on the other hand, despite high sequence homology to SidA and PvdA, is dependent on its natural substrate L-lysine for successful hydroxylation being unable to catalytically convert L-ornithine to N^5-hydroxy-ornithine (Thariath *et al.*, 1993).

With respect to substrate binding and positioning within the active site the importance of the substrate α-amino group is witnessed by the reduced efficiency of SidA to convert the ornithine variants D-ornithine and DFM-ornithine into their hydroxylation products. In both, D- and DFM-ornithine, the chirality of the C_α-atom is inverted relative to that of L-ornithine (Figure 4-1). This change in chirality as well as the additional negative charge of the di-flour-group in the case of DFM-ornithine will invariably result in suboptimal substrate recognition and binding thus reducing the overall efficiency of the catalytic reaction.

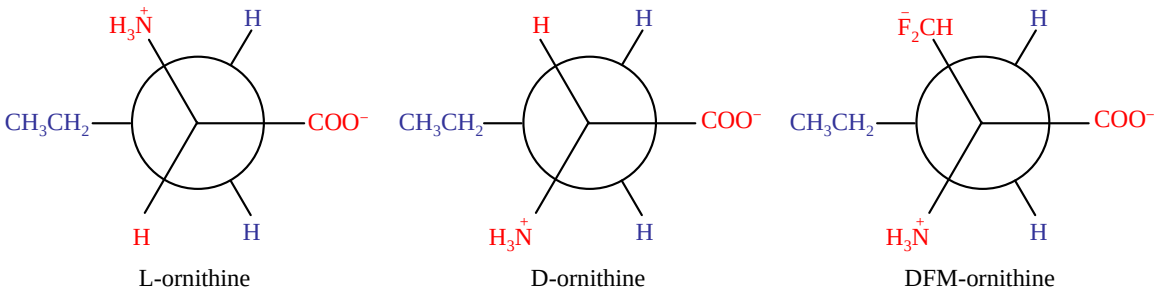

Figure 4-1: Newman projections of L-ornithine, D-ornithine and DFM-ornithine.

Substrate inhibition at substrate concentrations above 5 mM has been reported for IucD (Macheroux *et al.*, 1993) and PvdA (Meneely and Lamb, 2007). This was however only observed with the hydroxylation assay as a read-out for catalytic activity. As part of the present thesis only the NADPH oxidation assay has been used to determine the SidA kinetic constants. Using this assay, no decrease in the initial velocity was observed at ornithine concentrations above 5 mM. Due to the high sequence and functional similarities between SidA and its bacterial homologues, substrate inhibition could be expected to occur for SidA as well. As the effect is not detected by the NADPH oxidation assay it is likely that only the monooxygenase function is affected by substrate inhibition.

4.2 Substrate Binding is Required for Efficient FAD Reduction

As mentioned, in the absence of an appropriate substrate SidA was shown to display a slight NADPH oxidase activity resulting in the formation of H_2O_2 due to uncoupling of the reductive half of the enzymatic reaction (section 3.1.4). Such intrinsic NADPH oxidase activity has also been observed for other FMOs such as PvdA (Meneely and Lamb, 2007) and mFMO (Alfieri *et al.*, 2008) and is generally much lower than reactions involving a proper substrate (Palfey *et al.*, 1997). In PHBH for example, substrate binding is crucial to induce the so-called *out* conformation of the flavin isoalloxazine ring (Figure 4-2) (Gatti *et al.*, 1994), which is required for efficient hydride transfer from NADPH to the solvent exposed N5 of the isoalloxazine ring. In the absence of substrate, the monooxygenase activity is uncoupled because the *out* conformation can not be stabilized. The reductive half of the catalytic reaction continues, though with a far lower rate constant than in the presence of substrate. The resulting unstable C4a-

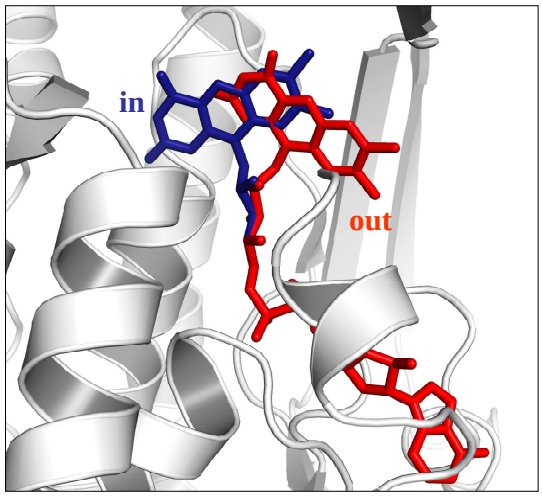

Figure 4-2: The two modes of flavin binding in PHBH. The flavin in PHBH from *P. fluorescence* has been modeled in two conformations (Gatti *et al.*, 1994): The flavin in the *out* position is highlighted in red, the alternative *in* position, is shown in blue.

hydroperoxyflavin finally decomposes to yield H_2O_2 (compare Figure 1-12, section 1.5).

Generally a reduced oxidase activity in the absence of substrate appears metabolically reasonable since an efficient NADPH oxidation without substrate would waste reducing equivalents and lead to increased levels of cytotoxic H_2O_2. In the case of SidA the turnover for the intrinsic NADPH-oxidase activity was ~1000-fold lower than for its monooxygenase function (kcat = 0.003 s^{-1} compared to 3.3 s^{-1} in the presence of L-ornithine). Thus, similar to PHBH, substrate binding to SidA is a prerequisite for efficient hydride transfer from NADPH to FAD.

4.3 Lysine Functions as NADPH Oxidase Effector

The increase in NADPH oxidation observed after addition of L-lysine to the catalytic reaction set-up suggests that L-lysine binds to the substrate binding site of SidA sufficiently well to induce efficient FAD-reduction. The additional methylene group would however impair the SidA monooxygenase activity either by physically obstructing the active site or by placing the receiving nitrogen out of reach of the activated oxygen molecule. In each case this would result in uncoupling of the two halves of the catalytic cycle and in the formation of H_2O_2, as it is described above. L-arginine and L-citrulline by contrast are neither hydroxylated nor do they promote SidA NADPH oxidase activity above its intrinsic level. These molecules do therefore not bind to the active site to such a degree as to allow hydroxylation or oxygen activation. Similar observations have been reported for PvdA which is also activated by L-lysine without catalyzing substrate hydroxylation (Meneely and Lamb, 2007). Conversely, in the case of IucD L-lysine is the natural substrate and addition of L-ornithine was neither reported to stimulate the enzyme's NADPH oxidase activity nor its monooxygenase function for conversion of L-ornithine into N^5-hydroxy-ornithine (Macheroux *et al.*, 1993; Thariath *et al.*, 1993).

4.4 SidA is a Class B Flavoprotein Monooxygenase

The biochemical and structural results of the present study unequivocally place SidA within class B of flavoprotein monooxygenases. This classification (van Berkel *et al.*, 2006) is mainly based on sequence and (if available) structural data on

flavoproteins. Members of this group of enzymes are found in all three kingdoms of life. They hydroxylate a wide variety of nucleophilic substrates including primary, secondary and tertiary amines as well as sulfur-, phosphorus-, selenium- and iodine-containing groups. Many of the mammalian isoforms participate in the detoxification of drugs and other xenobiotics. Corresponding enzymes in plants are involved in the biosynthesis of auxin (Zhao *et al.*, 2001) and in pathogen defense (Mishina and Zeier, 2006). Further prominent examples are PHBH (EC 1.14.13.2) involved in lignin degradation (Entsch and van Berkel, 1995) and Baeyer-Villiger monooxygenases (BVMOs) such as cyclohexanone monooxygenase (EC 1.14.13.22) that converts ketones into esters or lactones (Sheng *et al.*, 2001; Ryerson *et al.*, 1982). Class B flavoprotein monooxygenases generally share the following characteristics, irrespective of the substrates they convert (van Berkel *et al.*, 2006):

(I) they are encoded by a single gene,

(II) they contain a tightly bound FAD cofactor,

(III) they depend on NADPH as coenzyme,

(IV) they keep NADPH/$NADP^+$ bound throughout catalysis and

(V) they consist of two dinucleotide binding domains (Rossmann folds) for binding of FAD and NADPH, respectively.

Except for (IV) all of the features listed above have been experimentally shown to apply for SidA. With respect to (I), the *sid*A gene from *Aspergillus* has been thoroughly studied (Eisendle *et al.*, 2003) and has also been characterized within the framework of the *Aspergillus* genome project (Nierman *et al.*, 2005). The NADPH-dependence of SidA (III) was confirmed in an associated diploma work (Lisson, 2007). (II) and (V) have been experimentally confirmed within the present study and will be further outlined and discussed in the following sections.

4.5 SidA Tightly Embraces its Prosthetic Group

There are five known covalent flavin linkages to amino acids found in flavoenzymes (Figure A-3, Appendix). The majority of flavoprotein monooxygenases, however, binds their FAD cofactor non-covalently. While FAD is lost during protein purification of the SidA-homologues PvdA and IucD (Thariath *et al.*, 1993; Meneely and Lamb, 2007), SidA ($SidA^{AF}$ as well as $SidA^{AN}$) yielded the active proform. Although the flavin cofactor of SidA is not covalently bound (Lisson, 2007), retention of FAD is documented by the intense yellow color of the purified protein and of SidA crystals. Tight but non-covalent binding of FAD is generally observed in class B flavoprotein MOs. Examples include FMO from *S. pombe* (spFMO) (Eswaramoorthy *et al.*, 2006) and PAMO from *T. fusca* (Malito *et al.*, 2004). Crystal structures are available for both these enzymes revealing that FAD is kept in place by a network of hydrogen bonds which strengthen the association between cofactor and protein (Figure A-5, Appendix). In the case of SidA residues presumably responsible for hydrogen bonding to the isoalloxazine ring as well as to the FAD ribitol moiety include Arg141, Ser322, Ser463 and Trp87. Unlike its structural homologues that have been crystallized with substrate and $NADP^+$ bound the FAD of the SidA structure occupies a more twisted and shifted conformation within the catalytic cleft being turned in a ~65° angle and shifted ~5.1 Å in direction of the solvent. This may indicate for alternate conformations of the FAD cofactor in the absence and presence of substrate and cosubstrate within the different steps of the catalytic cycle as it was described for PHBH (Gatti *et al.*, 1994) (compare section 4.2 and Figure 4-2).

4.6 The Two-Domain Architecture and its Role in Catalysis

The SidA structural model has primarily been built on basis of Se derived phases, the calculated SeMet sites and secondary structure motif predictions. Sequence comparisons with potentially homologous structures were initially not used to avoid bias during model building. A subsequent structural superposition of SidA and its DALI-identified homologues as well as the analysis of specific fingerprint motifs (Table 4-2) revealed that corresponding motifs were located at roughly equivalent positions (Figure 4-3). In addition to numerical quality indicators such as R-factors the observed homologies thus confirm the principle correctness of the current SidA structure.

Table 4-2: Conserved sequence motifs of SidA and its structural and functional homologues.

Enzyme	FAD-binding	NADPH-binding	Substrate-binding*	FMO-identification
$SidA^{AN}$	CVGFGP	GSGQSA	DALMVATGYNRNAH	AELPQDPRIMHSSKY
$SidA^{AF}$	CVGFGP	GSGQSA	DALMVATGYNRNAH	AELPQDPRIIHSSKY
IucD	GVGTGP	GGGQSG	DVVIFATGYRSALP	KHMTQS . . CFHASEM
PvdA	GVGFGP	GGGQSA	DLVILATGYERQLH	RHLKGDGRVFHHSQY
mFMO	GAGPSG	GSSYSA	DAIILCTGYIHHFP	FG . . . . GRILHAHDF
spFMO	GAGPSG	GGASSA	DRVIYCTGYLYSVP	YAKAVPGSVLHSSLF
hFMO3	GAGVSG	GLGNSG	DCVIFATGYAFAYP	FK . . . . GKCFHSRDY

Variations of sequence motifs specific for SidA ($SidA^{AF}$ and $SidA^{AN}$) are underlined. Amino acids characteristic for respective sequence motifs are highlighted in red.
*) The role of this sequence motif in substrate binding has been suggested by Stehr *et al*. (1998) and is not based on structural data.

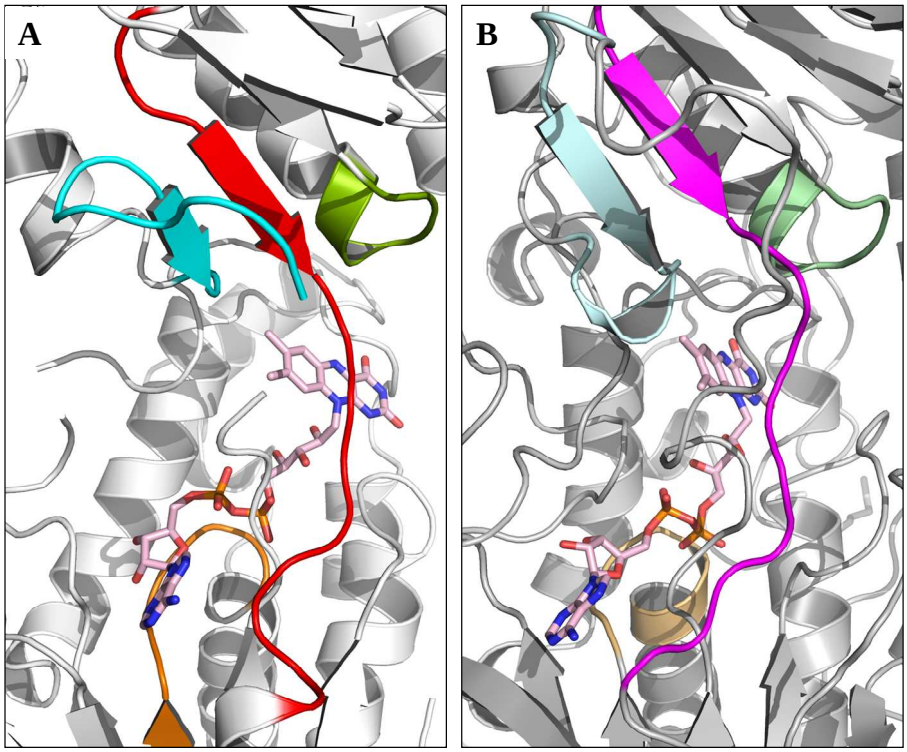

Figure 4-3: Overview of nucleotide-binding and fingerprint motifs in SidA (A) and mFMO (B). The NADPH-binding motif is highlighted in green and light-green, the FAD-binding motif is colored in orange and wheat, the FMO-fingerprint motif is colored in cyan and light-blue and the ATGY motif ($(D(X)_3(^{L}/_{F})ATGY(X)_4(^{H}/_{P}))$ is colored in red and magenta, respectively.

Within this study SidA revealed the highest structural homology with the FMO from *Methylophaga* sp. (Alfieri *et al.*, 2008). The latter has been discussed with respect to its high degree of sequence identity to human FMOs (~31 % sequence identity to hFMO3) for which no crystal structure is available as yet. The main feature SidA shares with its structural relatives including BVMOs such as PAMO and PHBH as well as glutathione reductase (TrxR), is the two-domain protein architecture. Both domains are connected by two or more flexible loop elements that are presumed to provide a certain degree of freedom for interdomain movements proposedly required during catalysis (Entsch *et al.*, 2005; Wang *et al.*, 2001; Malito *et al.*, 2004; Lennon *et al.*, 2000). Considering all similarities SidA shares with its structural homologues and class B flavoproteins, including specific sequence motifs and biochemical properties, it appears reasonable to at least partly derive enzyme function from its three-dimensional structure.

Indications for a two-domain protein architecture with connecting flexible loops were already obvious before a first structural model for SidA was available. As described, first samples of purified SidA were prone to proteolytic degradation over time. SDS-PAGE analysis revealed two distinct bands that were identified as two stable protein domains roughly corresponding to the larger FAD- and the smaller NADPH-binding domain (Figure 4-4).

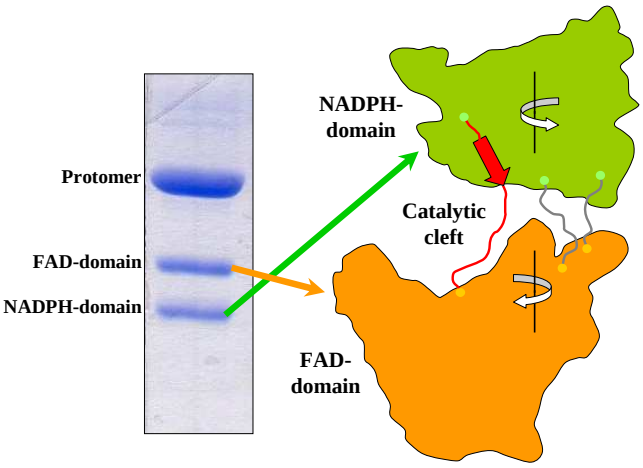

Figure 4-4: Schematic presentation of the SidA two-domain architecture. Left: The observed degradation of purified SidA samples demonstrated by SDS-PAGE. Right: The SidA structure consists of two domains with a catalytical cleft in between. The $NADP^+$-binding domain (green) is connected with the FAD-binding domain (orange) by at least three flexible loop regions thus allowing for a potential inter-domain motion (indicated by white arrows). The stretch containing the putative substrate binding site is highlighted in red.

N-terminal sequencing identified one cleavage site (between Arg311 and Ser312), which is located close to the FAD-binding domain in a loop region following an α-helix adjacent

to the NADPH-binding motif (compare Figure 3-23, p. 59 and Figure 3-43, p. 86). Later on during structure solution and model refinement this loop region (Phe288−Thr319) could not be defined by electron density in any of the four subunits of the SidA tetramer thus emphasizing its presumably high flexibility. Flexible loops between the two domains and within the NADPH-binding domain were also predicted for SidA based on secondary structure and disordered region prediction routines (section 3.3.4). Apart from potential loop regions at the N- and C-terminus, two major sequence stretches (corresponding to residues 277−315 and 341−383) were thus classified by the program DisEMBL as being extremely flexible. Correspondingly major parts of the proposed loops could not be located within electron density maps and hence included in the SidA structure, which supports the identification of disordered or flexible regions.

The described structural architecture has repeatedly been discussed with regard to inter-domain motion during catalysis (Malito *et al.*, 2004; Frederick *et al.*, 2001; Lennon *et al.*, 2000). Whereas two-component flavin hydroxylases such as *p*-hydroxyphenylacetate hydroxylase (HPAH) (Sucharitakul *et al.*, 2007) use two different enzymes for the oxidative and the reductive half of the monooxygenation reaction, single component hydroxylases have been shown to undergo significant protein and flavin dynamics to catalyze two different reactions. Protein dynamics have therefore been stated to be important for catalytic success within this class of enzymes. Well studied examples for such catalytically derived protein dynamics are PHBH (Ballou *et al.*, 2005) and the SidA structural homologue TrxR of *E. coli* (Lennon *et al.*, 2000). PHBH was thus presumed to catalyze two half-reactions in different active sites of the monomer (Ballou *et al.*, 2005), whereas TrxR has been found to undergo an inter-domain motion of 67° as part of the switch between its reduced and oxidized state (Lennon *et al.*, 2000). The connecting loops of TrxR were thus proposed to act as a “swivel” during catalysis (Lennon *et al.*, 2000). Similar functions were described for loops connecting the FAD with the NADPH-binding domain in PAMO (Malito *et al.*, 2004). One of these loops contains the characteristic fingerprint motif of BVMOs ($FXG(X)_3H(X)_3W(^{P}/_{D})$) (Fraaije *et al.*, 2002). The conserved histidine of this motif, which is also present in the FMO fingerprint sequence of SidA (His225; Table 4-2), has been shown to be crucial for catalysis and FAD-binding (Cheesman *et al.*, 2003; Fraaije *et al.*, 2002).

In SidA the flexible loops connecting the FAD- and NADPH-binding domain may equally well provide the structural basis for such inter-domain rotations during catalysis. The fact that some of this loops contain well conserved sequence motifs including residues that have been shown to be important for catalysis and cofactor binding (Cheesman *et al.*, 2003; Fraaije *et al.*, 2002) supports the idea that these loops may play a crucial role within the catalytic process of SidA.

In addition to structural features another indication for catalytically derived inter-domain motion may be provided by results obtained during soaking of SidA crystals with NADPH. SidA crystals were observed to crack a few seconds after soaking with NADPH, which may point at intra-crystal dynamics of the protein molecules. Similar observations have been reported for mFMO and were also discussed in conjunction with conformational rearrangements of this enzyme during catalysis (Alfieri *et al.*, 2008).

4.7 The Role of the ATGY Motif

The sequence identity between SidA, mFMO and spFMO amounts to only 18 % and 14 %, respectively. Despite this low sequence identity to its structural homologues the characteristic motifs for binding of FAD, NADPH and the FMO identifying sequence ($FXG(X)_3H(X)_3(^{Y}/_{F})$) (Fraaije *et al.*, 2002; Ziegler and Poulsen, 1998) are essentially conserved (Table 4-2). The $D(X)_3(^{L}/_{F})ATGY(X)_4(^{H}/_{P})$ sequence stretch harboring the ATGY motif has been suggested to be involved in substrate binding in SidA and related enzymes (Stehr *et al.*, 1998) and is also present in mFMO, spFMO and in the majority of mammalian FMOs including hFMO3 (reviewed in Krueger and Williams, 2005). A structural superposition of SidA, mFMO and spFMO reveals this motif to be located within the flexible loop region connecting the NADPH- and the FAD-binding domain (Figure 4-5). As discussed, loops connecting the NADPH- with the FAD-binding domain were shown to be crucial for catalysis within related enzymes (see section 4.2.3). The loop containing the ATGY motif has not been implicated as yet with regard to substrate binding in mFMO and spFMO. However, its high conservation amongst FMOs suggests a potential role during catalysis. Hence the $D(X)_3(^{L}/_{F})ATGY(X)_4(^{H}/_{P})$-motif can be considered as a second fingerprint motif of this enzyme class. As this motif is physically close to the active site, it may serve to shield the active site from the surrounding solvent.

In the crystal structure of the spFMO/substrate complex, the substrate methimazole (MMZ) occupies a similar site as $NADP^+$ does and similarly stacks on the FAD (Eswaramoorthy *et al.*, 2006). The flexible loop containing the conserved ATGY motif of spFMO flanks the prosthetic group and the substrate (Figure 4-5).

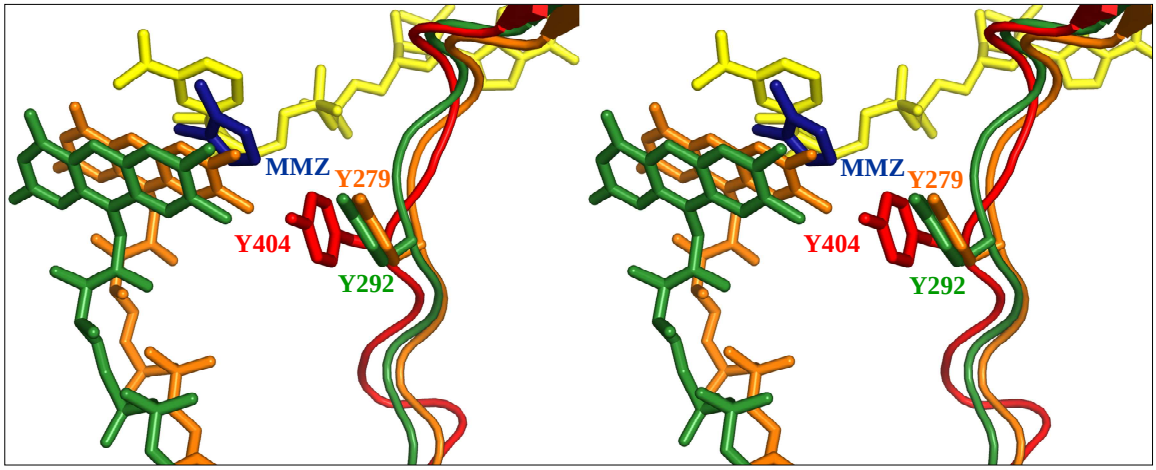

Figure 4-5: Stereo view of a superposition of the conserved $D(X)_3(^{L}/_{F})ATGY(X)_4(^{H}/_{P})$-motif. The superposed structures are SidA (in red), mFMO (in orange) and spFMO (in green). The coordinates for the position of a potential substrate like methimazole (MMZ) (in blue) and $NADP^+$ (in yellow) stem from spFMO complex structures (PDB entry: 2gv8 and 2gvc). The conserved tyrosine residue is the only residue of this motif that could move into close vicinity to the *re*-side of FAD to participate in the catalytic process.

In conclusion the ATGY motif may thus serve to shield the active site during catalysis and provide flexibility of the two protein domains assumed to be required for the catalytic process. The central tyrosine residue (Tyr292 in spFMO and Tyr404 in SidA) presumably participates in catalysis as it is able to adopt alternative conformations and move within hydrogen bond distance in direction of the spFMO-substrate methimazole as well as the NADPH. Moreover it is the only residue within this region sufficiently close to the catalytic key players. The adjacent glycine residue (Gly403 in SidA) may provide the necessary degree of flexibility within this loop to allow for a close contact between tyrosine and substrate or NADPH.

Within the current work substitution of Tyr404 with serine resulted in a SidA variant being devoid of FAD indicating the importance of this residue for cofactor binding. Since Tyr404 could not be shown to directly interact with FAD this residue may be important for the integrity of the H-bond network that is responsible for cofactor binding and moreover for protein stability. The latter has been evidenced by the fact that loss of the

FAD cofactor in the Y404S variant led to aggregation and precipitation 24-48 h after protein purification. This observation also indicates a stabilizing role of FAD for the entire enzyme architecture.

4.8 Cys62 and Cys66 Promote SidA Crystallization

Unlike the majority of its structural homologues, which are homodimers, SidA has been shown to exist as a homotetramer in solution and within respective crystals. Within this work cysteine residues Cys62 and Cys66 have been shown to contribute to SidA dimerization between subunits A/B and C/D, which finally constitute the tetramer. Due to the reducing environment within the fungal cytoplasm and within the bacterial cells that have been used as an expression system for SidA, disulfide formation between the mentioned subunits can be considered as an artifact occurring during protein purification and/or crystallization. As can be gathered from sequence comparisons those cysteines involved in disulfide bridge formation in $SidA^{AN}$ are not present at corresponding positions within $SidA^{AF}$ (Figure 3-1). Since crosslinking of protein subunits via introduction of disulfides has been reported a successful strategy to facilitate crystallization (Banatao *et al.*, 2006; Heinz and Matthews, 1994), in the case of $SidA^{AN}$ disulfide formation by the naturally present cysteines may be one explanation for the improved crystallizability compared to $SidA^{AF}$. If this disulfide formation does also contribute to improved X-ray diffraction remains to be elucidated, for increased protein stability introduced through disulfide crosslinking can also have its drawbacks. Unfavorable disulfide crosslinking can thus result in a strained geometry and in low quality crystals (Heinz and Matthews, 1994). Therefore a slight distortion of the SidA subunits or domains due to the described double cystine bridges can not be excluded and may be one reason for impaired X-ray diffraction of SidA crystals. Initial experiments with the cysteine substitution variant SidAC62S/C66S that has been generated within an associated diploma work (Lisson, 2007) resulted in crystals isomorphous to those initially obtained with the wild-type protein. The diffraction power of SidAC62S/C66S crystals was, however, limited to 7 Å (Lisson, 2007), which is rather an indication for a positive impact of Cys62 and Cys66 on SidA crystal quality.

4.9 SidA Crystals Reveal a Loose Packing

Within the present study numerous attempts have been made to improve crystal quality. Most of the methods applied were based on strategies within the process of crystal growth such as crystallization under oil and streak seeding. Furthermore two experimental approaches were made at very early stages of this work to provide for alternate crystal contacts by modification of surface residues through site-directed mutagenesis or methylation. Except for streak seeding none of these approaches led to a significant improvement of crystal quality and X-ray diffraction.

In general the quality of crystals is determined by the molecular packing of protein molecules. A loose packing and a large volume of disordered water can thus result in poor diffraction (Heras and Martin, 2005). SidA crystals have an estimated solvent content of ~60 %, which is in a common range for protein crystals, though at the upper level. Although these crystals proved to be unexpectedly stable to mechano-physical stress, they failed to diffract X-rays to high resolution, which represented the main limitation to structure determination by X-ray crystallographic techniques. Structure determination had thus to be performed at a medium resolution of only 3.2 Å.

Though the current SidA structure is not completed as yet visual inspection of the crystal packing indicated that subunits B and D of the tetramer are more loosely packed than A and C. Further analysis with PISA (http://www.ebi.ac.uk/msd-srv/prot_int/pistart.html) revealed that subunits A and C bear approximately 3-5 times more interfacing residues potentially involved in crystal packing than B and D (Table 4-3). One reason for the limited diffraction power may therefore reside in a too loose packing of the molecules within the SidA crystals that have been obtained so far. Aiming at crystals diffracting X-rays to higher resolution, future strategies should therefore focus on methods allowing for alternative crystal contacts and an optimized crystal packing.

Table 4-3: PISA output for protein interfaces between SidA chains A-D and crystallographically related subunits.

Chain	Symmetry operation*	Symmetry mate	$^{i}N_{res}$	Estimated interface area [Å^2]
A	y,x,-z	A	21 (21)	578.3 (578.3)
A	-x+1,-x+y,-z+1/3	D	7 (11)	60.3 (97.7)
B	x-y,-y+1,-z+2/3	C	3 (4)	33.3 (56.0)
B	x-y,-y+1,-z+2/3	A	3 (4)	22.1 (43.7)
C	-y+1,x-y,z+1/3	A	18 (17)	549.0 (538.1)
C	-x+1,-x+y,-z+1/3	D	4 (5)	48.8 (116.6)
D	-y+1,x-y+1,z+1/3	B	(3)	(38.6)
C	y,x,-z+1	C	(2)	(34)

* Indicates the symmetry operation that should be applied to the second interfacing structure in order to obtain the respective interface. The symmetry operation is specified in fractional space relatively to the given structure position.
Numbers in brackets refer to values obtained with an idealized SidA tetramer that has been generated on basis of the best defined monomer (chain A) resulting in an AAAA model and does not reflect the actual model corresponding to the currently available electron density.
$^{i}N_{res}$: Number of interfacing residues.

4.10 Protein Flexibility versus Model Errors: Major Obstacles for Structure Determination and Refinement

The difficulties encountered during refinement may have numerous sources. One factor involves the medium resolution of the available diffraction data, which can lead to an incorrect interpretation of the electron density map during manual insertion of amino acid residues. With a few exceptions such as the SeMet sites, most side chains could only be roughly assigned on basis of their size or bulkiness (compare Figure 3-41 and Figure A-6, Appendix). Moreover elements of secondary structure may be wrongly connected by loop regions. In addition to geometric outliers (compare Figure 3-42, section 3.5) the current SidA structure may thus still harbor some errors regarding the orientation and assignment of some of its side chains. The exceptionally high average B-factors (Table 3-5, section 3.5) may therefore not only indicate a high flexibility of certain regions within the structure but also indicate potential errors in the model. This is also reflected by the still suboptimal R-values. These should preferably lie in the range of ≤ 27 % for R_{work} and ≤ 32 % for R_{free} with regards to the maximum resolution (3.2 Å) that has been obtained.

Apart from the resolution limit of the available diffraction data the quality of electron-density maps is also related to how much of the macromolecule has crystallized within a unique conformation (DeLaBarre and Brunger, 2006). As outlined above, the correlation between SidA structure and monooxygenase function is based on the assumption of a highly flexible domain architecture. Accordingly protein flexibility may result in crystals containing different conformational states of the same molecule. Accordingly, flexible protein regions of SidA are only fragmentary defined or entirely lacking in the electron density. Comparable results have been discussed for PHBH. In the absence of substrate the PHBH wild-type protein failed to form crystals that diffracted X-rays to high resolution (van der Laan, 1986) probably because this form of the enzyme is interconverting between different conformational states (Entsch *et al.*, 2005). By contrast a mutant variant (R220Q) of PHBH, which stabilizes the so-called *open* conformation of the enzyme resulted in crystals that diffracted X-rays up to 1.8 Å (Wang *et al.*, 2001). The *open* conformation is presumed to occur only transiently in wild-type PHBH during exchange of substrate or product. In addition to what has been discussed within the previous section the presumed flexible nature of SidA may represent another obstacle in obtaining crystals diffracting X-rays to higher resolution ($\leq$ 2.5 Å). Since the described flexibility is assumed to be correlated with enzymatic functionality crystals of catalytically inactive SidA could lead to improved X-ray diffraction. The design of inactive SidA variants or the identification of small molecular compounds acting as inhibitors on SidA should therefore be one major goal in future works on this enzyme.

4.11 PvdA is a Tetramer with Similar Features as SidA

The L-ornithine N^5-monooxygenase PvdA from *P. aeruginosa* constituted a subtopic of this thesis and was used primarily for comparative analysis with SidA. Since siderophores are essential to the pathogenicity of *Pseudomonas* (Takase *et al*., 2000) the key enzyme in pyoverdin biosynthesis PvdA is also of general interest as a potential drug target in particular with respect to treating chronic *Pseudomonas* infections in cystic fibrosis patients (Britigan *et al.*, 1993; Haas *et al.*, 1991).

Within the current work PvdA has successfully been cloned, overexpressed and purified. However, crystallization proved unexpectedly difficult since PvdA is highly prone to

precipitation. The majority of crystallization set-ups thus resulted in protein precipitation and those crystals that have been obtained could neither be tested within X-ray experiments nor be reproduced. This tendency of PvdA to aggregate has already been described (Imperi *et al.*, 2008) and similar observations have been reported for IucD from *E. coli* (Thariath *et al.*, 1993). Both, PvdA and IucD, lose their FAD cofactor during purification indicating a weak association between protein and prosthetic group (Meneely and Lamb, 2007; Macheroux *et al.*, 1993; Plattner *et al.*, 1989). Due to the loss of FAD purified PvdA lacked catalytic activity, which could however partly be restored by adding FAD to the protein solution.

As reported for other flavoenzymes the prosthetic group can be important for protein stability and conformational integrity (Risse *et al.*, 1992). Therefore the loss of FAD during protein purification may be the main reason for the instability of purified PvdA. The latter is confirmed by the fact that unlike wild-type enzyme the FAD-free SidA variant Y404S was highly prone to aggregation (compare section 4.2). In this work incubation of PvdA in a FAD-containing buffer and co-crystallization with FAD, did not result in a successful reconstitution of the apoenzyme. Therefore alternative methods for FAD-reconstitution (Hefti *et al.*, 2003) have to be tested in future works on this enzyme.

Due to the different strength in cofactor binding compared to SidA, in PvdA an alternative set of residues participating in FAD-binding appears to be probable – though residues that have been proposed to be involved in hydrogen bonding between SidA and FAD are also conserved in PvdA. However, as yet not all residues responsible for FAD-binding in SidA have completely been determined with confidence the current SidA structure is a rather hypothetical basis for drawing conclusions regarding residues potentially involved in FAD-binding of PvdA.

According to literature PvdA was suggested to occur as a monomer in solution (Meneely and Lamb, 2007). The current study by contrast demonstrates that PvdA is arranged as homotetramer. PvdA thus equals SidA not only biochemically and in its primary structure but also in its quaternary composition. Thus the high degree of sequence identity between SidA and PvdA as well as the fact that both enzymes catalyze

the same reaction (L-ornithine hydroxylation) imply that PvdA will share the characteristic FMO-like architecture with SidA.

5 Outlook

5.1 Structure and Function of SidA

The described biochemical and structural results obtained within this work represent a promising basis for future works on SidA and related enzymes. Accordingly expression-, purification- and crystallization- protocols for SidA have been established and a first SidA crystal structure has been solved. Moreover two assays have been adapted for monitoring the SidA NADPH oxidase activity and its monooxygenase function.

On basis of the current SidA structure experiments can be designed to further unravel the biochemical and structural function of specific amino acid residues including those of conserved sequence motifs. Furthermore rational protein engineering through site-directed mutagenesis can be applied to aim at protein variants that result in SidA crystals which diffract X-rays to higher resolution. Moreover, structure determination with upcoming data sets can from now on be performed by simply using the current SidA structure as a model for MR calculations (compare section 3.4.2).

Within this work SidA could unequivocally be assigned a class B flavin-containing monooxygenase. Moreover the ATGY motif was proposed as a second fingerprint motif for this class of enzymes. The central tyrosine (Tyr404) of this motif was shown to be crucial for FAD binding and protein integrity. To unravel the role of other conserved residues with respect to catalysis and cofactor binding, successive substitution through site-directed mutagenesis could be performed. The structural homology to other FMOs such as mFMO and spFMO can be advantageous in targeting residues for such mutagenesis studies. Examples are Gln253 which occupies a similar position as Tyr212 in mFMO. The latter has been shown to be important in shielding the active site during catalysis together with $NADP^+$ (Alfieri *et al.*, 2008). First experiments, that yet have to be verified, point at impaired enzymatic activity for the SidA variant Q253A thus indicating a similar role for Gln253 in SidA as Tyr212 of mFMO. Further residues that could be investigated in more detail include the highly conserved Asp396 (compare Table 4-2), which could be replaced with either asparagine to change the charge of the side chain or with glutamate to substitute for a more bulky amino acid. Another interesting candidate

for mutational analysis would be Gly403. Being part of the ATGY motif, substitution of Gly403 with alanine may introduce a higher degree of rigidity into this catalytically important loop region.

As part of the FMO- and BVMO-identifying sequence His225 represents another interesting residue to substitute for. This conserved residue has been shown to be crucial for catalysis and FAD binding. Replacement with glutamine or alanine resulted in impaired or abolished enzymatic activity in cyclohexanone monooxygenase and in 4-hydroxy-acetophenone monooxygenase, respectively (Cheesman *et al.*, 2003; Fraaije *et al.*, 2002). This kind of mutational analysis may also provide a possibility to obtain enzyme variants that are captured within a certain conformational state. The design of mutant variants such as G403A may inhibit the presumed inter-domain motion thus keeping the enzyme in a unique conformation favorable for crystallization and X-ray diffraction as it has been demonstrated with the PHBH variant R220Q (Wang *et al.*, 2001). Alternatively crystals could be soaked or co-crystallized with potential substrate analogs or inhibitors, which may equally serve in stabilizing a unique protein conformation. Examples for soaking compounds include L-lysine and the NADPH analog 3-aminopyridine adenine dinucleotide phosphate ($AADP^+$). Using the iodine oxidation assay, which was adapted to a 96-well plate format, it is possible to screen several hundred compounds simultaneously for their potential to act as inhibitors or substrate analogs on SidA catalytic activity.

To investigate the SidA catalytic mechanism in detail kinetic experiments should be performed more thoroughly as it has been done within the framework of the current study. This accounts especially for the kinetic analysis of the intrinsic NADPH oxidase activity and the SidA monooxygenase function. The NADPH-oxidation assay that has been used for determination of kinetic parameters like K_M and k_{cat} is only meaningful with regards to the reductive half of the catalytic cycle. Therefore the monooxygenase function of SidA has to be analyzed using the iodine-oxidation assay as a read-out for catalytic activity and substrate hydroxylation, especially with regards to a potential substrate inhibition as it has been discussed (see section 4.1, p.110).

Due to the loose packing of molecules within SidA crystals future strategies should focus on methods allowing for alternative crystal contacts and an optimized crystal packing. This can usually be achieved by means of protein surface engineering as it has been described (sections 3.3.8 and 4.3). Alternatively dehydration of SidA crystals can be applied, which may result in shrinking of the crystal lattice and thus in more extensive packing contacts between molecules within the lattice (Heras and Martin, 2005; Esnouf *et al.*, 1998).

Furthermore, the role of the intermolecular disulfide forming residues Cys62 and Cys66 should be investigated in more detail. This can be achieved by comparative analysis between wild-type SidA and its cysteine substitution variant C62S/C66S. Crystals of SidA C62S/C66S have been shown to diffract X-rays to only 7 Å (Lisson, 2007). However, these were grown under conditions different from that optimized for the SidA wild-type protein. Therefore the C62S/C66S variant should be crystallized under those conditions described for the wild-type to finally clarify the importance of Cys62 and Cys66 with regard to crystal quality and X-ray diffraction.

Finally, on basis of the structural and biochemical data obtained with SidA from *A. nidulans* it appears a reasonable approach to continue the work on its orthologue from *A. fumigatus*. The high sequence identity between these two enzymes allows to convey structural and in part functional data revealed for $SidA^{AN}$ to corresponding sequence stretches of $SidA^{AF}$.

5.2 The SidA Homologue PvdA

Within the current work the SidA-related enzyme PvdA from *P. aeruginosa* was demonstrated to resemble SidA not only on basis of its amino acid sequence and its biochemical properties but also with regards to its quaternary structure. The main difference between these enzymes is the binding mode to their FAD cofactor. Since FAD binding could be associated with protein stability, reconstitution with FAD may help in PvdA crystallization. Though addition of FAD to a purified PvdA solution restored enzymatic activity incubation of PvdA in a FAD-containing buffer and co-crystallization with FAD did not result in a successful cofactor reconstitution. However, there are

alternative methods for FAD-reconstitution (Hefti *et al.*, 2003), which could not be tested within the current work but represent possible approaches for stabilizing the enzymatically active proform of PvdA.

References

Abarca, M. L. (2000). Taxonomy and identification of the species involved in nosocomial aspergillosis. *Rev. Iberoam. Micol.* **17**: 79-84.

Adams, P. D., Grosse-Kunstleve, R. W., Hung, L. W., Ioerger, T. R., McCoy, A. J., Moriarty, N. W., Read, R. J., Sacchettini, J. C., Sauter, N. K. and Terwilliger, T. C. (2002). PHENIX: building new software for automated crystallographic structure determination. *Acta Crystallogr. D. Biol. Crystallogr.* **58**: 1948-1954.

Agarwal, R. and Singh, N. (2006). Amphotericin B is still the drug of choice for invasive aspergillosis. *Am. J. Respir. Crit Care Med.* **174**: 102-103.

Alberts, A. W., Chen, J., Kuron, G., Hunt, V., Huff, J., Hoffman, C., Rothrock, J., Lopez, M., Joshua, H., Harris, E., Patchett, A., Monaghan, R., Currie, S., Stapley, E., bers-Schonberg, G., Hensens, O., Hirshfield, J., Hoogsteen, K., Liesch, J. and Springer, J. (1980). Mevinolin: a highly potent competitive inhibitor of hydroxymethylglutaryl-coenzyme A reductase and a cholesterol-lowering agent. *Proc. Natl. Acad. Sci. U. S. A.* **77**: 3957-3961.

Alfieri, A., Malito, E., Orru, R., Fraaije, M. W. and Mattevi, A. (2008). Revealing the moonlighting role of NADP in the structure of a flavin-containing monooxygenase. *Proc. Natl. Acad. Sci. U. S. A.* **105**: 6572-6577.

Alp, S. and Arikan, S. (2008). Investigation of extracellular elastase, acid proteinase and phospholipase activities as putative virulence factors in clinical isolates of *Aspergillus* species. *J. Basic Microbiol.* **48**: 331-337.

Altschul, S. F., Madden, T. L., Schaffer, A. A., Zhang, J., Zhang, Z., Miller, W. and Lipman, D. J. (1997). Gapped BLAST and PSI-BLAST: a new generation of protein database search programs. *Nucleic Acids Res.* **25**: 3389-3402.

Amitani, R., Taylor, G., Elezis, E. N., Llewellyn-Jones, C., Mitchell, J., Kuze, F., Cole, P. J. and Wilson, R. (1995). Purification and characterization of factors produced by Aspergillus fumigatus which affect human ciliated respiratory epithelium. *Infect. Immun.* **63**: 3266-3271.

Anaissie, E. J. (2008). Diagnosis and therapy of fungal infection in patients with leukemia - new drugs and immunotherapy. *Best. Pract. Res. Clin. Haematol.* **21**: 683-690.

Araujo, R. and Rodrigues, A. G. (2004). Variability of germinative potential among pathogenic species of Aspergillus. *J. Clin. Microbiol.* **42**: 4335-4337.

Archibald, F. (1986). Manganese: its acquisition by and function in the lactic acid bacteria. *Crit Rev. Microbiol.* **13**: 63-109.

Austwick, P. K. (1966). The role of spores in the allergies and mycoses of man and animals. In *The Fungus Spore* (Madelin, M. F., ed), pp. 321-333, Butterworths, London.

Ausubel, F. M., Brent, R., Kingston, R. E., Moor, D. D., Seidman, J. G., Smith, J. A. and Struhl, K. (2007). *Current protocols in molecular biology* New York: John Wiley and Sons Inc.

Awaya, J. D. and Dubois, J. L. (2008). Identification, isolation, and analysis of a gene cluster involved in iron acquisition by *Pseudomonas mendocina* ymp. *Biometals.* **21**: 353-366.

Azarenkova, N. M., Vaganova, T. I., Strongin, A. I. and Stepanov, V. M. (1976). Isolation and properties of the acid carboxypeptidase of *Aspergillus oryzae*. *Biokhimiia.* **41**: 20-26.

Baddley, J. W., Pappas, P. G., Smith, A. C. and Moser, S. A. (2003). Epidemiology of *Aspergillus terreus* at a university hospital. *J. Clin. Microbiol.* **41**: 5525-5529.

Ballard, S. A., Kelly, S. L., Ellis, S. W. and Troke, P. F. (1990). Interaction of microsomal cytochrome P-450 isolated from *Aspergillus fumigatus* with fluconazole and itraconazole. *J. Med. Vet. Mycol.* **28**: 327-334.

Ballou, D. P., Entsch, B. and Cole, L. J. (2005). Dynamics involved in catalysis by single-component and two-component flavin-dependent aromatic hydroxylases. *Biochem. Biophys. Res. Commun.* **338**: 590-598.

Banatao, D. R., Cascio, D., Crowley, C. S., Fleissner, M. R., Tienson, H. L. and Yeates, T. O. (2006). An approach to crystallizing proteins by synthetic symmetrization. *Proc. Natl. Acad. Sci. U. S. A.* **103**, 16230-16235.

Bardana, E. J., Jr., Gerber, J. D., Craig, S. and Cianciulli, F. D. (1975). The general and specific humoral immune response to pulmonary aspergillosis. *Am. Rev. Respir. Dis.* **112**: 799-805.

Bauer, C. (2001). Blut: Ein flüssiges Organsystem. In *Lehrbuch der Physiologie* (Klinke, R. and Silbernagl, S., eds), pp. 189-216, Georg Thieme Verlag, Stuttgart New York.

Beaty, N. B. and Ballou, D. P. (1981). The oxidative half-reaction of liver microsomal FAD-containing monooxygenase. *J. Biol. Chem.* **256**: 4619-4625.

Bennett, J. H. (1842). On the Parasitic Vegetable Structures found growing in Living Animals., *Trans. R. Soc. Edinburgh.* pp. 277-279.

Bergfors, T. (1999). Seeding. (Terese M.Bergfors., ed), pp. 141-153, Enrico A. Stura.

Bergfors, T. (2003). Seeds to crystals. *J. Struct. Biol.* **142**: 66-76.

Bernard, Y., Degoy, S., Lefaucheux, F. and Robert, M. C. (1994). A gel-mediated feeding technique for protein crystal growth from hanging drops. *Acta Crystallogr. D. Biol. Crystallogr.* **50**: 504-507.

Bhabhra, R. and Askew, D. S. (2005). Thermotolerance and virulence of Aspergillus fumigatus: role of the fungal nucleolus. *Med. Mycol.* **43**: S87-S93.

Birch, L. E. and Ruddat, M. (2005). Siderophore accumulation and phytopathogenicity in *Microbotryum violaceum*. *Fungal. Genet. Biol.* **42**: 579-589.

Boeshans, K. M., Liu, F., Peng, G., Idler, W., Jang, S. I., Marekov, L., Black, L. and Ahvazi, B. (2006). Purification, crystallization and preliminary X-ray diffraction analysis of the phage T4 vertex protein gp24 and its mutant forms. *Protein Expr. Purif.* **49**: 235-243.

Boutet, E., Lieberherr, D., Tognolli, M., Schneider, M. and Bairoch, A. (2007). UniProtKB/Swiss-Prot. *Methods Mol. Biol.* **406**: 89-112.

Bradford, M. M. (1976). A rapid and sensitive method for the quantitation of microgram quantities of protein utilizing the principle of protein-dye binding. *Anal. Biochem.* **72**: 248-254.

Brakhage, A. A. and Liebmann, B. (2005). *Aspergillus fumigatus* conidial pigment and cAMP signal transduction: significance for virulence. *Med. Mycol.* **43**: S75-S82.

Braun, V. and Killmann, H. (1999). Bacterial solutions to the iron-supply problem. *Trends Biochem. Sci.* **24**: 104-109.

Britigan, B. E., Hayek, M. B., Doebbeling, B. N. and Fick, R. B., Jr. (1993). Transferrin and lactoferrin undergo proteolytic cleavage in the *Pseudomonas aeruginosa*-infected lungs of patients with cystic fibrosis. *Infect. Immun.* **61**: 5049-5055.

Brizova, K., Kralova, B., Demnerova, K. and Vins, I. (1992). Isolation and characterization of alpha-glucosidase from *Aspergillus niger*. *J. Chromatogr.* **593**: 125-131.

Brunelle, A., Bi, Y. A., Lin, J., Russell, B., Luy, L., Berkman, C. and Cashman, J. (1997). Characterization of two human flavin-containing monooxygenase (form 3) enzymes expressed in *Escherichia coli* as maltose binding protein fusions. *Drug Metab Dispos.* **25**: 1001-1007.

Brunger, A. T. (1992). Free R value: a novel statistical quantity for assessing the accuracy of crystal structures. *Nature.* **355**: 472-475.

Brunger, A. T., Adams, P. D., Clore, G. M., DeLano, W. L., Gros, P., Grosse-Kunstleve, R. W., Jiang, J. S., Kuszewski, J., Nilges, M., Pannu, N. S., Read, R. J., Rice, L. M., Simonson, T. and Warren, G. L. (1998). Crystallography and NMR system: A new software suite for macromolecular structure determination. *Acta Crystallogr. D. Biol. Crystallogr.* **54**: 905-921.

Brunger, A. T. and Adams, P. D. (2002). Molecular dynamics applied to X-ray structure refinement. *Acc. Chem. Res.* **35**: 404-412.

Brunger, A. T. (2007). Version 1.2 of the Crystallography and NMR system. *Nat. Protoc.* **2**: 2728-2733.

Buchi, G., Kitaura, Y., Yuan, S. S., Wright, H. E., Clardy, J., Demain, A. L., Ginsukon, T., Hunt, N. and WOGAN, G. N. (1973). Letter: structure of cytochalasin E, a toxic metabolite of *Aspergillus clavatus* . *J. Am. Chem. Soc.* **95**: 5423-5425.

Bullen, J. and Griffiths, E. (1999). *Iron and infection. Molecular, physiological and clinical aspects.* Wiley, Chichester.

Busen, W. (1982). The subunit structure of calf thymus ribonuclease H i as revealed by immunological analysis. *J. Biol. Chem.* **257**: 7106-7108.

Byers, B. R. and Arceneaux, J. E. (1998). Microbial iron transport: iron acquisition by pathogenic microorganisms. *Met. Ions. Biol. Syst.* **35**: 37-66.

Caputo, R. (2003). Itraconazole (Sporanox) in superficial and systemic fungal infections. *Expert. Rev. Anti. Infect. Ther.* **1**: 531-542.

Carter, D. M., Miousse, I. R., Gagnon, J. N., Martinez, E., Clements, A., Lee, J., Hancock, M. A., Gagnon, H., Pawelek, P. D. and Coulton, J. W. (2006). Interactions between TonB from *Escherichia coli* and the periplasmic protein FhuD. *J. Biol. Chem.* **281**: 35413-35424.

Casadevall, A. and Pirofski, L. A. (1999). Host-pathogen interactions: redefining the basic concepts of virulence and pathogenicity. *Infect. Immun.* **67**: 3703-3713.

CCP4 (1994). The CCP4 suite: programs for protein crystallography. *Acta Crystallogr. D. Biol. Crystallogr.* **50**: 760-763.

Chang, Y. C., Tsai, H. F., Karos, M. and Kwon-Chung, K. J. (2004). THTA, a thermotolerance gene of *Aspergillus fumigatus*. *Fungal. Genet. Biol.* **41**: 888-896.

Chayen, N. E. (1997). The role of oil in macromolecular crystallization. *Structure.* **5**: 1269-1274.

Cheesman, M. J., Byron, K. M. and Rettie, A. E. (2003). Critical role of histidine residues in cyclohexanone monooxygenase expression, cofactor binding and catalysis. *Chem. Biol. Interact.* **146**: 157-164.

Clemons, K. V., Calich, V. L., Burger, E., Filler, S. G., Grazziutti, M., Murphy, J., Roilides, E., Campa, A., Dias, M. R., Edwards, J. E., Jr., Fu, Y., Fernandes-Bordignon, G., Ibrahim, A., Katsifa, H., Lamaignere, C. G., Meloni-Bruneri, L. H., Rex, J., Savary, C. A. and Xidieh, C. (2000). Pathogenesis I: interactions of host cells and fungi. *Med. Mycol.* **38** Suppl 1:99-111.

Clemons, K. V., Miller, T. K., Selitrennikoff, C. P. and Stevens, D. A. (2002). fos-1, a putative histidine kinase as a virulence factor for systemic aspergillosis. *Med. Mycol.* **40**: 259-262.

Cohen, A., Nelson, H. and Nelson, N. (2000). The family of SMF metal ion transporters in yeast cells. *J. Biol. Chem.* **275**: 33388-33394.

Coligan, J. E., Dunn, B. M., Ploegh, H. L., Speicher, D. W. and Wingfield, P. T. (2002). *Current protocols in protein science.* New York: John Wiley and Sons Inc.

Cooper, S. R., McArdle, J. V. and Raymond, K. N. (1978). Siderophore electrochemistry: relation to intracellular iron release mechanism. *Proc. Natl. Acad. Sci. U. S. A.* **75**: 3551-3554.

Costa, S. and Nucci, M. (2001). Can we decrease amphotericin nephrotoxicity? *Curr. Opin. Crit Care.* **7**: 379-383.

Cowtan, K. D. and Zhang, K. Y. (1999). Density modification for macromolecular phase improvement. *Prog. Biophys. Mol. Biol.* **72**: 245-270.

Crichton, R. (2001). *Inorganic Biochemistry of Iron Metabolism.*

Crouch, M. L., Castor, M., Karlinsey, J. E., Kalhorn, T. and Fang, F. C. (2008). Biosynthesis and IroC-dependent export of the siderophore salmochelin are essential for virulence of *Salmonella enterica* serovar Typhimurium. *Mol. Microbiol.* **67**: 971-983.

Csaky, T. Z. (1948). On the Estimation of Bound Hydroxylamine in Biological Materials.

Cudney, R., Patel, S., Weisgraber, K., Newhouse, Y. and McPherson, A. (1994). Screening and optimization strategies for macromolecular crystal growth. *Acta Crystallogr. D. Biol. Crystallogr.* **50**: 414-423.

Dale, G. E., Oefner, C. and D'Arcy, A. (2003). The protein as a variable in protein crystallization. *J. Struct. Biol.* **142**: 88-97.

de Lorenzo, V., Bindereif, A., Paw, B. H. and Neilands, J. B. (1986). Aerobactin biosynthesis and transport genes of plasmid ColV-K30 in Escherichia coli K-12. *J. Bacteriol.* **165**: 570-578.

DeLaBarre, B. and Brunger, A. T. (2006). Considerations for the refinement of low-resolution crystal structures. *Acta Crystallogr. D. Biol. Crystallogr.* **62**: 923-932.

DeLano, W. L. (2002). The PyMOL Molecular Graphics System. DeLano Scientific, San Carlos, CA, USA.

Demain, A. L., Hunt, N. A., Malik, V., Kobbe, B., Hawkins, H., Matsuo, K. and WOGAN, G. N. (1976). Improved procedure for production of cytochalasin E and tremorgenic mycotoxins by *Aspergillus clavatus*. *Appl. Environ. Microbiol.* **31**: 138-140.

Denning, D. W. (1998). Invasive aspergillosis. *Clin. Infect. Dis.* **26**: 781-803.

Denning, D. W., Anderson, M. J., Turner, G., Latge, J. P. and Bennett, J. W. (2002). Sequencing the *Aspergillus fumigatus* genome. *Lancet Infect. Dis.* **2**: 251-253.

Derewenda, Z. S. (2004). Rational protein crystallization by mutational surface engineering. *Structure.* **12**: 529-535.

Dick, S., Marrone, L., Duewel, H., Beecroft, M., McCourt, J. and Viswanatha, T. (1999). Lysine: N6-hydroxylase: stability and interaction with ligands. *J. Protein Chem.* **18**: 893-903.

Dix, D., Bridgham, J., Broderius, M. and Eide, D. (1997). Characterization of the FET4 protein of yeast. Evidence for a direct role in the transport of iron. *J. Biol. Chem.* **272**: 11770-11777.

Drechsel, H. and Jung, G. (1998). Peptide siderophores. *J. Pept. Sci.* **4**: 147-181.

Dunn, L. L., Rahmanto, Y. S. and Richardson, D. R. (2007). Iron uptake and metabolism in the new millennium. *Trends Cell Biol.* **17**: 93-100.

Edman, P. and Begg, G. (1967). A protein sequenator. *Eur. J. Biochem.* **1**: 80-91.

Eisendle, M., Oberegger, H., Zadra, I. and Haas, H. (2003). The siderophore system is essential for viability of Aspergillus nidulans: functional analysis of two genes encoding l-ornithine N 5-monooxygenase (sidA) and a non-ribosomal peptide synthetase (sidC). *Mol. Microbiol.* **49**: 359-375.

Eisendle, M., Schrettl, M., Kragl, C., Muller, D., Illmer, P. and Haas, H. (2006). The intracellular siderophore ferricrocin is involved in iron storage, oxidative-stress resistance, germination, and sexual development in Aspergillus nidulans. *Eukaryot. Cell.* **5**: 1596-1603.

Ekins, A., Khan, A. G., Shouldice, S. R. and Schryvers, A. B. (2004). Lactoferrin receptors in gram-negative bacteria: insights into the iron acquisition process. *Biometals.* **17**: 235-243.

Emery, T. (1976). Fungal ornithine esterases: relationship to iron transport. *Biochemistry.* **15**: 2723-2728.

Emsley, P. and Cowtan, K. (2004). Coot: model-building tools for molecular graphics. *Acta Crystallogr. D. Biol. Crystallogr.* **60**: 2126-2132.

Entsch, B. and van Berkel, W. J. (1995). Structure and mechanism of para-hydroxybenzoate hydroxylase. *FASEB J.* **9**: 476-483.

Entsch, B., Cole, L. J. and Ballou, D. P. (2005). Protein dynamics and electrostatics in the function of p-hydroxybenzoate hydroxylase. *Arch. Biochem. Biophys.* **433**: 297-311.

Entsch, B., Cole, L. J. and Ballou, D. P. (2005). Protein dynamics and electrostatics in the function of p-hydroxybenzoate hydroxylase. *Arch. Biochem. Biophys.* **433**: 297-311.

Esnouf, R. M., Ren, J., Garman, E. F., Somers, D. O., Ross, C. K., Jones, E. Y., Stammers, D. K. and Stuart, D. I. (1998). Continuous and discontinuous changes in the

unit cell of HIV-1 reverse transcriptase crystals on dehydration. *Acta Crystallogr. D. Biol. Crystallogr.* **54**: 938-953.

Eswaramoorthy, S., Bonanno, J. B., Burley, S. K. and Swaminathan, S. (2006). Mechanism of action of a flavin-containing monooxygenase. *Proc. Natl. Acad. Sci. U. S. A.* **103**: 9832-9837.

Feniskova, R. V. and Segal, R. B. (1953). Production of amylase of molds from the family of *Aspergillus*. Effect of conditions of growth on conidia formation in *Aspergillus oryzae*. *Mikrobiologiia.* **22**: 543-550.

Ferguson, A. D. and Deisenhofer, J. (2002). TonB-dependent receptors-structural perspectives. *Biochim. Biophys. Acta.* **1565**: 318-332.

Fleischmann, J. and Lehrer, R. I. (1985). Phagocytic mechanisms in host response. In *Fungi pathogenic for humans and animals. B. Pathogenicity and detection: II.* (D.H.Howard, ed), pp. 123-149, Marcel Dekker, Inc., New York, N.Y.

Fleming, R. E. and Bacon, B. R. (2005). Orchestration of iron homeostasis. *N. Engl. J. Med.* **352**: 1741-1744.

Forman, S. R., Fink, J. N., Moore, V. L., Wang, J. and Patterson, R. (1978). Humoral and cellular immune responses in *Aspergillus fumigatus* pulmonary disease. *J. Allergy Clin. Immunol.* **62**: 131-136.

Fortun, J., Martin-Davila, P., Montejo, M., Munoz, P., Cisneros, J. M., Ramos, A., Aragon, C., Blanes, M., San, J. R., Gavalda, J. and Llinares, P. (2009). Prophylaxis with caspofungin for invasive fungal infections in high-risk liver transplant recipients. *Transplantation.* **87**: 424-435.

Fraaije, M. W., Kamerbeek, N. M., van Berkel, W. J. and Janssen, D. B. (2002). Identification of a Baeyer-Villiger monooxygenase sequence motif. *FEBS Lett.* **518**: 43-47.

Frederick, K. K., Ballou, D. P. and Palfey, B. A. (2001). Protein dynamics control proton transfers to the substrate on the His72Asn mutant of p-hydroxybenzoate hydroxylase. *Biochemistry.* **40**: 3891-3899.

Fritz, G., Mittl, P. R., Vasak, M., Grutter, M. G. and Heizmann, C. W. (2002). The crystal structure of metal-free human EF-hand protein S100A3 at 1.7-A resolution. *J. Biol. Chem.* **277**: 33092-33098.

Gallin, J. I. and Zarember, K. (2007). Lessons about the pathogenesis and management of aspergillosis from studies in chronic granulomatous disease. *Trans. Am. Clin. Climatol. Assoc.* **118**: 175-185.

Garman, E. and Owen, R. L. (2007). Cryocrystallography of macromolecules: practice and optimization. *Methods Mol. Biol.* **364**: 1-18.

Gasteiger E., Gattiker A., Hoogland C., Ivanyi I., Appel R. D. and Bairoch A. (2003). ExPASy: The proteomics server for in-depth protein knowledge and analysis. *Nucleic Acids Res.* **31**(13): 3784-8.

Gatti, D. L., Palfey, B. A., Lah, M. S., Entsch, B., Massey, V., Ballou, D. P. and Ludwig, M. L. (1994). The mobile flavin of 4-OH benzoate hydroxylase. *Science.* **266**: 110-114.

Ge, L. and Seah, S. Y. (2006). Heterologous expression, purification, and characterization of an l-ornithine N(5)-hydroxylase involved in pyoverdine siderophore biosynthesis in *Pseudomonas aeruginosa*. *J. Bacteriol.* **188**: 7205-7210.

Gill, S. C. and von Hippel, P. H. (1989). Calculation of protein extinction coefficients from amino acid sequence data. *Anal. Biochem.* **182**: 319-326.

Girardin, H., Paris, S., Rault, J., Bellon-Fontaine, M. N. and Latge, J. P. (1999). The role of the rodlet structure on the physicochemical properties of *Aspergillus* conidia. *Lett. Appl. Microbiol.* **29**, 364-369.

Goodley, J. M., Clayton, Y. M. and Hay, R. J. (1994). Environmental sampling for aspergilli during building construction on a hospital site. *J. Hosp. Infect.* **26**: 27-35.

Gorbacheva, V. Y., Faundez, G., Godfrey, H. P. and Cabello, F. C. (2001). Restricted growth of ent(-) and tonB mutants of *Salmonella enterica* serovar Typhi in human Mono Mac 6 monocytic cells. *FEMS Microbiol. Lett.* **196**: 7-11.

Gouet, P., Courcelle, E., Stuart, D. I. and Metoz, F. (1999). ESPript: analysis of multiple sequence alignments in PostScript. *Bioinformatics.* **15**: 305-308.

Granier, T., Langlois, d. B., Gallois, B., Chevalier, J. M., Precigoux, G., Santambrogio, P. and Arosio, P. (2003). Structural description of the active sites of mouse L-chain ferritin at 1.2 A resolution. *J. Biol. Inorg. Chem.* **8**: 105-111.

Gromada, A. and Fiedurek, J. (1997). Selective isolation of *Aspergillus niger* mutants with enhanced glucose oxidase production. *J. Appl. Microbiol.* **82**: 648-652.

Gruene T. (2008). Macromolecular Phasing with SHELXC/D/E. CCP4 workshop Chicago.

Guerinot, M. L. (1994). Microbial iron transport. *Annu. Rev. Microbiol.* **48**: 743-72**.**

Guerrero, S. A., Hecht, H. J., Hofmann, B., Biebl, H. and Singh, M. (2001). Production of selenomethionine-labelled proteins using simplified culture conditions and generally applicable host/vector systems. *Appl. Microbiol. Biotechnol.* **56**: 718-723.

Haas, B., Kraut, J., Marks, J., Zanker, S. C. and Castignetti, D. (1991). Siderophore presence in sputa of cystic fibrosis patients. *Infect. Immun.* **59**: 3997-4000.

Haas, H., Eisendle, M. and Turgeon, B. G. (2008). Siderophores in fungal physiology and virulence. *Annu. Rev. Phytopathol.* **46*:*** 149-187.

Halliwell, B. and Gutteridge, J. M. C. (1989). *Free Radicals in Biology and Medicine.* Oxford: Clarendon Press.

Hanson, B. L., Schall, C. A. and Bunick, G. J. (2003). New techniques in macromolecular cryocrystallography: macromolecular crystal annealing and cryogenic helium. *J. Struct. Biol.* **142**: 77-87.

Harrison, P. M. and Arosio, P. (1996). The ferritins: molecular properties, iron storage function and cellular regulation. *Biochim. Biophys. Acta.* **1275**: 161-203.

Harrison, P. M., Hempstead, P. D., Artymiuk, P. J. and Andrews, S. C. (1998). Structure-function relationships in the ferritins. *Met. Ions. Biol. Syst.* **35**: 435-477.

Hassell, A. M., An, G., Bledsoe, R. K., Bynum, J. M., Carter, H. L., III, Deng, S. J., Gampe, R. T., Grisard, T. E., Madauss, K. P., Nolte, R. T., Rocque, W. J., Wang, L., Weaver, K. L., Williams, S. P., Wisely, G. B., Xu, R. and Shewchuk, L. M. (2007). Crystallization of protein-ligand complexes. *Acta Crystallogr. D. Biol. Crystallogr.* **63**: 72-79.

Hassett, R., Dix, D. R., Eide, D. J. and Kosman, D. J. (2000). The Fe(II) permease Fet4p functions as a low affinity copper transporter and supports normal copper trafficking in *Saccharomyces cerevisiae*. *Biochem. J.* **351**: 477-84.

Hay, R. J. (2003). Antifungal drugs used for systemic mycoses. *Dermatol. Clin.* **21**: 577-587.

Hedayati, M. T., Pasqualotto, A. C., Warn, P. A., Bowyer, P. and Denning, D. W. (2007). *Aspergillus flavus*: human pathogen, allergen and mycotoxin producer. *Microbiology.* **153**: 1677-1692.

Hefti, M. H., Milder, F. J., Boeren, S., Vervoort, J. and van Berkel, W. J. (2003). A His-tag based immobilization method for the preparation and reconstitution of apoflavoproteins. *Biochim. Biophys. Acta.* **20**: 139-143.

Heinz, D. W. and Matthews, B. W. (1994). Rapid crystallization of T4 lysozyme by intermolecular disulfide cross-linking. *Protein Eng.* **7**: 301-307.

Hempstead, P. D., Yewdall, S. J., Fernie, A. R., Lawson, D. M., Artymiuk, P. J., Rice, D. W., Ford, G. C. and Harrison, P. M. (1997). Comparison of the three-dimensional structures of recombinant human H and horse L ferritins at high resolution. *J. Mol. Biol.* **268**, 424-448.

Heras, B. and Martin, J. L. (2005). Post-crystallization treatments for improving diffraction quality of protein crystals. *Acta Crystallogr. D. Biol. Crystallogr.* **61**: 1173-1180.

Herbrecht, R., Denning, D. W., Patterson, T. F., Bennett, J. E., Greene, R. E., Oestmann, J. W., Kern, W. V., Marr, K. A., Ribaud, P., Lortholary, O., Sylvester, R., Rubin, R. H., Wingard, J. R., Stark, P., Durand, C., Caillot, D., Thiel, E., Chandrasekar, P. H., Hodges,

M. R., Schlamm, H. T., Troke, P. F. and de, P. B. (2002). Voriconazole versus amphotericin B for primary therapy of invasive aspergillosis. *N. Engl. J. Med.* **347**: 408-415.

Herrero, M., de, L., V and Neilands, J. B. (1988). Nucleotide sequence of the iucD gene of the pColV-K30 aerobactin operon and topology of its product studied with phoA and lacZ gene fusions. *J. Bacteriol.* **170**: 56-64.

Hertz-Fowler, C. and Pain, A. (2007). Specialist fungi, versatile genomes. *Nat. Rev. Microbiol.* **5**: 332-333.

Heymann, P., Gerads, M., Schaller, M., Dromer, F., Winkelmann, G. and Ernst, J. F. (2002). The siderophore iron transporter of *Candida albicans* (Sit1p/Arn1p) mediates uptake of ferrichrome-type siderophores and is required for epithelial invasion. *Infect. Immun.* **70**: 5246-5255.

Hissen, A. H., Wan, A. N., Warwas, M. L., Pinto, L. J. and Moore, M. M. (2005). The *Aspergillus fumigatus* siderophore biosynthetic gene sidA, encoding L-ornithine N5-oxygenase, is required for virulence. *Infect. Immun.* **73**: 5493-5503.

Hoegger, P. J., Kilaru, S., James, T. Y., Thacker, J. R. and Kues, U. (2006). Phylogenetic comparison and classification of laccase and related multicopper oxidase protein sequences. *FEBS J.* **273**: 2308-2326.

Hohl, T. M., Van Epps, H. L., Rivera, A., Morgan, L. A., Chen, P. L., Feldmesser, M. and Pamer, E. G. (2005). Aspergillus fumigatus triggers inflammatory responses by stage-specific beta-glucan display. *PLoS. Pathog.* **1**: e30.

Hohl, T. M. and Feldmesser, M. (2007). *Aspergillus fumigatus*: principles of pathogenesis and host defense. *Eukaryot. Cell.* **6**. 1953-1963.

Holm, L. and Sander, C. (1999). Protein folds and families: sequence and structure alignments. *Nucleic Acids Res.* **27**: 244-247.

Holm, L., Kaariainen, S., Rosenstrom, P. and Schenkel, A. (2008). Searching protein structure databases with DaliLite v.3. *Bioinformatics.* **24**: 2780-2781.

Hospenthal, D. R., Kwon-Chung, K. J. and Bennett, J. E. (1998). Concentrations of airborne *Aspergillus* compared to the incidence of invasive aspergillosis: lack of correlation. *Med. Mycol.* **36**: 165-168.

Howard, D. H. (1999). Acquisition, transport, and storage of iron by pathogenic fungi. *Clin. Microbiol. Rev.* **12**: 394-404.

Hsieh, Y. C., Liu, M. Y., Le, G. J. and Chen, C. J. (2005). Anaerobic purification and crystallization to improve the crystal quality: ferredoxin II from *Desulfovibrio gigas*. *Acta Crystallogr. D. Biol. Crystallogr.* **61**: 780-783.

Hubbard, S. J. (1998). The structural aspects of limited proteolysis of native proteins. *Biochim. Biophys. Acta.* **1382**: 191-206.

Hwang, L. H., Mayfield, J. A., Rine, J. and Sil, A. (2008). *Histoplasma* requires SID1, a member of an iron-regulated siderophore gene cluster, for host colonization. *PLoS. Pathog.* **4**: e1000044.

Ibrahim-Granet, O., Philippe, B., Boleti, H., Boisvieux-Ulrich, E., Grenet, D., Stern, M. and Latge, J. P. (2003). Phagocytosis and intracellular fate of Aspergillus fumigatus conidia in alveolar macrophages. *Infect. Immun.* **71**: 891-903.

Ichishima, E., Maeba, H., Amikura, T. and Sakata, H. (1984). Multiple forms of protyrosinase from *Aspergillus oryzae* and their mode of activation at pH 3.0. *Biochim. Biophys. Acta.* **786**: 25-31.

Imbert, M. and Blondeau, R. (1998). On the iron requirement of lactobacilli grown in chemically defined medium. *Curr. Microbiol.* **37**: 64-66.

Imperi, F., Putignani, L., Tiburzi, F., Ambrosi, C., Cipollone, R., Ascenzi, P. and Visca, P. (2008). Membrane-association determinants of the omega-amino acid monooxygenase PvdA, a pyoverdine biosynthetic enzyme from *Pseudomonas aeruginosa*. *Microbiology.* **154**: 2804-2813.

Jahn, B., Boukhallouk, F., Lotz, J., Langfelder, K., Wanner, G. and Brakhage, A. A. (2000). Interaction of human phagocytes with pigmentless *Aspergillus* conidia. *Infect. Immun.* **68**: 3736-3739.

Jelsch, C., Longhi, S. and Cambillau, C. (1998). Packing forces in nine crystal forms of cutinase. *Proteins.* **31**: 320-333.

Jenssen, H. and Hancock, R. E. (2009). Antimicrobial properties of lactoferrin. *Biochimie.* **91**: 19-29.

Jin, L. and Robert, E. (2004). Engineering Proteins to Promote Crystallization. In *Protein Crystallography in Drug Discovery*, pp. 209-216, Wiley-VCH Verlag GmbH and Co. KGaA.

Johnson, M. A., Lyle, G., Hanly, M. and Yeh, K. A. (1998). *Aspergillus*: a rare primary organism in soft-tissue infections. *Am. Surg.* **64**: 122-126.

Kabsch, W. (1993). Automatic processing of rotation diffraction data from crystals of initially unknown symmetry and cell constants. *J. Appl. Cryst.* **26**: 795-800.

Kamai, Y., Chiang, L. Y., Lopes Bezerra, L. M., Doedt, T., Lossinsky, A. S., Sheppard, D. C. and Filler, S. G. (2006). Interactions of *Aspergillus fumigatus* with vascular endothelial cells. *Med. Mycol.* **44** Suppl 1: S115-7.

Kamei, K. and Watanabe, A. (2005). *Aspergillus* mycotoxins and their effect on the host. *Med. Mycol.* **43** Suppl 1: S95-S99.

Karlsson, A. and Sauer-Eriksson, A. E. (2007). Heating of proteins as a means of improving crystallization: a successful case study on a highly amyloidogenic triple mutant of human transthyretin. *Acta Crystallogr. Sect. F. Struct. Biol. Cryst. Commun.* **63**: 695-700.

Kleywegt, G. J. and Jones, T. A. (1995). Where freedom is given, liberties are taken. *Structure* **3**: 535-540.

Kleywegt, G. J. and Brunger, A. T. (1996). Checking your imagination: applications of the free R value. *Structure.* **4**: 897-904.

Kleywegt, G. J. (1999). Experimental assessment of differences between related protein crystal structures. *Acta Crystallogr. D. Biol. Crystallogr.* **55**: 1878-1884.

Kona, R. P., Qureshi, N. and Pai, J. S. (2001). Production of glucose oxidase using *Aspergillus niger* and corn steep liquor. *Bioresour. Technol.* **78**: 123-126.

Konetschny-Rapp, S., Huschka, H. G., Winkelmann, G. and Jung, G. (1988). High-performance liquid chromatography of siderophores from fungi. *Biol. Met.* **1**: 9-17.

Kosman, D. J. (2003). Molecular mechanisms of iron uptake in fungi. *Mol. Microbiol.* **47**: 1185-1197.

Kragl, C., Schrettl, M., Abt, B., Sarg, B., Lindner, H. H. and Haas, H. (2007). EstB-mediated hydrolysis of the siderophore triacetylfusarinine C optimizes iron uptake of *Aspergillus fumigatus*. *Eukaryot. Cell.* **6**: 1278-1285.

Krissinel, E. and Henrick, K. (2007). Inference of macromolecular assemblies from crystalline state. *J. Mol. Biol.* **372**: 774-797.

Krueger, S. K. and Williams, D. E. (2005). Mammalian flavin-containing monooxygenases: structure/function, genetic polymorphisms and role in drug metabolism. *Pharmacol. Ther.* **106**: 357-387.

Kusne, S., Torre-Cisneros, J., Manez, R., Irish, W., Martin, M., Fung, J., Simmons, R. L. and Starzl, T. E. (1992). Factors associated with invasive lung aspergillosis and the significance of positive Aspergillus culture after liver transplantation. *J. Infect. Dis.* **166**: 1379-1383.

Lanternier, F. and Lortholary, O. (2008). Liposomal amphotericin B: what is its role in 2008? *Clin. Microbiol. Infect.* **14**: Suppl 4:71-83.

Larsen, T. O., Smedsgaard, J., Nielsen, K. F., Hansen, M. A., Samson, R. A. and Frisvad, J. C. (2007). Production of mycotoxins by *Aspergillus lentulus* and other medically important and closely related species in section Fumigati. *Med. Mycol.* **45**: 225-232.

Laskowski, R. A., MacArthur, M. W., Moss, D. S. and Thornton, J. M. (1993). PROCHECK: a program to check the stereochemical quality of protein structures. *Journal of Applied Crystallography* **26**: 283-291.

Lass-Florl, C., Griff, K., Mayr, A., Petzer, A., Gastl, G., Bonatti, H., Freund, M., Kropshofer, G., Dierich, M. P. and Nachbaur, D. (2005). Epidemiology and outcome of infections due to *Aspergillus terreus* : 10-year single centre experience. *Br. J. Haematol.* **131**: 201-207.

Latgé, J. P. (1999). *Aspergillus fumigatus* and aspergillosis. *Clin. Microbiol. Rev.* **12**: 310-350.

Latgé, J. P. (2001). The pathobiology of *Aspergillus fumigatus*. *Trends Microbiol.* **9**: 382-389.

Latgé, J. P. (2007). The cell wall: a carbohydrate armour for the fungal cell. *Mol. Microbiol.* **66**: 279-290.

Lawton, M. P. and Philpot, R. M. (1993). Molecular genetics of the flavin-dependent monooxygenases. *Pharmacogenetics.* **3**: 40-44.

Lennon, B. W., Williams, C. H., Jr. and Ludwig, M. L. (2000). Twists in catalysis: alternating conformations of *Escherichia coli* thioredoxin reductase. *Science.* **289**: 1190-1194.

Leslie, A. G. W. (1992). Recent changes to the MOSFLM package for processing film and image plate data. *Joint CCP4+ESF-EAMCB Newsletter on Protein Crystallography*.

Levitz, S. M. and Diamond, R. D. (1985). Mechanisms of resistance of *Aspergillus fumigatus* Conidia to killing by neutrophils in vitro. *J. Infect. Dis.* **152**: 33-42.

Lewis, R. E., Wiederhold, N. P., Chi, J., Han, X. Y., Komanduri, K. V., Kontoyiannis, D. P. and Prince, R. A. (2005). Detection of gliotoxin in experimental and human aspergillosis. *Infect. Immun.* **73**: 635-637.

Liebmann, B., Gattung, S., Jahn, B. and Brakhage, A. A. (2003). cAMP signaling in Aspergillus fumigatus is involved in the regulation of the virulence gene pksP and in defense against killing by macrophages. *Mol. Genet. Genomics.* **269**: 420-435.

Lin, S. J., Schranz, J. and Teutsch, S. M. (2001). Aspergillosis case-fatality rate: systematic review of the literature. *Clin. Infect. Dis.* **32**: 358-366.

Linding, R., Jensen, L. J., Diella, F., Bork, P., Gibson, T. J. and Russell, R. B. (2003). Protein disorder prediction: implications for structural proteomics. *Structure.* **11**: 1453-1459.

Lisson, K. (2007). Strukturelle Analyse der L-Ornithin N^5-Monooxygenase SidA aus *Aspergillus nidulans*. Diploma Thesis. Helmholtz Center for Infection Research, Braunschweig.

Loach, P. A. (1968). Oxidation-reduction potentials, absorbance bands and molar absorbance of compounds used in biochemical studies. In *Handbook of Biochemistry. Selected Data for Molecular Biology.* (Sober H.A, ed), pp. J27-J48.

Lopes Bezerra, L. M. and Filler, S. G. (2004). Interactions of *Aspergillus fumigatus* with endothelial cells: internalization, injury, and stimulation of tissue factor activity. *Blood.* **103**: 2143-2149.

Lountos, G. T., Jiang, R., Wellborn, W. B., Thaler, T. L., Bommarius, A. S. and Orville, A. M. (2006). The crystal structure of NAD(P)H oxidase from Lactobacillus sanfranciscensis: insights into the conversion of O2 into two water molecules by the flavoenzyme. *Biochemistry.* **45**: 9648-9659.

Macheroux, P., Plattner, H. J., Romaguera, A. and Diekmann, H. (1993). FAD and substrate analogs as probes for lysine N6-hydroxylase from *Escherichia coli* EN 222. *Eur. J. Biochem.* **213**: 995-1002.

Macheroux, P. (1999). UV-visible spectroscopy as a tool to study flavoproteins. In *Flavoprotein protocols* (Chapman, S. K. and Reid, G. A., eds), pp. 1-7, Humana Press, Totowa, N.J.

Malito, E., Alfieri, A., Fraaije, M. W. and Mattevi, A. (2004). Crystal structure of a Baeyer-Villiger monooxygenase. *Proc. Natl. Acad. Sci. U. S. A* **101**: 13157-13162.

Marrone, L. and Viswanatha, T. (1997). Effect of selective cysteine - alanine replacements on the catalytic functions of lysine: N6-hydroxylase. *Biochim. Biophys. Acta.* **1343**: 263-277.

Mattevi, A. (2006). To be or not to be an oxidase: challenging the oxygen reactivity of flavoenzymes. *Trends Biochem. Sci.* **31**: 276-283.

Matthews, B. W. (1968). Solvent content of protein crystals. *J. Mol. Biol.* **33**: 491-497.

McCoy, A. J., Grosse-Kunstleve, R. W., Storoni, L. C. and Read, R. J. (2005). Likelihood-enhanced fast translation functions. *Acta Crystallogr. D. Biol. Crystallogr.* **61**: 458-464.

Mei, B., Budde, A. D. and Leong, S. A. (1993). sid1, a gene initiating siderophore biosynthesis in *Ustilago maydis*: molecular characterization, regulation by iron, and role in phytopathogenicity. *Proc. Natl. Acad. Sci. U. S. A.* **90**: 903-907.

Mellado, E., ufauvre-Brown, A., Gow, N. A. and Holden, D. W. (1996). The Aspergillus fumigatus chsC and chsG genes encode class III chitin synthases with different functions. *Mol. Microbiol.* **20**: 667-679.

Meneely, K. M. and Lamb, A. L. (2007). Biochemical characterization of a flavin adenine dinucleotide-dependent monooxygenase, ornithine hydroxylase from *Pseudomonas aeruginosa*, suggests a novel reaction mechanism. *Biochemistry.* **46**: 11930-11937.

Mishina, T. E. and Zeier, J. (2006). The *Arabidopsis* flavin-dependent monooxygenase FMO1 is an essential component of biologically induced systemic acquired resistance. *Plant Physiol.* **141**: 1666-1675.

Monod, M., Paris, S., Sanglard, D., Jaton-Ogay, K., Bille, J. and Latge, J. P. (1993). Isolation and characterization of a secreted metalloprotease of *Aspergillus fumigatus*. *Infect. Immun.* **61**: 4099-4104.

Moreno, M. A., Ibrahim-Granet, O., Vicentefranqueira, R., Amich, J., Ave, P., Leal, F., Latge, J. P. and Calera, J. A. (2007). The regulation of zinc homeostasis by the ZafA transcriptional activator is essential for *Aspergillus fumigatus* virulence. *Mol. Microbiol.* **64**: 1182-1197.

Morris, R. J., Perrakis, A. and Lamzin, V. S. (2003). ARP/wARP and automatic interpretation of protein electron density maps. *Methods Enzymol.* **374**: 229-244.

Moser, J., Schubert, W. D., Beier, V., Bringemeier, I., Jahn, D. and Heinz, D. W. (2001). V-shaped structure of glutamyl-tRNA reductase, the first enzyme of tRNA-dependent tetrapyrrole biosynthesis. *EMBO J.* **20**: 6583-6590.

Mullins, J., Harvey, R. and Seaton, A. (1976). Sources and incidence of airborne *Aspergillus fumigatus* (Fres). *Clin. Allergy.* **6**: 209-217.

Mullins, J., Hutcheson, P. S. and Slavin, R. G. (1984). *Aspergillus fumigatus* spore concentration in outside air: Cardiff and St Louis compared. *Clin. Allergy.* **14**: 351-354.

Murshudov, G. N., Vagin, A. A. and Dodson, E. J. (1997). Refinement of macromolecular structures by the maximum-likelihood method. *Acta Crystallogr. D. Biol. Crystallogr.* **53**: 240-255.

Nelissen, B., De, W. R. and Goffeau, A. (1997). Classification of all putative permeases and other membrane plurispanners of the major facilitator superfamily encoded by the complete genome of *Saccharomyces cerevisiae*. *FEMS Microbiol. Rev.* **21**: 113-134.

Nenoff, P., Friedrich, T., Schwenke, H., Mierzwa, M., Horn, L. C. and Haustein, U. F. (1997). Rare fatal simultaneous mould infection of the lung caused by *Aspergillus flavus* and the basidiomycete *Coprinus sp*. in a leukemic patient. *J. Med. Vet. Mycol.* **35**: 65-69.

Nguyen, K. T., Wu, J. C., Boylan, J. A., Gherardini, F. C. and Pei, D. (2007). Zinc is the metal cofactor of Borrelia burgdorferi peptide deformylase. *Arch. Biochem. Biophys.* **468**: 217-225.

Nierman, W. C., Pain, A., Anderson, M. J., Wortman, J. R., Kim, H. S., Arroyo, J., Berriman, M., Abe, K., Archer, D. B., Bermejo, C., Bennett, J., Bowyer, P., Chen, D., Collins, M., Coulsen, R., Davies, R., Dyer, P. S., Farman, M., Fedorova, N., Fedorova, N., Feldblyum, T. V., Fischer, R., Fosker, N., Fraser, A., Garcia, J. L., Garcia, M. J., Goble, A., Goldman, G. H., Gomi, K., Griffith-Jones, S., Gwilliam, R., Haas, B., Haas, H., Harris, D., Horiuchi, H., Huang, J., Humphray, S., Jimenez, J., Keller, N., Khouri, H., Kitamoto, K., Kobayashi, T., Konzack, S., Kulkarni, R., Kumagai, T., Lafon, A., Latge, J. P., Li, W., Lord, A., Lu, C., Majoros, W. H., May, G. S., Miller, B. L., Mohamoud, Y., Molina, M., Monod, M., Mouyna, I., Mulligan, S., Murphy, L., O'Neil, S., Paulsen, I., Penalva, M. A., Pertea, M., Price, C., Pritchard, B. L., Quail, M. A., Rabbinowitsch, E.,

Rawlins, N., Rajandream, M. A., Reichard, U., Renauld, H., Robson, G. D., Rodriguez de, C. S., Rodriguez-Pena, J. M., Ronning, C. M., Rutter, S., Salzberg, S. L., Sanchez, M., Sanchez-Ferrero, J. C., Saunders, D., Seeger, K., Squares, R., Squares, S., Takeuchi, M., Tekaia, F., Turner, G., Vazquez de Aldana, C. R., Weidman, J., White, O., Woodward, J., Yu, J. H., Fraser, C., Galagan, J. E., Asai, K., Machida, M., Hall, N., Barrell, B. and Denning, D. W. (2005). Genomic sequence of the pathogenic and allergenic filamentous fungus *Aspergillus fumigatus*. *Nature.* **438**: 1151-1156.

Nolard, N. (1994). Les liens entre les risques d'aspergillose et la contamination de l'environnement. *Pathol Biol.* **43**: 706-710.

Oberegger, H., Schoeser, M., Zadra, I., Abt, B. and Haas, H. (2001). SREA is involved in regulation of siderophore biosynthesis, utilization and uptake in *Aspergillus nidulans*. *Mol. Microbiol.* **41**: 1077-1089.

Oide, S., Moeder, W., Krasnoff, S., Gibson, D., Haas, H., Yoshioka, K. and Turgeon, B. G. (2006). NPS6, encoding a nonribosomal peptide synthetase involved in siderophore-mediated iron metabolism, is a conserved virulence determinant of plant pathogenic ascomycetes. *Plant Cell.* **18**: 2836-2853.

Oliver, B. G., Panepinto, J. C., Fortwendel, J. R., Smith, D. L., Askew, D. S. and Rhodes, J. C. (2002). Cloning and expression of pkaC and pkaR, the genes encoding the cAMP-dependent protein kinase of Aspergillus fumigatus. *Mycopathologia.* **154**: 85-91.

Ong, S. T., Ho, J. Z., Ho, B. and Ding, J. L. (2006). Iron-withholding strategy in innate immunity. *Immunobiology.* **211**: 295-314.

Orciuolo, E., Stanzani, M., Canestraro, M., Galimberti, S., Carulli, G., Lewis, R., Petrini, M. and Komanduri, K. V. (2007). Effects of *Aspergillus fumigatus* gliotoxin and methylprednisolone on human neutrophils: implications for the pathogenesis of invasive aspergillosis. *J. Leukoc. Biol.* **82**: 839-848.

Ortiz-Maldonado, M., Entsch, B. and Ballou, D. P. (2004). Oxygen reactions in p-hydroxybenzoate hydroxylase utilize the H-bond network during catalysis. *Biochemistry.* **43**: 15246-15257.

Oswald, C., Sander, H. J., Smits, S. H., Bremer, E. and Schmitt, L. (2008). Microseeding – A Powerful Tool for Crystallizing Proteins Complexed with Hydrolyzable Substrates. *Int. J. Mol. Sci.* 1131-1141.

Otwinowski, Z. and Minor, W. (1997). Processing of X-ray diffraction data collected in oscillation mode. *Methods Enzymol.* 307-326.

Pahl, H. L., Krauss, B., Schulze-Osthoff, K., Decker, T., Traenckner, E. B., Vogt, M., Myers, C., Parks, T., Warring, P., Muhlbacher, A., Czernilofsky, A. P. and Baeuerle, P. A. (1996). The immunosuppressive fungal metabolite gliotoxin specifically inhibits transcription factor NF-kappaB. *J. Exp. Med.* **183**: 1829-1840.

Paisley, D., Robson, G. D. and Denning, D. W. (2005). Correlation between in vitro growth rate and in vivo virulence in *Aspergillus fumigatus*. *Med. Mycol.* **43**: 397-401.

Palfey, B. A., Ballou, D. P. and Massey, V. (1997). Flavin conformational changes in the catalytic cycle of p-hydroxybenzoate hydroxylase substituted with 6-azido- and 6-aminoflavin adenine dinucleotide. *Biochemistry.* **36**: 15713-15723.

Palfey, B. A., Ballou, D. P. and Massey, V. (1997). Flavin conformational changes in the catalytic cycle of p-hydroxybenzoate hydroxylase substituted with 6-azido- and 6-aminoflavin adenine dinucleotide. *Biochemistry.* **36**: 15713-15723.

Panepinto, J. C., Oliver, B. G., Fortwendel, J. R., Smith, D. L., Askew, D. S. and Rhodes, J. C. (2003). Deletion of the *Aspergillus fumigatus* gene encoding the Ras-related protein RhbA reduces virulence in a model of Invasive pulmonary aspergillosis. *Infect. Immun.* **71**: 2819-2826.

Paoli, M., Liddington, R., Tame, J., Wilkinson, A. and Dodson, G. (1996). Crystal structure of T state haemoglobin with oxygen bound at all four haems. *J. Mol. Biol.* **256**: 775-792.

Pape, T. and Schneider, T. R. (2004). HKL2MAP: a graphical user interface for phasing with SHELX programs. *J. Appl. Cryst.* **37**: 843-844.

Paris, S., Debeaupuis, J. P., Crameri, R., Carey, M., Charles, F., Prevost, M. C., Schmitt, C., Philippe, B. and Latge, J. P. (2003). Conidial hydrophobins of *Aspergillus fumigatus*. *Appl. Environ. Microbiol.* **69**: 1581-1588.

Parta, M., Chang, Y., Rulong, S., Pinto-DaSilva, P. and Kwon-Chung, K. J. (1994). HYP1, a hydrophobin gene from *Aspergillus fumigatus*, complements the rodletless phenotype in *Aspergillus nidulans*. *Infect. Immun.* **62**: 4389-4395.

Patterson, T. F., Kirkpatrick, W. R. and White, M. (2000). Invasive aspergillosis: disease spectrum, treatment practices, and outcomes., pp. 250-260, Medicine (Baltimore).

Pfaller, M. A., Pappas, P. G. and Wingard, J. R. (2006). Invasive Fungal Pathogens:Current Epidemiological Trends. *Clinical Infectious Diseases* **43**: S3-S14.

Pflugrath, J. W. (2004). Macromolecular cryocrystallography - methods for cooling and mounting protein crystals at cryogenic temperatures. *Methods.* **34**: 415-423.

Philippe, B., Ibrahim-Granet, O., Prevost, M. C., Gougerot-Pocidalo, M. A., Sanchez, P. M., Van der, M. A. and Latge, J. P. (2003). Killing of Aspergillus fumigatus by alveolar macrophages is mediated by reactive oxidant intermediates. *Infect. Immun.* **71**: 3034-3042.

Philpott, C. C. (2006). Iron uptake in fungi: a system for every source. *Biochim. Biophys. Acta.* **1763**: 636-645.

Plattner, H. J., Pfefferle, P., Romaguera, A., Waschutza, S. and Diekmann, H. (1989). Isolation and some properties of lysine N6-hydroxylase from *Escherichia coli* strain EN222. *Biol. Met.* **2**: 1-5.

Plattner, H. J. and Diekmann, H. (1994). Enzymology of siderophore biosynthesis in fungi. In *Metal Ions in Fungi.* (Winkelmann, G. and Winge, D. R., eds), pp. 99-117, New York, New York: Marcel Decker.

Pollack, J. R. and Neilands, J. B. (1970). Enterobactin, an iron transport compound from *Salmonella typhimurium*. *Biochem. Biophys. Res. Commun.* **38**: 989-992.

Ponka, P. (1997). Tissue-specific regulation of iron metabolism and heme synthesis: distinct control mechanisms in erythroid cells. *Blood.* **89**: 1-25.

Ponting, C. P., Schultz, J., Milpetz, F. and Bork, P. (1999). SMART: identification and annotation of domains from signalling and extracellular protein sequences. *Nucleic Acids Res.* **27**: 229-232.

Posey, J. E. and Gherardini, F. C. (2000). Lack of a role for iron in the Lyme disease pathogen. *Science.* **288**: 1651-1653.

Poulsen, L. L. and Ziegler, D. M. (1995). Multisubstrate flavin-containing monooxygenases: applications of mechanism to specificity. *Chem. Biol. Interact.* **96**: 57-73.

Protchenko, O., Shakoury-Elizeh, M., Keane, P., Storey, J., Androphy, R. and Philpott, C. C. (2008). Role of PUG1 in inducible porphyrin and heme transport in *Saccharomyces cerevisiae*. *Eukaryot. Cell.* **7**: 859-871.

Purkayastha, S., Madan, T., Shah, A., Krishnamurthy, H. G. and Sarma, P. U. (2000). Multifunctional antigens of *A. fumigatus* and specific antibodies. *Appl. Biochem. Biotechnol.* **83**: 271-283.

Ramanan, N. and Wang, Y. (2000). A high-affinity iron permease essential for *Candida albicans* virulence. *Science.* **288**: 1062-1064.

Rankin, NE. (1953). Disseminated aspergillosis and moniliasis associated with agranulocytosis and antibiotic therapy. *British medical journal* 918-919.

Ratledge, C. (2007). Iron metabolism and infection. *Food Nutr. Bull.* **28**: S515-S523.

Ray, K., Hines, C. S., Coll-Rodriguez, J. and Rodgers, D. W. (2004). Crystal structure of human thimet oligopeptidase provides insight into substrate recognition, regulation, and localization. *J. Biol. Chem.* **279**: 20480-20489.

Raymond, K. N., Dertz, E. A. and Kim, S. S. (2003). Enterobactin: an archetype for microbial iron transport. *Proc. Natl. Acad. Sci. U. S. A.* **100**: 3584-3588.

Reiss, J. (1976). Mycotoxins in foodstuffs. VI. Formation of sterigmatocystin in bread by *Aspergillus versicolor*. *Z. Lebensm. Unters. Forsch.* **160**: 313-319.

Rementeria, A., Lopez-Molina, N., Ludwig, A., Vivanco, A. B., Bikandi, J., Ponton, J. and Garaizar, J. (2005). Genes and molecules involved in *Aspergillus fumigatus* virulence. *Rev. Iberoam. Micol.* **22**: 1-23.

Rhodes, J. C., Oliver, B. G., Askew, D. S. and Amlung, T. W. (2001). Identification of genes of Aspergillus fumigatus up-regulated during growth on endothelial cells. *Med. Mycol.* **39**: 253-260.

Rhodes, J. C. (2006). *Aspergillus fumigatus*: growth and virulence. *Med. Mycol.* **44**: Suppl 1:S77-81.

Rippon, J. W. (1988). *Medical Mycology: The Pathogenic Fungi and the Pathogenic Actinomycetes.* Philadelphia.

Risse, B., Stempfer, G., Rudolph, R., Schumacher, G. and Jaenicke, R. (1992). Characterization of the stabilizing effect of point mutations of pyruvate oxidase from *Lactobacillus plantarum*: protection of the native state by modulating coenzyme binding and subunit interaction. *Protein Sci.* **1**: 1710-1718.

Romani, L. (2004). Immunity to fungal infections. *Nat. Rev. Immunol.* **4**: 1-23.

Ryerson, C. C., Ballou, D. P. and Walsh, C. (1982). Mechanistic studies on cyclohexanone oxygenase. *Biochemistry.* **21**: 2644-2655.

Saier, M. H., Jr., Beatty, J. T., Goffeau, A., Harley, K. T., Heijne, W. H., Huang, S. C., Jack, D. L., Jahn, P. S., Lew, K., Liu, J., Pao, S. S., Paulsen, I. T., Tseng, T. T. and Virk, P. S. (1999). The major facilitator superfamily. *J. Mol. Microbiol. Biotechnol.* **1**: 257-279.

Sambrook, J. and Russell, D. W. (2000). *Molecular Cloning - A Laboratory Manual* (Cold Spring Harbor: Cold Spring Harbor Laboratory Press).

Santos, R., Buisson, N., Knight, S., Dancis, A., Camadro, J. M. and Lesuisse, E. (2003). Haemin uptake and use as an iron source by *Candida albicans*: role of CaHMX1-encoded haem oxygenase. *Microbiology.* **149**: 579-588.

Schaffner, A., Douglas, H. and Braude, A. (1982). Selective protection against conidia by mononuclear and against mycelia by polymorphonuclear phagocytes in resistance to Aspergillus. Observations on these two lines of defense in vivo and in vitro with human and mouse phagocytes. *J. Clin. Invest.* **69**: 617-631.

Schmitt, H. J., Blevins, A., Sobeck, K. and Armstrong, D. (1990). *Aspergillus* species from hospital air and from patients. *Mycoses.* **33**: 539-541.

Schneider, T. R. and Sheldrick, G. M. (2002). Substructure solution with SHELXD. *Acta Crystallogr. D. Biol. Crystallogr.* **58**: 1772-1779.

Schneider, T. R. and Sheldrick, G. M. (2002). Substructure solution with SHELXD. *Acta Crystallogr. D. Biol. Crystallogr.* **58**: 1772-1779.

Schrettl, M., Bignell, E., Kragl, C., Joechl, C., Rogers, T., Arst, H. N., Jr., Haynes, K. and Haas, H. (2004). Siderophore biosynthesis but not reductive iron assimilation is essential for *Aspergillus fumigatus* virulence. *J. Exp. Med.* **200**: 1213-1219.

Schrettl, M., Bignell, E., Kragl, C., Sabiha, Y., Loss, O., Eisendle, M., Wallner, A., Arst, H. N., Jr., Haynes, K. and Haas, H. (2007). Distinct roles for intra- and extracellular siderophores during *Aspergillus fumigatus* infection. *PLoS. Pathog.* **3**: 1195-1207.

Schryvers, A. B., Bonnah, R., Yu, R. H., Wong, H. and Retzer, M. (1998). Bacterial lactoferrin receptors. *Adv. Exp. Med. Biol.* **443**: 123-133.

Schultz, J., Milpetz, F., Bork, P. and Ponting, C. P. (1998). SMART, a simple modular architecture research tool: identification of signaling domains. *Proc. Natl. Acad. Sci. U. S. A.* **95**: 5857-5864.

Segal, B. H., DeCarlo, E. S., Kwon-Chung, K. J., Malech, H. L., Gallin, J. I. and Holland, S. M. (1998). *Aspergillus nidulans* infection in chronic granulomatous disease. *Medicine (Baltimore).* **77**: 345-354.

Sen, T. Z., Jernigan, R. L., Garnier, J. and Kloczkowski, A. (2005). GOR V server for protein secondary structure prediction. *Bioinformatics.* **21**: 2787-2788.

Sessa, A., Meroni, M., Battini, G., Pitingolo, F., Giordano, F., Marks, M. and Casella, P. (1996). Nosocomial outbreak of *Aspergillus fumigatus* infection among patients in a renal unit? *Nephrol. Dial. Transplant.* **11**: 1322-1324.

Sheldrick, G. M. (2005). High throughput phasing with SHELXC/D/E.

Sheng, D., Ballou, D. P. and Massey, V. (2001). Mechanistic studies of cyclohexanone monooxygenase: chemical properties of intermediates involved in catalysis. *Biochemistry.* **40**: 11156-11167.

Singh, N., Arnow, P. M., Bonham, A., Dominguez, E., Paterson, D. L., Pankey, G. A., Wagener, M. M. and Yu, V. L. (1997). Invasive aspergillosis in liver transplant recipients in the 1990s. *Transplantation.* **64**: 716-720.

Singh, N., Avery, R. K., Munoz, P., Pruett, T. L., Alexander, B., Jacobs, R., Tollemar, J. G., Dominguez, E. A., Yu, C. M., Paterson, D. L., Husain, S., Kusne, S. and Linden, P. (2003). Trends in risk profiles for and mortality associated with invasive aspergillosis among liver transplant recipients. *Clin. Infect. Dis.* **36**: 46-52.

Smart, S. C., Sagar, K. B., el, S. J., Warltier, D. C. and Jones, L. R. (1997). Injury to the Ca2+ ATPase of the sarcoplasmic reticulum in anesthetized dogs contributes to myocardial reperfusion injury. *Cardiovasc. Res.* **36**: 174-184.

Smith, K. D. (2007). Iron metabolism at the host pathogen interface: lipocalin 2 and the pathogen-associated iroA gene cluster. *Int. J. Biochem. Cell Biol.* **39**: 1776-1780.

Soding, J., Biegert, A. and Lupas, A. N. (2005). The HHpred interactive server for protein homology detection and structure prediction. *Nucleic Acids Res.* **33**: W244-W248.

Sonnhammer, E. L., Eddy, S. R. and Durbin, R. (1997). Pfam: a comprehensive database of protein domain families based on seed alignments. *Proteins.* **28**: 405-420.

Sousa, R. (1995). Use of glycerol, polyols and other protein structure stabilizing agents in protein crystallization. *Acta Crystallogr. D. Biol. Crystallogr.* **51**, 271-277.

Spiro, T. G., Allerton, S. F., Renner, J., Terzis, A., Bils, R. and Saltman, P. (1966). The hydrolytic polymerization of iron (III). *J. Am. Chem. Soc.* **8**: 2721-2725.

Stanzani, M., Orciuolo, E., Lewis, R., Kontoyiannis, D. P., Martins, S. L., St John, L. S. and Komanduri, K. V. (2005). *Aspergillus fumigatus* suppresses the human cellular immune response via gliotoxin-mediated apoptosis of monocytes. *Blood.* **105**: 2258-2265.

Stehr, M., Diekmann, H., Smau, L., Seth, O., Ghisla, S., Singh, M. and Macheroux, P. (1998). A hydrophobic sequence motif common to N-hydroxylating enzymes. *Trends Biochem. Sci.* **23** : 56-57.

Stehr, M., Smau, L., Singh, M., Seth, O., Macheroux, P., Ghisla, S. and Diekmann, H. (1999). Studies with lysine N6-hydroxylase. Effect of a mutation in the assumed FAD binding site on coenzyme affinities and on lysine hydroxylating activity. *Biol. Chem.* **380**: 47-54.

Steyn, M. and Rabie, C. J. (1975). Production of sterigmatocystin. *J. Assoc. Off Anal. Chem.* **58**: 622-623.

Sucharitakul, J., Phongsak, T., Entsch, B., Svasti, J., Chaiyen, P. and Ballou, D. P. (2007). Kinetics of a two-component p-hydroxyphenylacetate hydroxylase explain how reduced flavin is transferred from the reductase to the oxygenase. *Biochemistry.* **46**: 8611-8623.

Sugui, J. A., Pardo, J., Chang, Y. C., Zarember, K. A., Nardone, G., Galvez, E. M., Mullbacher, A., Gallin, J. I., Simon, M. M. and Kwon-Chung, K. J. (2007). Gliotoxin is a virulence factor of *Aspergillus fumigatus*: gliP deletion attenuates virulence in mice immunosuppressed with hydrocortisone. *Eukaryot. Cell.* **6**: 1562-1569.

Sugui, J. A., Kim, H. S., Zarember, K. A., Chang, Y. C., Gallin, J. I., Nierman, W. C. and Kwon-Chung, K. J. (2008). Genes differentially expressed in conidia and hyphae of *Aspergillus fumigatus* upon exposure to human neutrophils. *PLoS. ONE.* **3**: e2655.

Suh, J. K., Poulsen, L. L., Ziegler, D. M. and Robertus, J. D. (1996). Molecular cloning and kinetic characterization of a flavin-containing monooxygenase from *Saccharomyces cerevisiae*. *Arch. Biochem. Biophys.* **336**: 268-274.

Sun, L. and Yagasaki, M. (2003). Screen for Oxidases by Detection of Hydrogen Peroxide with Horseradish Peroxidase. In *Directed Enzyme Evolution*, pp. 177-182, Humana Press.

Sutton, P., Waring, P. and Mullbacher, A. (1996). Exacerbation of invasive aspergillosis by the immunosuppressive fungal metabolite, gliotoxin. *Immunol. Cell Biol.* **74**: 318-322.

Szutowicz, A., Kobes, R. D. and Orsulak, P. J. (1984). Colorimetric assay for monoamine oxidase in tissues using peroxidase and 2,2'-azinodi(3-ethylbenzthiazoline-6-sulfonic acid) as chromogen. *Anal. Biochem.* **138**: 86-94.

Takase, H., Nitanai, H., Hoshino, K. and Otani, T. (2000). Requirement of the *Pseudomonas aeruginosa* tonB gene for high-affinity iron acquisition and infection. *Infect. Immun.* **68**: 4498-4504.

Takigawa, M., Enomoto, M., Nishida, Y., Pan, H. O., Kinoshita, A. and Suzuki, F. (1990). Tumor angiogenesis and polyamines: alpha-difluoromethylornithine, an irreversible inhibitor of ornithine decarboxylase, inhibits B16 melanoma-induced angiogenesis in ovo and the proliferation of vascular endothelial cells in vitro. *Cancer Res.* **50**: 4131-4138.

Taylor, A. B., Stoj, C. S., Ziegler, L., Kosman, D. J. and Hart, P. J. (2005). The copper-iron connection in biology: structure of the metallo-oxidase Fet3p. *Proc. Natl. Acad. Sci. U. S. A.* **102**: 15459-15464.

Taylor, G. (2003). The phase problem. *Acta Crystallogr. D. Biol. Crystallogr.* **59**: 1881-1890.

Tekaia, F. and Latgé, J. P. (2005). *Aspergillus fumigatus*: saprophyte or pathogen? *Curr. Opin. Microbiol.* **8**: 385-392.

Tenholder, M. F. (1985). The many faces of pulmonary aspergillosis. *Prim. Care.* **12**: 353-368.

Terwilliger, T. C. (2003). SOLVE and RESOLVE: automated structure solution and density modification. *Methods Enzymol.* **374**: 22-37.

Terwilliger, T. C., Grosse-Kunstleve, R. W., Afonine, P. V., Moriarty, N. W., Zwart, P. H., Hung, L. W., Read, R. J. and Adams, P. D. (2008). Iterative model building, structure refinement and density modification with the PHENIX AutoBuild wizard. *Acta Crystallogr. D. Biol. Crystallogr.* **64**: 61-69.

Thariath, A., Socha, D., Valvano, M. A. and Viswanatha, T. (1993). Construction and biochemical characterization of recombinant cytoplasmic forms of the IucD protein (lysine:N6-hydroxylase) encoded by the pColV-K30 aerobactin gene cluster. *J. Bacteriol.* **175**: 589-596.

Thau, N., Monod, M., Crestani, B., Rolland, C., Tronchin, G., Latge, J. P. and Paris, S. (1994). rodletless mutants of *Aspergillus fumigatus*. *Infect. Immun.* **62**: 4380-4388.

Thieken, A. and Winkelmann, G. (1992). Rhizoferrin: a complexone type siderophore of the Mucorales and entomophthorales (Zygomycetes). *FEMS Microbiol. Lett.* **73**: 37-41.

Thrane, C., Kaufmann, U., Stummann, B. M. and Olsson, S. (2004). Activation of caspase-like activity and poly (ADP-ribose) polymerase degradation during sporulation in *Aspergillus nidulans*. *Fungal. Genet. Biol.* **41**: 361-368.

Tomee, J. F., Wierenga, A. T., Hiemstra, P. S. and Kauffman, H. K. (1997). Proteases from *Aspergillus fumigatus* induce release of proinflammatory cytokines and cell detachment in airway epithelial cell lines. *J. Infect. Dis.* **176**: 300-303.

Tomlinson, G., Cruickshank, W. H. and Viswanatha, T. (1971). Sensitivity of substituted hydroxylamines to determination by iodine oxidation. *Anal. Biochem.* **44**: 670-679.

Tong, L. and Rossmann, M. G. (1997). Rotation function calculations with GLRF program. *Methods Enzymol.* **276**:594-611.

Tong, L. (2001). How to take advantage of non-crystallographic symmetry in molecular replacement: 'locked' rotation and translation functions. *Acta Crystallogr. D. Biol. Crystallogr.* **57**: 1383-1389.

Trakhanov, S. and Quiocho, F. A. (1995). Influence of divalent cations in protein crystallization. *Protein Sci.* **4**: 1914-1919.

Tsai, H. F., Chang, Y. C., Washburn, R. G., Wheeler, M. H. and Kwon-Chung, K. J. (1998). The developmentally regulated alb1 gene of *Aspergillus fumigatus*: its role in modulation of conidial morphology and virulence. *J. Bacteriol.* **180**: 3031-3038.

Vaguine, A. A., Richelle, J. and Wodak, S. J. (1999). SFCHECK: a unified set of procedures for evaluating the quality of macromolecular structure-factor data and their agreement with the atomic model. *Acta Crystallogr. D. Biol. Crystallogr.* **55**: 191-205.

van Berkel, W. J., Kamerbeek, N. M. and Fraaije, M. W. (2006). Flavoprotein monooxygenases, a diverse class of oxidative biocatalysts. *J. Biotechnol.* **124**: 670-689.

van der Helm, D. and Winkelmann, G. (1994). Hydroxamates and polycarboxylates as iron transport agents (siderophores) in fungi. In *Metal Ions in Fungi* (Winkelmann, G. and Winge, D. R., eds), pp. 39-98, Marcel Dekker, New York.

van der Laan, J. M. (1986). Dissertation. Univ. of Groningen, The Netherlands, Groningen.

Visca, P., Ciervo, A. and Orsi, N. (1994). Cloning and nucleotide sequence of the pvdA gene encoding the pyoverdin biosynthetic enzyme L-ornithine N5-oxygenase in *Pseudomonas aeruginosa*. *J. Bacteriol.* **176**: 1128-1140.

Voget, C. E., Mazza, L. A. and Balatti, A. P. (1988). Production of glucose oxidase using *Aspergillus niger* NRRL3. *Rev. Latinoam. Microbiol.* **30**: 53-57.

Vriend, G. (1990). WHAT IF: a molecular modeling and drug design program. *J. Mol. Graph.* **8**: 52-6, 29.

Vuillard, L., Rabilloud, T., Leberman, R., Berthet-Colominas, C. and Cusack, S. (1994). A new additive for protein crystallization. *FEBS Lett.* **353**: 294-296.

Vuillard, L., Braun-Breton, C. and Rabilloud, T. (1995). Non-detergent sulphobetaines: a new class of mild solubilization agents for protein purification. *Biochem. J.* **305**: 337-343.

Walsh, T. J., Petraitis, V., Petraitiene, R., Field-Ridley, A., Sutton, D., Ghannoum, M., Sein, T., Schaufele, R., Peter, J., Bacher, J., Casler, H., Armstrong, D., Espinel-Ingroff, A., Rinaldi, M. G. and Lyman, C. A. (2003). Experimental pulmonary aspergillosis due to *Aspergillus terreus*: pathogenesis and treatment of an emerging fungal pathogen resistant to amphotericin B. *J. Infect. Dis.* **188**: 305-319.

Walsh, T. J., Roilides, E., Cortez, K., Kottilil, S., Bailey, J. and Lyman, C. A. (2005). Control, immunoregulation, and expression of innate pulmonary host defenses against *Aspergillus fumigatus*. *Med. Mycol.* **43**: Suppl 1:S165-72.

Walter, T. S., Meier, C., Assenberg, R., Au, K. F., Ren, J., Verma, A., Nettleship, J. E., Owens, R. J., Stuart, D. I. and Grimes, J. M. (2006). Lysine methylation as a routine rescue strategy for protein crystallization. *Structure.* **14**: 1617-1622.

Wang, J., Ortiz-Maldonado, M., Entsch, B., Massey, V., Ballou, D., and Gatti, D. L. (2002). Protein and ligand dynamics in 4-hydroxybenzoate hydroxylase. *Proc. Natl. Acad. Sci. U S A.* **99**: 608-613.

Ward, P. P., Uribe-Luna, S. and Conneely, O. M. (2002). Lactoferrin and host defense. *Biochem. Cell Biol.* **80**: 95-102.

Waring, P., Eichner, R. D., Mullbacher, A. and Sjaarda, A. (1988). Gliotoxin induces apoptosis in macrophages unrelated to its antiphagocytic properties. *J. Biol. Chem.* **263** 18493-18499.

Wasylnka, J. A. and Moore, M. M. (2000). Adhesion of *Aspergillus* species to extracellular matrix proteins: evidence for involvement of negatively charged carbohydrates on the conidial surface. *Infect. Immun.* **68**: 3377-3384.

Wasylnka, J. A., Simmer, M. I. and Moore, M. M. (2001). Differences in sialic acid density in pathogenic and non-pathogenic *Aspergillus* species. *Microbiology.* **147**: 869-877.

Wasylnka, J. A. and Moore, M. M. (2002). Uptake of *Aspergillus fumigatus* Conidia by phagocytic and nonphagocytic cells in vitro: quantitation using strains expressing green fluorescent protein. *Infect. Immun.* **70**: 3156-3163.

Wasylnka, J. A. and Moore, M. M. (2003). *Aspergillus fumigatus* conidia survive and germinate in acidic organelles of A549 epithelial cells. *J. Cell Sci.* **116**: 1579-1587.

Wasylnka, J. A., Hissen, A. H., Wan, A. N. and Moore, M. M. (2005). Intracellular and extracellular growth of *Aspergillus fumigatus*. *Med. Mycol.* **43**: Suppl 1: S27-S30.

Wheaton, SW. (1890). Case primarily of tubercle, in which a fungus (aspergillus) grew in the bronchi and lung, stimulating actinomycosis. *Path Trans* **41**: 34-37.

Wiencek, J. M. (1999). New strategies for protein crystal growth. *Annu. Rev. Biomed. Eng.* **1**: 505-534.

Winkelmann, G. (1993). Kinetics, energetics, and mechanisms of siderophore iron transport in fungi. In *Iron Chelation in Plants and Soil Microorganisms.* (Barton, L. L. and Hemmings, B. C., eds), pp. 219-239, New York: New York Academic Press. Ref Type: Book Chapter

Woo, P. C., Chan, C. M., Leung, A. S., Lau, S. K., Che, X. Y., Wong, S. S., Cao, L. and Yuen, K. Y. (2002). Detection of cell wall galactomannoprotein Afmp1p in culture supernatants of *Aspergillus fumigatus* and in sera of aspergillosis patients. *J. Clin. Microbiol.* **40**: 4382-4387.

Yancey, R. J., Breeding, S. A. and Lankford, C. E. (1979). Enterochelin (enterobactin): virulence factor for *Salmonella typhimurium*. *Infect. Immun.* **24**: 174-180.

Youngchim, S., Morris-Jones, R., Hay, R. J. and Hamilton, A. J. (2004). Production of melanin by *Aspergillus fumigatus*. *J. Med. Microbiol.* **53**: 175-181.

Zhao, Y., Christensen, S. K., Fankhauser, C., Cashman, J. R., Cohen, J. D., Weigel, D. and Chory, J. (2001). A role for flavin monooxygenase-like enzymes in auxin biosynthesis. *Science.* **291**: 306-309.

Zhu, D. Y., Zhu, Y. Q., Xiang, Y. and Wang, D. C. (2005). Optimizing protein crystal growth through dynamic seeding. *Acta Crystallogr. D. Biol. Crystallogr.* **61**: 772-775.

Ziegler, D. M. and Poulsen, L. L. (1998). Catalytic mechanism of FMO-catalyzed N- and S-oxidations. In *Drug Metabolism. Towards the Next Millennium.* (Gooderham, N., ed), pp. 30-38, IOS Press, Amsterdam.

Zwart, P. H., Grosse-Kunstleve, R. W. and Adams, P. D. (2005). Xtriage and Fest: automatic assessment of X-ray data and substructure structure factor estimation.

Danksagung

Prof. Dr. Dirk Heinz danke ich herzlich für die Zeit in seiner Arbeitsgruppe und die Möglichkeit meine Promotionsarbeit unter hervorragenden Arbeitsbedingungen durchführen zu können. Sein Interesse an meinem Thema sowie seine stets offene Art und Diskussionsbereitschaft weiß ich sehr zu schätzen. Weiter möchte ich mich dafür bedanken, dass ich an zahlreichen interessanten Tagungen und Konferenzen teilnehmen und meine Arbeit mittels Postern und Vorträgen präsentieren durfte. Letzteres hat dazu beigetragen, dass ich mich nicht nur fachlich sondern auch persönlich weiter entwickeln konnte.

Prof. Dr. Michael Steinert danke ich sehr herzlich für die bereitwillige Übernahme des Zweitgutachtens.

Bei Prof. Dr. Ralf Mendel bedanke ich mich herzlich für die Übernahme des Prüfungsvorsitzes.

Bei Prof. Dr. Hubertus Haas möchte ich mich für die hervorragende Kooperation bedanken. Auch wusste er jedes „Angst“-röm verbesserte Auflösung zu schätzen und hat darüber hinaus mein Herz für Schimmelpilze erwärmen können.

Dr. Wolf-Dieter Schubert möchte ich ganz herzlich für seine nicht versiegen wollende Hilfsbereitschaft im reziproken wie im realen Raum danken. Ohne ihn hätte ich die unzähligen Stunden im Grafikraum nicht so unbeschadet überstanden. Für seine unendliche Geduld und dafür, dass er sich immer und ausnahmslos Zeit genommen hat, wenn ich Fragen hatte oder einen Rat brauchte, möchte ich mich ganz besonders bedanken.

Prof. Dr. Jürgen Wehland möchte ich für die Teilnahem und und seine Unterstützung im Rahmen meines Thesis Kommittees danken.

Ganz besonders möchte ich mich bei den Organisatoren und Teilnehmern von HEC9 und HEC10 bedanken. Das Interesse an meinem Thema, und die zahlreichen Diskussionen, Tipps, Tricks und Hilfestellungen, die sich im Rahmen der Konferenz entwickelten,

haben ganz wesentlich dazu beigetragen, dass das SidA Modell mittlerweile einer Proteinstruktur nahekommt.

Prof. Dr. Ralf Ficner und Prof. Dr. Dietmar Manstein möchte ich dafür danken, dass ich meine Kristalle an den Röntgenanlagen ihrer Labors testen durfte.

Bei Dr. Hartmut Niemann möchte ich mich ganz herzlich für viele fachliche Hilfestellungen und den heissen Tipp mit 1W4X bedanken. Danke auch für die vielen Diskussionen während der gemeinsamen allwöchentlichen Laufrunden, aus denen dann auch das ein oder andere Experiment hervorgegangen ist.

Dr. Thomas Wollert und Dr. Gregor Hagelüken gilt ein ganz besonders dickes Dankeschön! Die gemeinsame Zeit im Bü-mro und die vielen fachlichen wie fachfremden Diskussionen, werden mir in unvergesslicher Erinnerung bleiben. Thomas möchte ich besonders für die Einarbeitungs- und Eingewöhnungszeit in der SB danken und für den Nervenkitzel beim Zellaufschluss mittels Frenchpress und den ITC-Messungen. Gregor gilt ein besonderer Dank für die mentale und fachliche Unterstützung während des 48 h MAD-Experiments am DESY. Es gäbe noch zahlreiche Dinge, die ich an dieser Stelle aufführen müsste - der von euch titulierte „Wortspeicher“ ist noch längst nicht leer!

Katrin Rand und Lilia Polle möchte ich ganz herzlich für die vielen kleinen und großen Unterstützungen wärend meiner Doktorarbeit danken und für die wunderbare Arbeitsatmosphäre in unserem Büro. Die Zusammenarbeit mit euch war immer harmonisch und hat mir sehr viel Spaß gemacht. Bei Katrin möchte ich mich insbesondere bedanken für ihren Löwen-starken Einsatz bei den Messungen am ESRF und für die Einführung in die exotische Welt des anaeroben Arbeitens.

Dr. Joachim Reichelt möchte ich ganz herzlich für die zahlreichen Tipps und häufigen Hilfestellung im Grafikraum danken und dafür, dass Nobby angeschafft wurde.

Bei Kevin Walkling möchte ich mich ganz herzlich für seine Unterstützung während der letzten Wochen meiner Doktorarbeit bedanken. Dies gilt insbesondere für die Klonierung und Aufreinigung der SidAY404S Variante.

Ulrich Wiesand danke ich herzlich für seine bedingungslose Hilfsbereitschaft insbesondere bei Fragen Rund um die Chemie.

Kathrin Lisson möchte ich für die Beiträge und Erfahrungen danken, die im Rahmen ihrer Diplomarbeit entstanden sind.

Bei Rita Getzlaff möchte ich mich für die N-terminalen Sequenzierungen bedanken.

Ute Widow und Sabine Schmidt - die guten Seelen der SB. Ich möchte ich mich ganz herzlich dafür bedanken, dass der Laboralltag durch euch so reibungslos ablaufen konnte – und natürlich auch für die spitzen Atmosphäre während der Arbeit, drum herum und zwischendrin.

Dr. Victor Wray und Dr. Joop van den Heuvel möchte ich für die zahlreichen Motivationsschübe wärend der dunkleren Phasen meiner Arbeit danken.

Dr. Yvonne Carius danke ich für ihre Hilfsbereitschaft beim Enttwinnen, die fachliche Unterstützung und netten Worte während der letzten Wochen des Zusammenschreibens.

Weiterer Dank gilt: Christian Strube, Boris Grujic, Dr. Maike Bublitz, Dr. Alexander Eberth, Daniela Gebauer, Nadine Konisch, Stephanie Schulz, Ute Grumer, Christine Bentz, Carolin Schaper, Uwe Wengler, Steffen Meyer, Dr. Birgit Hofmann, Dr. Hans-Jürgen Hecht, Dr. Björn Klink, Claudia Hanko, Dr. Manfred Nimtz und Agnes Zimmer.

Meinen Eltern und ganz besonders meinem Bruder Thomas möchte ich für die Unterstützung und den Rückhalt während der gesamten Doktorarbeit danken.

Meinem Mann Norbert gebührt ein ganz besonders großes DANKESCHÖN. Ohne ihn hätte ich niemals eineinhalb Doktorarbeiten durchstehen können und er ist „Schuld“ daran, dass ich es doch noch bis hierhin geschafft habe. Lieber Norbert, für das Fädenziehen im Hintergrund, die Absorption meiner arbeitsbedingt oft schlechten Laune und dafür, dass du mich nun fast vier Jahre mit einem Protein namens SidA teilen musstest, möchte ich mich innigst bei dir bedanken. Auch für deine Mühe beim Korrekturlese-Marathon gebührt dir ein besonderes Dankeschön! Die vielen anderen großen und kleinen Dinge aufzuzählen, die du in dieser Zeit für mich getan hast, würden sicherlich weit mehr als 169 Seiten füllen.

Appendix

A.1 SidA Activity Resembles that of IucD and PvdA

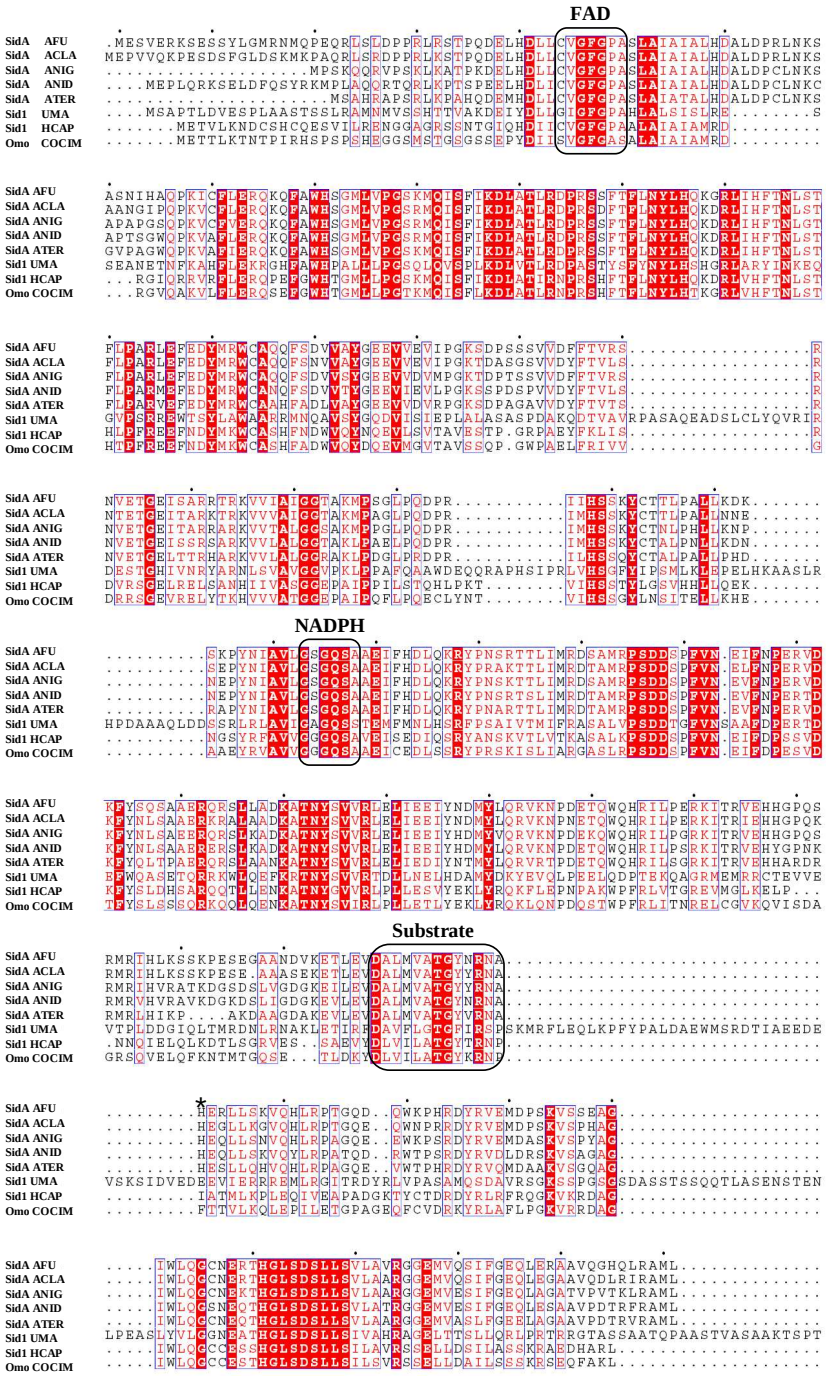

Figure A-1: Sequence alignment of SidA orthologs of different fungal species. AFU: *A. fumigatus*, ACLA: *A. clavatus*, ANIG: *A. niger*, ANID: *A. nidulans*, ATER: *A. terreus*, UMA: *Ustilago maydis*, HCAP: *Histoplasma capsulatum*, COCIM: *Coccidioides immitis*. Omo: ornithine monooxygenase. Nucleotide and putative substrate binding sites are marked by black boxes. The asterisk (*) marks His412 of *A. fumgatus* SidA that is part of the putative substrate binding motif.

A.2 The Flavin Cofactor

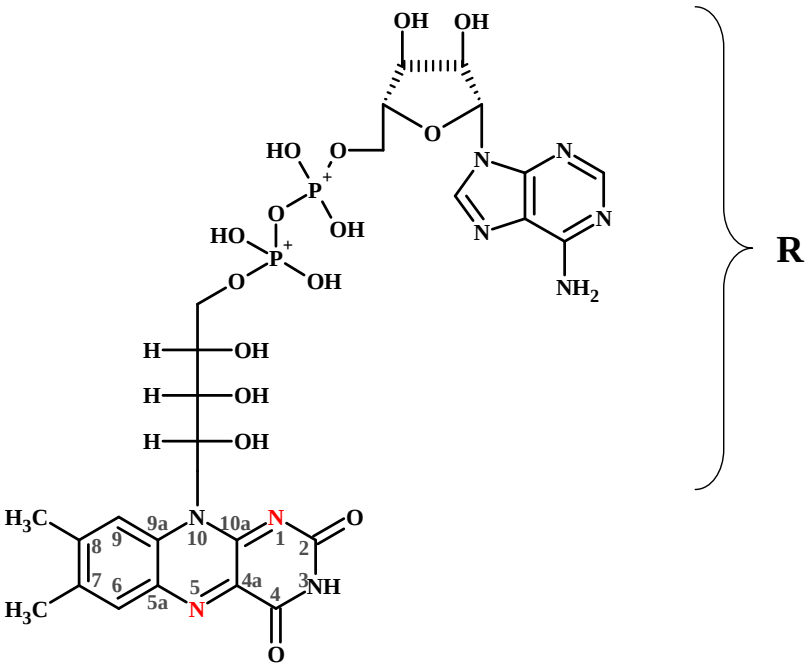

Figure A-2: Structure of the flavin adenine dinucleotide (FAD) cofactor. The conventional numbering scheme of the isoalloxazine ring is shown. Nitrogen atoms involved in hydrogen transfer during reduction by NADPH are highlighted in red. R: adenosine monophosphate and ribitol moiety.

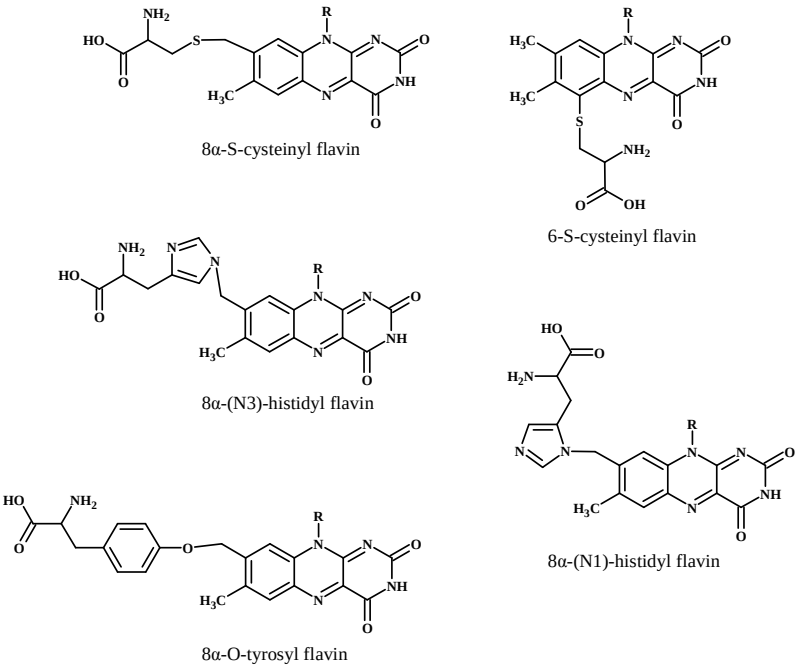

Figure A-3: Structures of the five known covalent flavin linkages to amino acids found in flavoenzymes.

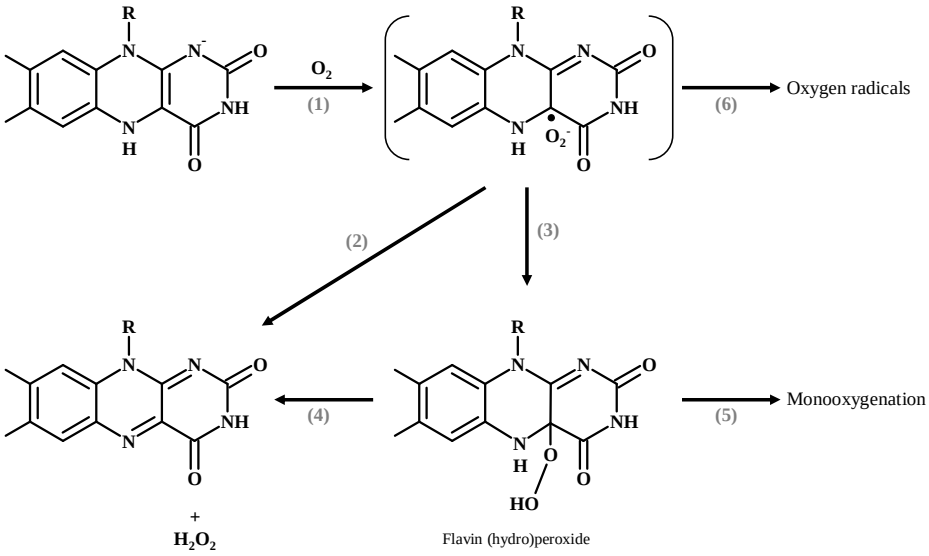

Figure A-4: Possible reaction routes of the two-electron reduced flavin cofactor with oxygen. (1) One-electron transfer reaction from the reduced flavin to molecular oxygen and formation of the semi-reduced flavin superoxide anion. (2) and (4) Formation of hydrogen peroxide. (3) Formation of the C4a-hydroperoxy-flavin. Reaction pathways (5) and (6) lead to the formation of oxygenated products or oxygen radicals, respectively. Scheme adopted from Mattevi (2006) and modified.

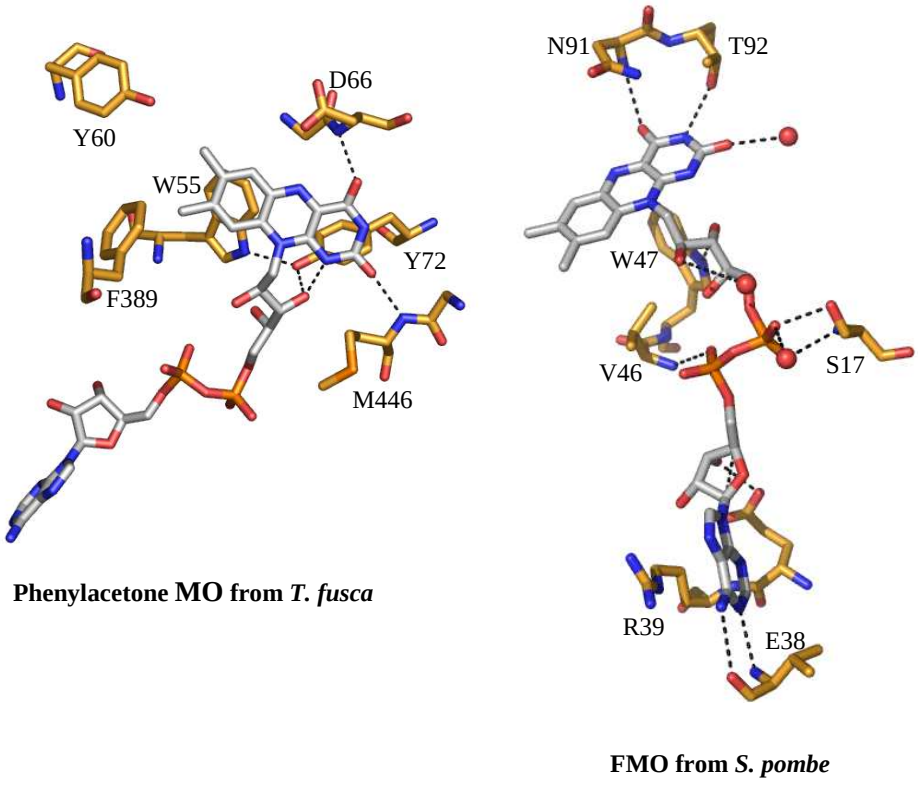

Phenylacetone MO from *T. fusca*

FMO from *S. pombe*

Figure A-5: Hydrogen bonding between FAD and amino acid residues in Phenylacetone monooxygenase from *T. fusca* and FMO from *S. pombe*. Tight binding between protein and cofactor is attributed to a network of hydrogen bonds (dashed lines) between FAD and protein backbone atoms or side chains. Water molecules are displayed as red spheres. For FAD nomenclature compare Figure A-2.

A.3 Data Collection

Table A-1: Overview of X-ray diffraction potential from different SidA crystals.

SidA variant	X-ray source	Max. Resolution	Space group	Cell [Å]	V_M [Å^3/Da]*	Monomers /AU	Solvent
A. fumigatus	DESY, X12	4.8 Å	$P222_1$	a = 75 b = 88 c = 169	2.5	2	49 %
A. nidulans	DESY, BW7a	4.6 Å	P222	a = 164 b = 100 c = 274	2.4	8	49 %
A. nidulans	DESY, X12	4.0 Å	P3	a = 146 b = 146 c = 200	2.7	8	54 %
A. nidulans SeMet	DESY, X12	3.5 Å	$P3_121$	a = 148 b = 148 c = 209	2.9	4	58 %
A. nidulans C151S	ESRF, ID 14-2	3.2 Å	$P3_121$	a = 148 b = 148 c = 209	2.9	4	58 %
A. nidulans	ESRF, ID 23-1	3.2 Å	$P3_121$	a = 148 b = 148 c = 208	2.9	4	58 %

Table A-2: Data set of a wild-type SidA crystal used in MR calculations.

Diffraction data	Native SidA
Beamline	ID 23-1 (ESRF)
Wavelength [Å]	0.90000
Unit cell [Å]	147.9, 147.9, 207.7
V_M [Å^3/Da]	2.9
Monomers/AU	4
Solvent [%]	58 %
Space goup	$P3_121$
Resolution range [Å]	48.0–3.2
Mosaicity [°]	0.66
Completeness [%]	99.9 (99.7)
Redundancy	5.2 (4.9)
Unique reflections	45013 (6465)
Wilson B-factor [Å^2]	75.3
I/σ	11 (2.0)
R_{merge} [%]	4.2 (39.8)

A.4 Model Building

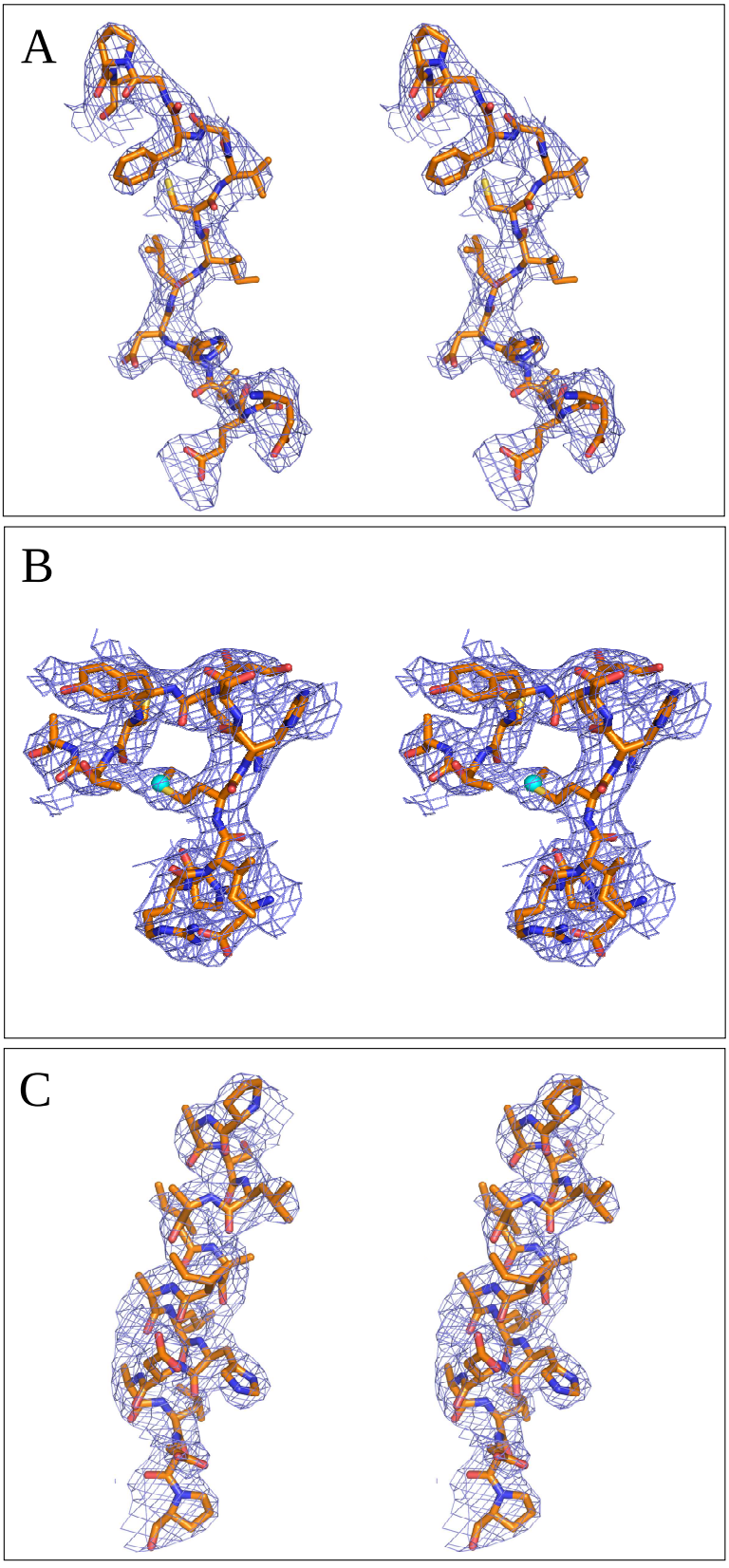

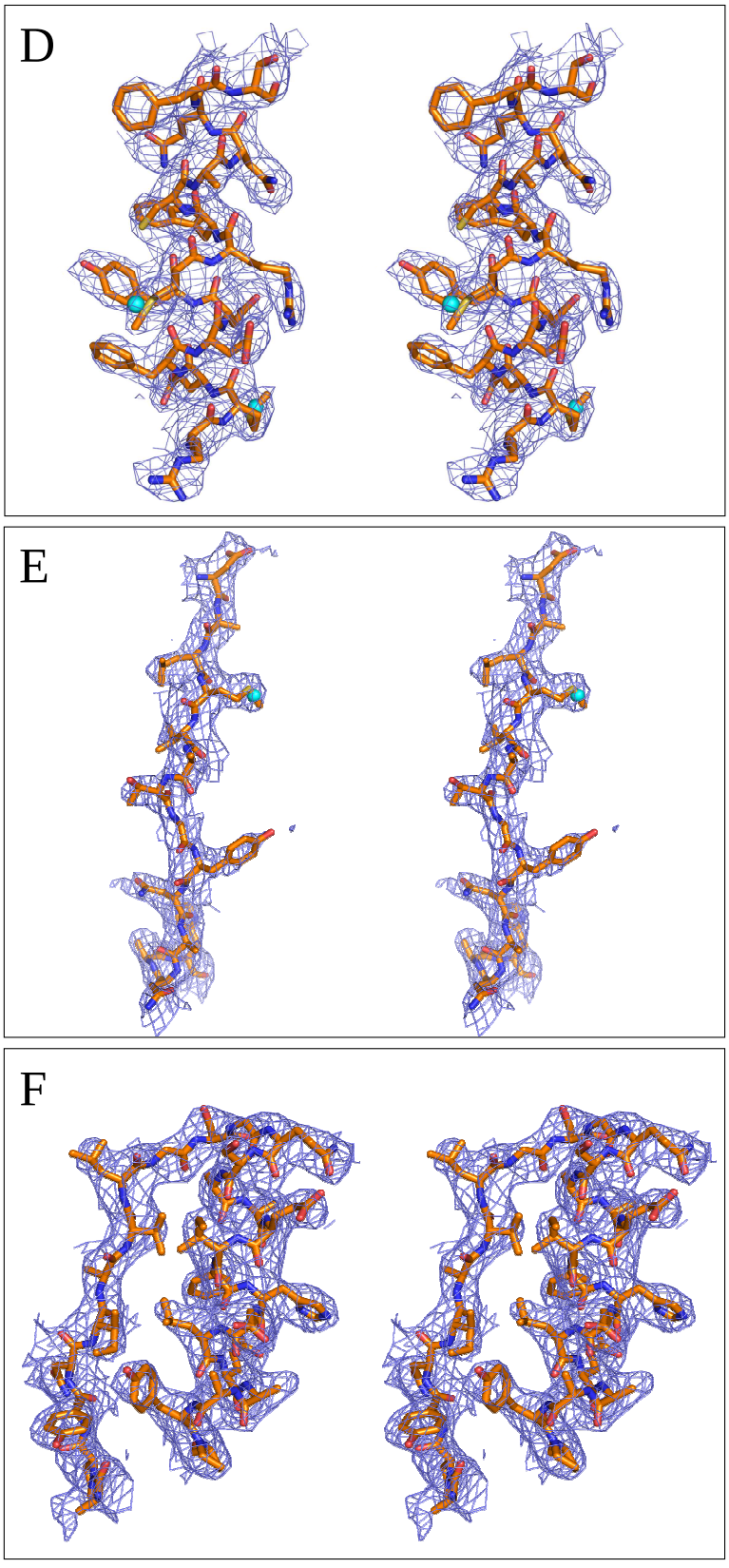
D
E
F

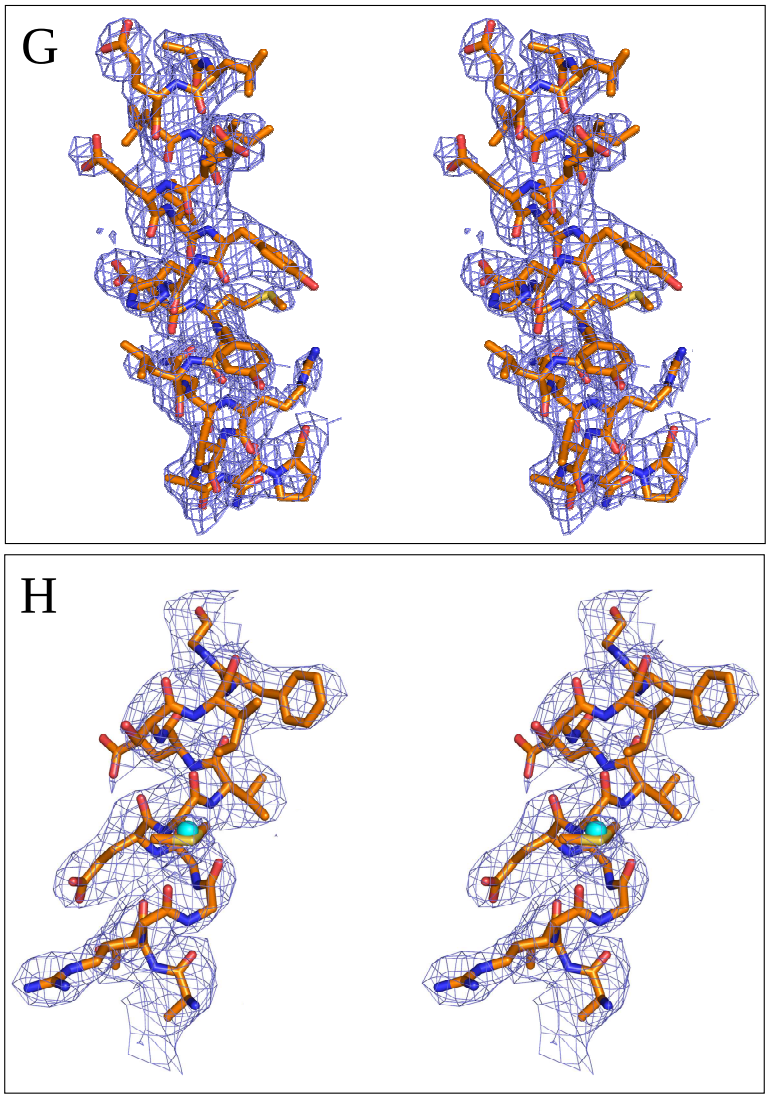

Figure A-6: Stereo view of selected regions in the SidA protomer with refined electron density. Panels A-H refer to respective figures on page 83 (section 3.5). The (2Fo-Fc)-map is shown as blue mesh and is contoured at 1.0 σ. SeMet-sites identified during phase calculation are shown as cyan spheres. (A) Glu34–Ala47 including the FAD binding motif; (B) Sequence stretch with FMO-identifying motif (Arg22-Ala232); (C) α-helix (I) (Ala47-Pro61); (D) α-helix (II) (Arg141-Phe155); (E) Sequence stretch Asp396-His409 including the ATGY motif; (F) Pro243-Pro267, including the NADPH-binding motif; (G) α-helix (IV) (Arg325-Pro344); (H) α-helix (V) (Ala469-Gly481).

A.5 The FMO from *Methylophaga sp*.

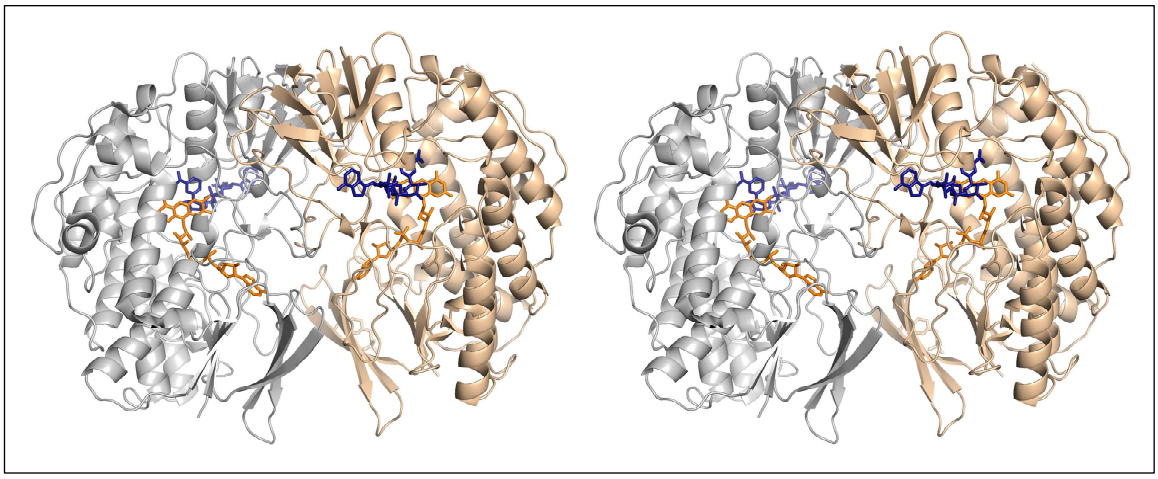

Figure A-7: Stereo view of the mFMO-dimer (PDB entry: 2vq7). The monomer's active sites (defined by the position of the FAD isoalloxazine ring) face each other via their convex sides. $NADP^+$ and FAD are shown as sticks in orange and blue, respectively.

Table of Figures

Figure 1-1: *Aspergillus fumigatus* morphology. 4
Figure 1-2: *Aspergillus* spp. pathogenicity spectrum. 5
Figure 1-3: Infection cycle of *Aspergillus* spp. leading to invasive aspergillosis (IA)..... 6
Figure 1-4: Key reactions of iron with reactive oxygen species..... 9
Figure 1-5: Schematic presentation of iron uptake systems in (A) *A. fumigatus* and (B) *S. cerevisiae*..... 10
Figure 1-6: Crystal structures of haemoglobin and ferritin. 12
Figure 1-7: Bacterial siderophores..... 13
Figure 1-8: Chemical structures of the *A. fumigatus* siderophores N', N'', N'''-triacetylfusarinine C and ferricrocin. 16
Figure 1-9: Schematic representation of the postulated *A. fumigatus* siderophore biosynthetic pathway..... 17
Figure 1-10: Growth phenotypes of *A. fumigatus* wild type and mutant strains. 18
Figure 1-11: Schematic presentation of the SidA domain structure (A) and the hydroxylation reaction catalyzed by SidA (B)..... 20
Figure 1-12: Theoretical scheme of the presumed SidA catalytic cycle. 21
Figure 2-1: Iodine oxidation assay for quantification of hydroxylated amines..... 30
Figure 2-2: Enzyme coupled assay for detecting H_2O_2 formation..... 31
Figure 3-1: Alignment of SidA from *A. fumigatus* (AFU) and SidA from *A. nidulans* (ANI)..... 38
Figure 3-2: Purification of SidA via Ni-NTA affinity chromatography..... 40
Figure 3-3: Ion exchange chromatography..... 41
Figure 3-4: SDS-PAGE of IEC-peak fractions. (A) Peak fractions of the IEC run are yellow due to bound FAD. (B) First lane: protein standard, second lane: flowthrough fraction..... 42
Figure 3-5: Gel permeation chromatography with IEC-purified SidA..... 42
Figure 3-6: Calibration curve of an analytical GPC. 43
Figure 3-7: Catalytic pH optimum of SidA. 44
Figure 3-8: Michaelis-Menten kinetics of $SidA^{AF}$ and $SidA^{AN}$ at different L-ornithine concentrations. 45
Figure 3-9: Detection of hydroxylated product formation by means of the iodine oxidation assay. 46
Figure 3-10: Absorbance spectra of SidA..... 48
Figure 3-11: H_2O_2 production of SidA. 49
Figure 3-12: Kinetic analysis of the intrinsic SidA NADPH oxidase activity. 49
Figure 3-13: $SidA^{AF}$ crystals..... 51
Figure 3-14: $SidA^{AN}$ crystals obtained after screening..... 52
Figure 3-15: Optimized $SidA^{AN}$ crystals. 53
Figure 3-16: Crystals obtained with SidA E311S/E313A/K317A/K320S. 54
Figure 3-17: GPC of SidA modified by methylation..... 54
Figure 3-18: Inferred location of SidA cysteine residues based on the crystal structure of PAMO..... 55
Figure 3-19: Non-reducing SDS-PAGE of purified SidA..... 56
Figure 3-20: Aerobically versus anaerobically grown SidA crystals. 57

Figure 3-21: Proteolytic degradation of SidA. 58
Figure 3-22: Crystals of $SidA^{AN}$ variants R311S (A) and R16S. 58
Figure 3-23: Overview of identified protease cleavage sites and predicted disordered loops within $SidA^{AN}$. 59
Figure 3-24: $SidA^{AN}$ crystals grown under vapor diffusion with a layer of oil placed over the reservoir solution. 60
Figure 3-25: SidA crystals that have been grown within a matrix of low-melting agarose. 61
Figure 3-26: Comparison of diffraction images before (A) and after (B) cryo-cooling of a $SidA^{AN}$ crystal. 62
Figure 3-27: Streak seeding. 63
Figure 3-28: Self-rotation function of a SidA crystal at $\kappa = 180^{o}$. 64
Figure 3-29: Pseudo-precession image of the *h0l*-plane of the peak data set of a SidA crystal. 65
Figure 3-30: X-ray fluorescence scan at the Se K-absorption edge. 69
Figure 3-31: SHELXC data statistics. 71
Figure 3-32: Se-substructure solution with SHELXD. 72
Figure 3-33: SHELXE output and first experimentally determined electron density map. 73
Figure 3-34: Non-crystallographic symmetry operators. 74
Figure 3-35: Experimental electron density map with NCS related Se sites. 75
Figure 3-36: Density modification of experimental data 76
Figure 3-37: Comparison of the electron density in a β-sheet region of SidA subunits A and D 77
Figure 3-38: Sequence-based secondary structure prediction for SidA and location of SeMet sites. 78
Figure 3-39: DM-modified experimental electron density map at 3.2 Å resolution. 79
Figure 3-40: Electron density maps for the flavin-cofactor in SidA subunits A-D. 80
Figure 3-41: Selected regions in the SidA protomer with refined electron density. 82
Figure 3-42: Ramachandran plot of the current SidA model. 84
Figure 3-43: Overview of secondary structure motifs of the current SidA structural model. 86
Figure 3-44: Refined, partial structural model of the SidA protomer. 88
Figure 3-45: DALI search results. 91
Figure 3-46: Superposition of the SidA structural model with homologous structures found by DALI. 92
Figure 3-47: The FAD-binding domain. 93
Figure 3-48: Conformation of FAD in SidA structural homologs. 94
Figure 3-49: Overview of the NADPH-binding site at the domain interface. 95
Figure 3-50: Presumed substrate binding region of SidA. 96
Figure 3-51: Surface representation of the SidA tetramer. 97
Figure 3-52: Surface representation of the geometric arrangement of the SidA tetramer. 98
Figure 3-53: Stereo view of tetrameric SidA with bound FAD. 99
Figure 3-54: Cysteine residues and disulfide bridges within the SidA structure. 100
Figure 3-55: Sequence alignment of SidA and PvdA. 101

Figure 3-56: PvdA purification steps: Ni-NTA affinity chromatography (A) and IEC (B). 102
Figure 3-57: Ion exchange chromatography. 103
Figure 3-58: Hydroxylation activity of PvdA. 104
Figure 3-59**:** DLS measurement with purified PvdA. 104
Figure 3-60: GPC with IEC-purified and FAD-supplemented PvdA. 105
Figure 3-61: Crystallization of PvdA**.** 106
Figure 4-1: Newman projections of L-ornithine, D-ornithine and DFM-ornithine. 109
Figure 4-2: The two modes of flavin binding in PHBH. 110
Figure 4-3: Overview of nucleotide-binding and fingerprint motifs in SidA (A) and mFMO (B). 114
Figure 4-4: Schematic presentation of the SidA two-domain architecture. 115
Figure 4-5: Stereo view of a superposition of the conserved $D(X)_3(^{L}/_{F})ATGY(X)_4(^{H}/_{P})$-motif. 118
Figure A-1: Sequence alignment of SidA orthologs of different fungal species 157
Figure A-2: Structure of the flavin adenine dinucleotide (FAD) cofactor. 158
Figure A-3: Structures of the five known covalent flavin linkages to amino acids found in flavoenzymes. 158
Figure A-4: Possible reaction routes of the two-electron reduced flavin cofactor with oxygen. 159
Figure A-5: Hydrogen bonding between FAD and amino acid residues in Phenylacetone monooxygenase from *T. fusca* and FMO from *S. pombe*. 159
Figure A-6: Stereo view of selected regions in the SidA protomer with refined electron density. 163
Figure A-7: Stereo view of the mFMO-dimer (PDB entry: 2vq7). 164

Lebenslauf

Persönliche Daten

Maike Rochon
geb. 1976 in Wipperfürth
deutsch

Schulische Ausbildung

1982 - 1986	Grundschule Halver/Ost
1986 - 1988	Realschule Halver
1988 - 1995	Anne-Frank Gymnasium Halver Abschluss: Abitur (1,4)

Akademische Ausbildung

1995 - 2001	Studiengang: Diplom-Biologie an der Universität Osnabrück Diplomarbeit: *Molekulare Funktionsweise des Typ III-Sekretionssystems in der Flagellenbiosynthese bei E. coli*-K12 Abschluss: Diplom (sehr gut)

Außerakademische Erfahrungen

2001 - 2002	Praktika & Redaktionelle Mitarbeit in den Bereichen Journalismus und Wissenschafts-PR

Wissenschaftliche Laufbahn

2002 - 2004	Wissenschaftliche Hilfskraft am Microbiology and Tumorbiology Center (MTC) des Karolinska Institut in Stockholm Projektschwerpunkt: *Investigation of the Innate Immune Response of Epithelial Cells on Major Components of the Biofilm Matrix of Enterobacteriaceae*
2005	Praktikum am Helmholtz-Zentrum für Infektionsforschung (HZI), Abteilung Strukturbiologie, Braunschweig Projektschwerpunkt: *Internalin A aus Listeria monocytogenes im Komplex mit humanem E-Cadherin*
2005 - 2009	Promotion am Helmholtz-Zentrum für Infektionsforschung (HZI), Abteilung Strukturbiologie, Braunschweig Promotionsthema: *Structural Analysis of the L-Ornithine N^5-Monooxygenase SidA from Aspergillus spp.*

Publikationen/Coautorenschaft

Wollert T., Pasche B., Rochon M., Deppenmeier S., van den Heuvel J., Gruber A. D., Heinz, D. W., Lengeling A. and Schubert W. D. (2007). Extending the host range of *Listeria monocytogenes* by rational protein design. Cell. **129**(5): 891-902

Rochon M. and Römling U. (2006). Flagellin in combination with curli fimbriae elicits an immune response in the gastrointestinal epithelial cell line HT-29. *Microbes Infect*. **8**: 2027-33

Wang X.*****, Rochon M.*****, Lamprokostopoulou A., Lünsdorf H., Nimtz M. and Römling U. (2006). Impact of biofilm matrix components on interaction of commensal *Escherichia coli* with the gastrointestinal cell line HT-29. *Cell Mol Life Sci.* **63**: 19-20 (*geteilte Erstautorenschaft)

Weber-Sparenberg C., Pöplau P., Brookman H., Rochon M., Möckel C., Nietschke M. and Jung H. (2006). Characterization of the type III export signal of the flagellar hook scaffolding protein FlgD of *Escherichia coli*. *Arch Microbiol*. **4**: 307-16